Investigations of the mechanisms of action of human small heat-shock proteins against amyloid fibril formation and pre-formed amyloid fibrils

Emily Selig

Submitted in total fulfilment of the requirements of the degree of Doctor of Philosophy

March 2020

Department of Biochemistry and Molecular Biology Bio21 Molecular Science and Biotechnology Institute, The University of Melbourne

Abstract

Small heat-shock proteins (sHSPs) are ubiquitously expressed molecular chaperones that protect the proteome against proteostasis failure. sHSPs comprise a conserved α-crystallin domain (ACD) flanked by variable N- and C-terminal regions (NTR and CTR, respectively). Heterogenous intermolecular interactions involving the NTR and CTR of sHSPs give rise to polydisperse ensembles of oligomers that readily exchange subunits. This polydispersity renders sHSPs refractory to biophysical characterization by X-ray diffraction and cryogenic electron microscopy, however the ACD can be crystallized. As such, much of the structural information regarding sHSPs has been derived from biophysical studies of this domain. The ACD adopts a β-sandwich fold and forms antiparallel dimers via an extended β-strand, creating a shared β-sheet between the two subunits. sHSP oligomers are widely regarded to act as storage forms of these chaperone-active, exchangeable dimers. Since ACD-only constructs form dimers, they have become widely used tools for investigating the chaperone properties of sHSP dimers. However, it is becoming evident that the NTR and CTR are also required for chaperone activity, and the exchange of sHSP monomers from oligomers has been observed. The chaperone function(s) of the monomers are largely unknown. We and others have begun to characterize the ACD monomer via NMR and sedimentation velocity analytical ultracentrifugation.

The first part of this thesis investigates the functional contributions of the three regions of sHSPs, the NTR, ACD and CTR. This was achieved by comparing the chaperone activities of various constructs of human αB-crystallin (αB-C, HSPB5) and heat-shock 27 kDa protein (Hsp27, HSPB1) during amyloid formation by α-synuclein and apolipoprotein C-II. Inhibition of the nucleation phase of amyloid fibril formation and disaggregation of mature fibrils was found to be dependent on the NTR and/or CTR of αB-C and the NTR of Hsp27. Both the NTR and CTR are required for forming strong interactions with fibrils and the CTR appears to play an important role in mediating lateral fibril-fibril association, which sequesters pre-formed fibrils into larger aggregates, a function that is believed to be cytoprotective. We conclude that important chaperone activities in inhibiting amyloid formation and in mediating interactions of sHSPs with amyloid fibrils are conferred by the NTR and CTR of these two sHSPs and that subunit exchange from sHSP oligomers likely regulates some of these chaperone functions. Despite this,

the ACD also possesses some chaperone activity against amyloid formation and this was investigated in the second part of this thesis.

In the second part of this thesis, we investigated the interaction of αB-C ACD with apolipoprotein C-II and α-synuclein amyloid fibrils using NMR. Significant resonance broadening was observed in the presence of amyloid fibrils, indicative of an ACD-fibril interaction. We subsequently demonstrated, by varying the concentration of fibril ends, that the ACD exhibits a preference for binding to fibril ends. We also demonstrate that both the ACD dimer and the ACD monomer can be observed via solution NMR under conditions that are close to physiological. NMR revealed that that for apolipoprotein C-II, the primary fibril-interacting species is monomeric and implicated the intra-dimer interface as an interactive site. Interestingly, αB-C ACD exhibited distinct modes of binding to monomeric and fibrillar α-synuclein. The αB-C ACD dimer was implicated in binding monomeric α-synuclein via a substrate interactive site distal to the dimer interface, while the αB-C ACD monomer appeared to interact with fibrillar α-synuclein. Fibril end binding by the ACD monomer was supported by our mutagenesis studies in which disulfide cross-linked ACD dimers were less effective at inhibiting amyloid fibril elongation and naturally occurring fibril end-to-end joining than non-covalent dimers.

Overall, the results presented here demonstrate the multiple mechanisms sHSPs use to protect cells from the process of amyloid fibril formation and the associated toxicity. The multiple chaperone activities are dependent on all three regions of the protein and the accessibility of these substrate binding sites were shown to depend on the ability of these proteins to dissociate from oligomers into various sub-oligomeric forms including monomers and dimers. Our results therefore provide further evidence for the dynamic nature of sHSP assemblies and the importance of this dynamism for substrate binding and chaperone function.

Declaration

This is to certify that

1. The thesis comprises only my original work towards the PhD,

2. Due acknowledgment has been made in the text to all other material used,

3. The thesis is less than 100,000 words in length, exclusive of tables, maps, bibliographies and appendices.

Emily Selig

Awards, presentations and publications

Awards:

Research Training Program Scholarship, Department of Education, Australian Government, Administered by The University of Melbourne	2016 - 2020
Travel Grant, 2018 FASEB Conference on Protein Folding in the Cell	2018
Postgraduate Travel Grant, Department of Biochemistry and Molecular Biology, Faculty of Medicine, Dentistry and Health Sciences, The University of Melbourne	2018

Oral Presentations:

Melbourne Protein Group Student Symposium, Melbourne, Victoria, Australia	17th July 2019
FASEB Protein Folding in the Cell conference, Olean, NY, USA	23rd July 2018
Proteostasis and Disease Symposium, Wollongong, NSW, Australia	21st November 2017
PhD Oration, Melbourne, VIC, Australia	20th November 2019

Poster presentations:

Melbourne Protein Group Student Symposium, Melbourne, Victoria, Australia	2016 – 2018
Lorne Protein Structure and Function Conference, Lorne, Victoria, Australia	2016 – 2020

Publications:

- Cox, D., Selig, E., Griffin, M.D.W., Carver, J.A., Ecroyd, H. (2016) "Small heat shock proteins prevent alpha-synuclein aggregation via transient interactions and their efficacy is affected by the rate of aggregation." *J. Biol. Chem.* 2016. 291(43): p. 22618-22629.
- Mobbs, J. I., Di Paolo, A., Metcalfe, R. D., Selig, E., Stapleton, D. I., Griffin, M. D. W., Gooley, P. R.

(2018) "Unravelling the Carbohydrate-Binding Preferences of the Carbohydrate-Binding Modules of AMP-Activated Protein Kinase." *Chembiochem*. 2018. **19**(3): p. 229-238.

- Selig, E., Zlatic, C.O., Cox, D., Mok, Y., Gooley, P.R., Ecroyd, H.E., Griffin, M.D.W. "N- and C-terminal regions of αB-crystallin and Hsp27 mediate inhibition of amyloid nucleation, fibril binding and fibril disaggregation." *J. Biol. Chem.* 2020. (Chapter 3 of this thesis, published online).

Acknowledgements

Firstly, I am extremely grateful to have had the opportunity to work for five years with my primary supervisor, Associate Professor Mike Griffin. You have very generously and patiently taught me both the theoretical and practical aspects of most of the techniques that I used throughout this thesis. I thank-you firstly for allowing me to work on a difficult project like this. Even though I do not always show it, the challenges I've faced both intellectually and technically in this project is what made it all the more fun for me, as I have a tendency to get bored easily. Together, I believe we worked through difficult research questions and devised useful and interesting experiments for answering these questions. Throughout this project you always gave me a lot of academic freedom to develop my own research questions and satisfy my own curiosity, however you always redirected me if my research took off on too much of a tangent! I am also very grateful for the time you have taken to improve my ability to present my work both orally and in written form. Lastly, in times when my confidence was down and I felt stressed and unhappy, you helped me get back on track with encouragement and kindness. I thank-you so much, Mike, for allowing me to be part of your research group for these years.

It has also been my pleasure to work with my secondary supervisor Professor Paul Gooley for a number of years. Paul also has a very curious and inquisitive mind. So much so, that you completely changed the focus of my 3rd year undergraduate project after reading a "very interesting chapter" of a book. However, I am very grateful for the curiosity you have brought to the table in this project. You got me thinking about my work in different ways and have consequently driven a lot of the work presented here, particularly in Chapter 4. Another great thing about working with you is that you have only a small tolerance for research that is presented badly (in written or oral form). Consequently, you have greatly improved my writing and presentation skills. Thank-you so much Paul.

It was also my great luck to be able to work with Professor Heath Ecroyd from the University of Wollongong during my candidature. Heath provided a large number of the materials required for us to start this project when I joined the group in 2015. However, more valuable to me is the kindness, encouragement and advice you have given me on countless occasions throughout this project, even though I am not officially a student of yours. An example of this is when you allowed me to conduct

some experiments in your lab for three weeks in 2019. Additionally, the numerous Skype calls we have had have been invaluable to me and I thank-you so much for making the time for me.

I would also like to thank the other members of my PhD committee: Danny Hatters, Katrina Binger and Sally Gras for their advice regarding my PhD project and also general career advice, which I hope I can make use of in the near future.

I would also like to thank all the members of the Griffin lab, past and present who have made my time here so enjoyable. In particular, I want to thank Courtney Zlatic, Riley Metcalfe and Cameron Oppy. Courtney is one of those rare people who is completely selfless and seems to derive a great sense of purpose from helping others. You taught me so much in the lab, advised me a great deal in relation to this thesis and helped improve my presentation and writing skills, but beyond that you have helped me in so many other areas of science and life. I feel incredibly lucky to have been able to work with you these years and call you a friend. Riley is a brilliant scientist and someone I admire a lot. I have definitely learnt a lot from you about how to communicate better with computers! You and I often approach research questions from different angles, and as a consequence of listening to your opinions (whether I asked for them or not…!), I have learnt a lot and gained some new perspectives. Additionally, you have taught me a lot about a variety of biophysical techniques that I have not used as extensively as you. Cameron Oppy is a very funny and interesting character, and I'm pretty sure that everyone loves having him around. It's been great to see you develop as a scientist and I am sure you will do well. I especially appreciate you for your Nokia phone, your hand drawn google maps, and our shared affinity for free food, however you are better at finding it than me!

I thank also two unofficial members of the Griffin Lab – Yee-Foong Mok (Melbourne Protein Characterisation) and Tim Ryan (Australian Synchrotron). Mok is the protein-protein interactions guru and has assisted me with every single piece of AUC data and CD data presented in this thesis, as well as assisting me with other equipment such as centrifuges and, on occasion, AKTAs. Thank-you so much for the hours and hours of assistance and technical help. One of my aims for my candidature was to get you to laugh at one of my jokes, I think I succeeded a few times! Tim Ryan is the SAXS wizard. We are all so grateful for your willingness to help us in the face of all sorts of technical challenges that can arise when collecting SAXS data, sometimes at very odd hours of the day/night! Thank-you also for your advice in generating various types of models from my SAXS data.

I am also extremely grateful to two postdocs at Bio21, Dezerae Cox and Ashish Sethi. You are both brilliant scientists who have advised me in relation to the work presented here and also given me valuable career advice, especially recently while I have been searching for jobs. You are both so generous with your time and feedback and I really admire you both as excellent early career researchers.

I want to thank all the members of the Tilley, Stojanovski and Gooley labs. In many ways it does not feel like we are from different research groups but are actually part of a larger group who work well together, share equipment, reagents and expertise. In particular I want to mention Yilin Kang, Laura Fielden, Tom Jackson, and Alex Anderson. Yilin is such a brilliant young scientist I can only look up to her in admiration. Your work ethic, and the way you seem to never make a mistake are truly amazing. I know you will be a successful and brilliant scientist. Laura is one of the kindest people I have ever met, it has been lovely to work alongside you these five years and see you develop into a great scientist and witness your success. I will miss you and playing netball with you when we are both no longer here. Tom and Alex are hilarious. Tom has an endless ability to perform karaoke to the radio, which permanently plays 80s hits. The two of you in combination can result in some very weird, but very funny banter. Thanks for "educating" me about flat earth theory, my world perspective has been forever changed for better or for worse.

In addition to my lab buddies, I want to thank all my friends within Bio21 and outside of Bio21. There are too many of you to mention you all, sorry! However, I want to mention my best friend, Brett. I'm so glad you can put up with me and my stressful personality! Thanks for always, always being there for me. I don't know what I would do without you.

Lastly, and most importantly, I want to thank my parents and my brother, Nicholas. None of you truly understand exactly what it is that I've been doing for the past five years but you love me all the same. Mum and Dad, there is no way I could've achieved half of what I have achieved without your help and love. I would have to exceed the word limit of this thesis to express just what you have done for me in my life, to raise me and provide me with great opportunities. I am sure I was not an easy child to raise, and even as an adult I'm sure I give you a fair deal of grief. I want to dedicate this work to you, Mum, Dad and Nicholas.

Abbreviations

Å	Ångström
AA	Amyloid A
αB-C	αB-crystallin
Aβ	Amyloid-β
ACD	α-Crystallin domain
AD	Alzheimer's disease
ADH	Alcohol dehydrogenase
AFM	Atomic force microscopy
AL	Amyloid light-chain
Amp	Ampicillin
ApoC-II	Apolipoprotein C-II
APP	Amyloid precursor protein
α-Syn	α-Synuclein
AUC	Analytical ultracentrifugation
β_2-m	β_2-microglobulin
BSA	Bovine serum albumin
CD	Circular dichroism
C. elegans	*Caenorhabditis elegans*
CPMG	Carr-Purcell-Meiboom-Gill pulse train
c(s)	Continuous sedimentation coefficient distribution model
CSP	Chemical shift perturbation
CTR	C-terminal region
CV	Column volume
D_2O	Deuterium oxide
DLB	Dementia with Lewy bodies
DLS	Dynamic light scattering
D. melanogaster	*Drosophila melanogaster*

DNA	Deoxyribonucleic acid
DTT	Dithiothreitol
E. coli	*Escherichia coli*
EDTA	Ethylenediaminetetraacetic acid
EM	Electron microscopy
ESI	Electrospray ionisation
FID	Free induction decay
FRET	Fluorescence resonance energy transfer
GuHCl	Guanidine hydrochloride
HCl	Hydrochloric acid
HDL	High density lipoprotein
HIC	Hydrophobic interaction chromatography
HSP	Heat-shock protein
Hsp27	Heat-shock 27 kDa protein
HSQC	Heteronuclear single quantum coherence
Htt	Huntingtin protein
IPTG	Isopropyl β-D-1-thiogalactopyranoside
Kan	Kanamycin
LB	Luria broth
LC-MS	Liquid chromatography mass spectrometry
LDL	Low density lipoprotein
ls-g*(s)	Sedimentation coefficient distribution by least-squares boundary model
$MgCl_2$	Magnesium chloride
μM	Micromolar
mM	Millimolar
MS	Mass spectrometry
MSA	Multiple system atrophy
MW	Molecular weight
NAC	Non amyloid-β component

NaCl	Sodium chloride
NFT	Neurofibrillary tangle
NH_4Cl	Ammonium chloride
NMR	Nuclear magnetic resonance
NTR	N-terminal region
OD	Optical density
PD	Parkinson's disease
PDB	Protein data bank
PEI	Polyethyleneimine
pK_A	Negative base-10 logarithm of the acid dissociation constant
PMSF	Phenylmethylsulfonyl fluoride
ppm	Parts per million
R_2	Transverse relaxation rate
R_g	Radius of gyration
ROS	Reactive oxygen species
rpm	Revolutions per minute
S	Svedberg
SAXS	Small angle X-ray scattering
S. cerevisiae	*Saccharomyces cerevisiae*
SD	Standard deviation
SDS-PAGE	Sodium dodecyl sulfate polyacrylamide gel electrophoresis
SEC	Size exclusion chromatography
SEM	Standard error of the mean
sHSP	Small heat-shock protein
SOD1	Superoxide dismutase 1
ssNMR	solid state nuclear magnetic resonance
SV	Sedimentation velocity
T_1	Longitudinal relaxation time
T_2	Transverse relaxation time

T_{50}	Time to half-maximal aggregation
TCEP	Tris(2-carboxyethyl)phosphine
TEM	Transmission electron microscopy
TEV	Tobacco etch virus
ThT	Thioflavin T
T_{lag}	Lag time
TOF	Time of flight
Tris	Tris(hydroxymethyl)aminomethane
UPS	Ubiquitin-proteasome system
UV	Ultraviolet
VLDL	Very low-density lipoprotein
WT	Wild type

Table of Contents

Abstract.....*iii*

Declaration.....*v*

Awards, presentations and publications.....*vi*

Acknowledgements.....*viii*

Abbreviations.....*xi*

List of Tables.....*xx*

List of Figures.....*xxii*

1 Chapter 1: Introduction 28

1.1 Protein folding and misfolding..... 29

1.1.1 Protein folding 29

1.1.2 Protein folding in vivo 31

1.1.3 Protein misfolding and aggregation 31

1.2 Protein aggregation in human diseases 33

1.2.1 Protein conformational diseases 35

1.2.2 The structure and properties of amyloid 35

1.2.3 The generality and specificity of amyloid fibril formation 37

1.2.4 Amyloid fibril formation: nucleation-dependent polymerization 37

1.2.5 The additional components of amyloid deposits 39

1.2.6 The toxic species 40

1.2.7 α-Synuclein and disease 41

1.2.8 Aggregation of α-synuclein 42

1.2.9 Biophysical characterization of α-synuclein fibrils 44

1.2.10 Apolipoprotein C-II and disease..... 45

1.2.11 Biophysical characterization of apolipoprotein C-II aggregation..... 45

1.3 Overview of the proteostasis network 46
1.3.1 The role of molecular chaperones 47
1.3.2 The HSP40/DNAJ family 48
1.3.3 The HSPA/HSP70 and HSPH/HSP110 families 48
1.3.4 The HSPC/HSP90 family 49
1.3.5 The HSPD/E chaperonins 49
1.3.6 The CCT/TRiC chaperonin 50
1.3.7 The HSPB/sHSP family 50
1.3.8 Protein degradation pathways 51
1.3.9 Proteostasis capacity throughout the human lifespan 52
1.4 How chaperones modulate amyloid formation 53
1.4.1 Inhibition of primary nucleation 54
1.4.2 Inhibition of secondary nucleation and elongation 55
1.4.3 Chaperone-mediated disaggregation 57
1.5 Small heat-shock proteins as molecular chaperones 58
1.5.1 The structure of small heat-shock proteins 58
1.5.2 The effects of post-translational modifications and amino acid mutations on the quaternary structure of small heat-shock proteins 63
1.5.3 Challenges in understanding the mechanisms of action of sHSPs 64
1.5.4 Small heat-shock proteins bind multiple species in the amyloid formation pathway 65
1.5.5 Is the ACD sufficient for chaperone activity? 66
1.6 Scope of project and aims 67
2 Chapter 2: Materials and Methods 70
2.1 Materials 71

2.2 Methods 72
2.2.1 In vitro mutagenesis 72
2.2.2 Cell cultures 73
2.2.3 Preparation and purification of apoC-II from bacterial inclusions 73
2.2.4 Expression and purification of αB-C ACD and Hsp27 ACD C137S 74
2.2.5 Expression and purification of αB-C ACD E117C, αB-C ACD C154 and Hsp27 ACD 75
2.2.6 Expression and purification of α-synuclein 75
2.2.7 Expression and purification of WT αB-C, αB-C E117C, WT Hsp27 and Hsp27 C137S 76
2.2.8 Expression and purification of Hsp27-3D 77
2.2.9 Expression and purification of Hsp27-3DΔCTR 78
2.2.10 Isotope labelling of αB-C ACD 79
2.2.11 Estimation of protein purity and protein mass 80
2.2.12 Fibril sonication 81
2.2.13 Circular dichroism spectroscopy 82
2.2.14 ApoC-II and α-syn amyloid formation using ThT fluorescence assays 82
2.2.15 Fibril pelleting assays using a sucrose cushion 84
2.2.16 Fluorescent apoC-II fibril pelleting assay 85
2.2.17 Sedimentation velocity analysis 85
2.2.18 Turbidity assays 88
2.2.19 Transmission electron microscopy 88
2.2.20 Precipitation of His-αB-C ACD using nickel-NTA resin 89
2.2.21 NMR spectroscopy 89
2.2.22 Small angle X-ray scattering 99

3 Chapter 3: The roles of the N- and C-terminal regions of sHSPs in inhibiting amyloid fibril formation……. 100

3.1 Abstract 101

3.2 Introduction 101

3.3 Results 104

3.3.1 The effects of full-length and truncated constructs of Hsp27 and αB-C on α-syn amyloid formation in vitro 104

3.3.2 The effects of full-length and truncated constructs of Hsp27 and αB-C on α-syn and apoC-II fibril elongation 107

3.3.3 The association of sHSPs with amyloid fibrils..... 111

3.3.4 The time-course of amyloid fibril binding by full-length and NTR+ACD sHSP constructs…….. 113

3.3.5 The dissociation of apoC-II amyloid fibrils induced by sHSPs 115

3.3.6 The effects of fibril binding by sHSPs on the size distributions of pre-formed amyloid fibrils…… 117

3.4 Discussion..... 121

3.5 Conclusions 128

3.6 Supplementary information..... 130

4 Chapter 4: The role of the ACD in inhibiting amyloid fibril elongation..... 172

4.1 Abstract 173

4.2 Introduction 174

4.3 Results 175

4.3.1 The α-crystallin domain of αB-crystallin halts apoC-II amyloid fibril growth and end-to-end joining……. 175

4.3.2 The ACD of αB-C transiently interacts with the ends of amyloid fibrils 183

4.3.3 Detection of αB-C ACD dimer-monomer exchange at pH 7.4 190
4.3.4 The αB-C ACD monomer binds apoC-II fibrils 200
4.3.5 αB-C ACD interacts with monomeric and fibrillar α-syn via distinct binding sites..... 205
4.3.6 αB-C ACD and Hsp27 ACD dimers can be cross-linked via an inter-subunit disulfide bridge..... 214
4.3.7 Disulfide cross-linking regulates the chaperone activity of αB-C ACD and Hsp27 ACD ... 222
4.4 Discussion 228
4.5 Conclusions 237
4.6 Supplementary information..... 239
5 Chapter 5: General Discussion 256
5.1 Rationale for this study 257
5.2 sHSPs inhibit amyloid fibril formation using multiple substrate interactive sites 258
5.3 N- and C-terminal regions of sHSPs and their interactions with amyloid fibrils..... 259
5.4 ACD interactions with amyloid fibrils 261
5.5 A model for the interactions of sHSPs with aggregation prone proteins 263
5.6 Potential similarities between sHSPs and other ATP-independent molecular chaperones..... 264
5.7 Why this study is important..... 266
5.8 Future Directions 267
5.9 Concluding remarks 269
6 References..... 270

Tables

Chapter 1

Table 1.1 Proteins/peptides that form amyloid associated with disease……34

Chapter 2

Table 2.1 Oligonucleotide sequences for the forward and reverse primers used for mutagenesis of sHSP constructs……72

Chapter 3

Supplementary Table 3.1 One-way ANOVA test results of Tlag and T50 parameters derived from results of unseeded α-syn amyloid formation kinetics in the presence or absence of the various sHSP constructs.....132
Supplementary Table 3.2 Weight-average sedimentation coefficients of sHSP constructs……136
Supplementary Table 3.3 Weight-average fibril sedimentation coefficients of pre-formed apoC-II fibrils incubated with αB-C constructs.....152
Supplementary Table 3.4 Weight-average fibril sedimentation coefficients of pre-formed apoC-II fibrils incubated with Hsp27 constructs.....154
Supplementary Table 3.5 Weight-average fibril sedimentation coefficients of pre-formed apoC-II fibrils incubated with Hsp27-3D.....156
Supplementary Table 3.6 Weight-average fibril sedimentation coefficients of pre-formed apoC-II fibrils incubated with WT Hsp27 for 0 hours.....158
Supplementary Table 3.7 Weight-average fibril sedimentation coefficients of pre-formed apoC-II fibrils incubated with Hsp27-3DΔCTR.....160
Supplementary Table 3.8 Weight-average fibril sedimentation coefficients of pre-formed apoC-II fibrils incubated with BSA.....162
Supplementary Table 3.9 Time to half maximal change in turbidity (T50) for each replicate and average T50 for α-syn fibrils incubated with FL Hsp27 constructs.....168

Chapter 4

Table 4.1 Weight-average fibril sedimentation coefficient alone or in the presence of αB-C constructs.....179

Table 4.2 Sedimentation velocity analysis of apoC-II fibril fragments at 20°C and 10°C.....182

Supplementary Table 4.1 ApoC-II fibril size distributions with αB-C constructs added during fibril formation obtained at 5 hours after the initiation of fibril assembly.....240

Supplementary Table 4.2 ApoC-II fibril size distributions with αB-C constructs added during fibril formation obtained at 72 hours after the initiation of fibril assembly.....240

Figures

Chapter 1

Figure 1.1 The energy landscape for protein folding 30
Figure 1.2 Examples of molecular models for the structures of amyloid fibrils 33
Figure 1.3 The cross-β structure of amyloid fibrils. 36
Figure 1.4 The nucleation-dependent polymerization mechanism of amyloid fibril formation 39
Figure 1.5 Schematic representation of the regions of α-syn. 42
Figure 1.6 Two examples of cryo-EM models generated using full-length α-synuclein 45
Figure 1.7 The positive feedback loop contributing to the failure of the proteostasis system under conditions of chronic stress and/or ageing 53
Figure 1.8 The mechanisms by which chaperones can modulate amyloid formation 54
Figure 1.9 Domain architecture of the ten human sHSPs, HSPB1-10 60
Figure 1.10 Crystal structures and atomic models for sHSPs 62
Figure 1.11 Depiction of the hierarchical assembly of sHSP oligomers from monomers and dimers 62
Figure 1.12 The effects of phosphorylation or serine substitution on the oligomeric size and chaperone activity of Hsp27 64
Figure 1.13 Crystal structure of the αB-C ACD dimer 67
Figure 1.14 Schematic representing the domain composition and quaternary structures of the sHSP constructs used for aim 1 69

Chapter 2

Figure 2.1 Structure of Thioflavin T 83
Figure 2.2 Schematic representing the sedimentation velocity analysis of molecules in solution under centrifugal force 86
Figure 2.3 Dependence of the energy levels of nuclear spin states of a ½ spin nuclei as a function of the magnetic field strength 90
Figure 2.4 Schematic for the conversion of the time-domain FID into frequency domain data via the Fourier transform. 91

Figure 2.5 Schematic for the representation of the two types of nuclear spin relaxation 93
Figure 2.6 Schematic for the processing of 2-dimensional NMR data..... 94
Figure 2.7 Stability of αB-C ACD over long NMR experiments..... 97

Chapter 3

Figure 3.1 Kinetics of unseeded α-syn amyloid formation in the presence of sHSPs..... 106
Figure 3.2 Kinetics of seeded α-syn amyloid formation and unseeded apoC-II amyloid formation in the presence of sHSPs 110
Figure 3.3 Fibril pelleting assay of pre-formed fibrils incubated with sHSP constructs 112
Figure 3.4 Time course pelleting assay of pre-formed amyloid fibrils incubated with full-length sHSP constructs 114
Figure 3.5 Analysis of the time-course of apoC-II fibril dissociation by WT αB-C..... 116
Figure 3.6 SV-AUC analysis of pre-formed apoC-II fibrils incubated with various sHSP constructs..... 119
Figure 3.7 Analysis of light scattering by α-syn amyloid fibrils in the presence of sHSPs 121
Figure 3.8 Two models for the mechanism of fibril binding and lateral tangling induced by sHSPs 126
Supplementary Figure 3.1 Raw ThT kinetics data of unseeded α-syn alone or with sHSP constructs……130
Supplementary Figure 3.2 ThT assay of unseeded α-syn alone, + BSA and each sHSP construct incubated alone……131
Supplementary Figure 3.3 Transmission electron microscopy of unseeded α-syn fibrils formed alone or in the presence of sHSPs……133
Supplementary Figure 3.4 SV-AUC analysis of sHSP constructs……135
Supplementary Figure 3.5 SAXS analysis of αB-C ACD at a concentration of 755 μM, pH 8.0……137
Supplementary Figure 3.6 SAXS analysis of Hsp27 ACD at a concentration of 726 μM, pH 8.0……138
Supplementary Figure 3.7 SAXS of Hsp27-3DΔCTR at a concentration of 253 μM, pH 8.0……139
Supplementary Figure 3.8 SAXS of Hsp27-3D at a concentration of 220 μM, pH 8.0……140
Supplementary Figure 3.9 Raw ThT kinetics data of seeded α-syn alone or with sHSP constructs……141
Supplementary Figure 3.10 ThT assay of seeded α-syn alone, + BSA and each sHSP construct incubated alone……143

Supplementary Figure 3.11 Raw ThT kinetics data of unseeded apoC-II alone or with sHSP constructs……144
Supplementary Figure 3.12 ThT assay of apoC-II incubated alone, + BSA and each sHSP construct incubated alone……145
Supplementary Figure 3.13 Transmission electron microscopy of unseeded apoC-II fibrils formed alone or in the presence of sHSP constructs……146
Supplementary Figure 3.14 Raw SV-AUC data of pre-formed apoC-II fibrils incubated with WT αB-C for 0-20 hours……147
Supplementary Figure 3.15 Pelleting assay of pre-formed apoC-II fibrils incubated alone or with 12.8 µM or 100 µM WT Hsp27 or Hsp27-3D……149
Supplementary Figure 3.16 Pelleting assay of preformed α-syn fibrils incubated alone or with WT αB-C……150
Supplementary Figure 3.17 Raw SV-AUC data of pre-formed apoC-II fibrils incubated with WT αB-C or αB-C ACD……151
Supplementary Figure 3.18 Raw SV-AUC data of pre-formed apoC-II fibrils incubated with Hsp27 constructs……153
Supplementary Figure 3.19 Raw SV-AUC data of pre-formed apoC-II fibrils incubated alone or with 6.4 µM Hsp27-3D……155
Supplementary Figure 3.20 Raw SV-AUC data of pre-formed apoC-II fibrils incubated alone or with WT Hsp27 for 0 hours……157
Supplementary Figure 3.21 Raw SV-AUC data of pre-formed apoC-II fibrils incubated alone or with Hsp27-3DΔCTR……159
Supplementary Figure 3.22 SV-AUC data of pre-formed apoC-II fibrils incubated alone or with BSA……161
Supplementary Figure 3.23 Transmission electron microscopy of preformed apoC-II fibrils incubated with sHSP constructs……164
Supplementary Figure 3.24 Raw OD data of α-syn fibrils incubated alone, and with WT Hsp27 or Hsp27-3D……166
Supplementary Figure 3.25 Transmission electron microscopy of pre-formed α-syn fibrils incubated alone or in the presence of sHSP constructs……170

Chapter 4

Figure 4.1 Pairwise sequence comparison of the amino acid sequences of WT αB-C and WT Hsp27.... 175
Figure 4.2 WT αB-C and αB-C ACD inhibit apoC-II fibril formation when added during the elongation phase 177
Figure 4.3 Analysis of the lengths of apoC-II fibrils formed in the presence of WT αB-C or αB-C ACD ... 178
Figure 4.4 αB-C ACD inhibits apoC-II fibril end-to-end joining at sub-stoichiometric molar ratios..... 181
Figure 4.5 ApoC-II fibrils are not co-precipitated with 6 x His-tagged αB-C ACD using nickel-NTA resin. ..... .183
Figure 4.6 αB-C ACD interacts preferentially with the ends of apoC-II fibrils..... 189
Figure 4.7 A reduction in pH perturbs the equilibrium between the major and minor state of αB-C ACD 193
Figure 4.8 αB-C ACD transitions between monomer and dimer over the pH range 6.0 – 7.4..... 195
Figure 4.9 Titrating GuHCl perturbs the equilibrium between the minor and major state of αB-C ACD. ..... .198
Figure 4.10 Nuclear spin transverse relaxation rates for assigned peaks and unassigned peaks in the spectra observed for a sample containing 750 μM αB-C ACD, pH 7.4, 25°C. 200
Figure 4.11 In the presence of apoC-II fibrils, peaks corresponding to the minor state are broadened to a greater extent than the peaks corresponding to the major state. 202
Figure 4.12 In the presence of apoC-II fibrils at pH 6.5, peaks corresponding to the minor state are broadened to a greater extent than the peaks corresponding to the major state 205
Figure 4.13 In the presence of monomeric α-syn, peaks corresponding to the major state are broadened to a greater extent than the peaks corresponding to the minor state 209
Figure 4.14 In the presence of fibrillar α-syn, peaks corresponding to the minor state are broadened to a greater extent than the peaks corresponding to the major state 212
Figure 4.15 Meta-analysis of the intensity ratio trends of unassigned peaks across multiple experiments represented as a Venn diagram 214

Figure 4.16 sHSP constructs containing cysteine residues at the intra-dimer interface form disulfide linked dimers *in vitro* 218
Figure 4.17 SV-AUC analysis of sHSP constructs under reducing or non-reducing conditions 221
Figure 4.18 Disulfide cross-linked dimers are less effective inhibitors of apoC-II aggregation than non-linked sHSP constructs 223
Figure 4.19 Disulfide cross-linked dimers are less effective inhibitors of apoC-II fibril elongation than non-linked sHSP constructs 224
Figure 4.20 Disulfide cross-linked dimers are less effective inhibitors of apoC-II fibril end-to-end joining than non-linked sHSP constructs 226
Figure 4.21 Disulfide linked αB-C constructs are more effective inhibitors of α-syn aggregation, while disulfide cross-linked Hsp27 dimers are less effective 227
Figure 4.22 Representation of poorly conserved residues between αB-C ACD and Hsp27 ACD 234
Figure 4.23 Crystal structures of αB-C ACD and Hsp27 ACD 237
Supplementary Figure 4.1 ApoC-II fibril formation kinetics and fibril size distributions with αB-C constructs added during elongation 239
Supplementary Figure 4.2 SV-AUC of apoC-II fibril fragments incubated with BSA, ovalbumin or lysozyme 242
Supplementary Figure 4.3 ^{15}N HSQC overlay of 50 μM αB-C ACD alone in 50 mM sodium phosphate, pH 7.4 before and after sonication 243
Supplementary Figure 4.4 HSQC analysis of 50 μM αB-C ACD in 50 mM sodium phosphate, pH 7.4 alone and in the presence of short or long apoC-II fibrils 246
Supplementary Figure 4.5 ^{15}N HSQC of 750 μM αB-C ACD alone at pH 7.4 and 6.5 247
Supplementary Figure 4.6 ^{15}N HSQC of 25 μM αB-C ACD alone at pH 7.4 and 6.0 248
Supplementary Figure 4.7 ^{15}N HSQC of 750 μM αB-C ACD alone at pH 5.9 and at 25 μM, pH 6.0 249
Supplementary Figure 4.8 ^{15}N HSQC of 100 μM αB-C ACD alone at pH 7.4 and in the presence of 10 mg/mL fragmented apoC-II fibrils 250
Supplementary Figure 4.9 ^{15}N HSQC of 250 μM αB-C ACD alone at pH 7.4 and in the presence of 10 mg/mL fragmented apoC-II fibrils 251
Supplementary Figure 4.10 CD spectroscopy of WT and mutated sHSP constructs 252

Supplementary Figure 4.11 SAXS analysis of Hsp27 ACD at a concentration of 750 μM, pH 8.0 in the presence of 2 mM TCEP……253
Supplementary Figure 4.12 SAXS analysis of Hsp27-3D at a concentration of 220 μM, pH 8.0 in the presence of 2 mM TCEP……254
Supplementary Figure 4.13 ThT fibril formation kinetics of apoC-II alone, + DTT, or + sHSPs constructs +/- DTT……255

Chapter 5

Figure 5.1 A model for the mechanisms used by sHSPs to inhibit amyloid formation and interact with pre-existing fibrils 264

Chapter 1: Introduction

Protein folding, misfolding and the human proteostasis network

1.1 Protein folding and misfolding

1.1.1 Protein folding

Protein folding is the process by which a polypeptide chain comprised of a linear sequence of amino acids acquires its native conformation. Though some proteins are natively unfolded or only fold upon binding to other molecules[1], most proteins adopt defined structures that require folding and assembly. The biological function of these proteins is therefore intimately dependent on correct protein folding. Since Anfsinsen *et al.* demonstrated that ribonuclease could refold into its native conformation *in vitro*[2], the question of how proteins fold has interested physical chemists and biochemists alike. Anfinsen's experiments demonstrated that the native 3-dimensional structures of proteins are encoded in their linear amino acid sequence. He proposed the thermodynamic hypothesis of protein folding whereby the native state is the conformation that minimizes Gibbs free energy, while unfolded conformations have comparably high free energy[3]. This hypothesis required that protein folding be driven by reductions in free energy. While this obeys the laws of thermodynamics, Levinthal calculated that if a polypeptide chain randomly sampled all the conformational space theoretically accessible, it would take years for proteins to fold. This is incompatible with experimental observations that proteins actually fold on the order of seconds[4]. Levinthal reasoned that proteins must fold via defined folding pathways, not via random sampling of all of the conformational space that is theoretically accessible. Thus, in the current paradigm of protein folding, a polypeptide chain is thought to sample a funnel-shaped potential energy landscape, from unfolded chains with high free-energy, through specific folding intermediates until they reach a more compact native state that is lower in free-energy[5], see Fig. 1.1. The forces that define the initial processes of folding are hydrophobic forces, which promote the burial of hydrophobic residues in the interior of a protein's fold[6,7], and to a lesser extent hydrophilic forces including hydrogen-bonding interactions, which contribute to the formation of secondary structure elements[8]. Interactions that are similar to those found in the native structure drive the formation of folding intermediates. Folding intermediates are often metastable and can therefore become kinetically trapped in local energy minima. In order to transition from a folding intermediate to the native state, the protein must overcome these kinetic barriers. If non-native interactions form during the protein folding, misfolded intermediates can accumulate. As with folding intermediates, these species can become kinetically trapped, and therefore misfolded proteins may accumulate. Though some small proteins can fold

spontaneously to their native state, most cannot because the number of possible conformations they can adopt is extremely large (~10^{49} for a 100 residue protein[9]). Large proteins with complex structures are particularly prone to non-native interactions because they are more likely to expose hydrophobic residues to the solvent during folding. Furthermore, in contrast to the thermodynamic hypothesis, it is now generally accepted that the native conformation represents a compromise between thermodynamic stability and the required conformational flexibility[10]. Consequently, the native state may be only marginally more stable than non-native intermediates, and therefore prone to misfolding.

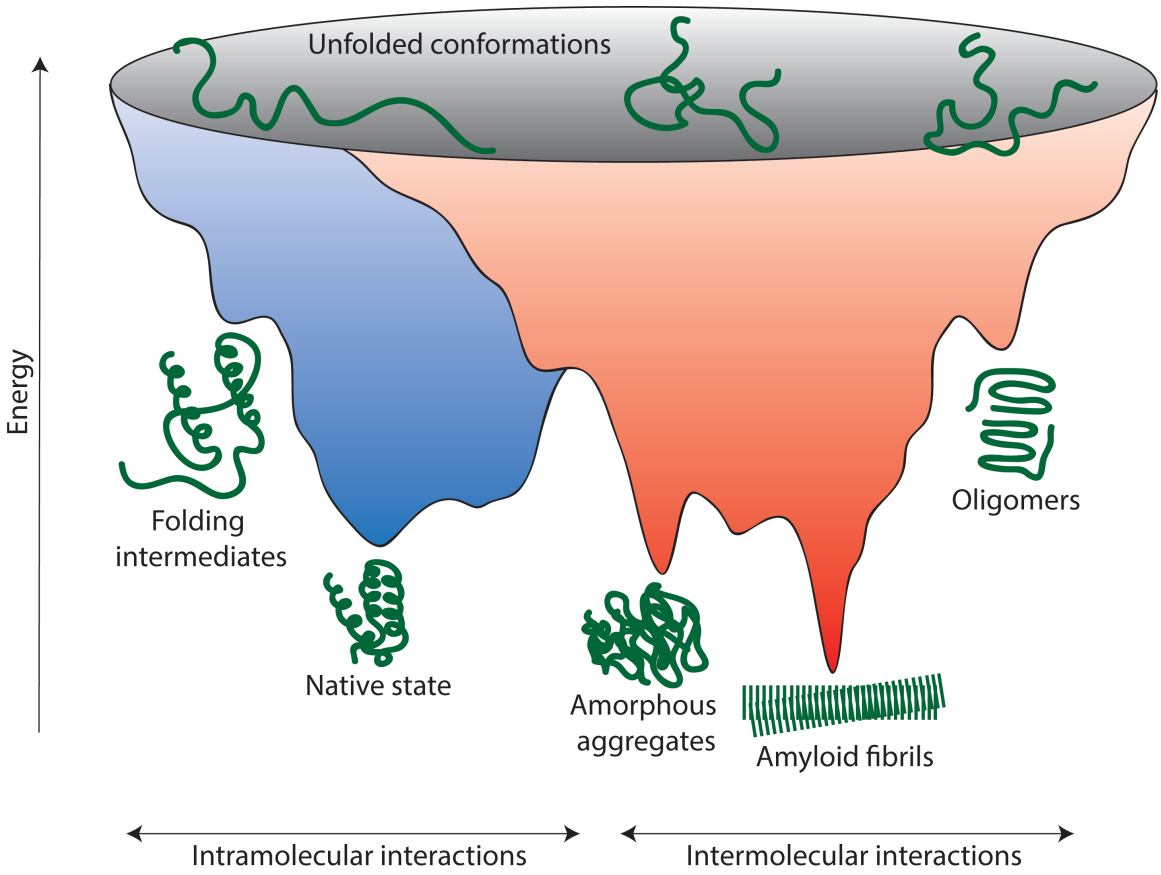


Figure 1.1. The energy landscape for protein folding. The funnel-shaped surface indicates how unfolded polypeptide chains can funnel towards either their native state via the formation of intramolecular contacts, or towards protein aggregates such as amyloid fibrils via the formation of intermolecular contacts. Folding intermediates, and partially misfolded conformations are known to exist at least transiently on route to the formation of either the native state or aggregated states.

1.1.2 Protein folding *in vivo*

In the cell, proteins become folded co-translationally[11–13]; that is, the nascent chain is folded as it is synthesized on the ribosome, or post-translationally in the cytoplasm or in other cellular compartments such as the endoplasmic reticulum (ER)[14]. Further complicating folding *in vivo* is the fact that newly synthesized proteins often require translocation to specific cellular compartments prior to folding. Unlike the theoretical protein folding scenario described above, folding *in vivo* is vectoral since the N-terminus is translated and exits the ribosome before the C-terminus. The exit tunnel from the large ribosomal subunit (~ 100 Å long and 20 Å wide) can accommodate some preliminary protein folding, for example, the formation of α-helices[15]. However, long-range native interactions between the N- and C-terminal regions of the polypeptide chain cannot form, therefore cooperative domain folding[16] is not possible until the polypeptide chain has been released from the ribosome. For large, multidomain proteins, individual domains typically fold sequentially during translation. Sequential folding along with the relatively slow rate of translation in eukaryotes (~ 4 amino acids s^{-1}, slow compared to the rate of domain folding) is thought to prevent the formation of non-native interactions between sequences in separate domains[17], thereby promoting protein folding and reducing the chances of misfolding and aggregation[18]. By comparison, the rate of protein translation in bacteria is ~20 amino acids s^{-1}. The reduced rate of protein translation, along with co-translational domain folding in eukaryotes may have facilitated the evolution of larger proteins with more individual domains (on average) as compared to their bacterial orthologs[19,20]. Nevertheless, protein folding, like all complex processes, is not infallible. A polypeptide chain that fails to fold into its native structure typically results in an inactive protein, however in some instances misfolded proteins have toxic functionality, which can impair cellular and organismal viability.

1.1.3 Protein misfolding and aggregation

Misfolded proteins accumulate because of the metastability of the proteome. Conditions that increase cellular stress, such as heat-shock, oxidative stress and toxic agents further affect the delicate balance between natively folded proteins, and misfolded intermediates. Mutations that reduce the metastability of the native state or affect the stability or formation of folding intermediates can also cause misfolded

intermediates to accumulate. While natively folded proteins must unfold to a degree in order to adopt misfolded conformations, intrinsically disordered proteins do not need to unfold and are constantly at risk of misfolding. Consequently, many proteins prone to misfolding in human protein conformational diseases are intrinsically disordered. Misfolded proteins are problematic because surface exposed hydrophobic groups tend to form intermolecular hydrophobic interactions, resulting in protein aggregation. Aggregates can be broadly classified as amorphous (i.e. lacking regular structure) or as amyloid fibrils. Amyloid fibrils are structured aggregates, defined by β-strands that align to form elongated β-sheets, which run parallel to the long axis of the fibril, see Fig. 1.2. The intermolecular β-sheets are particularly thermodynamically stable and may even be more stable than a protein's native conformation. Protein misfolding and aggregation is associated with two distinct types of human disease: loss-of-function and toxic gain-of-function. Loss-of-function diseases are typically the result of mutations that reduce the stability of the encoded protein such that it is prone to degradation. An example of this is cystic fibrosis, which is caused by mutations in both copies of the cystic fibrosis transmembrane conductance regulator (CFTR) protein[21]. The resulting CFTR protein is unstable and prone to degradation[22]. Toxic gain-of-function diseases involve the loss of cell viability thought to be due to the aggregation of metastable proteins. The amyloid-β (Aβ) peptide in Alzheimer's disease (AD)[23], α-synuclein (α-syn) in Parkinson's disease (PD)[24,25] and amylin in type II diabetes[26] are three prominent examples of intrinsically disordered proteins that aggregate in human diseases. Amyotrophic lateral sclerosis and senile systemic amyloidoses are protein conformational diseases in which the aggregating protein is not entirely intrinsically disordered[27,28]. Though heritable mutations can cause these diseases (as is the case for Huntington's disease[29]), or result in early onset forms (as seen in AD[30,31] and PD[32]), the majority of cases are age-dependent but manifest sporadically. Correct protein folding in the presence or absence of these types of mutations is heavily dependent on additional folding factors such as molecular chaperones[33]. The role of molecular chaperones is to assist a protein to overcome kinetics traps and/or prevent the formation of non-native interactions so that they may acquire and maintain their native conformations.

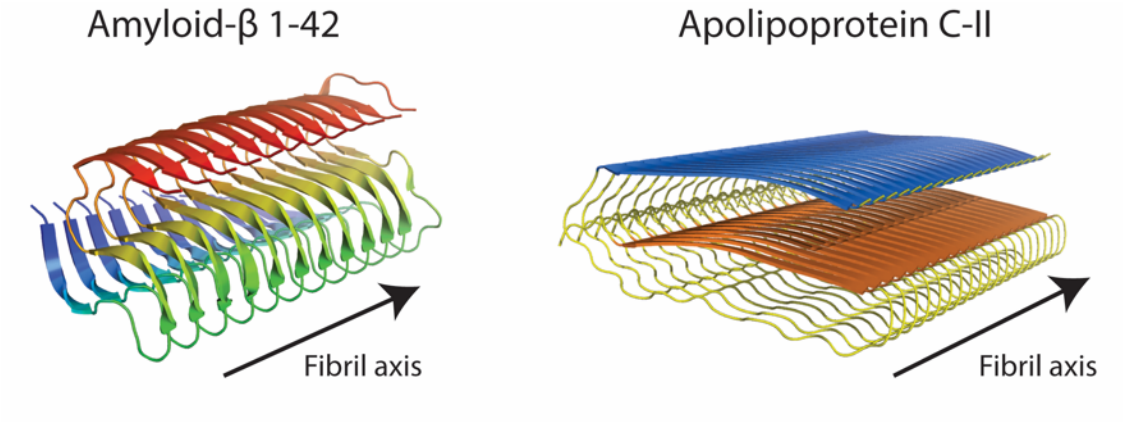


Figure 1.2. Examples of molecular models for the structures of amyloid fibrils. A) Fibrillar model of the Aβ(1-42) peptide (PDB: 2mxu[34]). B) Model of amyloid fibrils formed by apolipoprotein C-II[35]. β-strands run perpendicular to the long axis of the fibril and form intermolecular β-sheets that run parallel to the fibril axis.

1.2 Protein aggregation in human diseases

The term amyloid was first used by a German physician Rudolph Virchow in 1854 to describe the abnormal appearance of tissue derived from the cerebral corpora that exhibited positive iodine staining[36]. The term amyloid was coined because Virchow believed the substance causing the positive iodine staining was cellulose. Subsequently, Alois Alzheimer discovered aggregated proteinaceous deposits in the cerebral cortex of a 56-year-old patient in 1906. Now, the deposition of aggregated protein as extracellular plaques or intracellular inclusions is recognized as a hallmark of a wide variety of neurodegenerative and systemic diseases. Pathological protein aggregates typically consist of amyloid fibrils, however amorphous aggregation is also known to cause disease. For example, amorphous aggregates of crystallin proteins in the lens cause cataracts[37]. Some of the most prevalent protein conformational diseases associated with amyloid formation are summarized in Table 1.1. As a result of their association with a range of age-related and increasingly prevalent diseases, there is great scientific interest in understanding the conversion of proteins from their native state to pathogenic amyloid fibrils.

Table 1.1 Proteins/peptides that form amyloid fibrils associated with disease (Adapted from Chiti and Dobson (2017)[38]).

Protein/peptide	Number of residues	Structure	Primary associated disease(s)	Type of disease
Amyloid-β peptide (Aβ)	40 or 42	Intrinsically disordered	Alzheimer's disease[23]	Neuropathic Sporadic
α-synuclein (α-syn)	140	Intrinsically disordered	Parkinson's disease[39] Dementia with Lewy bodies[40] Multiple system atrophy[41]	Neuropathic Sporadic
Prion protein (PrP)	208	Intrinsically disordered: 1-102. All α, prion-like: 103-208	Creutzfeldt-Jakob disease[42] Fatal insomnia[43] Spongiform encephalopathy[44]	Neuropathic Sporadic Hereditary Infectious Iatrogenic
Microtubule-association protein tau	352-441	Intrinsically disordered	Alzheimer's disease[45] Pick disease[46] Progressive supranuclear palsy[47] Corticobasal degeneration[48] Frontotemporal dementia with parkinsonism[49]	Neuropathic Sporadic
Huntingtin exon 1 (HttEx1)	103-187	Intrinsically disordered	Huntington disease[50]	Neuropathic Hereditary
Immunoglobulin light chain (fragments)	~100	All β, Ig-like	Light-chain amyloidosis[51]	Systemic Sporadic
Immunoglobulin heavy chain (fragments)	~190	All β, Ig-like	Renal heavy-chain amyloidosis[52]	Systemic Sporadic
Serum amyloid A protein	45-104	All α, SAA-like four-helix bundle	Amyloid A (AA) amyloidosis[53]	Systemic Sporadic
Transthyretin	127	All β, prealbumin-like	Senile systemic amyloidosis[54] Familial amyloidotic polyneuropathy[55] Familial amyloid cardiomyopathy[56]	Systemic Sporadic and hereditary
β_2-microglobulin (β_2-m)	99	All β, Ig-like	Dialysis-related amyloidosis[57]	Systemic iatrogenic
Apolipoprotein A-I (fragments)	69-100	Intrinsically disordered	Apolipoprotein A-I amyloidosis[58]	Systemic Hereditary
Apolipoprotein C-II	79	Lipid bound: all α	Apolipoprotein C-II amyloidosis	Systemic

			(mainly renal)[59,60]	Hereditary
Lysozyme	130	α + β, lysozyme fold	Lysozyme amyloidosis[61]	Systemic Hereditary
Islet amyloid polypeptide (IAPP)	37	Intrinsically disordered	Type II diabetes[62]	Localised Sporadic
Insulin	(30 + 21)	All α, insulin-like fold	Injection-localised amyloidosis[63]	Localised iatrogenic

1.2.1 Protein conformational diseases

The amyloidoses are the main subgroup of protein misfolding diseases, in which insoluble amyloid fibrils accumulate in extracellular amyloid plaques or in cytoplasmic inclusions. Amyloidoses are categorized as either local or systemic. In local amyloidosis, amyloid deposition occurs at the site of precursor protein synthesis. In systemic amyloidosis, amyloid is deposited at multiple sites distant from precursor synthesis. Local amyloidoses include type II diabetes[64], and the neurodegenerative diseases AD[65], PD[39], Huntington's disease[50], and transmissible spongiform encephalopathies[66]. Examples of systemic amyloidoses include amyloid light chain (AL) amyloidosis, amyloid A (AA) amyloidosis and senile systemic amyloidosis[67]. Although there is a strong association between disease onset and the appearance of amyloid deposits, the specific cellular mechanisms linking amyloid with disease have not yet been fully determined. For type II diabetes, the islet amyloid polypeptide (IAPP) forms amyloid fibrils that are thought to play a causative role in pancreatic β-cell dysfunction and death[68]. For systemic amyloidoses it is likely that a primary cause of disease is the deposition of large quantities of amyloid in vital organs such as the liver, spleen and kidney[69]. However, in neurodegenerative disorders, the correlation between the disease stage and the total quantity of amyloid deposits is less clear, suggesting that small pre-fibrillar oligomers produced during the initial stages of protein aggregation also contribute to the pathogenicity of these diseases.

1.2.2 The structure and properties of amyloid

Amyloid fibrils appear as filamentous branched or unbranched structures a few nanometers in diameter and can be up to microns in length when viewed using transmission electron microscopy (TEM) or

atomic force microscopy (AFM). Besides a fibrillar morphology, amyloid fibrils also produce a distinct 'cross-β' X-ray fibre diffraction pattern[70] (Fig. 1.3) and exhibit bi-refringence when stained with the amyloid specific dye, Congo red[71]. Amyloid fibrils also bind the dye Thioflavin T (ThT)[72] causing a red-shift to the dyes intrinsic excitation wavelength and an increase in fluorescence emission intensity at 485 nm relative to free dye[73]. Amyloid fibrils consist of many copies of usually identical polypeptide chains, which arrange into intermolecular β-sheets. Each polypeptide chain generally contributes a single β-strand to each β-sheet within the fibril. The β-sheets extend the length of the fibril while the β-strands span the width of the fibril. This cross-β structure gives rise to meridional X-ray diffraction at around 4.7-4.8 Å, which reflects the spacing between β-strands within a β-sheet and equatorial diffraction at ~10 Å, which represents the spacing between the β-sheets (Fig. 1.3)[70]. The number of β-sheets within a fibril varies depending on the amino acid sequence of the precursor protein. For example, apolipoprotein C-II (apoC-II) forms amyloid fibrils with 2 well-ordered β-sheets per fibril[35], while α-syn forms fibrils with four or five β-sheets[74]. Mature amyloid fibrils are usually described as higher order structures in which two or more individual fibrils (usually termed protofibrils) twist around each other, however this is not true for every amyloid system[35].

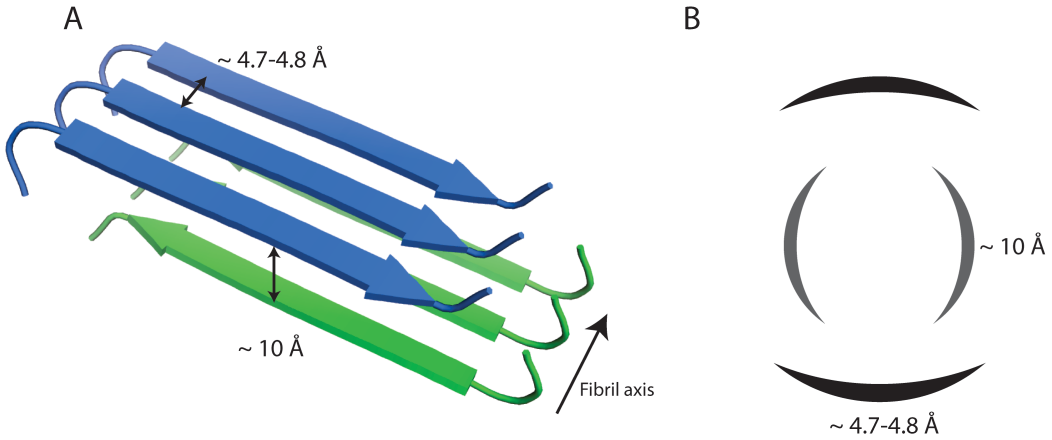


Figure 1.3. The cross-β structure of amyloid fibrils. A) Cartoon representation of an amyloid fibril formed by an 11 residue peptide of Aβ generated using cryo-EM microelectron diffraction (PDB: 5vos[75]). B) The typical X-ray fibre diffraction pattern obtained for amyloid fibrils. Meridional diffraction at 4.7-4.8 Å denotes the spacing between β-strands within a β-sheet and equatorial diffraction at ~10 Å denotes the inter-sheet spacing.

1.2.3 The generality and specificity of amyloid fibril formation

The structure of amyloid is remarkable because of the discovery in the late 1990s that a large variety of proteins lacking sequence, structural or functional similarity can form amyloid *in vitro*[76]. This discovery led to the suggestion that amyloid fibrils represent a thermodynamically stable alternative state that all polypeptide chains can theoretically adopt. The physical basis for this is the propensity for polypeptide chains to form backbone hydrogen bonds; the formation of intermolecular β-sheets is an effective way to achieve this. Furthermore, poly amino acid chains comprised of single amino acids have been shown to form amyloid[77], providing further evidence that the amino acid sequence is not a major determinant of the amyloid-formation propensity of a given protein. However, the amino acid sequence does determine the stability of a protein's native state and the packing of β-sheets within an amyloid fibril core[67]. Consequently, fibrils formed from more than one precursor protein are rare and cross-seeding of amyloid formation (using amyloid seeds formed from a different precursor protein) is ineffective[78]. Amyloid fibrils are also generally formed by small proteins, peptides or proteolytically cleaved fragments of proteins. This is partly because there are physical and chemical constraints on the length of the individual β-strands that comprise the β-sheets. β-strands have an intrinsic propensity to twist (due to the bond angles within the main polypeptide chain[79,80]). In addition to this, the energy penalty for the twisting of wider protofibrils into mature fibrils would be much larger than that for narrower protofibrils. Hence, the widths of these strands are typically limited to 10-20 nanometres.

1.2.4 Amyloid fibril formation: nucleation-dependent polymerization

The kinetics of amyloid fibril formation can broadly be described as reversible nucleation-dependent polymerization. In measuring the kinetics of amyloid formation, three phases can be distinguished: nucleation, elongation and equilibrium (Fig 1.4). The nucleation phase involves the structural rearrangement of a precursor protein from its globular or natively unfolded native state to a state enriched with β-structure that is usually oligomeric. Globular proteins must unfold to a degree in order to form these β-structure enriched states[81]. Though the oligomers are thought to adopt β-sheet structure, the arrangement of the β-strands is structurally distinct from their arrangement in amyloid fibrils[82,83]. Thus, the oligomers undergo further structural rearrangement eventually resulting in the

formation of small, fibrillar seeds. The nucleation phase is the most challenging phase to model mathematically due to the highly stochastic and heterogenous nature of nucleation. The elongation phase is characterized by the rapid addition of soluble precursor proteins to the ends of the fibrillar structures formed during nucleation. Thus the pre-existing seeds act as a template, which catalyse the conversion of soluble proteins into aggregates[84]. This seeding mechanism is analogous to that observed in crystallization. During the equilibrium phase, fibrils can break, rejoin and/or laterally associate, and monomers can continue to dissociate and associate from fibril ends[85–87]. Fibril fragmentation increases the concentration of fibril ends and therefore enhances the overall rate of fibril formation however the rate of elongation of individual fibrils is unchanged. Pre-existing fibrils not only seed further aggregation at their ends but they have also been shown to catalyse so-called secondary nucleation (the formation of new amyloidogenic oligomers) on the surface of the fibril[88,89]. Therefore, fibril fragmentation and secondary nucleation are processes that contribute to the relatively rapid conversion of soluble proteins to aggregates observed *in vitro*. Importantly, this seeding phenomenon is not limited to *in vitro* experiments but is now widely recognized as a major contributing factor to the propagation of protein aggregation and associated toxicity *in vivo*. Rodents expressing transgenic human amyloid precursor protein (APP) generate Aβ plaques spontaneously[90]. Inoculation of healthy rodents with transgenic or patient-derived Aβ plaques has been shown to induce the aggregation of endogenous Aβ and plaque formation[91]. Fragmented fibrils have also recently been demonstrated to propagate protein aggregation not only within cells, but between cells in a prion-like manner. Injection of tau aggregates into tau-transgenic mice stimulates the formation of tau lesions[92]. These lesions also spread from the injection site to neuronally connected areas of the brain, indicating that the tau aggregates can also be transported via neuronal uptake and release. This phenomenon of aggregate seeding and spreading via connected neurons is also observed in α-syn transgenic mice[93], and these mice also develop PD-like symptoms[94]. Therefore, seeding and secondary nucleation effects that can be readily observed *in vitro* are highly relevant processes in the progression of protein conformational diseases characterised by the spreading of protein aggregates.

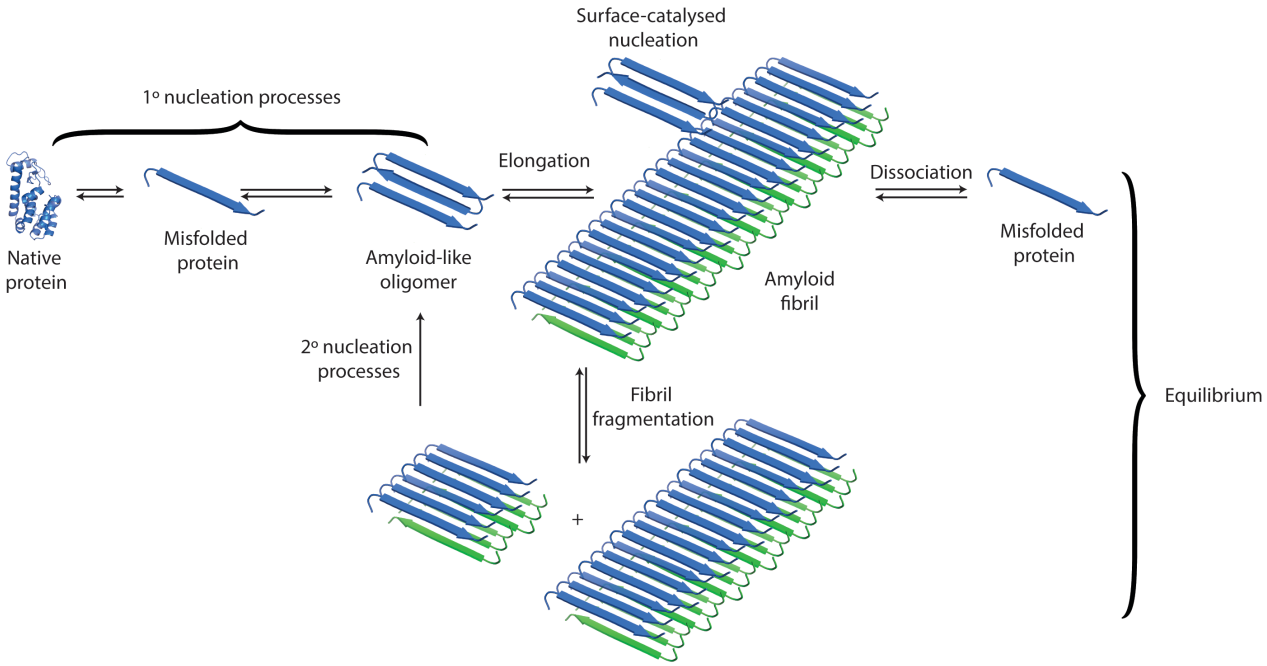


Figure 1.4. The nucleation-dependent polymerization mechanism of amyloid fibril formation. The first stage of amyloid formation is primary nucleation, whereby a natively folded or natively unfolded protein misfolds to form a conformation that is enriched with β-structure. Typically, multiple copies of an identical polypeptide chain that are misfolded will associate to form an oligomer enriched with β-structure. Oligomers undergo structural rearrangement, eventually forming an amyloid seed which elongates at its ends to form amyloid fibrils. Once fibrils are formed, secondary processes such as surface-catalysed secondary nucleation, fibril fragmentation and seeding contribute to the relatively rapid propagation of fibril formation observed both *in vitro* and *in vivo*. At equilibrium, fibrils can continue to break and rejoin, and undergo monomer dissociation and re-association at their ends.

1.2.5 The additional components of amyloid deposits

Amyloid deposits *in vivo* generally comprise additional components beyond fibrillar conformations of single polypeptide chains. Lipids such as cholesterol, cholesterol esters, phospholipids, free fatty acids and triglycerides are typically associated with amyloid plaques[95,96]. The association of these lipids with amyloid deposits is likely one of the reasons amyloid deposits were initially referred to as "lardaceous" deposits. Amyloid plaques can also contain other cellular debris and a variety of proteins that colocalize to amyloid deposits without becoming incorporated into the core amyloid fibril structure. Some examples of these are: Heparan sulfate proteoglycans in AD plaques and neurofibrillary tangles (NFTs)[97,98], apolipoprotein E in extracellular senile plaques and intracellular NFTs[99], sulfated

glycosaminoglycans in amyloid deposits from a range of neurodegenerative and systemic amyloidoses[100], immunoglobulins and complement proteins in senile plaques[101], and the chaperone proteins clusterin in NFTs[102], and heat-shock 27 kDa protein (Hsp27) and αB-crystallin (αB-C) in senile plaques and Lewy bodies[103–105]. The colocalization of these lipids and proteins to amyloid deposits is thought to indicate either their involvement in the development of the amyloid deposits or an induced response to the deposition of amyloid and cell death. Thus, these additional components of amyloid deposits are additionally of interest in understanding the pathogenesis of amyloidoses such as AD and PD.

1.2.6 The toxic species

Despite the strong histological association of amyloid fibrils with disease, the mechanisms of toxicity are still not well understood. Growing evidence suggests that misfolded monomeric species, soluble but non-native oligomers and smaller fibrillar structures are more cytotoxic than larger, mature fibrils, the end product of the aggregation process. This is proposed to be because these smaller forms expose more non-native hydrophobic regions on their surface than larger, matured fibrils[106,107]. The mechanisms of cellular toxicity are not well understood, but there are several well-characterised hypotheses including the disruption or deformation of cellular and mitochondrial membranes[108–110], sequestration of components of the proteostasis network[111,112], enhanced reactive oxygen species (ROS)[108] and cytoskeletal damage[113]. However, the recent paradigm shift in which the misfolded/non-native oligomers are recognized as cytotoxic and matured fibrils as somewhat of an inert end product is probably an oversimplification. The multitude of unnatural structures that are formed during the aggregation process all have the potential to form aberrant interactions with other cellular components such as membranes and solutes[114]. As an example, the kinetics of fibril growth by the human islet amyloid polypeptide was correlated with the kinetics of calcein leakage from large unilamellar vesicles[115]. Additionally, the presence of fibril seeds accelerated both the rate of fibril growth and the rate of calcein leakage, suggesting that the elongation of the fibrils caused the membrane damage[115]. It is also important to consider that pre-existing fibrils are templates upon which further nucleation (surface-catalysed secondary nucleation) can occur[88]. Pre-existing fibrils can also undergo fragmentation to increase the abundance of free fibril ends, which can propagate protein aggregation throughout and

between cells. Furthermore, fibrils remain in equilibrium with all of their non-native, cytotoxic precursors[116] (see Fig. 1.4).

1.2.7 α-Synuclein and disease

α-Syn is a 140 residue, 14 kDa, intracellular, presynaptic protein abundant in multiple regions of the brain. The biological role of α-syn has not been definitively determined however the prevailing hypothesis is that α-syn regulates the fusion of intracellular synaptic vesicles with the cell membrane at nerve terminals[117]. Three regions are distinguished in the primary sequence of α-syn: N- and C-terminal regions and a central 35-residue, hydrophobic non-Amyloid β component (NAC) region (Fig. 1.5). The N-terminal region and part of the NAC region contain seven imperfect 11-amino acids repeat sequences, KTKEGV (Fig. 1.5). In the cell, α-syn is primarily monomeric and cytosolic, but is also found bound to synaptic membranes[118,119]. The KTKEGV repeats are similar to those found in apolipoproteins and are important for the formation of lipid binding amphipathic α helices[120]. Indeed, the binding of α-syn to lipids[121] and/or membranes[120] is mediated by the formation of amphipathic α-helices in the N-terminal region. Cytosolic α-syn exists in a primarily disordered state but is stabilized by transient long-range interactions between the negatively charged C-terminus and moderately basic residues in the central region of the polypeptide chain[122]. The negatively charged C-terminal region remains intrinsically disordered in the lipid-free and lipid-bound state[121]. *In vitro*, recombinantly expressed α-syn forms rod-like amyloid fibrils approximately 10 nm in diameter[32]. *Drosophila melanogaster* transgenic for α-syn develop filamentous, intraneuronal inclusions and experience loss of dopaminergic neurons and other PD symptoms[123]. *In vivo*, fibrillar α-syn is found in Lewy body deposits, where loss of dopaminergic neurons in the substantia nigra occurs[39]. Lewy bodies in the cerebral cortex are also characteristic of dementia with Lewy bodies (DLB)[39], and α-syn is also a component of the glial and neuronal inclusion bodies found in multiple system atrophy (MSA)[124]. Thus, PD, DLB and MSA are classified as α-synucleinopathies, diseases characterized by intracellular aggregates of α-syn. Missense mutations of SNCA (see Fig. 1.5), the gene encoding α-syn, result in early onset PD[32], however the vast majority of PD cases are sporadic with no known genetic causes. In sporadic cases of PD, age-related conditions such as chronic neuroinflammation, oxidative stress, a decline in the capacity of the proteostasis network or a loss of metal homeostasis are thought to promote α-syn aggregation [125–127].

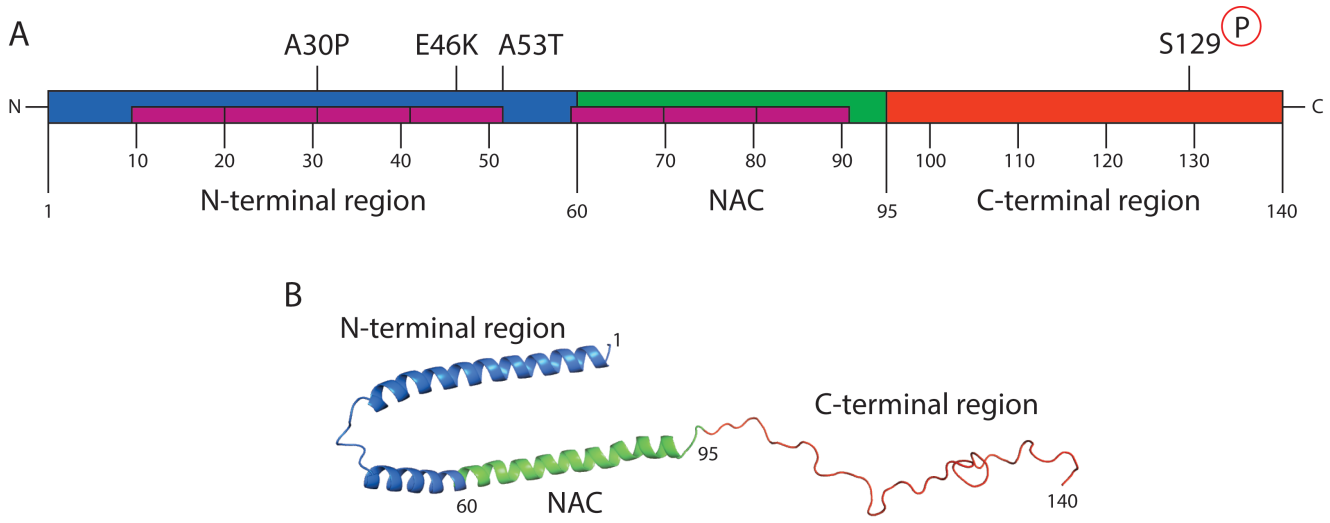


Figure 1.5. Schematic representation of the regions of α-syn. A) The N-terminal region (blue) forms amphipathic α-helices upon binding to membranes. The N-terminal region and central NAC region (green) contain seven repeats of a hexapeptide motif (purple rectangles) similar to those found in apolipoproteins. Several mutations (indicated above using the one-letter amino acid code) within the hexapeptide motifs of the N-terminal region are linked to early-onset PD. α-Syn phosphorylated at serine 129 is overrepresented in synucleinopathy lesions[128]. The NAC region is the hydrophobic region required for amyloid formation and forms β-strands within the core of the fibril. The C-terminal region (red) is acidic, negatively charged and intrinsically disordered at physiological pH. B) The structure of micelle-bound α-syn, colour coded as in (A) (PDB: 1xq8[129]). Both the N-terminal region and NAC region are observed to form α-helices. The C-terminal region is unstructured. Figure adapted from Gallegos *et al*.[130].

1.2.8 Aggregation of α-synuclein

Though α-syn-containing inclusions are the pathological hallmarks of α-synucleinopathies, the mechanisms underlying the aggregation of α-syn are complex. Like all proteins that form amyloid, the fibrillation of α-syn requires primary nucleation and/or secondary processes such as seeding from pre-existing aggregates or surface-catalysed secondary nucleation. Primary nucleation is exceptionally slow and heterogenous in nature, probably as a result of the high stability and high net charge of α-syn at physiological pH. Incubation of recombinantly expressed α-syn at 37°C, pH 7.4 only results in

aggregation after a period of months without agitation or the presence of chemicals/modifications that enhance its aggregation[131]. During primary nucleation, α-syn is thought to undergo partial folding to form an amyloidogenic intermediate. The partially folded intermediates are heterogenous in size and enriched with β-structure[132]. These intermediates are also thought to be a major neurotoxic conformation of α-syn. Factors that perturb the equilibrium between cytosolic and lipid-bound α-syn and/or destabilise either conformation promote primary nucleation. Examples of factors that can enhance α-syn aggregation include serine phosphorylation at position 129[128,133,134] (Fig. 1.5), polyamines[135], increased temperature, reduced pH[136], ionic strength[137], and a range of artificial factors such as air-water interfaces[138], SDS micelles[139], and mechanical agitation[136]. It is also hypothesized that the primary nucleation of α-syn can occur on the surface of lipid bilayers. Galvagnion *et al.* observed that the aggregation of α-syn was enhanced at low lipid:α-syn ratios but was inhibited at high lipid:α-syn ratios[140]. The authors proposed that at low lipid:α-syn ratios, free monomeric α-syn can interact with lipid bound α-syn, undergoing conformational change resulting in oligomer formation. In contrast, at high lipid:α-syn ratios, the majority of the α-syn is lipid bound, limiting interactions between free monomeric α-syn and its lipid-bound form. Hydrophobic residues within the NAC region, particularly 71-VTGVTAVAQKTV-82, are critical for the assembly of α-syn fibrils – deletion of these residues or insertion of charged residues within this motif inhibits amyloid fibril assembly[141]. In addition to environmental factors, mutations in the gene encoding α-syn have also been implicated in the pathogenesis of PD, although familial PD accounts for <10% of all cases. Despite this, the effects of these mutations on the stability of α-syn and its propensity to form fibrils provides useful insight into the mechanisms of fibrillation. Familial PD mutations are typically found within the KTKEGV motifs in the N-terminal region of the protein (Fig. 1.5), suggesting that these mutations may affect the association of α-syn with lipid bilayers and thereby alter its rate of nucleation. Currently there are six missense mutations linked with familial PD: A30P, E46K, H50Q, G51D, A53T, and A53E. Of these mutations , there is evidence that the A53T[32,142], E46K[143], H50Q[144] form both pre-fibrillar oligomers and fibrils more rapidly than the WT protein. The A30P, G51D and A53E mutations have not been conclusively shown to enhance the rate of fibril formation relative to the WT protein. Instead, these mutations have been proposed to destabilise the native, cytosolic conformation of α-syn by perturbing long-range contacts that form between the N-terminal region and the C-terminal region[145]. This enhances the rate of oligomerization for these

mutants, while their conversion from oligomers to fibrils is thought to occur more slowly than the WT protein.

1.2.9 Biophysical characterization of α-synuclein fibrils

As a consequence of its involvement in AD and PD, the structure of α-syn fibrils is of great interest. Circular dichroism (CD) can be used to track the conformational changes of recombinant α-syn as it transitions from a random coil assembly to a β-sheet state[146]. Electron microscopy (EM) reveals that recombinant α-syn assembles into rod-like amyloid fibrils structurally similar to those that can be isolated from the brains of patients with DLB and MSA[146]. Like all amyloid fibrils, α-syn fibrils generate cross-β X-ray fibre diffraction patterns[146]. Solid-state (ss) NMR has been used to determine the residues that contribute to the β-strands and the fold of the β-strands within a protofilament[147]. The central region of α-syn (residues 30-100) form several β-strands that adopt a Greek key-like fold[147,148]. Recent advances in cryo EM have also allowed for higher resolution structure determination of two polymorphs of α-syn fibrils[74] (Fig. 1.6). In these models, residues ~30-100 found in the N-terminal region and the central NAC region form four or five β-strands flanked by poorly defined N- and C-terminal extensions. Two filaments twist around each other in the observed structures. Two of the earliest cryo-EM models of full-length α-syn are shown in Fig. 1.6[74]. Advances in micro ED also recently made possible a 1.4 Å resolution structure to be solved from microscopic crystals formed from amyloid fibrils of a fragment of α-syn (residues 68-78)[149], confirming the importance of the NAC region in fibril assembly.

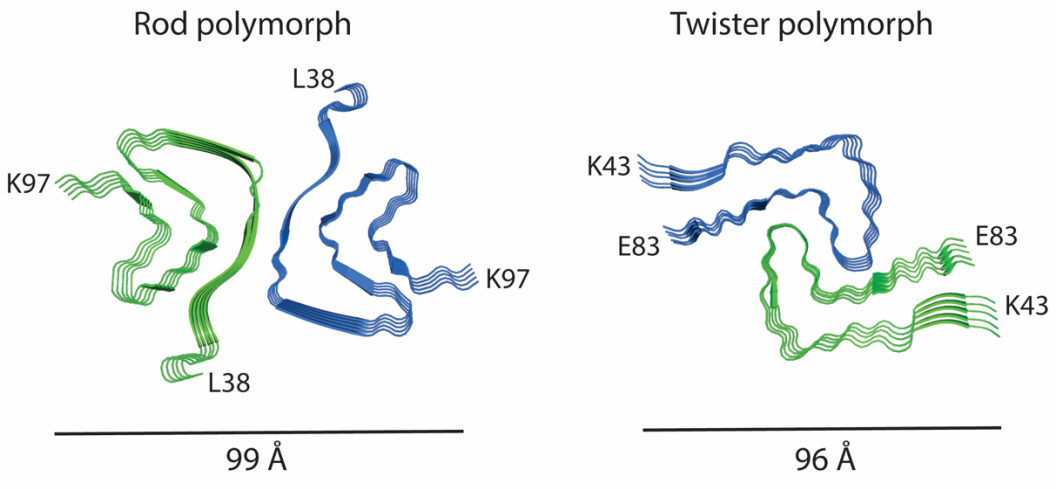


Figure 1.6. Two examples of cryo-EM models generated using full-length α-synuclein. The cryo-EM structures of the rod (left, PDB: 6CU7[74]) and twister (right, PDB: 6CU8[74]) polymorphs from a top-down view. Each polymorph consists of two filaments and 5 polypeptide chains are shown for each filament. The positions of the N- and C-terminal residues visible in the electron density maps are indicated for each polymorph. The width of the fibrils in Ångstroms is shown below each structure.

1.2.10 Apolipoprotein C-II and disease

Apolipoproteins are serum proteins found bound to the surface of lipoprotein particles such as low-density and high-density lipoproteins (LDL and HDL, respectively). Lipoprotein particles are responsible for the transport of phospholipids, triacylglycerol and cholesterol in the bloodstream. Apolipoproteins exhibit distinct lipid-bound and lipid-free conformational states. Like α-syn, in the lipid-bound state, apolipoproteins form amphipathic α-helices that enable lipid binding[150]. In the lipid-free state, apolipoproteins are prone to aggregation due to their conformational instability[151]. Several members of the apolipoprotein family are known to colocalise with or form amyloid fibrils *in vivo*. Human apolipoprotein (apo) A-I, A-II, B100, C-II and E are found co-localised to extracellular amyloid plaques *in vivo*, mainly in atherosclerotic plaques, or in the brain[58,99,152–156]. ApoA-I and apoC-II also form fibrils *in vitro,* which feature all the hallmark properties of amyloid[58,152]. In healthy individuals, apoC-II is a serum protein found associated with very low-density lipoprotein (VLDL) particles where it activates lipoprotein lipase[157,158], which catalyses the breakdown of triglycerides to fatty acids and glycerol. Lipid-bound apoC-II is comprised of amphipathic α helices[159]. Amyloid formation by apoC-II *in vitro* is well characterized[85,150,152,160–166] and recently, mutations in apoC-II have been found to cause renal amyloidosis[59,60].

1.2.11 Biophysical characterization of apolipoprotein C-II aggregation

Lipid free apoC-II is unstable and readily assembles into homogenous amyloid fibrils. The kinetics of apoC-II amyloid formation *in vitro* are well described by a reversible nucleation-elongation mechanism. Mature fibrils remain in equilibrium with a small proportion of free monomer, and undergo breaking, rejoining and lateral tangling[85]. Transmission EM of apoC-II fibrils formed *in vitro* typically reveals long, unbranched structures that adopt a twisted-ribbon morphology and can also form closed fibril loops[35,152]. X-ray fibre diffraction has also been used to investigate the structure of apoC-II fibrils. ApoC-

II fibrils give rise to meridonal reflections at 4.67 Å and equatorial reflections at 9.46 Å, indicating the spacing between β-strands within a β-sheet, and the spacing between β-sheets, respectively. This X-ray diffraction data indicates that unlike many other amyloid fibrils, apoC-II fibrils are comprised of only one protofilament[35]. TEM and AFM were used to determine the maximum dimensions for the width and height of apoC-II fibrils. This data, combined with X-ray diffraction data and hydrogen/deuterium exchange and proteolysis experiments[165] was used to construct a model for apoC-II fibrils. The resulting model is a β-strand-loop-β-strand structure shaped like the letter G (Fig. 1.2). The residues involved in the first β-strand are 20-36 and the residues in the second β-strand are 58-74[35].

1.3 Overview of the proteostasis network

Protein homeostasis, or proteostasis[167], is the term given to the exquisitely complex and interconnected pathways that control the abundance, stability and localization of proteins. Proteostasis pathways regulate the entire life cycle of a protein, from gene transcription and mRNA translation to protein synthesis, folding, trafficking and finally to protein degradation via autophagy or the proteasome. The maintenance of this delicate balance between protein production and timely clearance of damaged proteins is essential for cellular and organismal survival. Consequently, the genes that regulate proteostasis are evolutionarily conserved and often have overlapping functions to protect against proteostasis failure arising from mutations of single genes. Some examples of proteostasis machinery include transcription factors, RNA translation factors, molecular chaperones, trafficking regulators, and protein degradation machinery. As evidence for the importance of proteostasis, of the ~20,000 protein-encoding genes in the human proteome, approximately 2000 of these function within the proteostasis network to maintain proteome stability[168]. Dysregulation of proteostasis is strongly associated with a diverse range of debilitating and sometimes life-threatening diseases, collectively termed protein conformational diseases. Well-established links exist between genetic alterations of many of the individual components of the proteostasis network and these diseases[169]. However, an emerging concept is that the capacity of the proteostasis network can decline throughout the human lifespan in the absence of defined genetic causes[170]. This decline in the capacity of the proteostasis network is

thought to represent an early event in ageing and contribute to age-related protein conformational diseases.

1.3.1 The role of molecular chaperones

Molecular chaperones, also known as heat-shock proteins (HSPs), comprise one facet of the proteostasis network. In the course of evolution, HSPs evolved to protect cells against various forms of stress. HSPs were initially identified in *D. melanogaster* as proteins upregulated in response to heat-shock[171]. HSPs are defined as any factor that interacts with and promotes the folding of any protein without becoming incorporated into its final native structure[172]. Chaperone mechanisms include *de novo* folding, refolding, disaggregation, the prevention of aberrant intermolecular interactions, assistance in oligomeric assembly, protein trafficking, and assistance in proteolytic degradation. HSPs perform these functions via ATP-dependent or ATP-independent pathways. ATP-dependent HSPs are also termed "foldase" chaperones because they actively participate in the folding or refolding of substrates, or of the unfolding of misfolded/aggregated proteins, requiring energy in the form of ATP hydrolysis to do so. ATP-independent chaperones are termed "holdase" chaperones because they interact with and stabilize substrates but do not actively fold or refold them. In humans, HSPs are broadly classified into several families based on their molecular weight (MW): small heat-shock proteins (sHSPs, HSPBs), HSP40 (DNAJ), HSP70 (HSPA), HSP90 (HSPC) and HSP110 (HSPH)[173]. In addition to the human HSP families, the human genome also encodes two chaperonin families: HSP60/HSP10 (HSPD/HSPE) and CCT (TRiC)[173]. Chaperonins are distinguished from chaperones on the basis that they form large oligomeric complexes of two stacked rings with a central cavity[174]. The regulation of HSP expression can be classified into three types: (1) constitutively expressed and differentially regulated during development, (2) constitutively expressed and inducible, and (3) those that are only inducible[175]. For those that are inducible, their expression can be upregulated by conditions such as heat-shock, oxidative stress, changes in pH, fever, inflammation, infection or a range of other disease states[171,175]. These genes have heat-shock elements[176,177] in their promoter regions, which are bound by specific transcription factors called heat-shock factors that promote their expression during stress[178,179]. Broadly, HSPs aid in protein folding, help maintain the correct conformations of proteins throughout their lifetime, prevent misfolding and coordinate the timely degradation of damaged proteins via degradation pathways. HSPs

typically exert these functions via interactions with exposed hydrophobic regions on partially unfolded client proteins. By recognizing hydrophobic regions, HSPs are able to interact with a vast array of client proteins that expose different hydrophobic motifs. However, protein aggregation will occur if non-native folding intermediates and/or misfolded proteins accumulate to levels that exceed the capacity of the proteostasis network[180]. In such a situation, the cell stress response is initiated, which upregulates the expression of HSPs in an attempt to restore proteostasis.

1.3.2 The HSP40/DNAJ family

The HSP40 family is the largest HSP family in humans with approximately 50 members. HSP40 family members function to transfer substrates requiring folding to HSP70 family members. All HSP40 family members have a conserved, ~75-residue J-domain and function as homodimers. HSP40 family members bind to non-native/unfolded polypeptides in an ATP-independent manner via their C-terminal substrate binding domain[181]. HSP40 family members then recruit HSP70 members via tripeptide HPD motifs in their J-domain that interact with the nucleotide binding domain of HSP70[182]. At this stage HSP70 is in the ATP-bound state. This binding stimulates the ATPase activity of the nucleotide binding domain of HSP70 and allows for the ATP-dependent transfer of substrates from HSP40 to HSP70[183]. HSP40 also co-operates with HSP70 and HSP110 in protein disaggregation[184–186].

1.3.3 The HSPA/HSP70 and HSPH/HSP110 families

The human genome encodes 13 members of the HSP70 family. HSP70s are monomeric, ATP-dependent chaperone proteins. Members of the HSP70 family have been identified in the cytosol and nucleus[187,188], ER[189], mitochondria[190], exosomes[191], cell membrane[192,193] as well as in the extracellular milieu[194]. HSP70s typically work in tandem with HSP40 co-chaperones. In this system, ATP hydrolysis promotes the transfer of an unfolded client protein from the HSP40 co-chaperone to HSP70[183]. In the ADP-bound state following ATP hydrolysis, the substrate is tightly bound to HSP70[195]. The subsequent exchange of HSP70-bound ADP for ATP stimulates a conformational change in HSP70 that reduces the affinity of HSP70 for its substrate[195]. This promotes rapid cycles of substrate association and dissociation that are thought to iteratively drive the folding of the substrate[195].

The HSP110 family is closely related to the HSP70 family. The human genome encodes four members, three of which are cytosolic and one of which is localized to the ER. These HSPs function as nucleotide exchange factors for the HSP70 family members[196,197]. HSP110s therefore participate in HSP70-mediated protein folding. HSP110 has also been shown to be important for protein disaggregation in co-operation with HSP40 and HSP70[184–186].

1.3.4 The HSPC/HSP90 family

There are five human HSP90 family members, three of which are present in the cytosol (HSP90α, HSP90α A2 and HSP90β), one of which is localized to the ER (GRP94) and one of which is found in the mitochondria (TRAP1). HSP90 exists as a homodimer and is thought to function downstream of the HSP40/HSP70 system. The domain architecture of HSP90 is relatively well-conserved across the different isoforms and consists of an N-terminal ATP-binding domain, a charged linker region, the middle domain, which binds the γ phosphate of ATP to help regulate ATPase activity, and a C-terminal domain that mediates homodimerization of HSP90[198]. An ATP-dependent conformational cycle regulates HSP90 chaperone activity. In the "open conformation", HSP90 exists as a homodimer with inter-subunit contacts being formed between the C-terminal domain[198,199]. In this state, a substrate can bind the middle domain[18], and ATP binds the N-terminal domain[198]. ATP-binding promotes dimerization of the N-terminal domains, forming the "closed conformation"[198,199]. ATP-hydrolysis promotes substrate folding[18].

Proteins that are unable to be folded by HSP70 are transferred from the HSP40/70 system to HSP90 with the help of co-chaperones[200,201]. Major substrates for HSP90 chaperones are steroid receptor molecules[202] and signalling molecules such as kinases[203]. In addition to protein folding, HSP90 chaperones are crucial housekeeping genes that also participate in a range of regulatory pathways including apoptosis, cell cycle control, cell viability and cell signalling[18,204].

1.3.5 The HSPD/E chaperonins

HSPD/HSP60 is the human ortholog of bacterial GroEL and HSPE/HSP10 is the human ortholog of bacterial GroES. These chaperonins are primarily localized to organelles derived from endosymbiosis and

are therefore predominantly found in the mitochondria (and chloroplasts) but can also be found in the cytoplasm. HSP60 consists of two heptameric rings that are stacked back-to-back[205]. HSP10 is the co-chaperonin of HSP60 and forms the lid of the HSP60 folding chamber. Association of HSP10 with the HSP60 ring structure is ATP-regulated[205]. Once encapsulated, the substrate is allowed to fold for ~ 10 seconds before HSP10 dissociates and the substrate is released[18]. Subsequent cycles may be required to complete substrate folding. Mitochondrial HSP60 functions primarily to fold, refold and translocate mitochondrial proteins from the cytosol to the mitochondrial matrix[206,207]. To do this HSP60 maintains substrate proteins in an unfolded conformation for translocation across the mitochondrial inner membrane. Many of the substrates of the HSP60/HSP10 folding chamber have complex α/β or $\alpha + \beta$ folds[33].

1.3.6 The CCT/TRiC chaperonin

CCT/TRiC is the primary cytosolic chaperonin comprised of two stacked rings of eight paralogous subunits per ring. In contrast to the HSP60/HSP10 chaperonin, TRiC does not have an obligate co-chaperonin and instead has an in-built lid. TRiC functions in the cytosol to fold newly synthesized proteins and has been shown to be necessary for the folding of cytoskeletal proteins such as tubulin[208] and actin[209] and cell cycle regulators[210]. Each subunit of the TRiC ring has different chemical properties thereby providing binding sites for a wide range of substrates. TRiC also undergoes an ATP-dependent reaction cycle. In the nucleotide-free state TRiC exists in an "open conformation" and can bind substrates[174]. In the open conformation TRiC also has a high affinity for ATP, promoting nucleotide binding. ATP hydrolysis triggers a conformational change and closure of the lid, encapsulating the substrate and allowing for folding[174]. Release of ADP promotes substrate release. It is estimated that as much as 10% of the proteome is dependent upon TRiC for folding[211].

1.3.7 The HSPB/sHSP family

A prime example of the holdase class of chaperones are the sHSPs, which function to bind and stabilize partially folded proteins to prevent their aggregation[212]. sHSPs are ATP-independent and as a result they do not actively fold, refold or unfold clients[212]. ATP-independent chaperones are thought to be an important first line of defense in the cell under conditions of stress that deplete ATP, which would

reduce the capacity of ATP-dependent chaperones to maintain proteome integrity. When cellular ATP is restored, sHSPs can pass their substrates on to ATP-dependent machinery for refolding[213], or for degradation via autophagy[214] or the proteasome[215]. As evidence for their importance, sHSPs are found universally in all forms of life and at least four of the ten human sHSPs are ubiquitously expressed. There are additional sHSP isoforms that are highly expressed in skeletal and cardiac muscle. Several sHSPs, including αB-C, Hsp27 and HSPB8, are highly expressed in neurons and glial cells of patients with a range of neurodegenerative diseases including AD[105,216–218], encephalopathies[219] and PD[103]. Mutations in sHSPs are associated with neuronopathies[220] and myopathies[221]. sHSPs appear to interact with an exceptionally broad array of substrates. However, the mechanisms by which sHSPs interact with and stabilize their substrates remain somewhat elusive despite extensive research efforts over the past two decades.

1.3.8 Protein degradation pathways

There are two main protein degradation pathways in eukaryotic cells. These are the ubiquitin-proteasome system (UPS) and the autophagy-lysosome pathway. Proteasomes are barrel-shaped protein complexes with an internal pore[222,223] that function to degrade short lived proteins from the cytosol and nucleus, or retro-translocated ER proteins in a process called endoplasmic reticulum-associated degradation (ERAD)[224–226]. Proteins targeted for degradation are covalently modified with ubiquitin via E1 (ubiquitin-activating enzyme), E2 (ubiquitin-conjugating enzyme) and E3 (ubiquitin ligase) enzymes[227]. Substrates are usually polyubiquitinated, with chains of more than four ubiquitin molecules acting as a signal for targeting to the proteasome[228]. HSP70/90 family members can deliver substrates to the UPS in co-operation with additional co-chaperones[229].

The majority of long-lived cytosolic proteins, as well as organelles, are degraded in a process called macroautophagy or autophagy[230]. Autophagy involves the formation of double-membrane-bound structure called autophagosomes[231]. These structures fuse with acidic lysosomes to generate autophagolysosomes, in which the proteins and organelles are degraded. Autophagy has been shown to be an important mechanism of clearance for mutant huntingtin, mutant α-syn and tau[232–234].

Interference with the autophagy pathway slows the clearance of these species and leads to the accumulation of ubiquitinated aggregates.

1.3.9 Proteostasis capacity throughout the human lifespan

The accumulation of protein deposits in long-lived cells such as neurons later in life is thought to be associated with a general decline in the capacity of the proteostasis network over the human lifespan. Studies of model organisms such as mice, *Caenorhabditis elegans* and *D. melanogaster* indicated that maintaining proteostasis correlates with an increased lifespan[235–237]. However, there is a lack of evolutionary pressure for organisms to maintain proteostasis beyond the age at which reproduction is likely to occur. During ageing, misfolded and damaged proteins accumulate, posing an increasing burden to the proteostasis network. Additionally, the expression of ATP-dependent chaperones (HSP60 and HSP70) has been shown to decline in the human brain throughout ageing[238], which may further reduce the capacity of the proteostasis network. Once the accumulation of damaged proteins reaches a critical threshold, the proteostasis network becomes overwhelmed. This results in a positive feedback loop whereby additional accumulation of damaged proteins places further burden on the proteostasis network (Fig. 1.7)[180]. Interestingly, the expression of sHSPs has been demonstrated to increase in *C. elegans*[239], *D. melanogaster*[240] and mammalian skeletal muscle[241] and brain cells during ageing[242], suggesting that this phenomenon may be typical of ageing organisms. Additionally, sHSPs are commonly found colocalised to insoluble aggregates such as those isolated from *C. elegans*[239], *Escherichia coli*[243] and mammalian skeletal muscle[241]. The colocalisation of sHSPs to intracellular protein aggregates may function to sequester and/or coat the aggregates to reduce the aberrant, cytotoxic interactions of these aggregates with other cellular components[170].

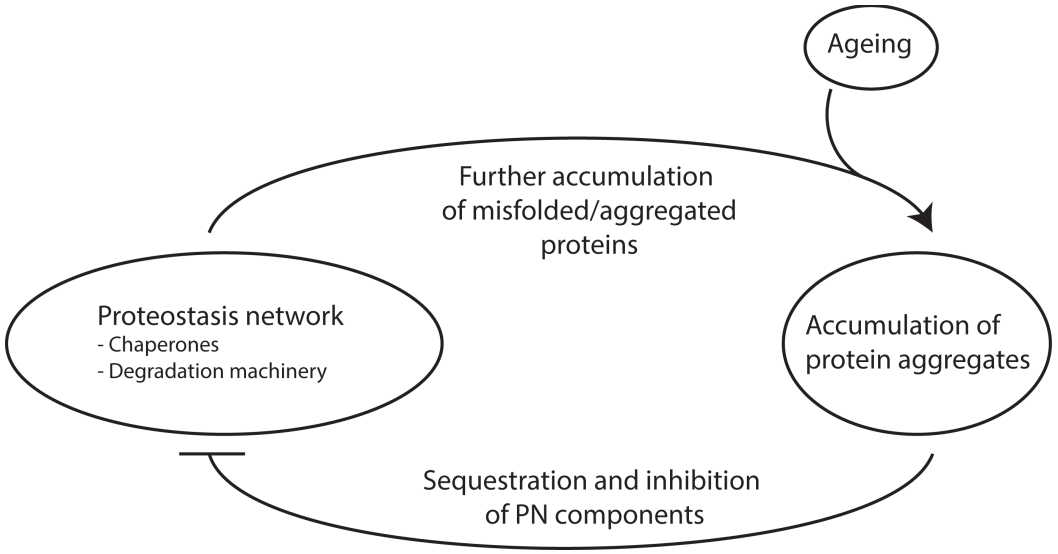


Figure 1.7. The positive feedback loop contributing to the failure of the proteostasis system under conditions of chronic stress and/or ageing. During ageing, the expression levels of components of the proteostasis network changes, and these changes may enhance the accumulation of damaged/aggregated proteins. Existing protein aggregates become associated with components of the proteostasis network, including proteasomes and chaperones, inhibiting the capacity of the proteostasis network to clear these aggregates. This results in further accumulation of damaged and aggregated proteins, which further sequesters and inhibits the proteostasis network.

1.4 How chaperones modulate amyloid formation

Increasing evidence both from *in vivo* and *in vitro* experiments indicate that molecular chaperones play additional roles in protein folding, beyond just interacting with proteins to assist in native folding. ATP-dependent and ATP-independent HSPs significantly and specifically inhibit the amyloid formation of a variety of model substrates and disease-related proteins[244]. The mechanisms employed by HSPs to modulate amyloid formation are complex. Each structural rearrangement and change in the oligomeric state of a protein that undergoes amyloid formation represents a molecular process that HSPs can act to inhibit (see Fig. 1.8). Indeed, there are numerous studies that report the modulation of primary and secondary nucleation, fibril elongation/seeding, fibril fragmentation and fibril dissociation/disaggregation by a variety of classes of HSPs. Furthermore, HSPs have been demonstrated to coat aggregates to reduce their cytotoxicity.

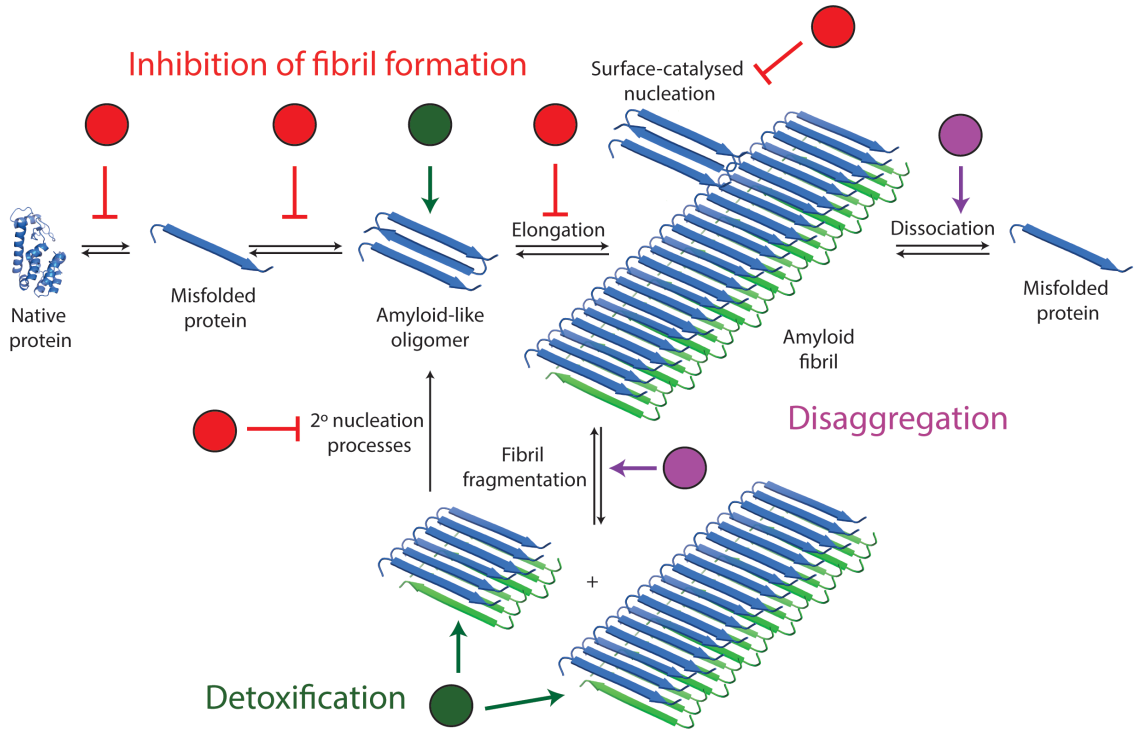


Figure 1.8. The mechanisms by which chaperones can modulate amyloid formation. The interactions between chaperones and amyloid-forming proteins can be classified as: inhibition of fibril formation (red), disaggregation of fibrils (purple), or detoxification as a result of binding (dark green). Inhibition of fibril formation can be further classified according to the assembly stage that the chaperone inhibits: protein misfolding, oligomer formation, elongation, secondary nucleation and/or seeding. Depolymerization is classified as either the enhancement of fibril fragmentation or the enhancement of the monomer dissociation from fibril ends. Detoxification is generally thought to occur when a chaperone colocalizes to an aggregate (oligomer or fibril) and in doing so, reduces the cytotoxicity of the aggregate. Figure adapted from Wentink *et al.*[244].

1.4.1 Inhibition of primary nucleation

The simplest mechanism for the inhibition of amyloid formation by HSPs involves the inhibition of primary nucleation, the earliest phase of amyloid formation. Studies of these processes have typically involved incubating an aggregation-prone protein in destabilizing conditions either alone or in the presence of a chaperone or combination of chaperones and monitoring protein aggregation over time. Members of all the major human HSP families have been shown to inhibit the nucleation phase of a variety of disease-related substrates such as tau[245], Aβ[246], β_2-microglobulin (β_2-m)[247] and α-syn[248]. Mok

et al. developed a high-throughput screening approach to investigate the ability of 30 human chaperones to inhibit the amyloid formation of tau[249]. This work identified new classes of chaperones that can specifically inhibit amyloid formation, for example, Hsp60[249]. In addition to this, by analysing the kinetics of tau aggregation, the authors could distinguish chaperones that mainly inhibited the nucleation phase, eg: Hsc70 and Hsp60, from those that primarily inhibited elongation, for example: Hsp27 and αB-C[249]. The mechanism by which these HSPs inhibit amyloid nucleation are likely via interactions with monomeric substrates and/or oligomeric structures formed during the nucleation phase. The detection of protein-protein interactions between HSPs and their monomeric substrates is therefore useful in determining whether HSPs inhibit primary nucleation. In some instances, interactions between the substrate in its monomeric form and the HSP can be detected in solution using techniques such as NMR[250], ITC[251], tryptophan fluorescence[252], dynamic light scattering (DLS)[253] and AUC[254,255]. However, in many cases where HSPs inhibit amyloid fibril formation, interactions between the HSP and the substrate protein are transient and difficult to detect. This, however, does not rule out an interaction between HSPs and their substrates. While no interaction between Hsp70 and α-syn could be detected using NMR, Dedmon *et al.* demonstrated that the incubation of Hsp70 with α-syn under conditions that promote its aggregation prevented the random-coil to β-structure transition that normally precedes α-syn fibril formation[250]. Similarly, the combination of the chaperones: Hsc70, DNAJB1 and the HSP110 family member, Apg2, completely suppressed the aggregation of Huntingtin (Htt) Exon 1 (Q48), which indicates that the trimeric chaperone complex interacts with Htt in its soluble form, however the authors did not further investigate the nature of this interaction[186].

1.4.2 Inhibition of secondary nucleation and elongation

The inhibition of amyloid formation can also be achieved via an interaction between HSPs and pre-fibrillar oligomers formed during nucleation, elongating fibrils, and/or matured fibrils. Experimentally, these interactions can be inferred from seeded fibril formation experiments under conditions where fibril formation is driven almost exclusively by secondary processes rather than primary nucleation. Alternatively, these interactions can be identified by purifying substrate oligomers or fibrils from complex mixtures and subsequent detection of HSPs. As an example, using dual colour TIRF microscopy and pelleting assays HSP70 was shown to colocalize to tau pre-fibrillar oligomers and fibrils but not to

tau monomers[245]. Pull-down experiments and/or size-exclusion chromatography have also shown interactions between HSPs from the HSP40[246], HSP90[251,256] and sHSP[257–259] families and pre-existing oligomeric of fibrillar aggregates. The interactions of these HSPs with pre-existing aggregates has been proposed to reduce the cytotoxicity of the aggregates. For example, the interaction of HSP70 with tau pre-fibrillar oligomers was shown to reduce their ability to permeabilise membranes[245]. Similarly, pre-fibrillar α-syn oligomers formed in the presence of HSP90 were less cytotoxic when exposed to neuroblastoma cells than pre-fibrillar oligomers formed by α-syn alone[251]. Preformed α-syn fibrils were also found to be toxic to murine endothelioma cells, while soluble α-syn was not[255]. Hsc70 colocalized to pre-formed α-syn fibrils, and these "coated" fibrils were significantly less toxic to the endothelioma cells than the fibrils that were not coated with Hsc70[255]. The human chaperonin TRiC, also interacts with pre-existing aggregates. Behrends *et al.* used single particle fluorescence analysis to demonstrate colocalization of TRiC to oligomeric aggregates containing Htt Exon 1 Q53[260]. In addition to this, Htt fibrils formed in the presence of TRiC were markedly shorter than those formed alone[260]. The authors speculated that TRiC may cap Htt fibrils to inhibit their elongation. In a subsequent study, Shahmoradian *et al.* used cryo-EM and single particle tomography to directly observe TRiC capping the ends of Htt Exon 1 Q51 amyloid fibrils[261]. Mannini *et al.* incubated a variety of HSPs with soluble, pre-fibrillar oligomers formed from three distinct substrate proteins to determine the generality of interactions between HSPs and pre-formed aggregates. Each HSP colocalized to the aggregates and promoted their assembly into larger species[262]. This study also demonstrated that the interactions of HSPs with the oligomers reduced their cytotoxicity and ability to permeabilise membranes, indicating that these functions may be generic abilities of HSPs[262]. Subsequently, αB-C was also shown to sequester apoC-II amyloid fibrils into much larger fibril tangles reminiscent of inclusion bodies as well as inhibit the fragmentation of these fibrils[258]. Together, these studies suggest that HSPs interact with soluble oligomers and fibrils and in doing so, reduce their cytotoxicity. Additionally, HSPs may actively sequester protein aggregates into larger aggresome-like structures within cells to enable asymmetric inheritance of the aggregates in dividing cells[263].

1.4.3 Chaperone-mediated disaggregation

Other mechanisms by which HSPs can reduce the cytotoxicity of pre-existing amyloid fibrils is by enhancing their dissolution. Disaggregation of existing protein aggregates has been classically studied in organisms that contain HSP100 family members, which are absent in metazoans. As an example, a transgenically-expressed temperature-sensitive luciferase fusion protein aggregates upon mild heat-stress in *S. cerevisiae*[264]. However, these aggregates are cleared in yeast expressing the HSP100 family member Hsp104, but not in yeast lacking Hsp104 expression, highlighting the importance of HSP100 in the dissolution of the luciferase aggregates[264]. HSP70 family members are thought mediate the dissociation of individual polypeptides from aggregates, which are then translocated through the central channel of HSP100 family members before active refolding can take place[265]. In metazoans, which lack HSP100 family members, it is thought that HSP70 family members are able to clear pre-existing protein aggregates with the help of HSP40 co-chaperones and HSP110 NEFs. As an example, Hsc70, DNAJB1 and HSP110 induced slow depolymerization of α-syn fibrils, generating shorter fibrils over time and enhancing the population of non-toxic α-syn monomers[266]. In a separate study, Scior *et al.* used a combination of TEM and pelleting assays to show that Hsc70, DNAJB1 and the HSP110 family member, Apg2, could disaggregate Htt Exon 1 (Q48) fibrils[186]. In addition to the HSP40/70/110 system in metazoa and the HSP70/100 system in other organisms, sHSPs have recently emerged as factors that can promote disaggregation. Members of the sHSP family are commonly observed in insoluble protein aggregates such as those induced by heat-shock in *E. coli*[267], *S. cerevisiae*[268] as well as in senile plaques and Lewy bodies isolated from human patients[103–105]. A model substrate, citrate synthase, formed large oligomeric complexes when incubated with the sHSP, Hsp25, upon heat-shock[269]. However, the substrate could be efficiently reactivated from these complexes at a permissive temperature, but not when the heat-shock was performed in the presence of a non-chaperone control protein instead of Hsp25[269]. Additionally, the presence of the sHSP, Hsp26 in insoluble protein aggregates formed by firefly luciferase in *S. cerevisiae* enhanced the disaggregation and reactivation of the substrate by Hsp104[268]. Using native mass spectrometry (MS), Esposito *et al.* demonstrated that αB-C disaggregated pre-fibrillar oligomers formed by β_2-m[247]. Binger *et al.* also demonstrated that αB-C enhanced the dilution-induced disaggregation of apoC-II fibrils[258]. Using a pelleting assay, Duennwald *et al.* found that the sHSP αB-C also potentiated the depolymerization of α-syn fibrils by the HSP40/70/110 system[270]. The mechanism

by which sHSPs enhance aggregate dissolution is not understood but could be due to changes in the physicochemical properties of the aggregates such that polypeptide chains can be more readily disentangled by HSP70 family members and their associated co-chaperones[265,268].

1.5 Small heat-shock proteins as molecular chaperones

1.5.1 The structure of small heat-shock proteins

The monomeric mass of sHSPs ranges from 15-40 kDa. The sequence of sHSPs can be divided into a central, highly conserved, ~90 residue domain termed the α-crystallin domain (ACD) that is flanked by dynamic N- and C-terminal regions (NTR and CTR, respectively) (Fig. 1.9). Mammalian sHSPs assemble into polydisperse oligomers that can range from dimers to 40- or 50-mers[271,272]. Polydispersity of mammalian sHSP oligomers is due to the rapid exchange of monomeric or dimeric subunits under physiological conditions[273]. Consequently, much of the structural information regarding mammalian sHSPs has come from high-resolution structures of monodisperse plant or prokaryotic sHSPs[274,275]. Examples of these are the solved crystal structure of a 24-mer of a sHSP, Hsp16.5, from a hyperthermophilic archaeon[274], and the structure of a 12-mer sHSP, Hsp16.9, from wheat[275]. Mammalian ACDs adopt an immunoglobulin (Ig)-like β-sandwich fold with six β-strands (Fig. 1.10). The NTR is thought to contain two short α-helices and a small stretch of β-sheet near the ACD however heterogenous NMR resonances indicate significant conformational mobility for this region[276]. The CTR is intrinsically disordered with limited sequence homology across the sHSP family except for a conserved IXI/V motif. Crystal structures also exist for the isolated ACD of several human sHSPs, including αA-C, αB-C, Hsp27 and Hsp20[277–280] (Fig. 1.10 H-I). These structures reveal that for mammalian sHSPs, the ACD mediates dimerization via the formation of an interchain β-sheet between a long β-strand termed β6/7 in each subunit[279,280] (Fig. 1.10 H-I). These crystal structures also suggest that the IXI/V motif in the CTR contributes to oligomer assembly by binding bidirectionally to a cleft created between strands β4 and β8 at the outward-facing edge of the ACD of nearby dimers[279,280] (Fig. 1.10 H-I). Additional solid state-(ss)-NMR, small angle X-ray scattering (SAXS) and EM studies enabled modelling of αB-C oligomers at atomic-level resolution (Fig. 1.10 F and G)[276]. These studies also confirmed the importance of the ACD for sHSP dimerization, and of the NTR and CTR for higher order multimerisation. This model is further

supported by the observation that sHSP constructs lacking the NTR do not form large multimers[281]. However, static 3-dimensional models of sHSP oligomers of defined sizes should be interpreted with caution since the functions of these proteins are likely to be dependent on structural heterogeneity/flexibility. Ion mobility MS has been extensively used to study the size-distribution of oligomers of αB-C and Hsp27 at higher resolution than is afforded by other techniques such as AUC[282–285]. These findings have shown that oligomers can be comprised of an even or odd number of subunits, however even numbered oligomers are more abundant[286]. Therefore, subunit exchange can occur via the movement of monomers or dimers. A limitation of these studies is that native MS is a gas-phase technique, whereas these proteins only exist physiologically in solution. Whether the transition from the solution-phase to the gas-phase affects the oligomeric size distributions of sHSPs has not been determined. Mathematical models for the exchange of monomers from oligomers require the breakage of three inter-subunit contacts: the intra-dimer ACD-ACD, and two inter-dimer ACD-CTR interfaces[285,287]. Subunit exchange of dimers requires the breakage of four ACD-CTR interfaces[285]. Interestingly, the strengths of these interfaces are thought to be allosterically regulated such that an increase in the strength of an ACD-CTR interface results in a weakening of the ACD-ACD interface, and vice versa[285]. Based on all of this structural information, the assembly of sHSP oligomers is thought to occur hierarchically; two ACDs interact to form a dimer, their CTRs dock onto the ACDs of nearby dimers via the IXI/V motif to form small oligomers and the NTR contributes to higher order oligomeric assembly via interactions that have not yet been well characterised (Fig. 1.11).

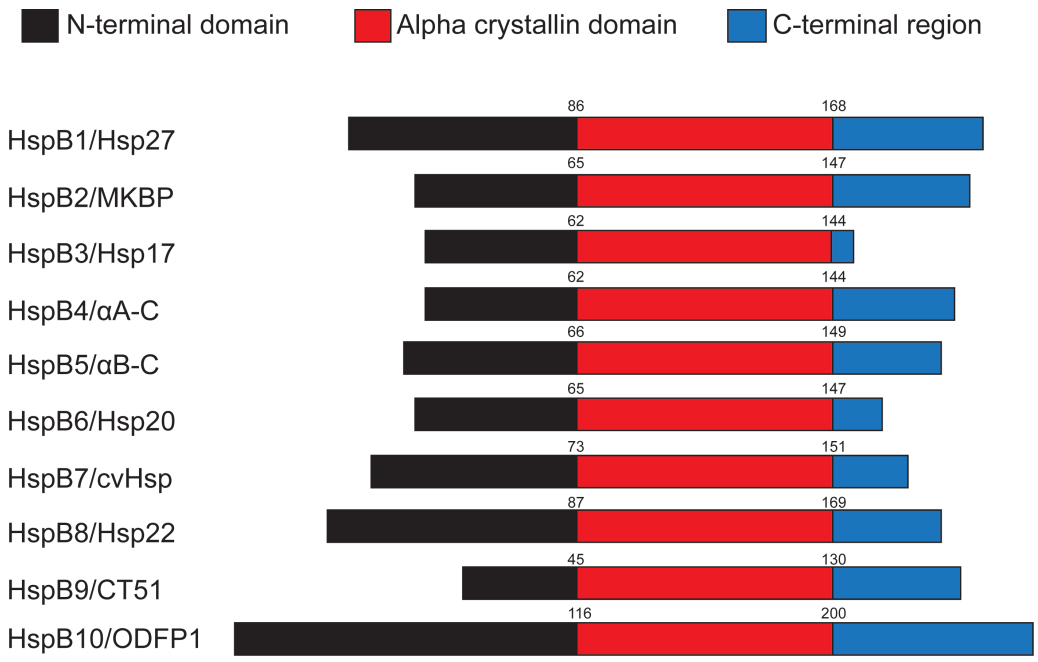


Figure 1.9. Domain architecture of the ten human sHSPs, HSPB1-10. Each sHSP has poorly conserved NTR and CTR (black and blue, respectively), and a conserved ACD of ~90 residues (red).

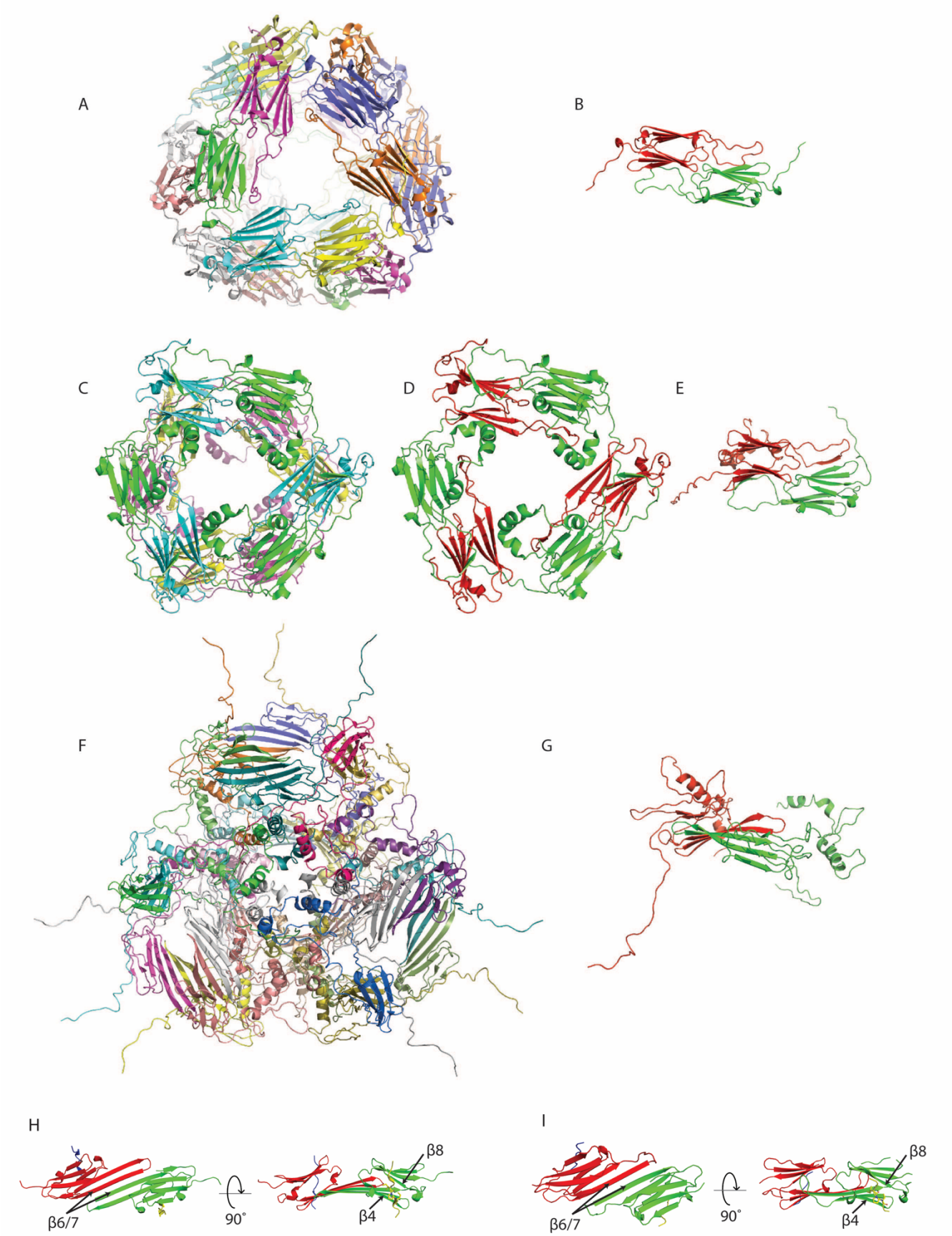

A
B
C
D
E
F
G
H
β6/7
90˚
β4
β8
I
β6/7
90˚
β4
β8

Figure 1.10. Crystal structures and atomic models for sHSPs. A) Crystal structure of a 24-mer of a sHSP (Hsp16.5) from the hyperthermophilic archaeon *Methanococcus jannaschii* (PDB: 1SHS[274]). B) Crystal structure of an isolated full-length dimer of Hsp16.5 from Methanococcus jannaschii (PDB: 1SHS[274]). C) Crystal structure of a 12-mer of a sHSP (Hsp16.9) from *Triticum aestivum* (wheat) (PDB: 1GME[275]). D) Oligomeric substructure of Hsp16.9 showing the bridging of three dimers to form a hexamer which is partly mediated by the binding of the CTR to a hydrophobic groove formed by the ACD (PDB: 1GME[275]). E) Structure of a dimer of Hsp16.9 (PDB: 1GME[275]). F) Model of a 24-mer of αB-C derived from a triple hybrid approach[276] depicting the two different conformations of the NTR, the patching of the ACD hydrophobic groove of adjacent dimers by a conserved motif within the CTR, and the dimeric interface formed between the extended β-strand 6/7 of two subunits[276] (PDB: 3J07). G) Model of a dimer within the αB-C 24-mer derived from the triple hybrid approach depicting the intermolecular β-sheet formed between both subunits of the dimer, and the two conformations of the NTR[276] (PDB: 3J07). H) Crystal structure of the excised ACD (red and green) of αB-C (residues 68-153) in complex with a fragment of the CTR (blue and yellow, residues 156-164). Structure depicts both the intermolecular β-sheet formed between both subunits of the dimer via the extended β-strand 6/7 and the patching of the β-4/8 hydrophobic groove by the CTR[279] (PDB: 4M5S). I) Solved crystal structure of the excised ACD (red and green) of Hsp27 (residues 84-176) in complex with a fragment of the CTR (blue and yellow, residues 179-186). Structure depicts both the intermolecular β-sheet formed between both subunits of the dimer via the extended β-strand 6/7 and the patching of the β-4/8 hydrophobic groove by the CTR[279] (PDB: 4MJH).

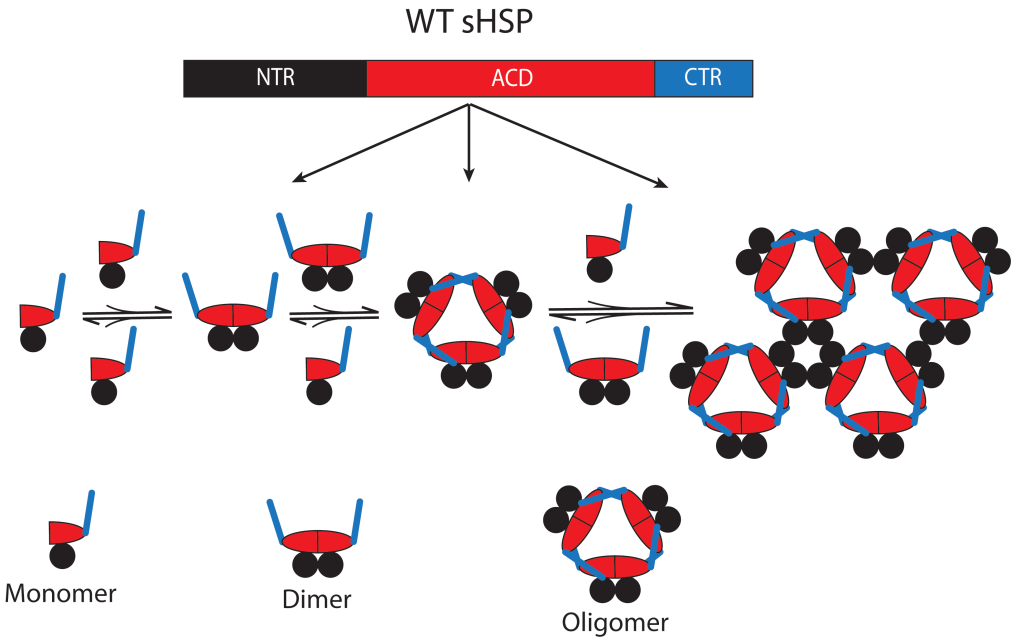


Figure 1.11. Depiction of the hierarchical assembly of sHSP oligomers from monomers and dimers. The domains of a full-length sHSP are coloured as follows: NTR, black; ACD, red; CTR, blue. WT sHSP such as αB-C and Hsp27 assemble into oligomers via multiple intermolecular interactions. Two ACDs interact to form dimers, the CTR interacts with an ACD from a separate dimer to facilitate the formation of small oligomers such as hexamers, and poorly defined interactions involving the NTR promote the formation of larger oligomers. Figure adapted from Delbecq et al[287].

1.5.2 The effects of post-translational modifications and amino acid mutations on the quaternary structure of small heat-shock proteins

Located within the NTR of some sHSPs are three conserved serine residues, which are post-translationally phosphorylated *in vivo*. The reversible phosphorylation of these serine residues (positions, 15, 78 and 82) in Hsp27 by stress-induced protein kinases results in the formation of predominantly dimers of Hsp27 (Fig. 1.12)[283,288]. Furthermore, mimicking the phosphorylation of Hsp27 at these three residues using serine-to-aspartate mutations (Hsp27-3D) also induces dimerization of Hsp27 (Fig. 1.12)[283,289]. Additional mutations in the C-terminal IXI/V motif that disrupt the interaction of the IXI/V motif with the β4/β8 groove can further shift the equilibrium towards Hsp27 dimers[290,291], however for this study we focused on Hsp27-3D only. The development of these dimeric constructs of Hsp27 has been particularly useful in enhancing structure-function studies of Hsp27 because they enable higher resolution structural analysis of Hsp27 using NMR. In the context of the phosphomimetic of Hsp27, peptide binding studies and paramagnetic relaxation enhancement experiments conducted using NMR identified heterogenous interactions between the NTR and the ACD[290]. Mutations that reduced the interactions of the NTR with the ACD were found to enhance the chaperone activity of Hsp27 towards tau[292]. Additionally, the phosphomimicking serine-to-aspartate mutations also increased the chaperone activity of Hsp27 against both amorphously aggregating targets and fibril forming species[283]. Overall, these findings suggest that smaller, sub-oligomeric forms of sHSPs are the major chaperone-active species[283] and this is due to the increased solvent exposure of chaperone-active regions (particularly the NTR) that are relatively more occluded in the context of Hsp27 oligomers. While αB-C also undergoes stress-induced phosphorylation at three serine residues in its NTR, this only alters the kinetics of subunit exchange such that the preference for oligomers with an even number of subunits is reduced[284].

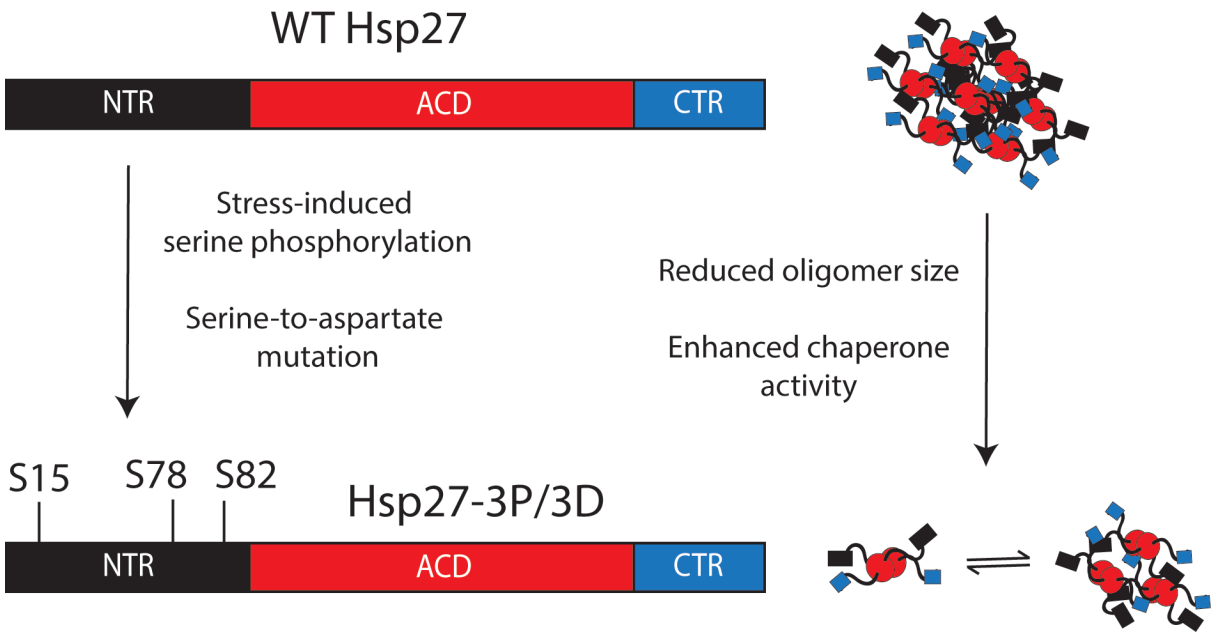


Figure 1.12. The effects of phosphorylation or serine substitution on the oligomeric size and chaperone activity of Hsp27. Stress-induced protein kinases phosphorylate Hsp27 on three serine residues (15, 78 and 82) in the N-terminal region. This leads to a reduction in oligomer size such that the protein predominantly assembles into dimers. Triply phosphorylated Hsp27 has an enhanced chaperone activity against some substrates relative to the unphosphorylated form. Mimicking phosphorylation at these three serine residues using serine-to-aspartate mutations mimics the effects of phosphorylation on oligomer size and chaperone activity.

1.5.3 Challenges in understanding the mechanisms of action of sHSPs

Though sHSPs have been observed to form high MW complexes with amorphously aggregating proteins in order to inhibit their aggregation[293–296], detecting interactions between sHSPs and amyloid-prone targets has been challenging. This is because the interactions between sHSPs and amyloid-prone targets are thought to be transient and low-affinity. Detection of transient protein-protein interactions is technically challenging because of the fast kinetics of dissociation. The polydisperse ensemble these sHSPs populate and the rapid subunit exchange further complicates the use mass-transport techniques such as analytical ultracentrifugation (AUC) or size-exclusion chromatography (SEC). Techniques such as NMR or fluorescence resonance energy transfer (FRET) which report on the proximity of chemical groups in solution on a much faster timescale are more widely used tools for investigating transient

protein-protein interactions. However, solution-state NMR is also challenging due to the slow tumbling rate of the large oligomers of WT sHSPs. Furthermore, some of the intermediates of protein off-folding pathways that sHSPs interact with exist only transiently and are therefore difficult to isolate. Despite these challenges, all three domains of sHSPs have been implicated in both substrate binding and chaperone activity against a broad range of targets[279,297,298]. NMR[292,295,299,300], proteolysis experiments[301], mutagenesis studies[298,300] and cross-linking investigations[302] found that hydrophobic motifs located at the edges of the ACD β-sandwich and in the NTR and CTR are capable of binding exposed hydrophobic motifs on misfolded intermediates to inhibit their aggregation. Since oligomer disassembly is associated with the exposure of these regions[303–305], sub-oligomeric forms of sHSPs, particularly dimers are widely regarded as the active chaperone species. Polydisperse oligomers are believed to serve as reservoirs of these sub-oligomeric forms, which are readily released under conditions of stress[306].

1.5.4 Small heat-shock proteins bind multiple species in the amyloid formation pathway

In addition to inhibiting the nucleation and elongation of a number of amyloid-prone targets including apoC-II[307] and α-syn[308], sHSPs, including αB-C and Hsp27 have been found to bind along the length and at the ends of mature apoC-II[258], Aβ(1-42)[309] and α-syn fibrils[310]. This binding has been proposed to cap fibrils to inhibit their elongation[295], however this was inferred mainly from ThT assays and no direct evidence was presented. The associations of sHSPs with pre-existing fibrils is also thought to promote monomer dissociation from fibril ends[247,310], prevent fibril fragmentation, and/or to prevent aberrant interactions between fibrils and other cellular components. As an example, the sHSP Hsp27 has been shown to specifically inhibit amyloid formation by α-syn[257], $A\beta_{40/42}$[311,312] and tau[291]. Hsp27 is proposed to exert these inhibitory effects via interactions with monomers[254], oligomers[291] and/or fibrils[257]. Similarly, the sHSP αB-C also inhibits amyloid formation by α-syn[254,313], $A\beta_{40/42}$[259] and β2-M[259]. The interaction of αB-C with matured α-syn fibrils is proposed to enhance amyloid fibril dissociation by the ATP-dependent HSPs, Hsp110, Hsp70 and Hsp40[270]. Furthermore, the interaction of αB-C with matured apoC-II fibrils directly enhances their dilution-induced dissociation and promotes their assembly into inclusion-like tangles, which are less prone to fragmentation[258]. These various studies demonstrate the multi-faceted ways in which sHSPs can interact with amyloid-prone proteins to reduce their toxicity[262].

1.5.5 Is the ACD sufficient for chaperone activity?

The structural biology of human sHSPs has been significantly advanced over the past decade by the solved crystal structures of the ACD of several human sHSPs[277–280]. However, the relative chaperone activity of these constructs, which predominantly form dimers, and full-length sHSP constructs, which form oligomers, remains somewhat controversial. Hochberg *et al.* demonstrated that a truncated construct encoding only residues 68-153 (the ACD) of αB-C forms predominantly dimers and exhibits near-identical chaperone activity to wild-type (WT) αB-C against amorphously aggregating α-lactalbumin (α-lac), and the amyloid forming proteins κ-casein and Aβ(1–42)[279]. Based on these assays, the authors proposed that the chaperone activity of αB-C is primarily conferred by the ACD. However, this hypothesis was formed on the basis of ThT fluorescence yields in ThT assays and no other methodologies were used to confirm these findings. Furthermore, Laganowsky *et al*. (2010) observed little or no chaperone activity for a dimeric construct of αB-C comprising residues 68-157 against the amorphous aggregation of alcohol dehydrogenase (ADH), insulin, lactalbumin, lysozyme, and ovotransferrin[280]. ACD-only constructs of Hsp27 (with ~50% sequence identity and ~80% sequence similarity to αB-C ACD) have also been found to be ineffective chaperones compared to their full-length counterparts[279,300,314]. These conflicting results suggest that the NTR and/or CTR are likely also involved in the chaperone activity of these proteins. In the context of Hsp27, full-length phosphomimetics that form predominantly dimers have been shown to chaperone substrates more effectively than WT Hsp27 which forms predominantly oligomers[283,289], suggesting that the oligomers are less effective chaperones. However, Augusteyn *et al*. (2004) observed an increase in chaperone activity when αB-C was chemically cross-linked to prevent oligomeric dissociation[315]. Thus, the differential chaperone activities of ACD-only constructs, full-length but dimeric constructs and WT oligomeric constructs of sHSPs, remain poorly characterised.

Even the mechanism by which the ACD may interact with substrates is not well established, however one of the widely accepted substrate binding sites is the hydrophobic β4/β8 cleft at the edge of the ACD β-sandwich (Fig 1.13). Substrates are thought to compete with the IXI/V motif in the CTR for binding to this site. Using NMR, Freilich *et al.* demonstrated the competitive binding of the internal IXI/V motif and also the repeat region of tau to the β4/β8 cleft of Hsp27[300]. However, the relevance of this interaction is

somewhat unclear. The authors subsequently determined that an ACD-only construct of Hsp27 was ineffective at inhibiting tau aggregation[300]. More recently, Alderson *et al.* examined the effect of removal of the naturally occurring intra-dimer disulfide in Hsp27 ACD[314]. The presence or absence of the intra-dimer disulfide is an important and sometimes overlooked factor in investigations of the chaperone activity of Hsp27 because this disulfide is likely to be in the reduced state in the intracellular environment. This was shown to destabilise the ACD dimer and enhanced its chaperone activity against α-lac, α-syn and insulin aggregation[314]. In this study, Alderson *et al.* proposed that μs – ms dynamics regulate the transition of the Hsp27 ACD from a chaperone inactive dimer to a chaperone active monomer[314], implying that the substrate binding site may also be involved in dimer formation. Supporting this, Rajagopal *et al.* demonstrated that the dimer interface in αB-C is destabilized by a reduction in pH or by mutating a conserved histidine residue near the intra-dimer interface[316]. These mutants were more effective chaperones against the amorphous aggregation of α-lac and ADH[316].

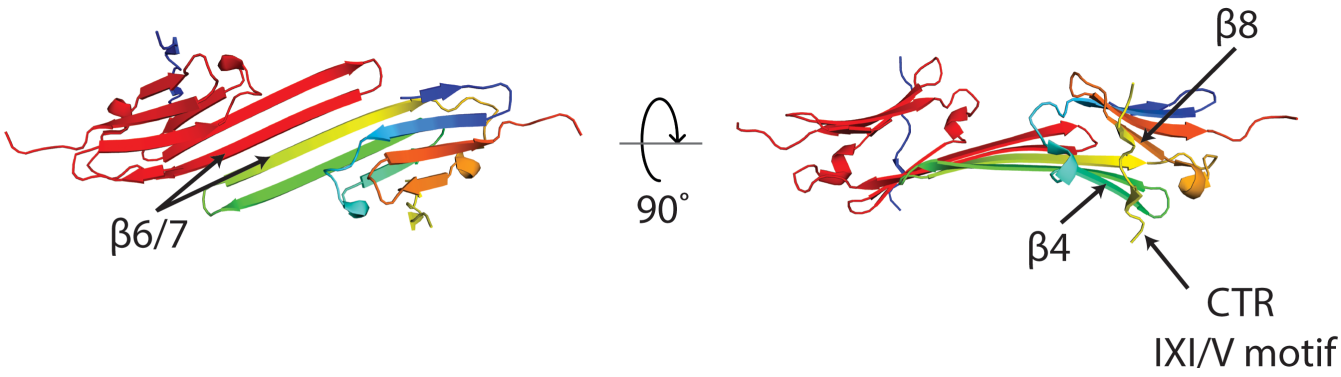


Figure 1.13. Crystal structure of the αB-C ACD dimer (PDB: 4m5s)[279]. One subunit is coloured red and the other subunit is coloured from blue – red from the N-terminus to C-terminus (using PyMOL). The dimer interface is formed via an intermolecular β-sheet between β-strand 6/7 of each subunit. The edge of the ACD β-sandwich is formed by β-strands 4 and 8, which are indicated in one of the subunits in the dimer structure. The IXI/V motif in the CTR docks to the β4/8 cleft to facilitate oligomerization in full-length sHSPs.

1.6 Scope of project and aims

How can these conflicting observations be rationalized in order to gain an understanding of the mechanism of action of sHSPs? Firstly, given the broad diversity of sHSP substrates, and that sHSPs are

effective chaperones at sub-stoichiometric ratios, it is likely that sHSP subunits possess multiple substrate binding sites located across all three domains [297,298]. The binding sites may differ for different targets, and sHSP subunits may bind more than one substrate molecule at a time. Secondly, it is noteworthy that sHSPs appear to inhibit both amorphous aggregation and amyloid formation, yet the structure(s) of the substrates are likely to differ substantially between these two types of aggregation, and at different stages of the aggregation pathway. Lastly, the exact nature of the interactions between sHSPs and their substrates must be rigorously tested. For example, does the sHSP interact with the monomeric, oligomeric or fibrillar form of the given substrate? The interaction between a sHSP and a substrate in its monomeric form would differentially inhibit its aggregation kinetics relative to a sHSP that interacts with the substrate in its fibrillar form. Furthermore, are these interactions transient and short-lived, or long-lived, resulting in sequestration of the sHSP? In some of the studies mentioned in previous sections, the authors have not determined the nature of the interaction between the sHSP and the substrate. This work therefore seeks to advance our understanding of how sHSPs inhibit amyloid fibril formation, with specific emphasis on substrate-sHSP interactions and the mechanism of action of the ACD of αB-C and Hsp27. The mechanisms by which sHSPs inhibit amorphous protein aggregation are beyond the scope of this work.

This project is divided into two research aims. The first aim was to improve our understanding of the structure/function relationship of these proteins by comparing the chaperone activities of an array of constructs in which the structures and domain compositions have been modified. Such comparisons should provide insights into the roles of the three domains of sHSPs, and furthermore the importance of the quaternary structures of these proteins in performing their various chaperone roles. The second aim was to focus on the highly conserved ACD, for which high resolution structural data exists, and identify any interactions of this domain with amyloid fibrils.

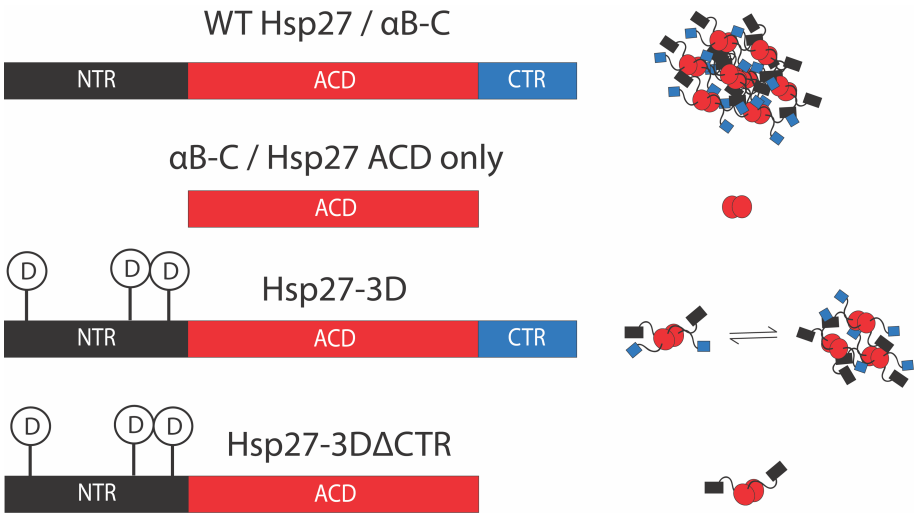


Figure 1.14. Schematic representing the domain composition and quaternary structures of the sHSP constructs used for aim 1. WT αB-C and WT Hsp27 assemble into oligomers of an undefined size. Importantly, these oligomers exchange subunits that may be either monomeric or dimeric. αB-C ACD and Hsp27 ACD assemble into primarily dimers, however αB-C ACD exists in equilibrium with a small proportion of monomer at pH 7.4. Due to an intra-dimer disulfide, Hsp27 ACD exists as disulfide cross-linked dimers, however reducing agents can be used to reduce the disulfide bridge and allow for monomer-dimer exchange. Three serine-to-aspartate mutations in the N-terminal region of Hsp27 mimic natural serine phosphorylation in this region and reduce the average size of Hsp27, such that the protein primarily assembles into dimers, existing in equilibrium with a small proportion of small oligomers. Removal of the CTR from this construct results in the formation of almost exclusively dimers (at least in the absence of reducing agents). We did not detect the assembly of this construct into larger oligomers.

For the first aim, the array of constructs that we have used in our chaperone activity assays is depicted in Fig. 1.14. The differences in the quaternary structures of these proteins and their domain compositions allows, by a process of deduction, some conclusions to be drawn regarding the structure/function relationships of these chaperones.

Chapter 2: Materials and Methods

2.1 Materials

A pET11a vector was used for apoC-II expression. pET24a vectors encoding human α-syn, αB-C ACD (residues 68-153), αB-C ACD E117C (residues 68-153) and Hsp27 ACD (residues 84-176), pET24d vectors encoding WT αB-C and αB-C E117C and pET3a vectors encoding human Hsp27 and Hsp27-3D (with S15D, S78D and S82D mutations) were kindly provided by Professor Heath Ecroyd (The University of Wollongong, NSW, Australia). Tobacco Etch Virus (TEV) protease with L56V and S135G stabilizing mutations was expressed and purified according to the methods developed by Cabrita *et al.* (2007)[317].

BL21 (DE3) *E. coli* cells purchased from Invitrogen (CA, USA) were made chemically competent through $CaCl_2$ treatment[318]. Oligonucleotide primers used for mutagenesis were purchased from Sigma-Aldrich (MO, USA). Pfu Turbo DNA polymerase used for mutagenesis was purchased from Agilent Technologies (CA, USA). Plasmid purification (miniprep) kits were purchased from either Promega (WI, USA) or Qiagen Inc (MD, USA). DEAE Sephacel resin, Sephacryl S300-HR resin, Sephacryl S200-HR resin, XK chromatography columns, 5 mL HisTrap HP columns and a HiPrep 16/60 column packed with Sephacryl S-100 HR resin were purchased from GE Healthcare-Amersham Biosciences (NJ, USA). Low-range SDS-PAGE MW standards were purchased from Bio-Rad Life Sciences (NSW, Australia). Amicon Ultra 15 mL filters and Benzonase nuclease were purchased from Millipore (MA, USA). ThT, high-grade guanidinium hydrochloride (GuHCl), polyethylenimine (PEI), Roche cOmplete™ EDTA-free protease inhibitor cocktail tablets and lysozyme were purchased from Sigma-Aldrich (MO, USA). Isopropyl β-D-1-thiogalactopyranoside (IPTG) and the protease inhibitor phenylmethylsulfonyl fluoride (PMSF) was purchased from Thermo Fisher Scientific (MA, USA). Dithiothreitol (DTT) and tris(2-carboxyethyl)phosphine (TCEP) were purchased from Astral Scientific (VIC, Australia). Alexa-488 labeled apoC-II^{S61C} was a kind gift from Associate Prof. Mike Griffin (Department of Biochemistry and Molecular Biology, The University of Melbourne). $^{15}NH_4Cl$ and deuterium oxide (D_2O) was purchased from Cambridge Isotope laboratories (MA, USA).

2.2 Methods

2.2.1 *In vitro* mutagenesis

Primers were designed to mutate residue 137 in WT Hsp27, Hsp27 ACD, Hsp27-3D and Hsp27-3DΔCTR from cysteine to serine. Additionally, primers were designed for the insertion of a stop codon at the position corresponding to residue 177 in Hsp27-3D (to create Hsp27-3DΔCTR). A cysteine residue was also added to the C-terminal end of αB-C ACD via mutagenesis. The sequences of these primers are listed in Table 2.1

Table 2.1 Oligonucleotide sequences for the forward and reverse primers used for mutagenesis of sHSP constructs

Construct name	Parent plasmid	Direction of primer	Sequence of primer
Hsp27 C137S, Hsp27-3D C137S, Hsp27-3DΔCTR C137S	pET3a	Forward	TACATCTCCCGGTCCTTCACGCGGAAATACACG
		Reverse	CGTGTATTTCCGCGTGAAGGACCGGGAGATGTAGC
Hsp27 ACD C137S	pET24a	Forward	TACATCTCCCGGTCCTTCACGCGGAAATACACG
		Reverse	CGTGTATTTCCGCGTGAAGGACCGGGAGATGTAGC
Hsp27-3DΔCTR	pET3a	Forward	CCACGCAGTCCTAAGAGATCACCATCC
		Reverse	GATGGTGATCTCTTAGGACTGCGTGG
αB-C ACD C154	pET24a	Forward	GGAAACAGGTCTCTTGTTAACTCGAGCACCACC
		Reverse	GGTGGTGCTCGAGTTAACAAGAGACCTGTTTCC

Mutations were made using the Pfu Turbo DNA polymerase and according to the QuikChange II site directed mutagenesis kit protocol (Agilent Technologies, CA, USA). Mutations in the parent plasmid were confirmed by DNA sequencing (Australian Genome Research Facility, VIC, Australia). Mutated plasmids were subsequently transformed into chemically competent XL-1 blue cells and isolated using plasmid miniprep kits (either Qiagen Inc, MD, USA or Promega, WI, USA). These mutated plasmids were used for subsequent protein expression according to the protocols outlined below.

2.2.2 Cell cultures

All liquid cultures used for expression were incubated at 37°C, 200 rpm, unless specified otherwise. Ampicillin (amp) was used at a concentration of 100 µg/mL. Kanamycin (kan) was used at a concentration of 50 µg/mL. Plasmid vectors encoding the relevant protein were transformed into chemically competent BL21 (DE3) cells using the heat-shock method. Cells were recovered in 800 µL of Luria Broth (LB; 1% (w/v) tryptone, 1% (w/v) NaCl, 0.5% (w/v) yeast extract) for 1 hour, spread onto LB agar (1.5% (w/v)) plates containing the relevant antibiotic and incubated at 37°C overnight. A single colony was inoculated into 100 mL starter culture of LB containing the relevant antibiotic and incubated overnight.

2.2.3 Preparation and purification of apoC-II from bacterial inclusions

ApoC-II was expressed and purified as previously described[152] with some modifications. Briefly, 4 L expressions were initiated by inoculating LB-amp with 1% (v/v) starter culture and when an optical density (OD) of 0.8 at 600 nm was reached IPTG was added (1 mM final concentration), and flasks were incubated for 2.5 hours. Cells were harvested at 6340 x g, 4°C for 10 mins (F10S rotor, RC-6 plus Sorvall, Thermo Scientific). Pellets were resuspended in 300 mL of TN buffer (50 mM Tris HCl, 100 mM NaCl, pH 8.0) and stored at -20°C until use. Lysozyme (80 mg), 1 µL Benzonase nuclease and $MgCl_2$ (6 mM) were added to the thawed cell suspension which was stirred for 30 minutes at 20°C. Inclusion bodies were pelleted by centrifugation at 17600 x g, 4°C for 30 minutes (F21-8x50y rotor, RC-6 plus Sorvall, Thermo Scientific) and washed twice by centrifugation as above with 100 mL TN buffer with 0.1% TritonX-100 and a third wash step with TN buffer alone. The pellet was resuspended in 30 mL of 6 M Urea, 10 mM Tris HCL, pH 8.0. Inclusion bodies were sonicated at an amplitude of 40% for 30 second intervals (Q500 sonicator, 3.2 mm microtip probe, QSonica, USA) until clear and viscous. The suspension was centrifuged at 30310 x g, 4°C for 30 minutes (F21-8x50y rotor, RC-6 plus Sorvall, Thermo Scientific) and the supernatant was loaded onto a DEAE Sephacel resin anion-exchange column pre-equilibrated with 6 M Urea, 10 mM Tris HCl, pH 8.0. ApoC-II was eluted from the resin using a linear gradient of 6M Urea, 10 mM Tris HCl, 1M NaCl, pH 8.0 to a final concentration of 0.5 M NaCl at a flow rate of 2 mL/min over six column volumes (CVs). ApoC-II containing fractions were pooled and concentrated to 10 mL using

Amicon ultracentrifugal filter units (Merck, MA, USA) and loaded onto a 2.5 x 100 cm XK 26/100 gel filtration column packed with Sephacryl S200-HR resin pre-equilibrated with 6 M Urea, 10 mM Tris HCl, pH 8.0. ApoC- II was eluted using the same buffer at a flow rate of 2 mL/min. ApoC-II containing fractions were pooled and dialysed against 10 mM ammonium bicarbonate, frozen in liquid nitrogen, lypophilised and resuspended in 5 M GuHCl, 10 mM Tris HCl, pH 8.0. The concentration of apoC-II was verified by absorbance readings using a DU800 spectrophotometer (Beckman Coulter, CA, USA) at 280 nm using an extinction coefficient for apoC-II of 1.453 $mg^{-1}mL^{-1}cm^{-1}$. Purified stocks were kept at -20°C at approximately 30 mg/mL.

2.2.4 Expression and purification of αB-C ACD and Hsp27 ACD C137S

Human αB-C ACD (residues 68-153) and Hsp27 ACD C137S (residues 84-176) were expressed with N-terminal 6 x His-tags and purified according to an established protocol[280] with minor modifications. Kan was used for selection and induction was performed using a concentration of 0.5 mM IPTG for 4 hours. Cell pellets were resuspended in 30 mL of TNA buffer (20 mM TrisCl pH 8.0, 500 mM NaCl, 40 mM imidazole) and stored at -20°C until use. Upon thawing, Benzonase nuclease (5 µL), $MgCl_2$ (6 mM final concentration), PMSF (1 mM final concentration), half of one cOmplete™ protease inhibitor cocktail tablet (Roche) and 80 mg lysozyme were added to the resuspended cells. The resuspended cells were stirred at RT for 30 mins and lysed by ultrasonication at an amplitude of 40% for 30 second intervals (Q500 sonicator, 3.2 mm microtip probe, QSonica, USA) until clear and viscous. Lysate was clarified by centrifugation at 30,310 x g for 30 mins at 4°C (F21-8x50y rotor, RC-6 plus Sorvall, Thermo Scientific) and filtration through a 0.22 µm syringe-driven filter. The clarified lysate was applied to a 5 mL HisTrap column pre-equilibrated with TNA buffer and eluted with a linear gradient to 100% TNB buffer (20 mM TrisCl pH 8.0, 500 mM NaCl, 500 mM imidazole) over 20 CVs. Fractions containing His-tagged αB-C ACD or Hsp27 ACD C137S were pooled and TEV protease was added at a protein mass ratio of approximately 1:4 (TEV:His-ACD). The mixture was dialysed against 20 mM TrisCl pH 8.0, 100 mM NaCl overnight at 4°C. TNB buffer was added to the mixture to a final imidazole concentration of 40 mM and the mixture was applied to a 5 mL HisTrap column pre-equilibrated with TNA buffer. The flow through was collected, containing truncated αB-C ACD or Hsp27 ACD C137S. The flow through was concentrated to ~ 2.5 mL using Amicon ultracentrifugal filter units and loaded onto a HiPrep 16/60 gel filtration column packed

with Sephacryl S-100 HR resin pre-equilibrated in 50 mM sodium phosphate pH 7.4, 0.02% sodium azide. Fractions eluting from the gel filtration column were pooled, concentrated and frozen in liquid nitrogen. The concentrations of αB-C ACD and Hsp27 ACD C137S were verified by absorbance readings using a DU800 spectrophotometer (Beckman Coulter, CA, USA) at 280 nm using extinction coefficients of 0.15 $mg^{-1}mL^{-1}cm^{-1}$ for αB-C ACD and 0.822 $mg^{-1}mL^{-1}cm^{-1}$ for Hsp27 ACD C137S. Purified stocks were kept at -80°C at concentrations of approximately 1 – 25 mg/mL depending on the desired application.

2.2.5 Expression and purification of αB-C ACD E117C, αB-C ACD C154 and Hsp27 ACD

Human αB-C ACD E117C (residues 68-153), αB-C ACD C154 (residues 68-153 with a C-terminal cysteine) and Hsp27 ACD (residues 84-176) were expressed and purified identically to that described above for αB-C ACD and Hsp27 ACD C137S with the exception that 5 mM DTT was used in the overnight TEV cleavage reaction and dialysis buffer, and in TNA buffer during the subtractive IMAC step. The concentrations of αB-C ACD E117C and Hsp27 ACD were verified by absorbance readings using a DU800 spectrophotometer (Beckman Coulter, CA, USA) at 280 nm using extinction coefficients of 0.157 $mg^{-1}mL^{-1}cm^{-1}$ for αB-C ACD E117C, 0.148 $mg^{-1}mL^{-1}cm^{-1}$ for αB-C ACD C154 and 0.827 $mg^{-1}mL^{-1}cm^{-1}$ for Hsp27 ACD. Purified stocks were kept at -80°C at concentrations of approximately 1 – 25 mg/mL depending on the desired application.

2.2.6 Expression and purification of α-synuclein

The expression and purification of α-syn was performed according to an established protocol[319] with minor modifications. Briefly, 4 L expressions were initiated by inoculating LB-amp with 1% (v/v) starter culture and when an OD of 0.8 at 600 nm was reached IPTG was added (0.5 mM final concentration), and flasks were incubated for 4 hours. Cells were harvested at 6340 x g, 4°C for 10 mins (F10S rotor, RC-6 plus Sorvall, Thermo Scientific). Pellets were resuspended in 300 mL of TN buffer (50 mM Tris HCl, 100 mM NaCl, pH 8.0) and stored at -20°C until use. PMSF (1.3mM) and lysozyme (0.1 mg/mL), was added to the thawed cell suspension, which was stirred on ice for 30 mins. 2 µL benzonase nuclease and $MgCl_2$ (6 mM) was added and the lysate was incubated at 37°C for 30 mins at 200 rpm. The lysate was clarified at 524 x g, 4°C for 10 mins (SX4750 rotor, Allegra benchtop centrifuge, Beckman Coulter). The supernatant

was centrifuged first at 25,000 x g, 4°C for 30 mins then at 100,000 x g, 4°C for 30 mins (Ti70 rotor, Optima L-100 XP Ultracentrifuge, Beckman Coulter). DTT (10mM), PEI (Sigma-Aldrich, MO, USA) (0.12% (w/v)) and ethylenediaminetetraacetic acid (EDTA) (1mM) were added to the supernatant, which was stirred at 20°C for 30 mins and then centrifuged at 100,000 x g, 4°C for 30 mins (Ti70 rotor, Optima L-100 XP Ultracentrifuge, Beckman Coulter). The pH of the supernatant was adjusted to 4.0 using HCl and was stirred at 20°C for 30 mins. The suspension was centrifuged at 100,000 x g, 4 °C for 30 mins (Ti70 rotor, Optima L-100 XP Ultracentrifuge, Beckman Coulter) and the pH of the supernatant was adjusted to 8.0 using NaOH. The supernatant was then loaded onto a DEAE Sephacel resin anion-exchange column pre-equilibrated with 20 mM Tris-HCl, 1 mM EDTA, 0.02% sodium azide, pH 8.5. α-Syn was eluted from the column using a linear gradient of 20 mM Tris-HCl, 2 M NaCl, 1 mM EDTA, 0.02% sodium azide, pH 8.5 to 0.5 M NaCl at a flow rate of 2.5 mL/min over six CVs. Fractions containing α-syn were pooled and concentrated to 10 mL using Amicon ultracentrifugal filter units. The concentrated α-syn was loaded onto a 2.5 x 100 cm XK 26/100 gel filtration column packed with Sephacryl S200-HR resin pre-equilibrated with 6 M Urea, 10 mM Tris HCl, pH 8.0. α-Syn was eluted from the column using the same buffer at 2 mL/min. The fractions were pooled and dialysed against 10 mM ammonium bicarbonate, lypophilised and resuspended in 6 M GuHCl, 10 mM Tris HCl, pH 8.0. The concentration of α-syn was verified using an extinction coefficient of 0.412 $mg^{-1}mL^{-1}cm^{-1}$ and purified stocks were kept at -20°C at concentrations of 75-140 mg/mL.

2.2.7 Expression and purification of WT αB-C, αB-C E117C, WT Hsp27 and Hsp27 C137S

Human WT αB-C, αB-C E117C, WT Hsp27 and Hsp27 C137S were expressed and purified as described previously[320] with minor modifications. Briefly, 4 L expressions were initiated by inoculating LB-amp with 1% (v/v) starter culture and when an OD of 0.8 at 600 nm was reached IPTG was added (0.5 mM final concentration), and flasks were incubated for 4 hours. Cells were harvested at 6340 x g, 4°C for 10 mins (F10S rotor, RC-6 plus Sorvall, Thermo Scientific). Pellets were resuspended in 300 mL of TN buffer (50 mM Tris HCl, 100 mM NaCl, pH 8.0) and stored at -20°C until use. Upon thawing, PMSF (1 mM final concentration), half of one cOmplete™ protease inhibitor cocktail tablet (Roche), 80 mg lysozyme and deoxycholate (3.2 mM final concentration) were added to the resuspended cells, which were then incubated at room temperature for 30 mins with occasional mixing. Subsequently, Benzonase nuclease

(5 µL) and $MgCl_2$ (6 mM final concentration) were added and the mixture was again incubated at room temperature with occasional mixing until it was no longer viscous. EDTA was added to a final concentration of 680 µM and the mixture was centrifuged at 40,000 x g (Ti70 rotor, Optima L-100 XP Ultracentrifuge, Beckman Coulter) for 15 min at 4°C. The supernatant was collected and DTT and PEI were added to final concentrations of 21.6 mM and 2.4 µL/ml, respectively. The sample was incubated for 10 mins at room temperature with constant stirring and centrifuged again at 40,000 x g for 15 min at 4°C. The supernatant was collected and filtered using a 0.22 µm syringe-driven filter. The supernatant was then loaded onto a DEAE Sephacel resin anion-exchange column pre-equilibrated with 20 mM Tris-HCl, 1 mM EDTA, 0.02% sodium azide, pH 8.5 at a flow rate of 2.5 mL/min. The proteins were eluted from the column using a linear gradient to 10% TNB buffer (20 mM Tris-HCl, 1 mM EDTA, 0.02% sodium azide, pH 8.5, 1M NaCl) over 2 CVs followed by a linear gradient to 20% TNB buffer over 3 CVs and finally a linear gradient to 100% TNB buffer over a further 2 CVs. Fractions containing WT αB-C, αB-C E117C, WT Hsp27 or Hsp27 C137S were pooled and concentrated to 10 mL using Amicon ultracentrifugal filter units. The concentrated WT αB-C, αB-C E117C, WT Hsp27 or Hsp27 C137S was loaded onto a 2.5 by 100 cm XK 26/100 gel filtration column packed with Sephacryl S300-HR resin pre-equilibrated with phosphate buffer (50 mM sodium phosphate buffer + 0.02% sodium azide, pH 7.4). The proteins were eluted from the column using phosphate buffer at 2 mL/min. Peak fractions were concentrated and snap frozen in liquid nitrogen. The concentrations of WT αB-C, αB-C E117C, WT Hsp27 and Hsp27 C137S were verified by absorbance readings using a DU800 spectrophotometer (Beckman Coulter, CA, USA) at 280 nm using extinction coefficients of 0.693 $mg^{-1}mL^{-1}cm^{-1}$ for WT αB-C, 0.694 $mg^{-1}mL^{-1}cm^{-1}$ for αB-C E117C, 1.786 $mg^{-1}mL^{-1}cm^{-1}$ for WT Hsp27 and 1.777 $mg^{-1}mL^{-1}cm^{-1}$ for Hsp27 C137S. Purified stocks were kept at -80°C at approximately 2 – 7 mg/mL.

2.2.8 Expression and purification of Hsp27-3D

Human Hsp27-3D was initially expressed and partially purified with an N-terminal 6 x His tag and a TEV protease cleavage site. Low yields, difficulty in cleaving the N-terminal tag and insolubility hindered purification (data not shown). SV-AUC was used to assess the oligomeric state of His-tagged and untagged Hsp27-3D. The continuous size distribution (c(s)) profiles obtained indicated that although

untagged Hsp27-3D is predominantly dimeric, His-tagged Hsp27-3D forms a large oligomeric complex approximately 2 MDa in size (data not shown). The large size of this complex was presumed to occlude some of the TEV protease cleavage sites, thereby severely reducing the efficiency of the protease and the final yield of untagged Hsp27-3D. Therefore, a plasmid construct encoding human Hsp27-3D without an N-terminal His-tagged was obtained from Prof. Heath Ecroyd (School of Biosciences, University of Wollongong). Expression and purification of untagged Hsp27-3D was carried out as for WT Hsp27 with the following changes. Peak fractions eluting from the Sephacryl S300-HR 26/100 column were pooled and 4 M ammonium sulfate was added to a final ammonium sulfate concentration of 750 mM. These pooled fractions were loaded onto a fast flow 26/10 Phenyl-Sepharose hydrophobic interaction chromatography (HIC) column. The protein was eluted using a linear gradient from 50 mM sodium phosphate pH 7.4, 1 M ammonium sulfate to 50 mM sodium phosphate pH 7.4 over 20 CVs, and a subsequent gradient from 50 mM sodium phosphate pH 7.4 to dH_2O over 15 CVs. Peak fractions containing Hsp27-3D were concentrated to approximately 3 mL and applied to a pre-equilibrated HiPrep 16/60 gel filtration column packed with Sephacryl S-100 HR resin and eluted in 50 mM phosphate pH 7.4, 0.02% sodium azide. Fractions containing Hsp27-3D were pooled, concentrated and snap frozen in liquid nitrogen. The concentration of Hsp27-3D was verified using an extinction coefficient of 1.779 $mg^{-1}mL^{-1}cm^{-1}$ and purified stocks were kept at -80°C at concentrations of approximately 3 – 10 mg/mL.

2.2.9 Expression and purification of Hsp27-3DΔCTR

Human Hsp27-3DΔCTR (residues 1-176) was expressed and purified according to published methods used to purify WT Hsp27[321]. Briefly, 4 L expressions were initiated by inoculating LB-amp with 1% (v/v) starter culture and when an OD of 0.8 at 600 nm was reached IPTG was added (0.5 mM), and flasks were incubated for 4 hours. Cells were harvested at 6340 x g, 4°C for 10 mins (F10S rotor, RC-6 plus Sorvall, Thermo Scientific). Pellets were resuspended in 300 mL of TN buffer (50 mM Tris HCl, 100 mM NaCl, 1 mM EDTA, pH 8.0) and stored at -20°C until use. Upon thawing, PMSF (1 mM final concentration), half of one cOmplete™ protease inhibitor cocktail tablet (Roche) and 80 mg lysozyme were added to the resuspended cells, which were then incubated at room temperature for 20 mins on ice with occasional mixing. The cells were transferred to a 250 mL flask containing 80 mg of solid deoxycholate. The flask was placed in a 37°C shaking incubator at 150 rpm for 15 mins. Subsequently

Benzonase nuclease (5 µL) and $MgCl_2$ (6 mM final concentration) were added and the mixture was again incubated at 150 rpm, 37°C for 15 mins or until it was no longer viscous. The lysate was clarified by centrifugation at 30310 x g for 15 mins at 4°C (F21-8x50y rotor, RC-6 plus Sorvall, Thermo Scientific). The supernatant was transferred to a clean 250 mL flask and placed on a slow shaker (~20 rpm) at room temperature. 4 M ammonium sulfate was added to a final concentration of 40% (v/v) dropwise over approximately 3 mins. The flask was left at room temperature at 20 rpm for 30 mins. This mixture was centrifuged at 30310 x g for 15 mins at 20°C (F21-8x50y rotor, RC-6 plus Sorvall, Thermo Scientific). The supernatant was discarded and the pellet, containing Hsp27-3DΔCTR was dissolved in 30 mL of 20 mM Tris, 10 mM $MgCl_2$, 30 mM NH_4Cl, pH 7.6. This sample was dialysed against the same buffer at 4°C overnight and the mixture was then centrifuged again at 30310 x g for 15 mins at 20°C (F21-8x50y rotor, RC-6 plus Sorvall, Thermo Scientific). The supernatant was loaded onto a DEAE Sephacel resin anion-exchange column pre-equilibrated with TMA buffer (20 mM Tris, 10 mM $MgCl_2$, 30 mM NH_4Cl, pH 7.6) at 2.5 mL/min. The protein was eluted from the column using a linear gradient to 10% TMB buffer (20 mM Tris, 10 mM $MgCl_2$, 30 mM NH_4Cl, pH 7.6, 1M NaCl) over 2 CVs followed by a linear gradient to 20% TMB buffer over 3 CVs and finally a linear gradient to 100% TMB buffer over a further 2 CVs. Fractions containing Hsp27-3DΔCTR were pooled and concentrated to ~ 2.5 mL using Amicon ultracentrifugal filter units and loaded onto a HiPrep 16/60 gel filtration column packed with Sephacryl S-100 HR resin pre-equilibrated in 50 mM sodium phosphate pH 7.4, 0.02% sodium azide. Fractions eluting from the gel filtration column were pooled and concentrated and snap frozen in liquid nitrogen. The concentration of Hsp27-3DΔCTR was verified using an extinction coefficient of 2.051 $mg^{-1}mL^{-1}cm^{-1}$ and purified stocks were kept at -80°C at concentrations of 2 – 6 mg/mL.

2.2.10 Isotope labelling of αB-C ACD

A 100 x micronutrient mixture was prepared with the following components: 6g/L $FeSO_4$, 6 g/L $CaCl_2$, 1.2 g/L $MnCl_2$, 0.8 g/L $CoCl_2$, 0.7 g/L $ZnSO_4$, 0.3 g/L $CuCl_2$, 20 mg/L H_3BO_3, 0.25 g/L $(NH_4)_6Mo_7)_{24}.4H_2O$ and 5 g/L EDTA. Uniformly ^{15}N-labeled αB-C ACD was expressed in BL21 DE3 *E. coli* cells using the autoinduction protocol[322]. 2 L cultures were grown at 37 °C, 200 rpm in N-5052 media (50 mM K_2HPO_4, 50 mM KH_2PO_4, 5 mM Na_2SO_4, 2 mM $MgSO_4$, 0.5% (w/v) glycerol, 0.05% (w/v) glucose, 0.2% (w/v) lactose and 0.6 x micronutrient mixture (6 mL/L)) containing $^{15}NH_4Cl$ (1 g/L) as the sole nitrogen source

for 8 hours and at 16°C until a static OD was reached, at which point the cells were harvested by centrifugation as outlined above (section 2.2.4). Purification was performed as described above (section 2.2.4). The percentage of ^{15}N labelling ($N_{\%}$) was calculated using the following equation:

$$N_{\%} = \frac{MW_{theoretical} - MW_{determined}}{N_{Nitrogen}} * 100 \ (Eq. 2.1)$$

Where $MW_{determined}$ is the deconvoluted mass derived from MS (section 2.2.11), $MW_{theoretical}$ is the theoretical MW of the protein assuming all nitrogen atoms are ^{15}N isotopes and $N_{Nitrogen}$ is the number of nitrogen atoms in the protein. The concentration of ^{15}N-labelled αB-C ACD was verified using an extinction coefficient of 0.15 $mg^{-1}mL^{-1}cm^{-1}$ and purified stocks were kept at -80°C at concentrations of 1.5 – 2.5 mM.

2.2.11 Estimation of protein purity and protein mass

The purity of all protein stocks was determined to be ≥95% using SDS-PAGE and liquid chromatography MS (LC-MS). For all SDS-PAGE assays, 20 µL aliquots were diluted in 2 x SDS loading buffer (0.1% Bromophenol Blue, 2% SDS, 10 mM Tris HCl, 20% glycerol, pH 8.45) and boiled at 100°C for 5-10 minutes prior to gel loading. 16 % acrylamide Tris-tricine SDS-PAGE gels were run at 70 V for 15 minutes and 110 V for 2.5 hours using a cathode (0.2 M Tris HCl) and anode (0.1 M Tris HCl, 0.1 M Tricine, 0.1% SDS) running buffer. Gels were stained using 50% (v/v) methanol, 10% (v/v) acetic acid and 0.1% (w/v) Coomassie Brilliant Blue R-250 overnight and destained using 50% (v/v) methanol and 10% (v/v) acetic acid overnight.

LC-MS provides high resolution information regarding the MW of proteins/peptides. Samples are injected onto a reverse-phase chromatography column whereby hydrophobic interactions drive interactions of the polypeptides with the stationary phase. The polypeptides are eluted in a manner dependent on their hydrophobicity using a gradient of increasing acetonitrile concentrations. The eluate is sprayed as charged droplets through the electrospray ionization (ESI) capillary needle into an electric field with a high potential difference between the needle tip and the counter electrode. The potential difference results in the repulsion of the charged droplets away from the ESI needle towards the

counter electrode. The droplets also traverse a gradient of decreasing gas pressure due to the counter-flow of heated N_2 gas. This results in solvent evaporation from the charged droplets. As the droplet radius is decreased, the density of charges on the surface of the droplet increases. Eventually the droplet reaches a size at which the surface tension cannot sustain the surface charge (the Rayleigh limit). At this point a "Coulombic explosion" occurs and the droplet is broken apart. This process continues eventually producing "naked" charged analyte molecules which can have varying associated charges. These charged molecules are accelerated into a time of flight (TOF) mass analyser. The ions traverse the TOF analyser according to their mass/charge (m/z) ratio to a detector which measures the intensities of all the ions with differing m/z ratios. This generates a spectra of signal intensities versus m/z ratios, which can be deconvoluted to generate estimates of protein masses.

For MS, a 6520 Accurate-Mass Q-TOF LC/MS (Agilent) coupled with HPLC was used. 10 µL samples were injected onto a Jupiter 5 µm C5 300 Å column at a flow rate of 0.2 mL/min. The following protocol was used to elute proteins from the column: 100% A buffer (0.1% formic acid) from 0 – 3 minutes, a gradient from 0 – 100% B buffer (acetonitrile with 0.1% formic acid) from 3 – 15 minutes, 100% B buffer from 15 – 16 minutes, a gradient from 0 – 100% A buffer from 16 – 17 minutes and a final equilibration with 100% A buffer from 17 – 20 minutes. A gas temperature of 350°C was used for ESI and the capillary voltage was set to 3500 V. The MS-TOF fragmentor voltage was set to 130 V. Spectra deconvolution was performed using Agilent MassHunter Qualitative Analysis B.06.00 software with a limited m/z range set at 600-2000.

2.2.12 Fibril sonication

Ultrasonication has been well established as a method of fragmenting amyloid fibrils, resulting in fibril populations with uniform lengths[87]. Furthermore, sonication has previously been demonstrated to reduce the lengths (and therefore increase the number of free fibril ends) of apoC-II fibrils via SV-AUC[85]. For SV-AUC or NMR experiments using fragmented fibrils, or for ThT experiments using fibril seeds, apoC-II or α-syn fibrils were sonicated at an amplitude of 20% (1.6 mm mictrotip probe, Q500 sonicator, QSonica, USA) on ice for fourteen 30 second on/off-pulses.

2.2.13 Circular dichroism spectroscopy

CD spectroscopy is widely used to analyse the secondary structure of proteins based on their absorbance of circularly polarised light. In this work, CD spectroscopy was used to determine the effects of point mutations on the secondary structure of various sHSP constructs. Far-UV CD spectra were collected at protein concentrations of 0.15 – 0.2 mg/mL in 0.1 M sodium phosphate, pH 7.4. An AVIV-410SF Spectrometer (AVIV Biomedical Inc., USA) with a quartz cuvette with a path length of 1 mm was used to collect data over the wavelength range 190 - 260 nm in 1.0 nm steps with an averaging time of 4 seconds. Buffer signal contribution was also corrected for by subtracting the buffer θ_{obs} from the θ_{obs} of the protein solution. Data was converted to mean residue ellipticity (MRE) using the formula:

$$\theta = \frac{\theta_{obs} * \left(\frac{MW}{n_{aa}}\right)}{10 * c * l} \ (Eq. 2.2)$$

Where MRE is θ in deg.cm^{2}dmol^{-1}, θ_{obs} is the raw ellipticity in mdeg (corrected for buffer contribution as above), MW is the molecular weight in gmol^{-1}, n_{aa} is the number of amino acids in the protein, c is the concentration in mg/mL^{-1}, and l is the path length of the cuvette in cm.

2.2.14 ApoC-II and α-syn amyloid formation using ThT fluorescence assays

Amyloid fibrils are characterised by their ability to bind to the dye ThT (Fig 2.1). The binding of ThT to amyloid fibrils results in a red shift in the intrinsic excitation wavelength of the dye and an increase in fluorescence at 485nm relative to free dye. Consequently, ThT has been used to monitor amyloid fibril formation using both fluorescence microscopy and fluorescence spectroscopy, however the latter is the more common methodological approach. The molecular mechanism for the increase in ThT fluorescence upon binding to amyloid fibrils is not completely understood, however it is thought that fibril binding restricts the rotation of benzothiazole and benzamine rings about a shared C-C bond, resulting in an increase in fluorescence[323]. Though ThT is relatively specific for binding to amyloid fibrils it can bind to non-amyloid structures[324], thus ThT fluorescence should be used in conjunction with other methodologies to probe for amyloid formation.

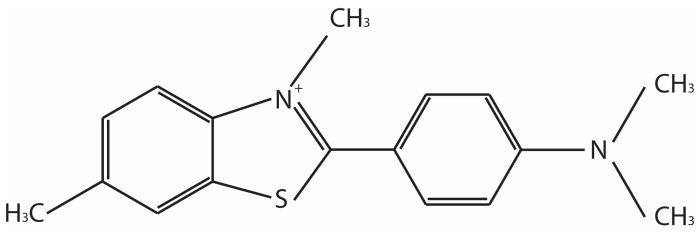


Figure 2.1. Structure of Thioflavin T.

For this work, ThT fluorescence assays were used as an approach to monitor fibril formation. ApoC-II and α-syn were rapidly diluted from GuHCl stocks into fibrillation buffer (0.1 M sodium phosphate, pH 7.4, 0.1% sodium azide) to generate monomeric stocks immediately prior to each experiment. These monomeric stocks were aliquoted into wells of a clear, flat-bottomed 96-well tissue culture plate to a final concentration of 56 µM (apoC-II) or 200 µM (α-syn). For ThT assays, 10 µL of a 100 µM ThT stock (prepared in 0.1 M sodium phosphate pH 7.4, 0.1% sodium azide) was also added along with the required volume of the relevant sHSP or a matching volume of buffer. The total assay volume in each case was 100 µL. Plates were incubated in a FLUOstar® Omega microplate reader (BMG Labtech, VIC, Australia) for up to 200 hours. For unseeded apoC-II fibril formation, plates were incubated at 30°C without shaking. For unseeded α-syn fibril formation, a 2-mm diameter glass bead (Sigma) was added to each well to ensure mixing. Plates were incubated at 37°C with orbital mixing at 700 rpm during the incubation. For seeded α-syn fibril formation, fibrils formed using the unseeded method were sonicated on ice using a Q500 probe sonicator for 14 rounds of 30 sec on/off pulses at an amplitude of 20%. This seed fibril stock was added to fresh, monomeric α-syn to a concentration of 5% of the total α-syn concentration. The mixture was incubated in the microplate reader at 45°C for up to 30 hours without shaking. ThT fluorescence was measured using excitation and emission filters of 440 and 480 nm, respectively.

At the end of unseeded α-syn fibril formation, data for the change in ThT fluorescence over time were fitted with Boltzmann sigmoidal curves using GraphPad Prism version 8 (GraphPad Software Inc., San Diego, CA). Parameters from these fits were used to estimate the length of the lag phase using equations previously derived[254]. The equation of the Boltzmann curve is:

$$F = F_i + \frac{F_f - F_i}{1 + e^{\left(\frac{T_{50} - T}{k}\right)}} \ (Eq. 2.3)$$

where F is the fluorescence intensity at a given time point, T (in units of hours); F_i is the initial fluorescence intensity; F_f is the final fluorescence intensity; T_{50} is the time to half maximal change in ThT fluorescence and k is a factor relating to the steepness of the change in ThT fluorescence. The equation used to derive estimates of the lag time (T_{lag}) is:

$$T_{lag} = \frac{4kF_i}{F_f - F_i} + T_{50} - (2k) \ (Eq. 2.4)$$

At the end of seeded α-syn fibril formation and unseeded apoC-II fibril formation, data for the change in ThT fluorescence over time were fit with one-phase association curves using GraphPad Prism version 8 (GraphPad Software Inc., San Diego, CA). The equation for the one-phase association model is:

$$F = F_i + \left(F_f - F_i\right)\left(1 - e^{(-kT)}\right) \ (Eq. 2.5)$$

where F is the fluorescence intensity at a given time point, T (in units of hours); F_i is the initial fluorescence intensity; F_f is the plateau in fluorescence intensity and k is a factor relating to the steepness of the change in ThT fluorescence. The equation used to derive estimates of the T_{50} is:

$$T_{50} = \frac{\ln 2}{k} \ (Eq. 2.6)$$

Fits to the raw data were only used for downstream analysis when the goodness of fit as estimated by R^2 values was > 0.97. To analyse the statistical significance of the difference in the mean T_{50} and T_{lag} values derived from fits to the raw data, one-way ANOVA tests with post-hoc Tukey's multiple comparisons tests were performed using GraphPad in Prism version 8 (GraphPad Software Inc., San Diego, CA).

2.2.15 Fibril pelleting assays using a sucrose cushion

Fibril formation for pelleting assays was performed in an identical manner to that described for the ThT assays with the exception that ThT was omitted from the buffers. ApoC-II and α-syn fibrils were

separated from monomeric apoC-II, monomeric α-syn, oligomeric sHSPs, and dimeric sHSPs using centrifugal force according to an established protocol[258]. Briefly, 100 µL aliquots of each sample were layered on top of 100 µL of 20% (w/v) sucrose dissolved in fibrillation buffer. Samples were centrifuged at 385,000 x g, 20°C for 30 min (TLA-100 rotor OptimaMax centrifuge, Beckman Coulter). The top 80 µL of the supernatant and the bottom 80 µL of the sucrose layers were collected and the pellets were resuspended in 100 µL of fibrillation buffer. The total non-centrifuged (T), supernatant (Sup), sucrose (Suc) and pellet (P) fractions were analysed by SDS-PAGE.

2.2.16 Fluorescent apoC-II fibril pelleting assay

Separate GuHCl stocks of WT unlabeled apoC-II and S61C Alexa 488 labeled apoC-II prepared as previously described [325] were rapidly diluted into fibrillation buffer at a ratio of 9:1 WT:S61C Alexa 488 to a total apoC-II concentration of 0.5 mg/mL. This mixture was incubated at 30°C for 1 week to allow fibrils to form. Pre-formed fibrils were aliquoted and incubated alone or in the presence of each sHSP construct at 30°C for a further 24 hours. 80 µL aliquots of each incubation was centrifuged as described above without a sucrose layer. 20 µL was kept as the total uncentrifuged sample. The supernatant and pellet layers were collected. The supernatant fractions were analysed by SDS-PAGE without Coomassie blue staining and gels were imaged immediately using a ChemiDoc MP imaging system with the Pro-Q Emerald 488 application (530/28 filter set). The total and pellet layers were analysed in the same way but on separate gels.

2.2.17 Sedimentation velocity analysis

AUC is a powerful technique for obtaining estimates of the size and shape of molecules in solution under centrifugal force. The principles underlying AUC are simple: larger (more massive) and less elongated particles will sediment more quickly than smaller and more elongated particles at a given centrifugal force. The rate of sedimentation of molecules can be interpreted based on a number of forces acting on the particles. These are the frictional/drag force of the particle (which is dependent on the shape of the particle), the buoyant force of the particle (which is dependent on the chemical composition of the molecule and the solvent), and the force resulting from the applied centrifugal field (which also depends on the mass of the particle). In addition to these forces, the viscosity of the solution also affects the rate

of sedimentation. The sedimentation rate of molecules in solution is measured by recording the absorbance, interference or fluorescence properties of a solution containing the molecule of interest as a function of the radial position over the course of the sedimentation experiment (Fig. 2.2). This creates "sedimentation boundaries" which move towards the bottom of the solution column over time (Fig. 2.2). Though higher resolution techniques exist for the characterisation of the size distributions of biological molecules, the advantage of AUC is that it is theoretically simple. Numerical solutions to the Lamm equations, which describe the sedimentation and diffusion properties of molecules in solution, can be derived from first principles[326]. Furthermore, the characterisation of the size distributions of apoC-II amyloid fibrils by AUC has been well established[85,327,328].

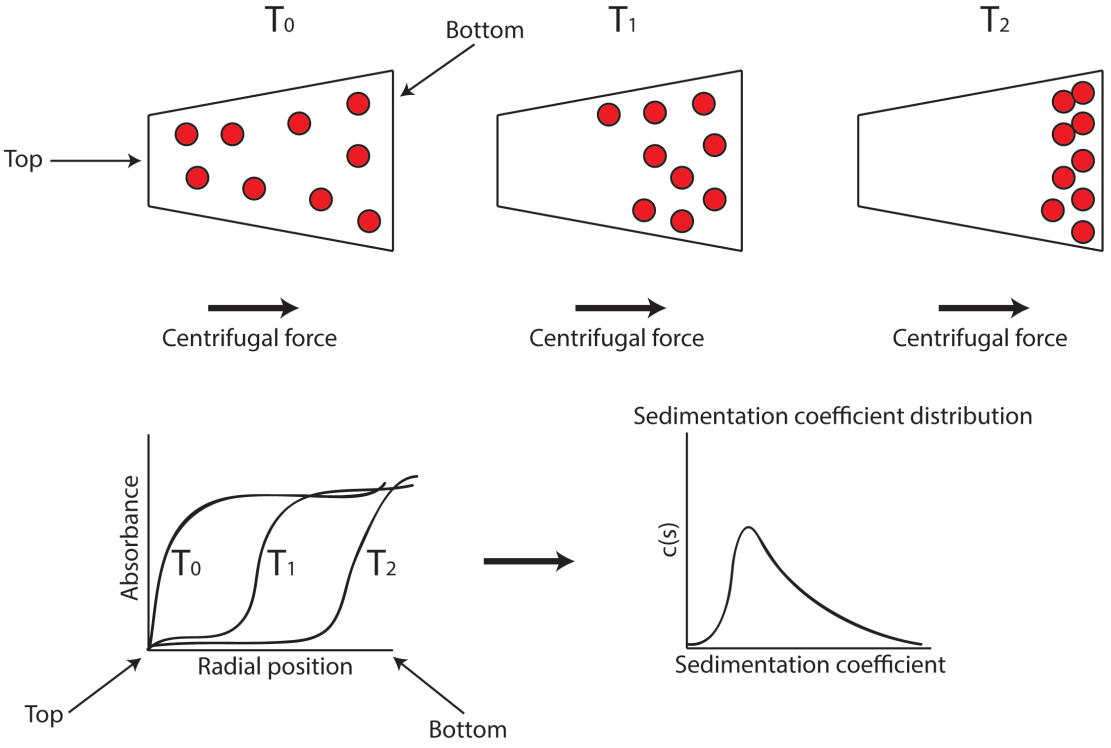


Figure 2.2. Schematic representing the sedimentation velocity analysis of molecules in solution under centrifugal force. Initially, the molecules are evenly distributed throughout the solution column. Over time ($T_0 - T_2$), under centrifugal force, the molecules move to the bottom of the solution column. The sedimentation of the molecules during the course of the experiment is monitored by measuring UV absorbance across the solution column from top to bottom over time. These measurements generate sedimentation boundaries which are dependent on the rate of sedimentation, the rate of diffusion and the heterogeneity of the sample of interest. These boundaries are fit to models derived from the Lamm equations to

generate size distributions/sedimentation coefficient distributions, which are directly related to the size of the molecules in solution.

For all AUC experiments, samples of 380 µL were loaded into one sector of a 12-mm double-sector charcoal-filled epon centrepiece and 400 µL of the relevant reference solution was loaded into the other sector of the cell. Radial absorbance scans were taken using an XL-1 analytical ultracentrifuge (Beckman Coulter, CA, USA) equipped with a Ti50 rotor at 20°C, collecting scans at 4 min intervals with a radial step size of 0.003 cm. All SV-AUC experiments of pre-formed apoC-II fibrils incubated with sHSP constructs for 72 hours were analysed at a rotor speed of 8,000 rpm (5,161 x *g*) with detection wavelengths between 275 – 290 nm. All SV-AUC experiments of apoC-II fibrils formed with sHSP constructs 168 hours were analysed at a rotor speed of 8,000 rpm (5,161 x *g*) with detection wavelengths between 275 – 290 nm. For all of these experiments, the c(s) distributions were obtained by fitting the data using SEDFIT with the hydrodynamic scaling law derived from the worm-like chain model described previously[327] using Tikhonov-Phillips regularization by second derivative[326,328]. All SV-AUC experiments of fragmented apoC-II fibrils were analysed at a rotor speed of 10,000 rpm (8,064 x g) with detection wavelengths of between 275 – 290 nm. The apparent sedimentation coefficient distributions (ls-g*(s)) were obtained by least-squares boundary modelling[328] using Tikhonov-Phillips regularization by second derivative[326,328]. Weight-average fibril sizes were approximated from their weight-average sedimentation coefficients using a sedimentation coefficient vs MW relationship previously derived[327]. SV-AUC data for all ACD-only constructs, Hsp27-3D and Hsp27-3DΔCTR in the absence of apoC-II fibrils were analysed at a rotor speed of 50,000 rpm (201,600 x *g*) with detection wavelengths of between 225 – 280 nm. SV-AUC data for WT αB-C and WT Hsp27 in the absence of apoC-II fibrils were acquired using a rotor speed of 40,000 (129,000 x *g*) rpm and a detection wavelength of 237 nm. SV-AUC data for WT αB-C incubated in the presence of apoC-II fibrils for 0 – 20 hours was acquired using a rotor speed of 40,000 (129,000 x *g*) rpm and a detection wavelength of 232 nm. The continuous sedimentation coefficient distribution c(s) model using regularization by maximum entropy was used to fit SV-AUC data for all of these experiments[326]. For all SV-AUC data presented, a regularisation parameter of p = 0.95 was used with 250 sedimentation coefficient increments over the selected sedimentation coefficient range (which necessarily varies for different experiments). The area under peaks in all the c(s) distributions presented here were obtained by integrating the distributions

over the specified sedimentation coefficient range using the SEDFIT software[326]. The buffer density (ρ), buffer viscosity (η) and partial specific volume ($\bar{\nu}$) used for the analysis of all sHSP constructs analysed in isolation of apoC-II fibrils were calculated using the SEDNTERP software (version 14.6e)[329]. Estimates of the MW of sedimenting particles were obtained using the SEDFIT software, which employs the Svedberg relationship to relate the molar mass of a sedimenting particle with its sedimentation coefficient, frictional coefficient and partial-specific volume, in a solvent with a given density[326].

2.2.18 Turbidity assays

For assays conducted in a FLUOstar® Omega microplate reader (BMG Labtech, VIC, Australia), aliquots of 100 µL of α-syn fibrils were incubated at 37°C without shaking in the presence or absence of the various sHSP constructs. OD was recorded using a 355 nm filter for up to 25 min at 20 sec intervals. The time to half maximal change in fibril OD was determined by fitting the raw data to a 4-parameter sigmoidal Hill equation:

$$OD = OD_0 + \left(\frac{at^b}{c^b + t^b}\right) \quad (Eq. 2.7)$$

where OD is the optical density at a given time, t (in min), OD_0 is the optical density at time zero, a is the difference between the final and initial optical density, c is the time to half maximal change in optical density and b is a scaling factor relating the steepness of the curve. For assays conducted using a DU800 spectrophotometer (Beckman Coulter), absorbance measurements of 100 µL of α-syn fibrils incubated in the presence or absence of the various sHSP constructs were recorded at 360 nm at the indicated time point after the addition of the sHSP. The path length was 10 mm and at each time point a reference sample was used to obtain absorbance in arbitrary units (AU).

2.2.19 Transmission electron microscopy

TEM is a useful methodology for the analysis of amyloid fibrils, which typically appear as filamentous, unbranched structures that may be either curly or relatively straight[330]. Here, TEM was used to examine the morphology and the lengths of amyloid fibrils. Carbon-coated Formvar 300 mesh copper grids were glow discharged under reduced atmospheric pressure for 30 seconds at 25 mA. 4 µL aliquots of diluted

samples were adsorbed onto the grid for 60 seconds. The sample was blotted off using filter paper and the grid was stained twice with 4 μL of 2 % potassium phosphotungstate (pH 6.8) and air dried. The grid was observed under a Talos L120C TEM (ThermoFisher Scientific) operating at 120 kV. Images were captured digitally using a Ceta 16M digital camera (ThermoFisher Scientific).

2.2.20 Precipitation of His-αB-C ACD using nickel-NTA resin

Recombinant proteins are commonly expressed with short affinity tags, for instance a polyhistidine (6 x His) tag. These proteins can be purified from cell lysate using immobilised metal affinity chromatography since the immobilised Ni^{2+} ions chelate the histidine residues in the tag. 20 μL of nickel-NTA resin slurry was mixed with 80 μL of apoC-II fibrils (56 μM) alone, or in the presence of 12.8 μM αB-C ACD or 6 x His-tagged αB-C ACD. Resin was purified from the mixture by centrifugation at 1000 x rpm (74 x g) for 1 min at 20°C. The top 20 μL was removed as the unbound fraction. The remaining ~ 60 μL supernatant was removed and set aside. 80 μL of binding buffer (0.1 M sodium phosphate pH 7.4, 400 mM NaCl, 20 mM imidazole) was added and the samples were resuspended. The resin was washed again by centrifugation. The top 80 μL was removed as the first wash fraction and two more wash steps were completed. 80 μL of elution buffer (0.1 M sodium phosphate pH 7.4, 400 mM NaCl, 500 mM imidazole) was mixed with the resin and a further centrifugation step was completed to elute bound proteins. These steps were repeated a total of three times. The unbound, first wash fractions and first elution fractions were analysed by SDS-PAGE.

2.2.21 NMR spectroscopy

2.2.21.1 General theory of NMR spectroscopy

The nuclei of particular isotopes of some elements have a quantum property referred to as spin. This property means that the nuclei of these isotopes behave like microscopic magnets. Isotopes most commonly used for applications in biochemistry have nuclear spin quantum numbers of ½, however a range of nuclear spin quantum numbers can exist. The number of possible orientations of nuclear spin is $2I + 1$, where I refers to the spin quantum number of a given isotope. When these nuclei are exposed to an external magnetic field, the different orientations of nuclear spin have different energies.

Therefore, if spin ½ isotopes are exposed to an external magnetic field, two different orientations of nuclear spin are possible, and these two orientations have two different energies (Fig. 2.3). The two different nuclear spin states are referred to as the α and β states, where the α state has a lower energy and the nuclear spin is aligned with the external magnetic field. The two spin states will be nearly equally populated, however the α state will be marginally more populated when the sample is exposed to an external magnetic field (Fig. 2.3). The energy difference between the nuclear spin states depends on the strength of the external magnetic field (B_0) (Fig. 2.3). At a selected magnetic field strength, the energy difference between the two states will correspond to a particular wavelength of microwave radiation. Therefore, microwave radiation can be used to convert the nuclei from one nuclear spin state to another and this phenomenon is called nuclear magnetic resonance (NMR). NMR can therefore be achieved by varying the wavelength of microwave radiation at a fixed magnetic field strength; however, it is more common to use a fixed wavelength of microwave radiation and vary the magnetic field to achieve resonance.

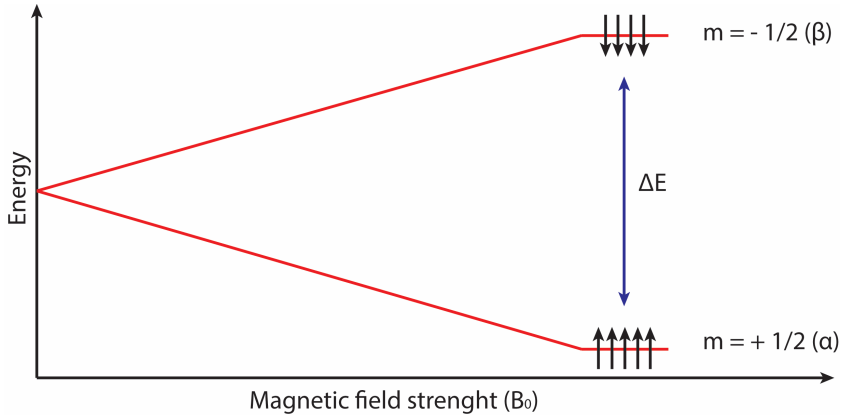


Figure 2.3. Dependence of the energy levels of nuclear spin states of a ½ spin nuclei as a function of the magnetic field strength. The difference in the energy levels (ΔE) between the lower energy α and higher energy β state increases with increasing strength of the applied magnetic field (B_0). The α state is marginally more highly populated under the influence of an external magnetic field.

The energy levels of the nuclear spin of a given nucleus are also exceptionally sensitive to the surrounding chemical environment. This is due to the electron cloud surrounding the nucleus, which produces a small local magnetic field opposing the direction of the applied field. This effect is called shielding and results in the nuclei resonating at a slightly lower magnetic field than they would in the

absence of the effects of shielding. For example, hydrogen atoms in different surrounding chemical environments within the same molecule will have different degrees of shielding, resulting in different spin energy levels and will therefore resonate at different magnetic field strengths. The differences in magnetic resonance are expressed as differences in chemical shift, which is defined with respect to a reference material in parts per million (ppm) and is derived according to:

$$\delta = \frac{\left(v - v_{ref}\right) * 10^6}{v_0} \ (Eq\ 2.8)$$

Where v is the experimentally obtained resonant frequency, v_{ref} is the frequency of a reference material and v_0 is the operating frequency of the spectrometer.

To obtain resonance frequencies, a pulse of microwave radiation is used to excite all nuclei of a selected isotope from the lower energy α state to the higher energy β state simultaneously. The excited nuclei will subsequently relax back to the ground state and in the process, microwave radiation is emitted. This radiation is detected as a superposition of all emitted frequencies, which undergo constructive/destructive interference. Therefore, the emitted radiation displays characteristics of a time-dependent exponentially damped sinusoid and is called a free induction decay (FID) (Fig. 2.4). A mathematical process termed a Fourier transform converts this time domain data to frequency domain data (Fig. 2.4).

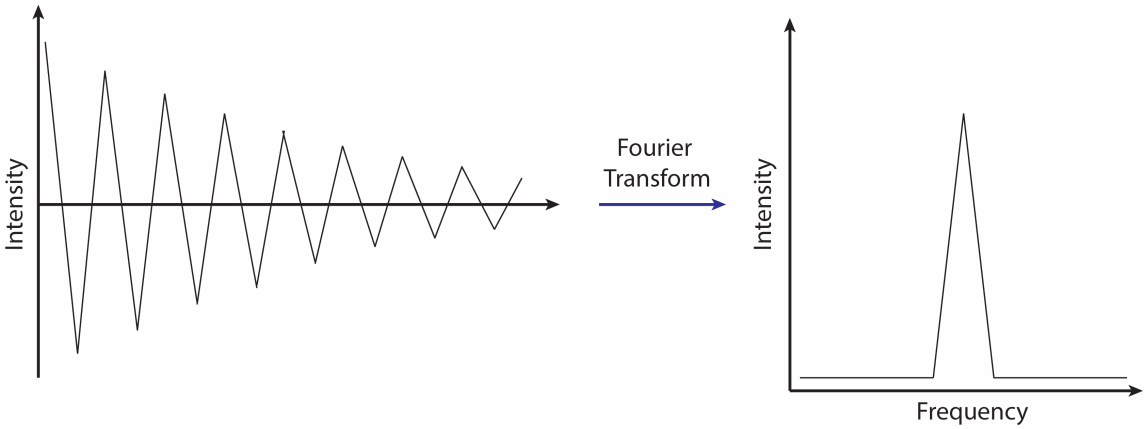


Figure 2.4. Schematic for the conversion of the time-domain FID into frequency domain data via the Fourier transform.

2.2.21.2 Relaxation mechanisms in NMR spectroscopy

Broadly, two mechanisms account for the decay in the net magnetization vector. One is the return of nuclear spin states from the excited state to the ground state (a gain or loss of magnetization along the z-axis) (Fig. 2.5). The second involves the loss of nuclear spin coherence in the x-y plane and is therefore due to gain or loss of magnetization in this plane (Fig. 2.5). These two mechanisms are distinguished as two types of nuclear spin relaxation. The first is T_1 relaxation which is also called spin-lattice decay and is caused by molecular motion/reorientation of molecules that create transient local magnetic fields with components that exactly match the resonance frequency of the nucleus of interest. These local fields stimulate relaxation of the nucleus, and the excess spin energy that is released is detected. The second type of relaxation is called T_2 relaxation or spin-spin relaxation. This involves the loss of nuclear spin coherence in the x-y plane and is therefore due to gain or loss of magnetization in this plane (Fig. 2.5). This type of magnetization is also due to transient local magnetic fields however the components of these fields do not need to match the resonance frequency of the nucleus of interest. Another source of T_2 relaxation is due to chemical exchange processes whereby chemical shifts are swapped on a timescale relevant to NMR. For proteins, the average molecular reorientation rates occur too slowly for efficient T_1 relaxation, therefore T_2 relaxation occurs at a faster rate than T_1 relaxation. Another reason that T_2 relaxation occurs at a faster rate than T_1 relaxation is that return of magnetization from the x-y plane to the z plane inherently causes loss of magnetization in the x-y plane.

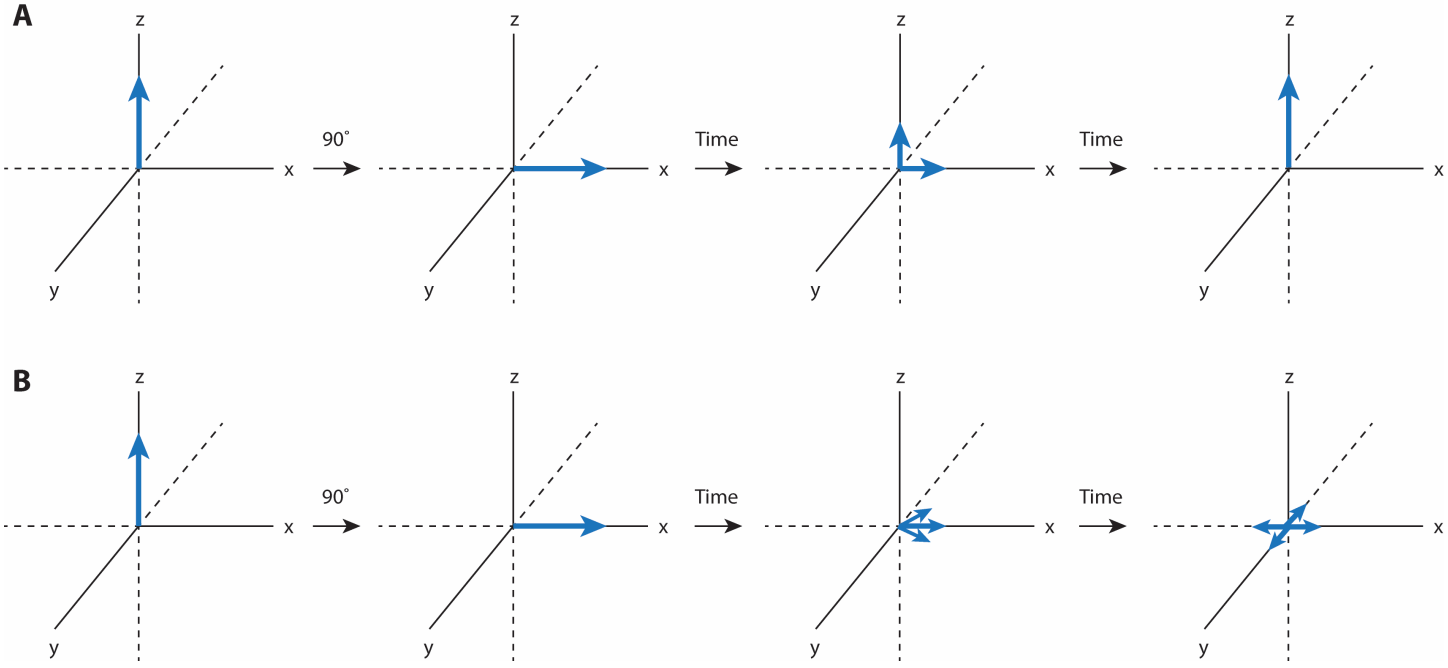


Figure 2.5. Schematic for the representation of the two types of nuclear spin relaxation. A) A representation of T_1 relaxation processes whereby the net magnetization in the x-y plane decays due to transitions of the spin to the z plane over time. B) A representation of T_2 relaxation processes whereby the net magnetization in the x-y plane decays due to a loss of phase coherence in the x-y plane over time. Figure adapted from Hans J. Reich (2018)[331].

2.2.21.3 2-dimensional NMR spectroscopy

1-dimensional NMR spectroscopy is a powerful analytical technique for the study of small molecules, however for larger and more complex molecules such as proteins significant overlap of resonances occurs making interpretation of the spectra difficult. To overcome these difficulties, an additional dimension is introduced in the form of a second frequency dimension, most commonly ^{15}N. The additional dimension provides enhanced resolution of the signals across the spectra. A common methodology for 2-dimensional NMR is correlation spectroscopy, which exploits spin-coupling of adjacent nuclei, for example ^{1}H and ^{15}N within amide bonds of proteins. For these experiments, magnetization is transferred from hydrogen to nitrogen with an initial pulse, allowed to evolve on nitrogen for a period of time t_1 and then transferred back to hydrogen with a second (retro) pulse for detection during the t_2 time period (Fig. 2.6). The t_1 evolution time is incrementally increased for a 2-dimensional correlation experiment (Fig. 2.6), thus the nitrogen resonance frequency is detected

indirectly via its effect (as a result of the duration of the t_1 evolution time) on the magnetization of the adjacent hydrogen. The resonance frequency of hydrogen is detected directly. The FID is subsequently detected in the t_2 detection time. Fourier transforms with respect to t_1 and t_2 generate 3-dimensional spectra with two frequency dimensions corresponding to hydrogen and nitrogen and signal intensities represented by contour lines. For this thesis, $^{1}H^{15}N$ heteronuclear single quantum coherence (HSQC) NMR spectroscopy was performed to probe the interactions of αB-C ACD with monomeric or fibrillar substrates.

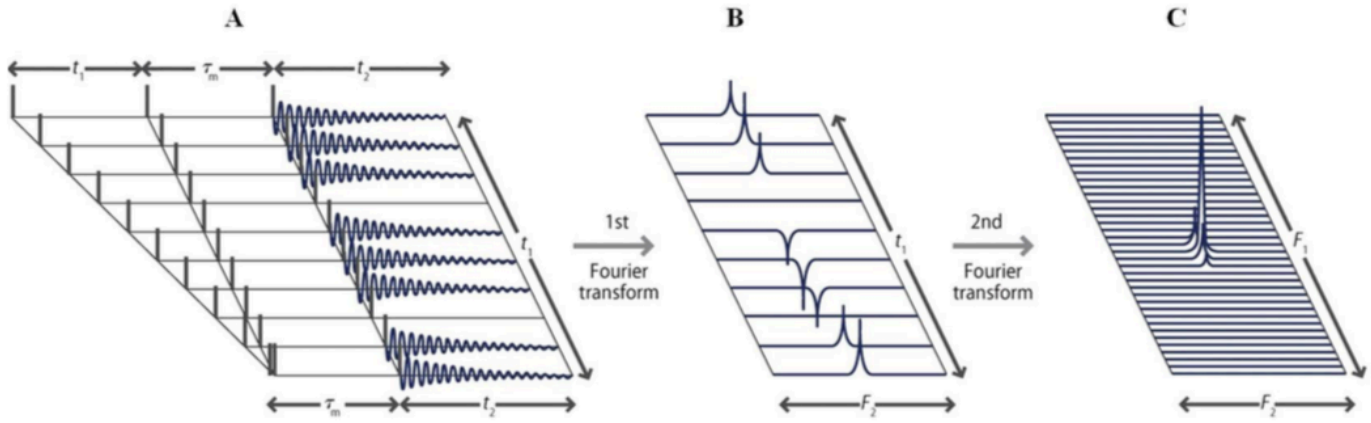


Figure 2.6. Schematic for the processing of 2-dimensional NMR data. A) The FID observed in t_2 is dependent on the duration of t_1. 90° pulses are depicted by vertical lines in (A). A Fourier transform with respect to t_2 converts the t_2 time domain data to frequency domain (F_2) data in (B), which is represented as a function of t_1. A second Fourier transform with respect to t_1 converts the t_1 time domain data to the F_1 frequency domain data shown in (C). Figure adopted from Williamson (2012) [332].

2.2.21.4 Sample preparation and ^{15}N Heteronuclear single quantum correlation NMR spectroscopy

^{15}N-labeled αB-C ACD comprises residues 68-153, identical to the material used for assignment of backbone chemical shifts in previous work (Benesch *et al.*, unpublished, obtained via personal communication).

For all HSQC experiments in which pre-formed apoC-II or α-syn fibrils were added to ^{15}N αB-C ACD, ^{15}N αB-C ACD was prepared in sodium phosphate buffer (50 mM sodium phosphate, pH 7.4 or 6.5, 0.02% sodium azide, 1 mM EDTA, 10% D_2O) and reference spectra were collected first. Fibrils were prepared as described in section 2.2.14 with ThT omitted from the buffers. α-Syn fibrils were prepared using the

unseeded method. Fibrils were twice pelleted by centrifugation at 385,000 x g for 30 minutes at room temperature as described above. After the first spin, fibrils were resuspended in an equal volume of buffer matching that of the buffer used for the reference spectra, to ensure complete buffer matching. After the second spin, the fibrils were resuspended directly into the sample containing ^{15}N αB-C ACD used for the collection of the reference spectra. HSQC spectra were then recorded for this sample, containing both ^{15}N αB-C ACD and fibrils. To obtain spectra for ^{15}N αB-C ACD in the presence of fragmented fibrils, the sample containing ^{15}N αB-C ACD and the resuspended fibrils was sonicated according to the protocol outlined in section 2.2.12. To test whether the process of sonication affected the HSQC spectra of ^{15}N αB-C ACD alone, samples containing ^{15}N αB-C ACD were also sonicated in the absence of fibrils prior to data acquisition and the resulting spectra were compared to spectra obtained prior to sonication. For experiments in which HSQC spectra were obtained for ^{15}N αB-C ACD at multiple different pHs, a reference spectrum was initially recorded at pH 7.4. The sample was subsequently recovered and HCl (1 M) was titrated into the sample to achieve the desired pH. Adjusting the pH in this way required the addition of 2 – 4 μL of 1M HCl, thus the effect of dilution is negligible. For experiments in which GuHCl was titrated with ^{15}N αB-C ACD, a reference spectrum was first obtained on a sample containing 0 mM GuHCl. Subsequently, the sample was recovered and a stock of 6 M GuHCl was titrated with this sample to achieve a final GuHCl concentration of 50 mM. This process was repeated for spectra obtained at 100, 200, 300 and 400 mM GuHCl. Thus, a dilution of 7% was required between the reference spectra and the 400 mM GuHCl spectra. For HSQC spectra acquired for ^{15}N αB-C ACD in the presence of 1000 μM monomeric α-syn, α-syn was first diluted from a GuHCl stock to a concentration of 1000 μM in sodium phosphate buffer and to a final volume of 550 μL. This sample was dialysed against a matching buffer at 4°C for 24 hours to remove GuHCl. A reference spectrum was collected on a sample containing 500 μM ^{15}N αB-C ACD in sodium phosphate buffer at a volume of 550 μL. This sample was then recovered and mixed with the sample of dialysed α-syn. The mixture, containing both α-syn and ^{15}N αB-C ACD, was then concentrated using Amicon ultracentrifugal filter units to a final volume of 550 μL and another HSQC was recorded on this sample.

The majority of NMR results presented in this thesis are short experiments with a duration of up to 6 hours. However, to test the stability of ^{15}N αB-C ACD over longer timescales, HSQCs were recorded on

samples of ^{15}N αB-C ACD (1 mM) at pH 7.4 and pH 6.5 before and after incubation at 35°C for up to three days. Comparisons of the spectra obtained prior to and after incubation revealed no major differences in peak positions or peak intensities (Fig. 2.7), indicating that αB-C ACD is stable in these conditions and over the timescales of the experiments presented in this thesis.

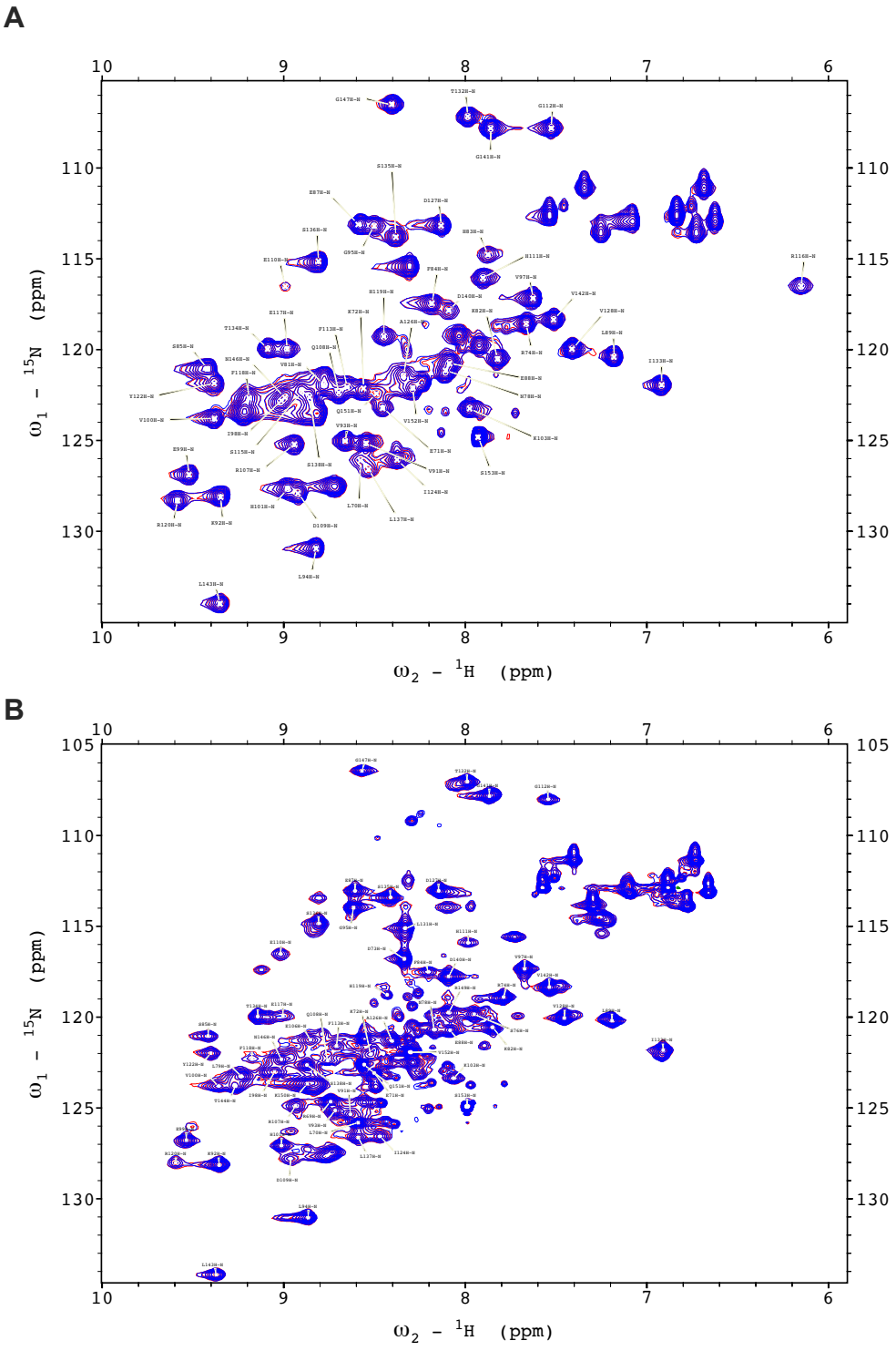


Figure 2.7. Stability of αB-C ACD over long NMR experiments. A) Overlay of 1 mM ^{15}N αB-C ACD alone, pH 7.4 before (red) and after (blue) incubation at 35°C for 72 hours. B) Overlay of 1 mM ^{15}N αB-C ACD alone, pH 6.5 before (red) and after (blue) incubation at 35°C for 72 hours.

NMR spectra were obtained on either a Bruker Avance II 800 MHz spectrometer equipped with TXI cryoprobe and a single axis field gradient (Gz) or a Bruker Avance HDIII 700 MHz spectrometer. All spectra were recorded at 298 K unless stated otherwise. Generally, 16 scans were collected per FID, however for spectra acquired at 25 μM, 64 scans were collected. A ^{15}N frequency of 70.94 MHz or 81.08 MHz was used for the 700 MHz and 800 MHz spectrometers, respectively. 2048 and between 200 - 300 complex data points were used for ^{1}H and ^{15}N, respectively. The spectral width was 12.02 and 30.00 ppm for ^{1}H and ^{15}N, respectively. NMR spectra were processed using NMRPipe[333] and analysed in SPARKY (Goddard, T.D. and Kneller, D.G., University of California, San Francisco). All spectra were phased as well as possible using nmrDraw in NMRPipe, however, spectra have generally been plotted at low contour levels in order to detect peaks with low signal intensities. In addition to this, some peaks undergo peak-doubling in a pH dependent manner. In some instances, these factors result in spectra that appear to be poorly phased. ^{1}H chemical shifts were referenced indirectly using water proton signals in the NMRPipe software. ^{15}N chemical shifts were referenced using ^{15}N/^{1}H ratio as described previously [334]. Chemical shift perturbations were calculated using[335]:

$$\Delta\delta ppm = \left(\left(\Delta\ ^{1}H\right)^{2} + \left(0.154\Delta^{15}N\right)^{2}\right)^{\frac{1}{2}} \quad (Eq.\ 2.9)$$

2.2.21.5 Backbone ^{15}N transverse nuclear spin relaxation parameters

^{15}N transverse nuclear relaxation parameters, R_2, were measured at a ^{15}N frequency of 70.94 MHz with 2048 and 300 complex data points over spectral widths of 12.02 and 30.00 ppm for ^{1}H and ^{15}N, respectively at pH 7.4, 298K. Pulse sequences with sensitivity enhancement provided in the Bruker pulse sequence library were used, as previously described[336]. 16 scans per FID were collected with a recycle time of 2.6 s. Relaxation delays of 16.96 (×2), 33.92, 50.88 (×2), 67.84, 84.8, 101.76 (×2), 118.72 and 135.68 ms were used. The repeated spectra were used to estimate instrumental error. ^{15}N relaxation parameters were determined by fitting the raw decay data to a single exponential decay using the software GraphPad Prism version 8 (GraphPad Software Inc., San Diego, CA). The equation for the one-phase decay to zero is:

$$Y = (Y_0)e^{(-Kt)} \ (Eq. 2.10)$$

Where Y is the signal intensity at a given delay increment, t, Y_0 is the signal intensity at the smallest delay increment and K is a rate constant relating to the steepness of the decay.

2.2.22 Small angle X-ray scattering

As its name implies, SAXS is a solution-based X-ray scattering methodology performed at very low scattering angles. A sample is irradiated with X-ray radiation and the scattering intensity is detected at low scattering angles from the X-ray beam. Based on the Debye scattering equation[337], the angle of X-ray scattering is inversely related to inter-atomic distances within the molecule of interest, thus the detection and quantification of scattered X-rays at low angles provides modest resolution structural information (1 – 100 nm, depending on the angular range of the experimental set-up). Therefore, SAXS is useful for probing the shapes and sizes of large proteins and protein complexes. SEC-SAXS data were collected on the SAXS/WAXS beamline at the Australian Synchrotron. Sample-to-detector distance was 2682 mm (Hsp27-3D), 1428 mm (αB-C ACD and Hsp27 ACD), 3533 mm (Hsp27-3DΔCTR) with an X-ray beam energy of 10.4 keV and wavelength of 1.03320 Å. Data were collected over an s-range of 0.0125 – 0.648 $Å^{-1}$ (αB-C ACD and Hsp27 ACD), 0.00527 – 0.0336 $Å^{-1}$ (Hsp27-3D) or 0.00425 – 0.383 $Å^{-1}$ (Hsp27-3DΔCTR) where $s = (4\pi\sin\theta)/\lambda$. A Superdex 200 increase 5/150 size exclusion column (GE healthcare) pre-equilibrated in 20 mM sodium phosphate, pH 8, 0.1 % (w/v) sodium azide was used in line with the SAXS apparatus. Data were collected at loading concentrations of 5 mg/mL and 7.5 mg/ml. Buffer averaging and subtraction was performed using the chromixs software[338] in the ATSAS package[339]. The radius of gyration (R_g) and distance distributions were obtained using the primus software[340] in the ATSAS package. Experimental scattering data were fit to theoretical scattering data calculated from published crystal structures using the crysol software[341] in the ATSAS package.

Chapter 3: The roles of the N- and C-terminal regions of sHSPs in inhibiting amyloid fibril formation

3.1 Abstract

Small heat-shock proteins (sHSPs) are ubiquitously expressed molecular chaperones that inhibit amyloid fibril formation; however, their mechanisms of action remain poorly understood. sHSPs comprise a conserved α-crystallin domain flanked by variable N- and C-terminal regions. To investigate the functional contributions of these three regions, we compared the chaperone activities of various constructs of human αB-crystallin (HSPB5) and heat-shock 27-kDa protein (Hsp27, HSPB1) during amyloid formation by α-synuclein and apolipoprotein C-II. Using an array of approaches, including thioflavin T fluorescence assays and sedimentation analysis, we found that the N-terminal region of Hsp27 and the terminal regions of αB-crystallin are important for delaying amyloid fibril nucleation and for disaggregating mature apolipoprotein C-II fibrils. We further show that the terminal regions are required for stable fibril binding by both sHSPs and for mediating lateral fibril–fibril association, which sequesters preformed fibrils into large aggregates and is believed to have a cytoprotective function. We conclude that although the isolated α-crystallin domain retains some chaperone activity against amyloid formation, the flanking domains contribute additional and important chaperone activities, both in delaying amyloid formation and in mediating interactions of sHSPs with amyloid aggregates. Both these chaperone activities have significant implications for the pathogenesis and progression of diseases associated with amyloid deposition, such as Parkinson's and Alzheimer's diseases.

3.2 Introduction

Small heat-shock proteins (sHSPs) are a major family of heat-shock proteins, present in all kingdoms of life, that have a low monomeric molecular mass, ranging from 15 to 40 kDa. sHSPs generally comprise a central, ~90 residue α-crystallin domain (ACD) and variable-length N- and C-terminal regions (NTR and CTR, respectively). Despite their small monomeric size, metazoan sHSPs are structurally diverse, often existing as a heterogenous array of oligomeric states. The isolated ACD typically forms a stable dimer[277,278,280] suggesting that the NTR and CTR regulate higher order oligomerisation[342]. As a result, relatively few high-resolution structures of sHSPs have been solved. The majority of solved structures are of the isolated ACD[277–280] or of monodisperse sHSP oligomers formed from plant and prokaryotic sHSPs[274,275].

The human genome encodes 10 sHSPs, with gene names *HSPB1-10*. Among the best studied of these are HSPB1 (heat-shock 27 kDa protein, Hsp27) and HSPB5 (αB-crystallin, αB-C), which are ubiquitously expressed[343]. The sHSPs are involved in a diverse range of cellular processes that include regulating cell growth, differentiation and motility[344,345], apoptosis[346], autophagy[214], cytoskeletal dynamics[347,348] and regulation of the intracellular redox state[349]. The unifying feature of sHSPs in these processes is that they act as ATP-independent molecular chaperones. The sHSPs can work cooperatively with ATP-dependent chaperones to refold substrate proteins[350], or participate in shuttling destabilised or misfolded proteins for proteolytic degradation[351]. As a result, sHSPs are a key component of protein quality control as part of cellular proteostasis. Mutations in genes encoding sHSPs are associated with the pathology of a variety of diseases such as neuropathies[352], myopathies[221] and cataracts[353].

There is growing evidence that Hsp27 and αB-C are involved in the cellular response to protein aggregation in a variety of neurodegenerative diseases. A pathological hallmark of neurodegenerative diseases, such as Parkinson's disease (PD) and Alzheimer's disease (AD), is the intra- or extra-cellular aggregation of specific proteins to form amyloid fibrils. α-Synuclein (α-syn) and apolipoprotein C-II (apoC-II) are two examples of proteins that form amyloid fibrils both *in vitro* and *in vivo*. ApoC-II is a serum protein found associated with very low-density lipoprotein (VLDL) particles where it regulates blood triglycerides. VLDL-bound apoC-II is comprised of amphipathic α helices[159], however lipid-free apoC-II is unstable and prone to aggregation. Amyloid formation by apoC-II *in vitro* is well characterized[85,152,165] and mutations in apoC-II cause renal amyloidosis[59,60]. The biological roles of α-syn are not well understood; however, it is highly expressed in multiple regions of the brain and is thought to play a role in vesicular trafficking and neurotransmitter release[354]. Like apoC-II, the N-terminal region of α-syn adopts an amphipathic α-helical conformation upon binding to membranes or lipid-containing vesicles[120]. However, α-syn aggregates to form amyloid fibrils that are the principle proteinaceous components of Lewy bodies found in dopaminergic neurons in the substantia nigra of PD patients[24,40]. The expression levels of sHSPs such as Hsp27 and αB-C correlate with the degree of dementia in the brains of AD and PD patients[355–357]. In intracellular models of PD, Hsp27 and αB-C reduce amyloid formation by α-syn[358]. *In vitro*, sHSPs have been shown to inhibit amyloid formation by Aβ[259], β2-

microglobulin[259], α-syn[358], tau[291], superoxide dismutase 1 (SOD1)[359] and apoC-II[258]. Furthermore, sHSPs colocalise with deposits of aggregated proteins associated with a variety of protein misfolding diseases[257,360], demonstrating their role in the cellular response to amyloid formation.

The precise mechanisms by which sHSPs bind proteins to inhibit amyloid fibril formation remain elusive. This is in part because Hsp27 and αB-C form polydisperse oligomers[282,288] that exist in equilibrium with dimeric forms[342,361]. Furthermore, serine phosphorylation in the N-terminal domain of Hsp27 and αB-C has the dual effect of regulating both the extent to which the sHSP oligomers dissociate into smaller species, including dimers, and their chaperone activity[283,284], suggesting that the exchange of sub-oligomeric species may be important for chaperone activity. Interestingly, the dimeric, isolated ACD of αB-C was found to inhibit both amorphous and fibrillar protein aggregation[279]; however, potential substrate binding sites on αB-C have also been identified in the N- and C-terminal regions[298,301,362].

To determine the importance of the regions outside the conserved ACD for the ability of Hsp27 and αB-C to inhibit amyloid fibril formation, we directly compared the chaperone activities of wild-type (WT) Hsp27 and αB-C with their ACD-only counterparts against the amyloid formation of two well-characterised proteins, α-syn and apoC-II. Additionally, we investigated the chaperone activities of a full-length Hsp27 construct with three serine-to-aspartate mutations designed to mimic the triply phosphorylated, dimeric form of Hsp27 (Hsp27-3D) as well as a truncated form of this construct lacking the CTR (Hsp27-3DΔCTR). Using *in vitro* aggregation assays we show that constructs containing both the NTR and ACD more effectively delay amyloid fibril nucleation and/or reduce the rate of fibril elongation than ACD-only constructs. Additionally, the binding of Hsp27 to pre-formed fibrils and the disaggregation of apoC-II fibrils was found to be conferred by primarily the NTR. Similarly, the ACD-only construct of αB-C was insufficient for mediating fibril binding and apoC-II fibril disaggregation. Full-length sHSPs also induced the tangling of pre-formed fibrils into larger aggregates. ACD-only constructs did not display this activity and a construct containing only the NTR and ACD displayed a reduced ability to tangle pre-formed fibrils relative to its full-length counterpart. Thus, while the ACD retains some chaperone activity *in vitro*, the N- and C-terminal regions confer distinct and important chaperone functions against amyloid fibril formation.

3.3 Results

3.3.1 The effects of full-length and truncated constructs of Hsp27 and αB-C on α-syn amyloid formation *in vitro*

The chaperone activities of full-length and truncated sHSPs were investigated using well-established *in vitro* apoC-II and α-syn amyloid formation assays. Spontaneous fibril formation by α-syn was induced by incubating the protein at 200 μM, 37°C, with constant agitation. All sHSP variants delayed amyloid formation of α-syn to some extent, with the exception of Hsp27 ACD (Fig. 3.1A-F, Supplementary Fig. 3.1). We did not observe a time-dependent increase in ThT fluorescence when sHSPs were incubated alone, and bovine serum albumin (BSA) did not inhibit the amyloid formation of unseeded α-syn fibril formation (Supplementary Fig. 3.2). By fitting the raw data to a 4-parameter Boltzmann curve (see Supplementary Fig. 3.1), we derived the duration of the lag phase (T_{lag}) and the time to half maximal ThT fluorescence (T_{50}) (Fig. 3.1 G and H, respectively). Differences in the T_{lag} and T_{50} observed across the samples were analysed using one-way ANOVA with post-hoc Tukey test. The full-length constructs (WT αB-C, WT Hsp27 and Hsp27-3D) and Hsp27-3DΔCTR significantly increased the T_{lag} relative to α-syn incubated alone ($p < 0.01$), suggesting these constructs delay fibril nucleation. Conversely, ACD-only constructs of αB-C and Hsp27 did not significantly increase the T_{lag}. All sHSP constructs except Hsp27 ACD significantly increased the T_{50} (Fig. 3.1 H), suggesting that the rate of α-syn fibril elongation was reduced relative to α-syn incubated alone. Supplementary Table 3.1 shows statistical analysis of differences in T_{lag} and T_{50} between the different sHSP constructs. This analysis shows that the chaperone activity of Hsp27-3DΔCTR was more similar to that of WT Hsp27 and Hsp27-3D than to Hsp27 ACD. These findings demonstrate that the NTR of Hsp27 and the terminal regions of αB-C are important for delaying amyloid fibril formation by α-syn *in vitro* during both the nucleation phase and the elongation phase.

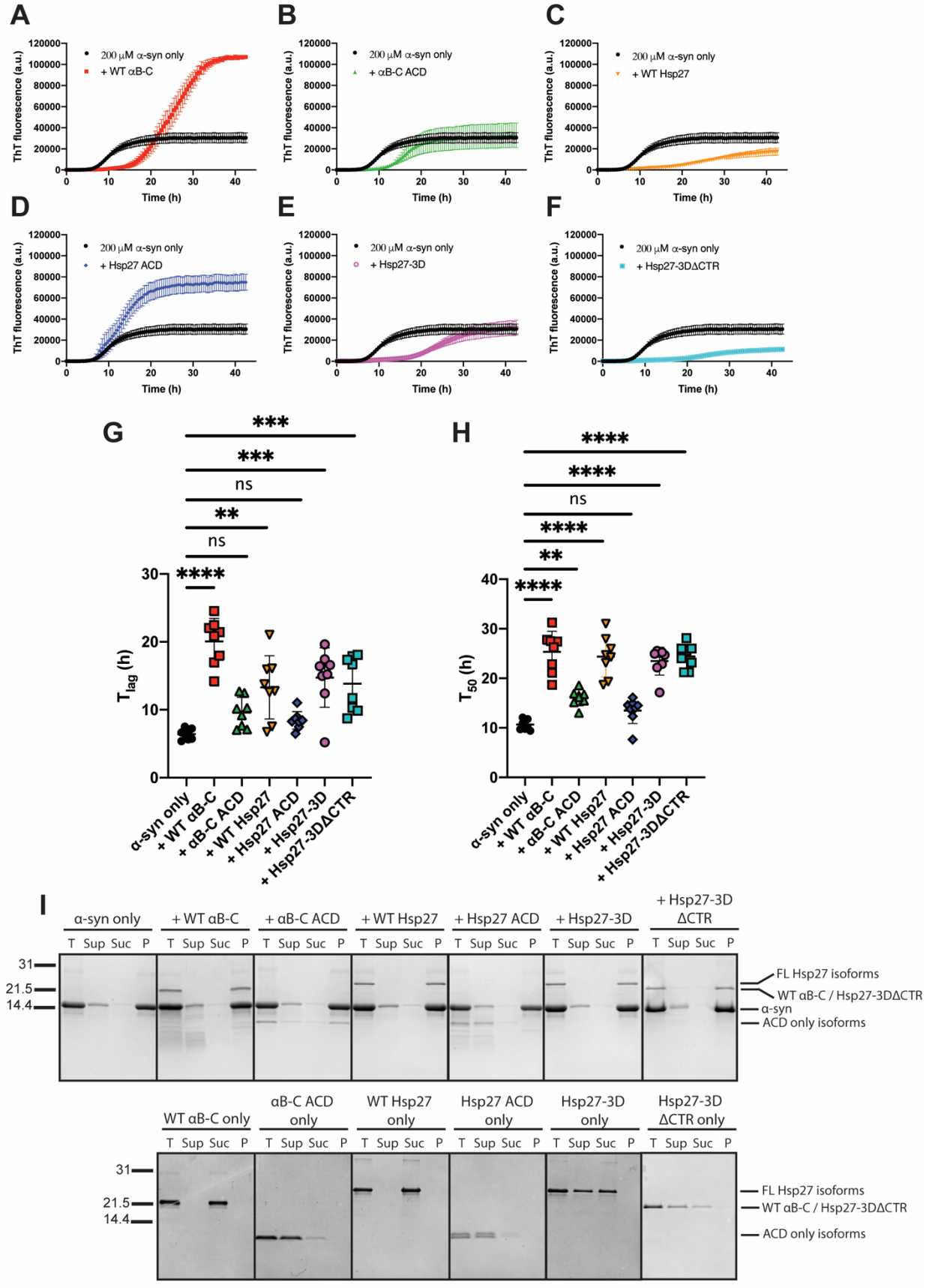

A
B
C
D
E
F
ThT fluorescence (a.u.)
Time (h)
200 μM α-syn only
+ WT αB-C
+ αB-C ACD
+ WT Hsp27
+ Hsp27 ACD
+ Hsp27-3D
+ Hsp27-3DΔCTR
G
H
T_{lag} (h)
T_{50} (h)
α-syn only
+ WT αB-C
+ αB-C ACD
+ WT Hsp27
+ Hsp27 ACD
+ Hsp27-3D
+ Hsp27-3DΔCTR
I
T Sup Suc P
31
21.5
14.4
FL Hsp27 isoforms
WT αB-C / Hsp27-3DΔCTR
α-syn
ACD only isoforms
WT αB-C only
αB-C ACD only
WT Hsp27 only
Hsp27 ACD only
Hsp27-3D only
Hsp27-3D ΔCTR only

Figure 3.1. Kinetics of unseeded α-syn amyloid formation in the presence of sHSPs. ThT-monitored amyloid formation of (A-F) α-syn (200 μM) alone (black) or in the presence of the indicated sHSP (10 μM); WT αB-C (red, A); αB-C ACD (green, B); WT Hsp27 (orange, C); Hsp27 ACD (blue, D); Hsp27-3D (magenta, E) and Hsp27-3DΔCTR (cyan, F). Samples were assayed in quadruplicate in two independent experiments. Data are presented as mean ± standard error of the mean (SEM), where n = 8. T_{lag} (G) and T_{50} (H) values are displayed using scatter plots as mean ± SD with individual datapoints shown (n = 8). Significance values were determined using a one-way ANOVA test with a post-hoc Tukey's multiple comparisons test. * Denotes $p < 0.05$, ** denotes $p < 0.01$, *** denotes $p < 0.001$, **** denotes $p < 0.0001$. I) Unseeded α-syn fibrils were formed alone (200 μM) or in the presence of 10 μM of the indicated sHSP construct for 48 hours, 37°C and then pelleted as described in the methods section. The supernatant (Sup), sucrose (Suc) and pellet (P) layers were collected and analysed by SDS-PAGE alongside the total (T) uncentrifuged samples. Also shown are controls of each sHSP construct incubated alone under identical conditions.

Across all samples, large differences in the final ThT plateaus were observed (Fig. 3.1 A-F). ThT fluorescence can be influenced by non-fibrillar structures, changes in sample viscosity, and the morphology of amyloid fibrils[363,364]. To determine whether the final ThT fluorescence readings correlated with the fraction of aggregated α-syn, we used pelleting assays[258]. In these assays amyloid fibrils were pelleted through a 20% (w/v) sucrose layer such that small, soluble proteins remained in the supernatant fraction, while large oligomers such as those formed by WT Hsp27 and αB-C entered and remained in the sucrose layer. Thus, we were able to separate fibrils, large oligomers and small species (e.g. dimers and monomers) in these assays. The supernatant, sucrose and pellet layers as well as a sample prior to centrifugation (total) were analysed by SDS-PAGE. We observed that the portion of soluble α-syn remaining at the end of the assays appeared to be unaffected by the presence of sHSPs (Fig. 3.1 I). Thus, the observed differences between the total ThT fluorescence yields for α-syn fibrils formed alone and those formed in the presence of the sHSPs (Fig. 3.1) was not due to a difference in the fraction of aggregated α-syn. Furthermore, we used TEM to confirm that the ThT-reactive species formed in the presence of all sHSP constructs were fibrillar (Supplementary Fig. 3.3). Therefore, although the sHSP constructs reduced the rate of α-syn amyloid formation, under these conditions the sHSPs did not halt amyloid assembly at the nucleation stage or significantly alter the total fraction of aggregated α-syn after 42 hours, once all samples had reached a ThT fluorescence plateau.

We also confirmed that the quaternary structures of our sHSP constructs were consistent with those observed previously[279,283,289] using sedimentation velocity analytical ultracentrifugation (SV-AUC) and SAXS (Supplementary Fig. 3.4 – 3.8, Supplementary Table 3.2). WT αB-C and WT Hsp27 both form predominantly oligomers as shown by SV-AUC (Supplementary Fig. 3.4). αB-C ACD, Hsp27-3DΔCTR and Hsp27 ACD all predominantly form dimers (Supplementary Figs. 3.4 – 3.7). Hsp27-3D also predominantly assembles into dimers rather than the large polydisperse oligomers formed by the WT protein (Supplementary Fig. 3.4, 3.8). However, an additional, asymmetric peak in the sedimentation coefficient distribution at ~4 S was evident for Hsp27-3D, indicating that this protein also forms higher order assemblies to some extent. In contrast, the sedimentation coefficient distributions obtained for Hsp27-3DΔCTR and Hsp27 ACD show a single species for which the derived estimates of MW (using the Svedberg equation) match the expected MW of the dimer. The heterogeneity of Hsp27-3D was further evident in the SEC-SAXS data: Hsp27-3D elutes from the SEC column as an asymmetric peak, whereas the elution profiles of Hsp27 ACD and Hsp27-3DDCTR showed greater symmetry. Nevertheless, Hsp27-3D predominantly forms dimers under the conditions used in our assays in this work.

3.3.2 The effects of full-length and truncated constructs of Hsp27 and αB-C on α-syn and apoC-II fibril elongation

To specifically assess the effects of sHSPs on the elongation of α-syn fibrils we used a seeded assay[136]. In these experiments, α-syn began to aggregate immediately and a ThT fluorescence plateau was reached after approximately 10 hours (Fig. 3.2A, Supplementary Fig. 3.9 A). The non-chaperone control protein, BSA, did not inhibit seeded α-syn fibril formation, and no time-dependent changes in ThT fluorescence were observed for sHSPs incubated alone (Supplementary Fig. 3.10). Estimates of the T_{50} were obtained by fitting the data to a one-phase association model (Fig. 3.2 B, Supplementary Fig. 3.9). All sHSP constructs except Hsp27 ACD significantly increased T_{50} (Fig. 3.2 B). The ACD-only constructs were relatively less effective at delaying seeded α-syn fibril formation than the constructs containing the NTR (Fig. 3.2 B). Pelleting assays indicated that the portion of α-syn remaining soluble at the end of the assay was likely increased by all of the sHSP constructs relative to α-syn seeded alone (Fig. 3.2 C). However, the enhancement of α-syn in the supernatant and its depletion from the pellet was particularly evident for WT αB-C (Fig. 3.2 C). These findings are consistent with the results of the seeded ThT fluorescence

assay (Fig. 3.2 A), and the relative efficacy of the sHSP constructs was comparable to the results of the unseeded assay (Fig. 3.1).

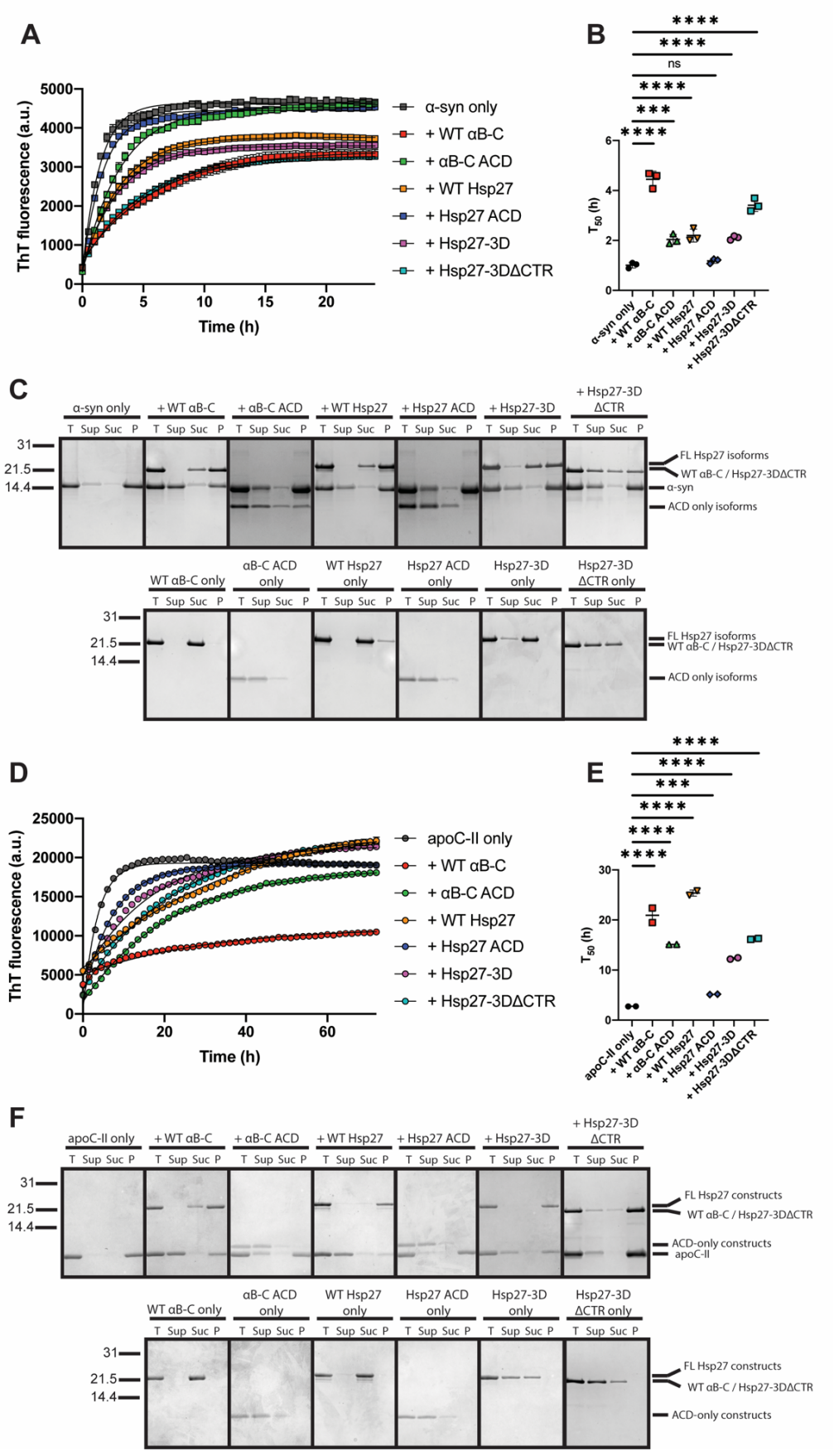

A
ThT fluorescence (a.u.)
Time (h)
α-syn only
+ WT αB-C
+ αB-C ACD
+ WT Hsp27
+ Hsp27 ACD
+ Hsp27-3D
+ Hsp27-3DΔCTR
B
T_{50} (h)
ns
C
α-syn only
+ WT αB-C
+ αB-C ACD
+ WT Hsp27
+ Hsp27 ACD
+ Hsp27-3D
+ Hsp27-3D ΔCTR
T Sup Suc P
31
21.5
14.4
FL Hsp27 isoforms
WT αB-C / Hsp27-3DΔCTR
α-syn
ACD only isoforms
WT αB-C only
αB-C ACD only
WT Hsp27 only
Hsp27 ACD only
Hsp27-3D only
Hsp27-3D ΔCTR only
D
apoC-II only
E
F
FL Hsp27 constructs
ACD-only constructs
apoC-II

Figure 3.2. Kinetics of seeded α-syn amyloid formation and unseeded apoC-II amyloid formation in the presence of sHSPs. A) α-syn amyloid formation (200 μM, 5% fibril seeds, 45°C) alone (black), or in the presence of the indicated sHSP (50 μM): αB-C WT (red), αB-C ACD (green), WT Hsp27 (orange), Hsp27 ACD (blue), Hsp27-3D (magenta) and Hsp27-3DΔCTR (cyan). Data are presented as mean ± SEM, where n = 3. Fits to the data are overlaid. The SEM is small and the error bars are generally not visible. B) Scatter plot of T_{50} values derived from fits to the raw data. Data are presented as mean ± SD with individual data points shown, where n = 3. Significance values were determined using a one-way ANOVA test with a post-hoc Tukey's multiple comparisons test. *** denotes $p < 0.001$, **** denotes $p < 0.0001$. C) α-Syn fibrils were formed for 24 hours (200 μM, 5% fibril seeds, 45°C) alone or in the presence of the indicated sHSP (50 μM). These samples were then centrifuged and the supernatant (Sup), sucrose (Suc) and pellet (P) layers were collected and analysed by SDS-PAGE alongside a sample prior to centrifugation (total, T). Also shown are control samples of each sHSP incubated alone under identical conditions. D) ApoC-II (56 μM) unseeded amyloid fibril formation alone at 30°C (black) or in the presence of the indicated sHSP (12.8 μM): αB-C WT (red), αB-C ACD (green), WT Hsp27 (orange), Hsp27 ACD (blue), Hsp27-3D (magenta) and Hsp27-3DΔCTR (cyan). Data are presented as mean ± SEM where n = 2 with fits to the data overlaid. The SEM is small and the error bars are generally not visible. E) Scatter plot of T_{50} values derived from fits to the raw data. Data are presented as mean ± SD with individual data points shown, where n = 2. Significance values were determined using a one-way ANOVA test with a post-hoc Tukey's multiple comparisons test. *** denotes $p < 0.001$, **** denotes $p < 0.0001$. F) ApoC-II fibrils were formed at 30°C for 72 hours alone (56 μM) or in the presence of 12.8 μM of the indicated sHSP construct. These samples were then centrifuged as described above and the supernatant (Sup), sucrose (Suc) and pellet (P) layers were collected and analysed by SDS-PAGE alongside a sample prior to centrifugation (total, T). Also shown are control samples of each sHSP incubated alone under identical conditions.

ApoC-II aggregates readily at room temperature without agitation or seeding[152]. Consequently, a lag phase is not typically observed for apoC-II aggregation (Fig. 3.2 D, Supplementary Fig. 3.11). These data were fit to a one-phase association model to obtain estimates of the T_{50} (Supplementary Fig. 3.11). BSA did not inhibit apoC-II fibril formation, and no time-dependent changes in ThT fluorescence were observed for sHSPs incubated alone (Supplementary Fig. 3.12). All sHSP constructs significantly increased the T_{50}, thus these constructs delayed fibril elongation by apoC-II (Fig. 3.2 E). WT αB-C was the most effective chaperone against fibril elongation, and Hsp27 ACD was the least effective (Fig. 3.2 D, E). ACD-only constructs were again less-effective than constructs containing the NTR with respect to increasing the T_{50} (Fig. 3.2 E). TEM was also used to confirm fibril formation by apoC-II in the absence of sHSPs and in the presence of a subset of the sHSP constructs (Supplementary Fig. 3.13).

The sucrose pellet assay demonstrated that all sHSP constructs resulted in a portion of apoC-II remaining soluble at the end of the aggregation assay, in contrast to apoC-II incubated alone where we did not observe a band corresponding to apoC-II in the supernatant (Fig. 3.2 F). Qualitative analysis suggests that the full-length WT constructs induced the highest proportion of soluble apoC-II remaining, followed by Hsp27-3D, Hsp27-3DΔCTR, αB-C ACD, and Hsp27 ACD (Fig. 3.2 F). Taken together, these experiments indicate that constructs containing the NTR are relatively more effective than constructs containing only the ACD against both amyloid forming proteins tested.

3.3.3 The association of sHSPs with amyloid fibrils

Our pelleting assays allow us to determine to what extent each sHSP construct stably co-sediments with apoC-II and α-syn fibrils. Previous studies employed fluorescence and electron microscopy to establish that the co-sedimentation behaviour of αB-C and Hsp27 with apoC-II and α-syn fibrils observed in pelleting assays is due to spatial co-localisation of these sHSPs with the fibrils[257,258,310]. We have therefore used pelleting assays as a high-throughput approach to monitor fibril co-localisation by sHSPs. WT Hsp27, Hsp27-3D, and WT αB-C were all found primarily in the pellet fraction when present during the aggregation of apoC-II or α-syn (Fig. 3.1 I, 3.2 C and F). Interestingly, Hsp27-3DΔCTR co-sedimented with both apoC-II and α-syn fibrils to a lesser extent than WT Hsp27, suggesting that the CTR of Hsp27 contributes to fibril binding. When incubated with elongating apoC-II fibrils, ACD-only constructs remained primarily in the soluble fraction, suggesting that they did not form stable associations with the fibrils at levels detectable by SDS-PAGE (Fig. 3.2 F). Similarly, when incubated in the presence of elongating α-syn fibrils, Hsp27 ACD remained primarily in the soluble fraction. However, αB-C ACD was found in the pellet fraction when present during both unseeded and seeded α-syn fibril elongation (Fig. 3.1 I, Fig. 3.2 C). The differences in the extent of fibril colocalization observed for full-length Hsp27 constructs compared to Hsp27-3DΔCTR and Hsp27 ACD indicates that both the NTR and CTR of Hsp27 contribute to fibril binding.

To further investigate the co-sedimentation of each sHSP construct with amyloid fibrils, mature pre-formed apoC-II and α-syn amyloid fibrils were incubated with each sHSP construct for 72 hours. The fibrils were then pelleted and analysed as described above. All full-length constructs and Hsp27-3DΔCTR

were located primarily in the pellet fractions, suggesting that these constructs stably associate and co-sediment with pre-formed apoC-II and α-syn fibrils (Fig. 3.3). Neither Hsp27 ACD nor αB-C ACD co-sedimented with pre-formed fibrils of apoC-II or α-syn at levels detectable by SDS-PAGE. This indicates that αB-C ACD can only associate with α-syn fibrils when it is present during amyloid fibril elongation, but not once the mature fibrils have been formed. Taken together these data suggest that the ACD of αB-C is insufficient for fibril binding and that both the NTR and CTR of Hsp27 have roles in fibril binding.

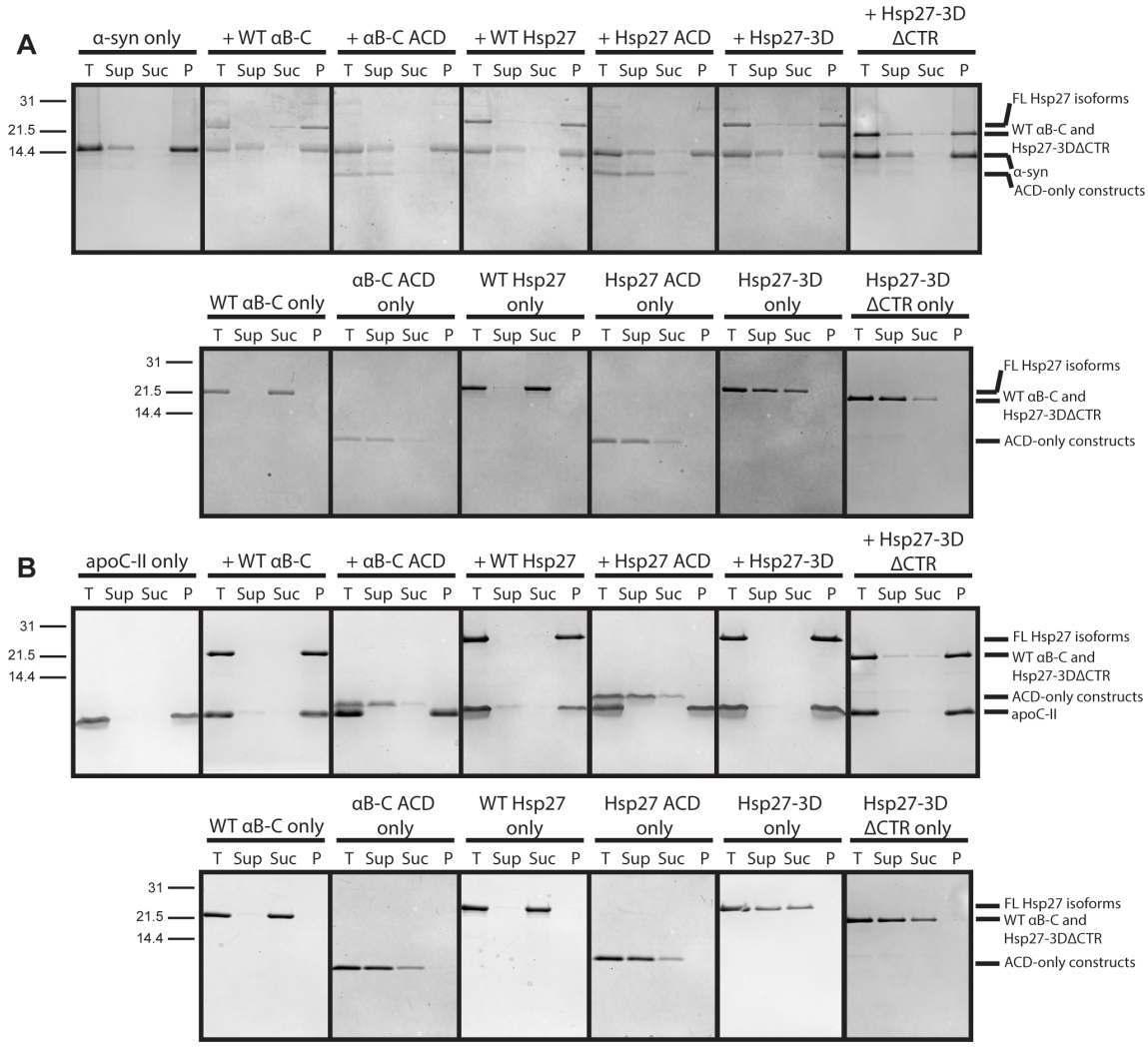


Figure 3.3. Fibril pelleting assay of pre-formed fibrils incubated with sHSP constructs. α-Syn fibrils (200 μM) were formed for 48 hours, 37°C and apoC-II fibrils (56 μM) were formed for 72 hours, 30°C. These pre-formed α-syn fibrils (A) and apoC-II fibrils (B) were then incubated alone, or with the indicated sHSP at 10 μM (for α-syn) or 12.8 μM (for apoC-II) for a further 72 hours. Following this incubation, each sample was pelleted as described above and the supernatant (Sup), sucrose (Suc) and

pellet (P) layers were collected and analysed by SDS-PAGE alongside the total (T) uncentrifuged samples. Also shown are controls of each sHSP construct incubated alone for 72 hours and centrifuged as described above.

3.3.4 The time-course of amyloid fibril binding by full-length and NTR+ACD sHSP constructs

We next determined the time frame over which the full-length sHSP constructs and Hsp27-3DΔCTR associate with both apoC-II and α-syn amyloid fibrils. Initially, pre-formed apoC-II or α-syn fibrils were incubated with each construct for 0, 0.5, 2 or 6 hours. We observed a gradual decrease in the amount of WT αB-C detected in the sucrose layer over the incubation period with both apoC-II and α-syn fibrils, coupled with a concomitant increase in the amount detected in the pellet fraction (Fig. 3.4 A and 3.4 B). Some WT αB-C remained in the sucrose fraction even after incubation for 6 hours with apoC-II fibrils (Fig. 3.4 B). This suggests that the interaction of WT αB-C with amyloid fibrils occurs slowly over the hour-timescale. In contrast, the majority of WT Hsp27 co-sedimented with both fibril types at 0 hours (Fig. 3.4 C and 3.4 D), with only a small fraction remaining in the sucrose fraction at 0 hours in the presence of α-syn fibrils (Fig. 3.4 C). Hsp27-3D was identified only in the pellet fraction at 0 hours and remained in this fraction throughout the time course, suggesting that Hsp27-3D associated completely with apoC-II and α-syn fibrils within the dead-time of our assay (Fig. 3.4 E and 3.4 F). For Hsp27-3DΔCTR, the majority of the protein was observed in the pellet fraction at all incubation time points with both fibril types (Fig. 3.4 G and 3.4 H), however we always observed a faint band corresponding to Hsp27-3DΔCTR in the supernatant, even after 72 hours (Fig. 3.3 A and B). These results indicate that WT Hsp27, Hsp27-3D, and Hsp27-3DΔCTR rapidly associate with amyloid fibrils, while WT αB-C associates with pre-formed fibrils slowly. Hsp27-3D may bind to α-syn fibrils faster than WT Hsp27. The presence of a population of unbound Hsp27-3DΔCTR throughout the time course suggests that its affinity for fibrils is reduced relative to the full-length constructs.

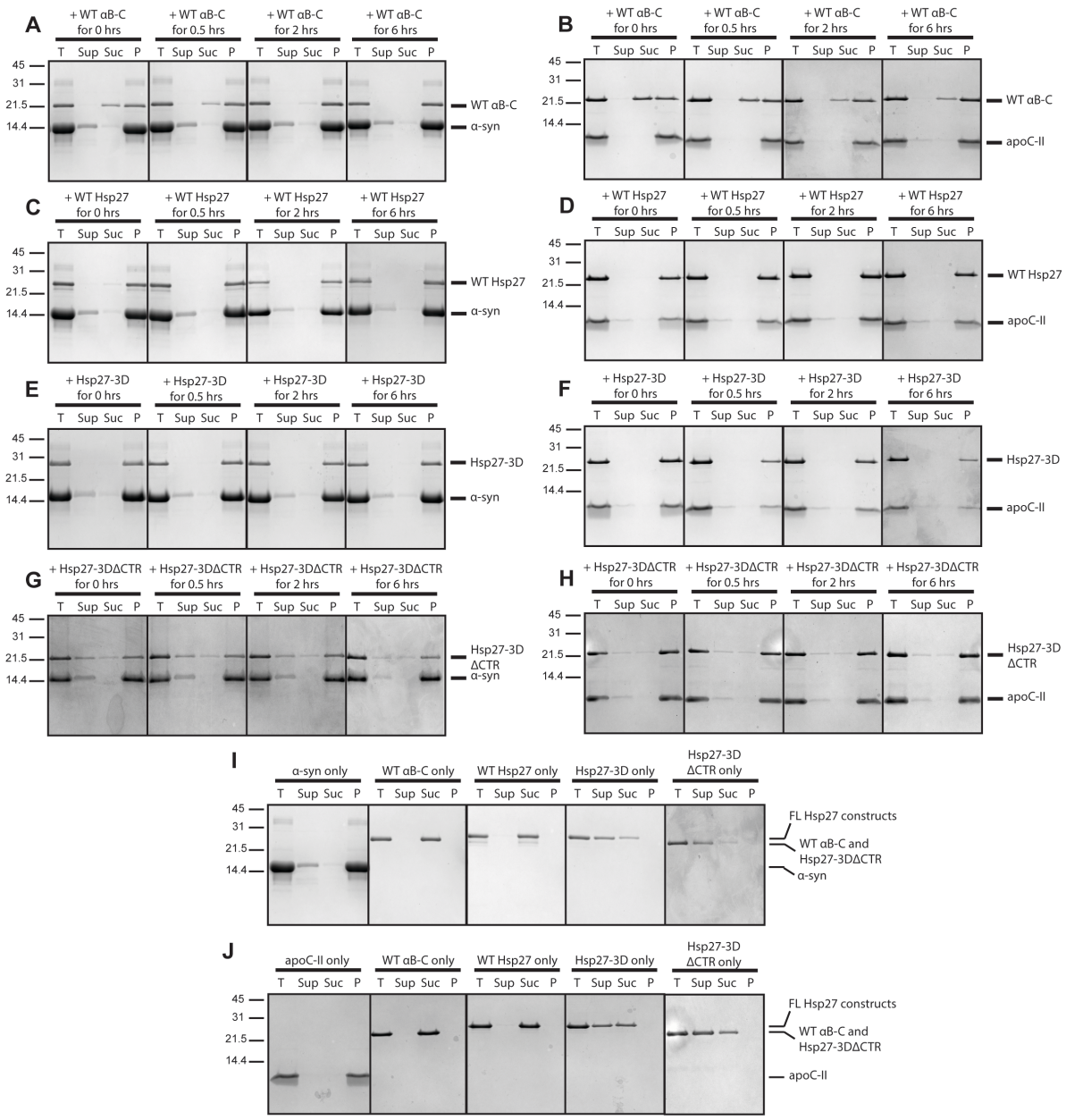


Figure 3.4. Time course pelleting assay of pre-formed amyloid fibrils incubated with full-length sHSP constructs. α-Syn fibrils (200 μM) were formed for 48 hours, 37°C and apoC-II fibrils (56 μM) were formed for 72 hours, 30°C. Fibrils were then incubated with the indicated sHSP construct at 10 μM (for α-syn) or 12.8 μM (for apoC-II) for 0-6 hours. Following this incubation, each sample was centrifuged as described above. The supernatant (Sup), sucrose (Suc) and pellet (P) layers were collected and analysed by SDS-PAGE alongside the total (T) uncentrifuged samples. Pre-formed α-syn fibrils incubated with (A) αB-C WT; (C) WT Hsp27; (E) Hsp27-3D; (G) Hsp27-3DΔCTR. Pre-formed apoC-II fibrils incubated with (B) αB-C WT; (D) WT

Hsp27; (F) Hsp27-3D; (H) Hsp27-3DΔCTR. (I-J) Pre-formed α-syn or apoC-II fibrils and sHSP constructs incubated alone for 6 hours at identical concentrations to those described above.

3.3.5 The dissociation of apoC-II amyloid fibrils induced by sHSPs

Previous studies have shown that, at equilibrium, a free pool of soluble protein exists in dynamic exchange with amyloid fibrils[87]. For apoC-II fibrils, this free pool accounts for ~5-10% of the total protein concentration[160]. Close inspection of the fibril binding time course data (Fig. 3.4) showed a minor band corresponding to apoC-II in the supernatant fraction in the presence of the sHSPs (Fig. 3.4 B, D, F and H) that was not observed for apoC-II incubated alone (Fig. 3.4 J). These findings warranted a more quantitative study of the process of apoC-II fibril dissociation, and whether the presence of sHSPs affects this process. We analysed apoC-II fibrils incubated in the presence of WT αB-C for 0-20 hours using SV-AUC (Fig. 3.5 B-D, Supplementary Fig. 3.14). In this experiment, a rotor speed of 40,000 rpm (129,000 x *g*) was used since this centrifugal force causes the fibrils to pellet within minutes, whereas the oligomers formed by WT αB-C and any soluble, monomeric apoC-II sediment over a period of hours. This regime enables us to monitor the relative proportions of both oligomeric WT αB-C and soluble, monomeric apoC-II. The peak at ~1 S corresponds to monomeric apoC-II and is visible when fibrils are incubated alone (Fig. 3.5 B). However, with increasing incubation time in the presence of WT αB-C the proportion of soluble apoC-II increases (Fig. 3.5 C). The peak at ~13 S, corresponding to oligomeric WT αB-C, decreases with increasing incubation time (Fig. 3.5 D). This observation is consistent with an increasing proportion of WT αB-C associating with the apoC-II fibrils over time (Fig. 3.4 and Fig. 3.5 A) as fibrils sediment too quickly to be observed in this AUC experiment. Pelleting assays also demonstrated that WT Hsp27 and Hsp27-3D disaggregated apoC-II fibrils in a concentration-dependent manner (Supplementary Fig. 3.15). To further assess apoC-II fibril dissociation, we formed fluorescently labelled apoC-II fibrils using 10% S61C Alexa 488-labelled apoC-II. These fibrils were incubated alone or in the presence of each sHSP construct for 24 hours. The fibrils were pelleted, and the supernatant was analysed by SDS-PAGE without Coomassie blue staining. Imaging for Alexa 488-labelled apoC-II indicated that all sHSP constructs containing the NTR enhanced the proportion of soluble apoC-II (Fig. 3.5 E), while the ACD-only constructs did not. Therefore, the NTR of Hsp27 and the terminal regions of αB-C are

important for apoC-II fibril dissociation. These results extend our previous findings that WT αB-C enhances the dilution-induced dissociation of apoC-II fibrils[258].

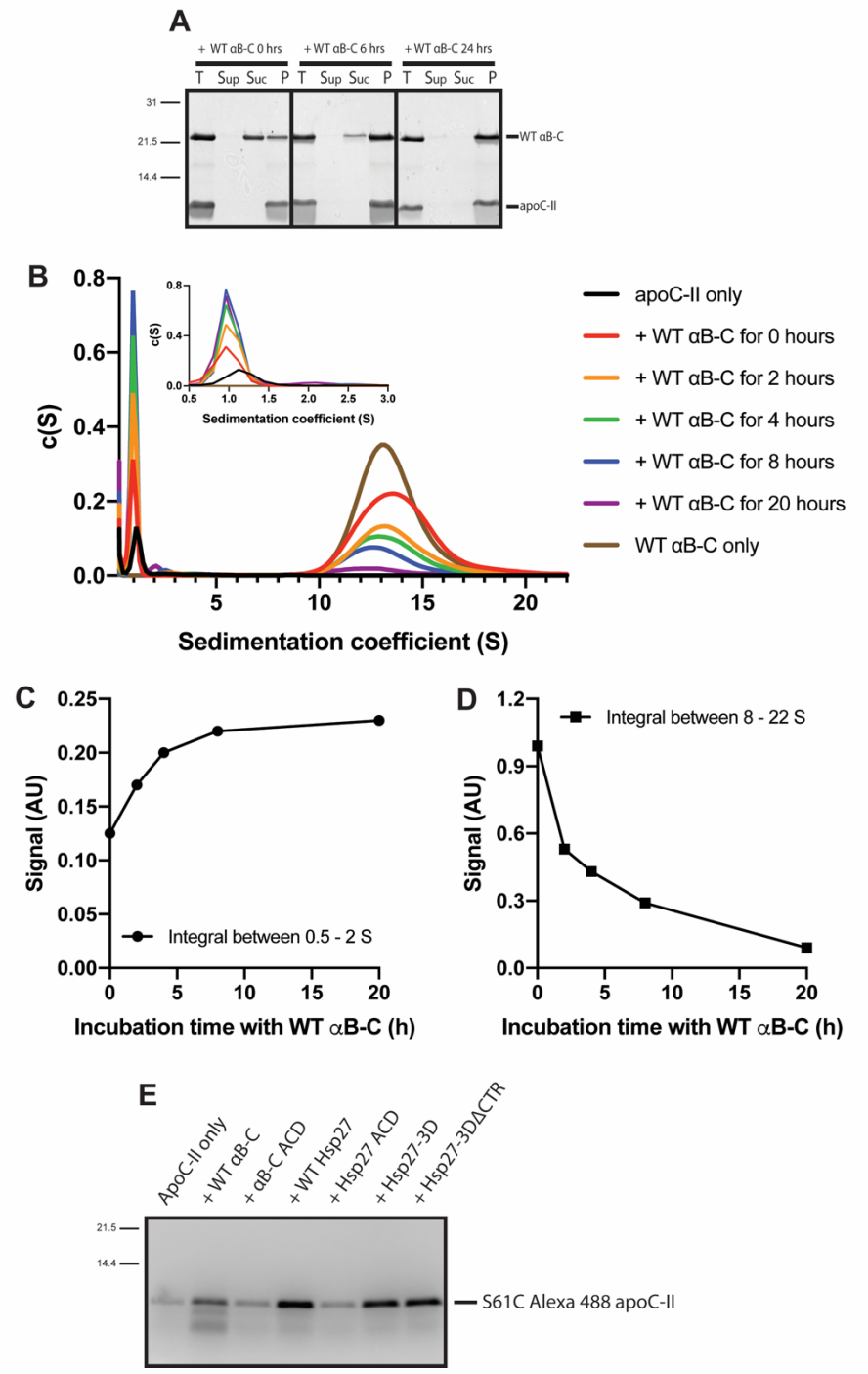


Figure 3.5. Analysis of the time-course of apoC-II fibril dissociation by WT αB-C. ApoC-II fibrils (56 µM) were formed for 72 hours, 30°C. A) Fibrils were incubated with WT αB-C (12.8 µM) for 0-24 hours. Each sample was centrifuged as described

above. The supernatant (Sup), sucrose (Suc) and pellet (P) layers were collected and analysed by SDS-PAGE alongside the total (T) uncentrifuged samples. B) SV-AUC analysis of pre-formed apoC-II fibrils (56 μM) incubated with WT αB-C (12.8 μM) for 0 (red), 2 (orange), 4 (green), 8 (blue) or 20 (purple) hours prior to SV-AUC. ApoC-II fibrils (black) and WT αB-C (brown) incubated alone for 20 hours are also shown. Plots of the integral of the peak between 0.5 and 2 S (C) and between 8 and 22 S (D) in the c(s) distribution shown in (B) as a function of incubation time with WT αB-C. E) ApoC-II fibrils (56 μM) formed with 10% S61C Alexa488 labelled apoC-II were incubated with the indicated sHSP construct (12.8 μM) for 24 hours and centrifuged as described above. The supernatant fractions were analysed by SDS-PAGE and imaged using a filter set for Alexa-488 as described in the methods section.

In contrast to our observations for apoC-II, pelleting assays did not indicate that the proportion of soluble α-syn in equilibrium with the fibrils was increased by the presence of the sHSP constructs (Fig. 3.4 A, C, E, G and I). Nevertheless, we tested the ability of WT αB-C to induce dissociation of pre-formed α-syn fibrils using a pelleting assay (Supplementary Fig. 3.16). This experiment showed no observable dissociation of α-syn fibrils by WT αB-C under the conditions and timescales that we tested in this work. Longer incubation times or additional factors such as dilution or ATP-dependent HSPs may be required for the dissociation of α-syn fibrils, as has previously been observed[266,270].

3.3.6 The effects of fibril binding by sHSPs on the size distributions of pre-formed amyloid fibrils

We next determined the effect of sHSPs on the size distributions of pre-formed apoC-II fibrils using SV-AUC (Fig. 3.6, Supplementary Figs. 3.17 – 3.21 and Supplementary Tables 3.3 – 3.7). The interaction of WT αB-C with apoC-II fibrils resulted in an increase in the weight-average fibril sedimentation coefficient as indicated by a shift in the sedimentation coefficient distribution towards higher S values (Fig. 3.6 A). We interpret this as an increase in the lateral association of mature fibrils with one another mediated by WT αB-C. In contrast, αB-C ACD, which did not stably colocalise with apoC-II fibrils (Fig. 3.3 B), did not increase the weight-average sedimentation coefficient of the fibrils. Instead we observed a small but reproducible shift in the sedimentation coefficient distributions towards smaller S values (Fig. 3.6 B). Similarly, WT Hsp27 increased, and Hsp27 ACD decreased, the average size of the fibrils (Fig. 3.6 C-D). The binding of Hsp27-3D to apoC-II fibrils resulted in immediate and visible precipitation such that, when present at the same concentration as the other sHSP constructs (12.8 μM), the fibrils sediment

too rapidly to accurately determine the sedimentation coefficient distributions (Fig. 3.6 E, Supplementary Fig. 3.18 D). At a lower concentration (6.4 μM), the binding of Hsp27-3D to the fibrils also results in a large increase in the fibril size distribution (Fig. 3.6 F, Supplementary Fig. 3.19 B, Supplementary Table 3.5). Given the observation that full-length Hsp27 constructs appear to bind fibrils faster than our methodologies allow us to detect (Fig. 3.4 D and F), and that Hsp27-3D resulted in the visible precipitation of apoC-II fibrils within a matter of minutes, we also tested the effect of WT Hsp27 on the size distribution of pre-formed apoC-II fibrils after a shorter incubation period; immediately after the addition of Hsp27 (Fig. 3.6 G, Supplementary Fig. 3.20, Supplementary Table 3.6). The resulting fibril size distribution closely matched that observed after 72 hours. The duration of the AUC experiment is approximately 5-6 hours; therefore, this result indicates that the lateral fibril-fibril association caused by WT Hsp27 primarily occurs within the first few hours after the addition of the sHSP to the fibrils. Interestingly, despite the stable interaction of Hsp27-3DΔCTR with pre-formed apoC-II fibrils (Fig. 3.3 B), this construct did not increase the size distributions of the apoC-II fibrils to the same extent as the full-length Hsp27 constructs (see Figs. 3.6 C and F and H, Supplementary Fig. 3.21, Supplementary Table 3.7). This result suggests that the CTR region of Hsp27 plays an important role in promoting lateral association and/or tangling of apoC-II fibrils. Incubation of BSA, a non-chaperone control, with pre-formed apoC-II fibrils did not result in a change to the weight-average fibril sedimentation coefficient (Supplementary Fig. 3.22, Supplementary Table 3.8). Thus, full-length Hsp27 constructs, WT αB-C and, to a lesser extent Hsp27-3DΔCTR, increase the size distributions of apoC-II fibrils. This apparent increase in size is likely due to fibril cross-linking mediated by the sHSP, as has been previously observed using WT αB-C[258]. The ACD constructs do not exert this effect, which is consistent with our observation that the ACD constructs do not bind stably to apoC-II fibrils (Fig. 3.3 B). The lateral fibril-fibril association observed in the presence of full-length sHSPs using AUC was further confirmed using TEM (Supplementary Fig. 3.23). Pre-formed fibrils incubated alone or in the presence of the ACD-only constructs appeared relatively dispersed on the EM grids, whereas those incubated in the presence of WT αB-C, WT Hsp27 or Hsp27-3D appeared to form denser fibril tangles (Supplementary Fig. 3.23).

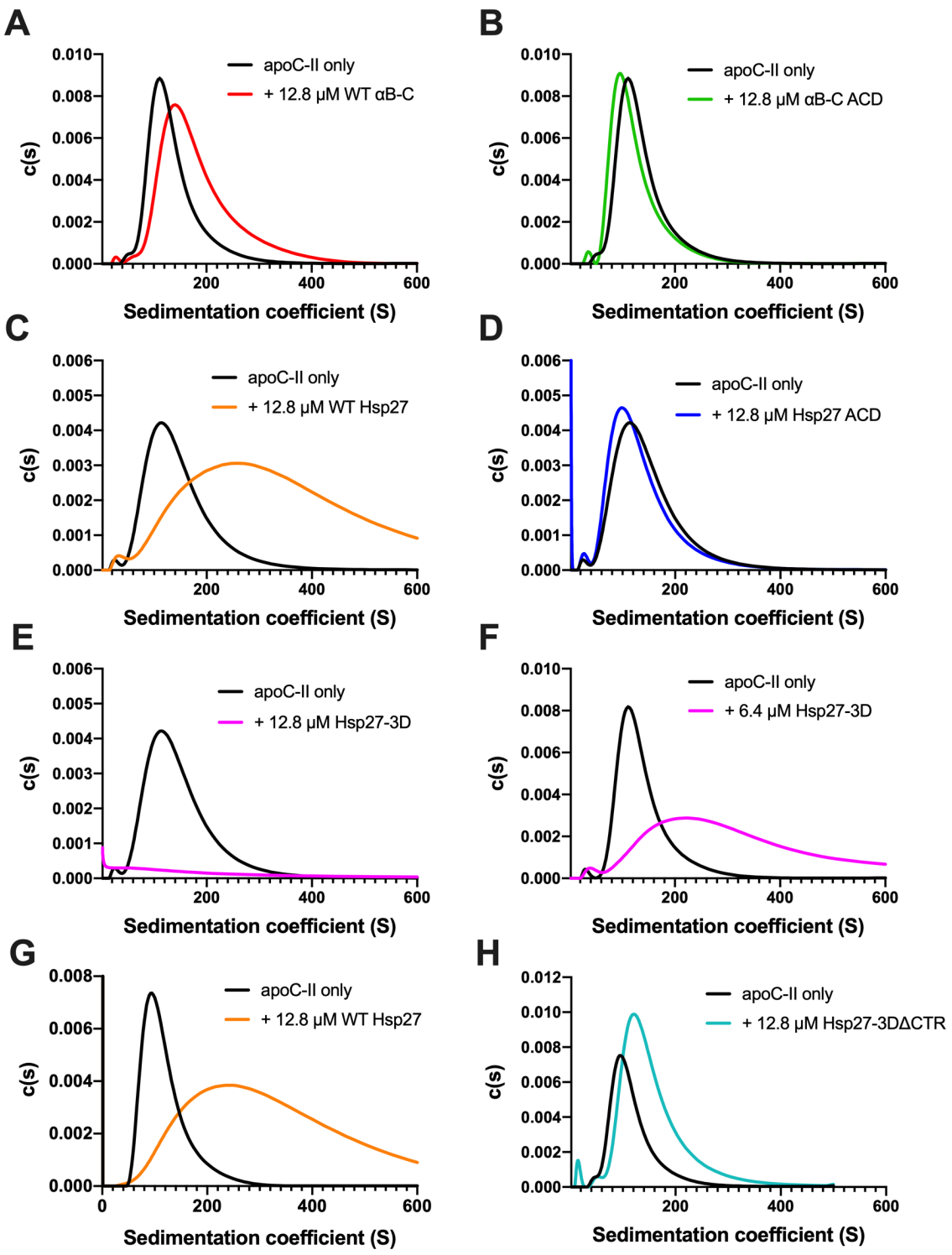


Figure 3.6. SV-AUC analysis of pre-formed apoC-II fibrils (56 μM) incubated with various sHSP constructs. ApoC-II fibrils (56 μM) were formed for 72 hours, 30°C. Subsequently, these fibrils were incubated either alone, or with the indicated sHSP for a further 72 hours unless otherwise indicated. In each panel apoC-II fibrils incubated alone is shown in black. ApoC-II incubated

with: A) 12.8 μM WT αB-C; B) 12.8 μM αB-C ACD; C) 12.8 μM WT Hsp27; D) 12.8 μM Hsp27 ACD; E) 12.8 μM Hsp27-3D; F) 6.4 μM Hsp27-3D; G) 12.8 μM WT Hsp27 for 0 hours; H) 12.8 μM Hsp27-3DΔCTR.

As α-syn fibrils are too large for SV-AUC analysis, even at the lowest available rotor speed, we monitored the assembly of α-syn fibrils into larger aggregates mediated by the various sHSP constructs by light scattering over a period of up to 6 hours. Using this approach, a time-dependent increase in the light scattering of α-syn fibrils incubated in the presence of all full-length sHSPs was detected, but not with Hsp27-3DΔCTR or the ACD-only sHSPs (Fig. 3.7 A). Full-length Hsp27 and Hsp27-3D induced an increase in light scattering within 30 min, whereas the increase in light scattering induced by WT αB-C occurred over 2 hours. These observations are consistent with the rate of α-syn fibril binding by these full-length sHSPs observed in our pelleting assays (Fig. 3.4), suggesting that fibril binding and the formation of larger fibrillar aggregates are related processes. That we could not detect an increase in turbidity of α-syn fibrils incubated with Hsp27-3DΔCTR is consistent with the observation that this construct did not cause lateral association of apoC-II fibrils to the same extent as the full-length Hsp27 constructs, providing further evidence that the CTR of Hsp27 is important for this chaperone function. We subsequently used a continuous assay to more accurately track the increase in light scattering mediated by the presence of sHSPs. WT αB-C did not induce a significant increase in light scattering over the first 20 min of incubation (Fig. 3.7 B), consistent with its slower rate of fibril binding. The turbidity of α-syn fibrils incubated with Hsp27-3D increased more rapidly than that of fibrils incubated with WT Hsp27 (Fig 3.7 B-C, Supplementary Fig. 3.24 B-G, Supplementary Table 3.9). These results are also consistent with our observation that Hsp27-3D may bind α-syn fibrils more rapidly than WT Hsp27 (Fig. 3.4 C and E). Overall, these light scattering experiments support our observations that by binding to fibrils, full-length sHSPs mediate their association into larger aggregates. To further confirm that the full-length sHSP constructs induced lateral fibril-fibril association of α-syn fibrils we used TEM (Supplementary Fig. 3.25). α-Syn fibrils incubated alone or in the presence of ACD-only sHSPs appeared dispersed on the grids, whereas those incubated in the presence of WT αB-C, WT Hsp27 or Hsp27-3D appeared as larger networks of tangled fibrils (Supplementary Fig. 3.25). Fibrils incubated in the presence of Hsp27-3DDCTR appeared to form slightly larger fibril tangles than those observed for α-syn fibrils incubated alone.

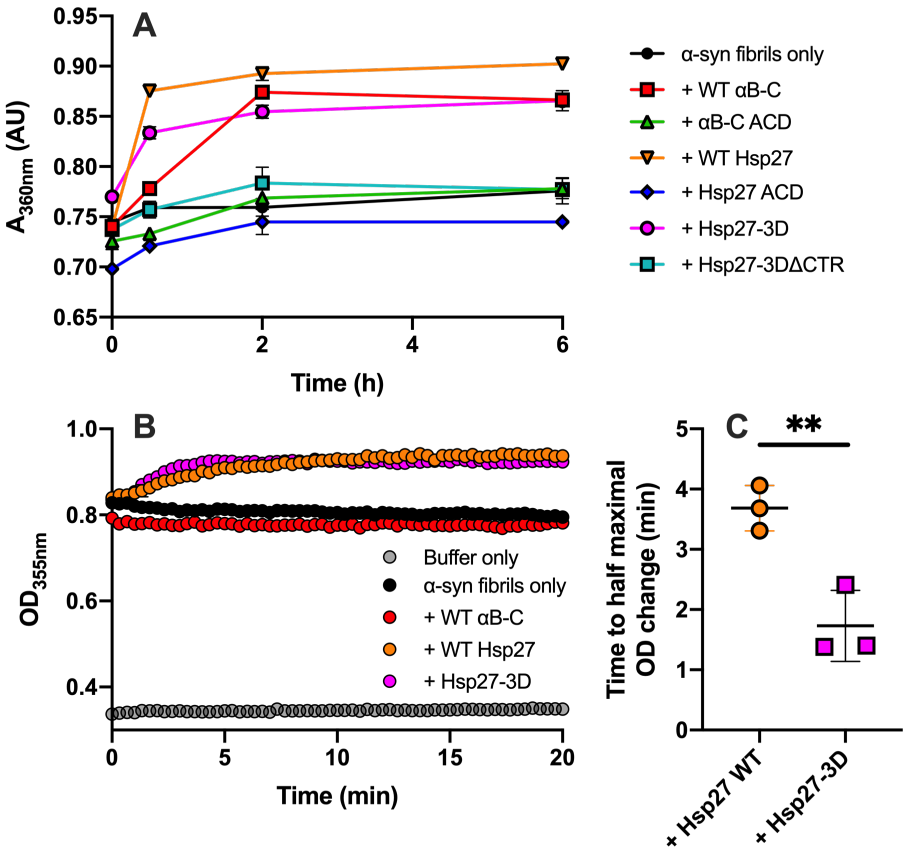


Figure 3.7. Analysis of light scattering by α-syn amyloid fibrils in the presence of sHSPs. α-Syn fibrils (200 µM) were formed for 48 hours, 37°C. A) Absorbance measurements at 360 nm of pre-formed α-syn fibrils incubated alone (black) or in the presence of 10 µM WT αB-C (red), αB-C ACD (green), WT Hsp27 (orange), Hsp27 ACD (blue), Hsp27-3D (magenta) or Hsp27-3DΔCTR (cyan) for up to 6 hours. (B) Turbidity measurements for buffer alone (grey), for pre-formed α-syn fibrils incubated alone (black) and for preformed α-syn fibrils in the presence of 10 µM WT αB-C (red), 10 µM WT Hsp27 (orange) and 10 µM Hsp27-3D (magenta). Data are presented as mean ± SEM where n = 3. C) Analysis of the time taken for half maximal change in turbidity (T_{50}) of α-syn fibrils incubated with WT Hsp27 (orange) or Hsp27-3D (magenta) derived from fits to the raw data using a 4-parameter sigmoidal Hill-plot. Data are presented as mean ± SD with individual data points shown, where n = 3. A paired t-test was used to compare the T_{50} for WT Hsp27 versus Hsp27-3D. ** denotes $p < 0.01$.

3.4 Discussion

It is well established that the human sHSPs Hsp27 and αB-C are molecular chaperones that inhibit the aggregation of a wide range of client proteins[257,259,343,359]. Over the past decade, significant progress has been made in understanding the hierarchical interactions that regulate the oligomerisation of αB-C and

Hsp27. An inter-chain β-sheet formed between two ACDs mediates dimerization[280], the CTR interacts with the ACD of adjacent dimers to facilitate the formation of small oligomers[287,342], and varied interactions involving the NTR regulate higher-order oligomerisation[342]. Recent work suggested that the isolated ACD of αB-C, which forms a stable dimer, retains chaperone activity comparable to that of the full-length protein[279]. While there is not yet a clear consensus regarding how Hsp27 or αB-C interact with client proteins to inhibit or delay their aggregation, potential substrate binding sites have been identified within the N- and C-terminal regions, as well as in the ACD[295,301,362]. To determine the roles that the NTR, ACD and CTR play in inhibiting amyloid fibril formation, we compared the relative chaperone activities of an array of full-length and truncated constructs of Hsp27 and αB-C against amyloid fibril formation by two disease-associated proteins, apoC-II and α-syn. Importantly, although the ACD-only constructs retain some ability to delay amyloid fibril formation, they lack several specific chaperone properties that we show are conferred by the NTR and CTR. We found that the NTR of Hsp27 and the terminal regions of αB-C are important for delaying the early stages of amyloid formation, for allowing sHSPs to associate with amyloid fibrils, and for inducing apoC-II amyloid fibril disaggregation. The CTR of Hsp27 and either or both of the terminal regions of αB-C were implicated in the lateral association of fibrils that comes about through sHSPs binding stably to fibrils.

We used ThT assays and fibril pelleting assays to assess the relative chaperone abilities of several constructs of αB-C and Hsp27. In the unseeded amyloid fibril formation assays we observed several differences between the final ThT yields for apoC-II or α-syn fibrils formed in the presence of the αB-C constructs compared to the Hsp27 constructs. However, the α-syn pelleting assay showed no difference in the fraction of aggregated α-syn in the presence of these two sHSP constructs. Furthermore, the pelleting assay performed at the end of unseeded apoC-II fibril formation also indicated that despite differences in the final ThT fluorescence yields, the presence of WT αB-C, WT Hsp27 or Hsp27-3D all resulted in a substantial amount of apoC-II remaining soluble. TEM confirmed the formation of α-syn fibrils in the presence of all of the sHSP constructs and of apoC-II fibrils in the presence of WT αB-C and Hsp27-3D. We hypothesise that the differences in ThT fluorescence could be due to differences in the colocalization of the sHSPs with the fibrils, which may differentially affect the binding of ThT to the fibrils and therefore ThT fluorescence. Alternatively, the various sHSP constructs may induce changes in fibril

morphology. It is known that α-syn fibrils exist in various polymorphs[74]. It is plausible that these polymorphs bind ThT to differing extents. Another explanation is that the differences in ThT fluorescence we observe are due to differences in the lateral association of the fibrils, induced by the sHSPs, as the fibrils form. This work shows that this lateral fibril-fibril association occurs more slowly in the presence of WT αB-C than for WT Hsp27. The fluorescence yields observed in ThT assays should therefore be interpreted cautiously and verified using orthogonal methodologies, particularly for investigations of molecules that may bind or alter the morphology of the aggregates. Thus, for this work we used ThT fluorescence as a reporter of the duration of the lag phase and the T_{50} in combination with pelleting assays and TEM.

Across all of our fibril formation assays, the full-length and NTR+ACD constructs were superior chaperones compared to the ACD-only constructs. Only constructs containing the NTR significantly increased the T_{lag} for α-syn fibril formation. ACD-only constructs were also less effective at delaying α-syn and apoC-II fibril elongation than those with the NTR. WT Hsp27, Hsp27-3D and Hsp27-3DΔCTR delayed fibril nucleation and elongation by both α-syn and apoC-II to similar extents, indicating that neither the formation of high molecular weight Hsp27 oligomers nor the CTR of Hsp27 are required for delaying amyloid formation. Taken together, our results indicate that the NTR of Hsp27 and the terminal regions of αB-C play essential roles in delaying the nucleation phase of amyloid formation and contribute to reducing the rate of fibril elongation.

Pelleting assays with pre-formed fibrils demonstrated that full-length and NTR+ACD constructs disaggregate apoC-II amyloid fibrils; in contrast, we did not observe apoC-II fibril dissociation induced by the ACD-only constructs. It is likely that by interacting with a soluble form of apoC-II that exists in equilibrium with the fibrils, these sHSP constructs shift the equilibrium in favour of fibril dissociation. This mechanism agrees with previous work investigating the inhibition of apoC-II and α-syn amyloid formation by WT αB-C[257,258]. Interestingly, AUC data showed that the release of soluble apoC-II monomers from apoC-II fibrils occurred at a similar rate to the binding of WT αB-C to fibrils, suggesting a possible correlation between fibril binding by sHSPs and the process of fibril dissociation. Our data

cannot rule out promotion of fibril disaggregation resulting, at least in part, from destabilization of apoC-II fibrils through direct interaction of the sHSPs with the fibrils.

The interaction of sHSPs with pre-formed protein aggregates has been proposed not only to inhibit fibril elongation, but also to reduce the cytotoxicity of fibrils, either by coating the aggregates and reducing their reactive surface area[262] or by sequestering them into larger inclusion body-like structures[258]. The assay conditions used in this study do not favour secondary nucleation processes[136], thus we can only speculate as to how the interactions of sHSPs with pre-formed fibrils might affect this process. It is likely that the stable binding of fibrils by sHSPs and the lateral fibril-fibril associations induced by the sHSPs observed in this study would reduce the surface area of the fibrils available for secondary nucleation processes. The stable interaction of WT αB-C with apoC-II and Aβ fibrils has been observed previously[258,259], as has an interaction between WT αB-C, WT Hsp27 and Hsp27-3D with α-syn fibrils[257,310]. Here, we have observed that the stable interaction of sHSPs with pre-formed amyloid fibrils is dependent on sequences within the NTR and CTR. Our pelleting assays showed that only the full-length and NTR+ACD constructs interacted with both elongating and mature apoC-II and α-syn fibrils. In these assays, the NTR+ACD construct appeared to have a reduced capacity to co-sediment with both types of fibrils, indicating that the CTR must also contribute to fibril binding directly (i.e. through a direct CTR-fibril interaction) or indirectly (i.e. via a CTR-sHSP interaction) (Fig. 3.8). Whilst we were unable to detect any stable interaction between the ACD-only constructs and apoC-II fibrils, we did observe an interaction between αB-C ACD and elongating α-syn fibrils. However, when αB-C ACD was added to pre-formed α-syn fibrils this interaction was not observed. This suggests that αB-C ACD can interact with some element present when α-syn fibrils are elongating, but not once they are formed. The fact that Hsp27 ACD did not form stable interactions with elongating α-syn fibrils suggests differences in the interaction between these two ACD-only constructs and α-syn.

We found that WT Hsp27 binds fibrils more rapidly than WT αB-C and this capacity is further enhanced in Hsp27-3D. Assuming that dissociated sHSP species (e.g. dimers) are the predominant fibril-binding species, the difference in the rate of fibril binding observed between WT αB-C and WT Hsp27 may be due to differences in the rate of dissociation of sHSP dimers from their oligomeric form and/or the rate

of fibril binding by a sHSP dimer. WT Hsp27 binds to fibrils over a period of minutes whereas WT αB-C binds over a period of hours, meaning that either the rate of fibril binding by a Hsp27 dimer is greater than that of αB-C, or that the rate of Hsp27 dimer dissociation from a Hsp27 oligomer is faster, or a combination of both of these effects. Hsp27-3D and Hsp27-3DΔCTR both appeared to interact with fibrils faster than WT Hsp27 and this difference is most likely due to differences in the quaternary structure of these constructs. Hsp27-3D and Hsp27-3DΔCTR primarily exist as dimers in solution[289], which we confirmed here by AUC (Supplementary Fig. 3.4). Thus, for Hsp27-3D and Hsp27-3DΔCTR fibril binding can be considered a one-step process whose rate depends only on the rate at which dimers bind to fibrils, independent of oligomer dissociation.

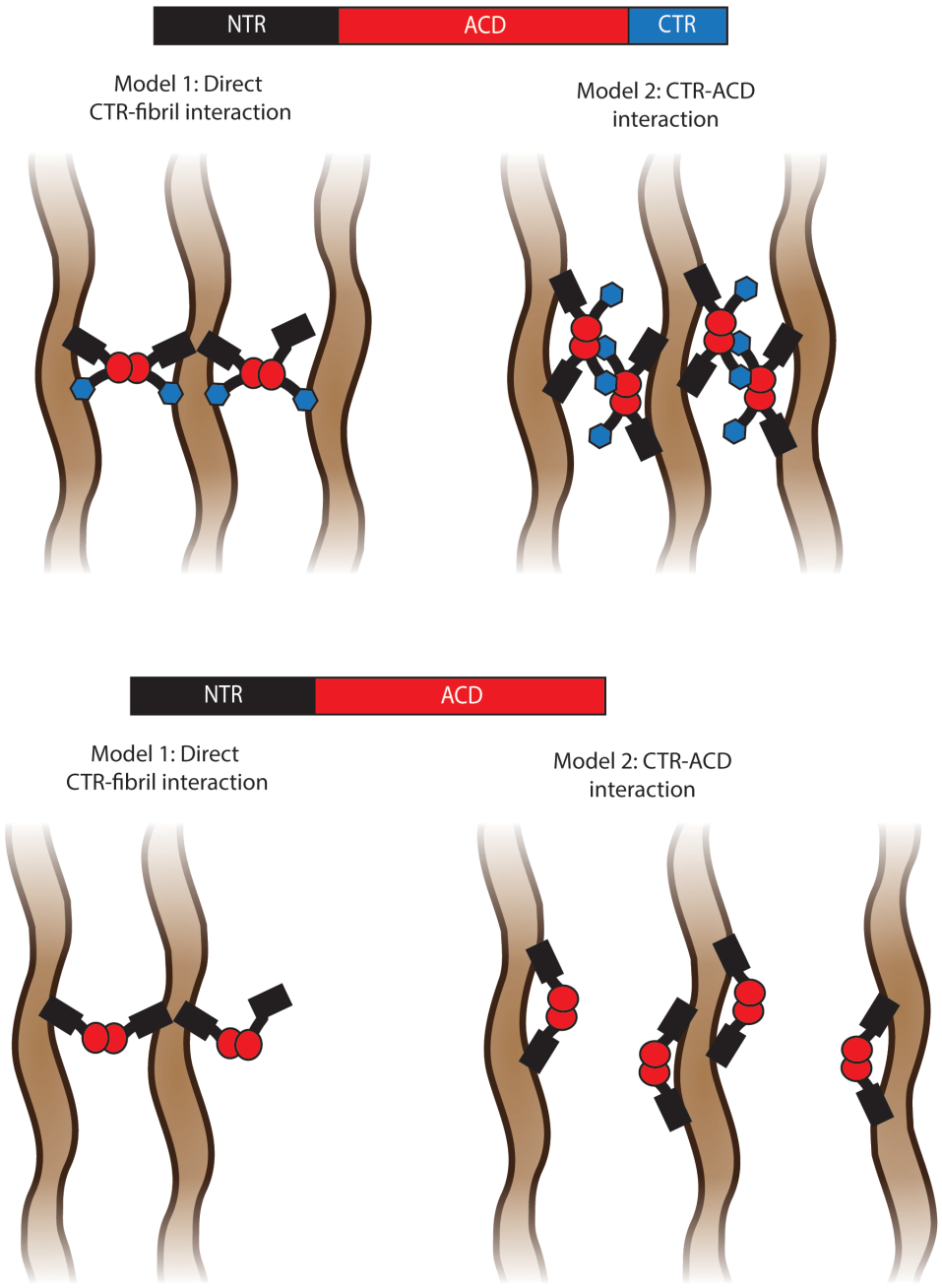


Figure 3.8. Two models for the mechanism of fibril binding and lateral tangling induced by sHSPs. The domains of sHSPs are coloured as follows: NTR (black), ACD (red), CTR (blue). Amyloid fibrils are depicted in brown. In the first model, both the NTR and CTR contribute directly to fibril binding. In the absence of the CTR, an individual sHSP dimer has a reduced fibril binding affinity and a reduced ability to cause lateral fibril association. In the second model, the CTR of one sHSP that is bound to fibrils via its NTR docks onto the ACD of another fibril-bound sHSP. This CTR-mediated oligomerisation results in tangling of the associated fibrils. In the absence of the CTR, CTR-ACD interactions cannot form and this type of sHSP oligomerization is not possible.

Our fibril binding studies revealed that the full-length and NTR+ACD constructs increased the weight-average sedimentation coefficient of apoC-II fibrils, suggesting formation of large fibril aggregates through lateral fibril-fibril association. Full-length Hsp27 constructs, particularly Hsp27-3D, were more effective at binding and lateral association of apoC-II fibrils than WT αB-C and Hsp27-3DΔCTR. Both full-length Hsp27 constructs rapidly enhanced the turbidity of the α-syn fibril sample, whereas WT αB-C enhanced the turbidity of the fibril sample over a longer time frame. Additionally, both WT Hsp27 and Hsp27-3D increased the weight average sedimentation coefficient of apoC-II fibrils to a far greater extent than WT αB-C. Under the assumption that sHSPs interact reversibly with pre-formed fibrils, each cycle of fibril binding has the potential to bring two or more fibrils in close proximity. Therefore, the capacity of each sHSP construct to induce lateral fibril-fibril association could be dependent upon the rate at which they bind, dissociate from and re-associate with fibrils. The slower rate at which WT αB-C enhanced the turbidity of the α-syn fibrils, and the reduced extent to which it enhanced the size distribution of apoC-II fibrils is likely due to its substantially slower rate of fibril association relative to the Hsp27 constructs. Since Hsp27-3DΔCTR was also less effective than the full-length Hsp27 constructs at lateral association of apoC-II fibrils and increasing the light scattering of α-syn fibrils, we conclude that the CTR of Hsp27 is important for this component of the interaction between sHSPs and amyloid fibrils. Two distinct mechanisms may account for these observations (Fig. 3.8). It is possible that the two NTRs present on full-length sHSP dimers each interact simultaneously with two separate fibrils, resulting in the lateral association of these fibrils. In this model, the CTR may also be directly involved in binding to additional fibrils, and therefore when this domain is absent the fibril-binding affinity is reduced, reducing the extent to which the sHSPs can induce lateral association of the fibrils. An alternative explanation is that the CTR does not make direct contact with fibrils but instead engages another fibril-bound sHSP dimer via a CTR-ACD interaction (Fig. 3.8), indirectly resulting in lateral association of the bound fibrils. The CTR is important for the hierarchical assembly of sHSP oligomers via its docking interaction with the ACD of neighbouring subunits[287]. In this case, since Hsp27-3DΔCTR cannot form these CTR-mediated dimer-dimer interactions, it has a reduced ability to tangle the fibrils. The specificity of the interactions between the NTR and/or CTR and amyloid fibrils could be further investigated by performing the fibril binding and fibril association assays in the presence of the NTR and/or CTR in isolation of the ACD. To

further interrogate the specific interactions that contribute to fibril binding and lateral fibril association, the sequences in the NTR/CTR could be mutated, reversed or swapped between αB-C and Hsp27.

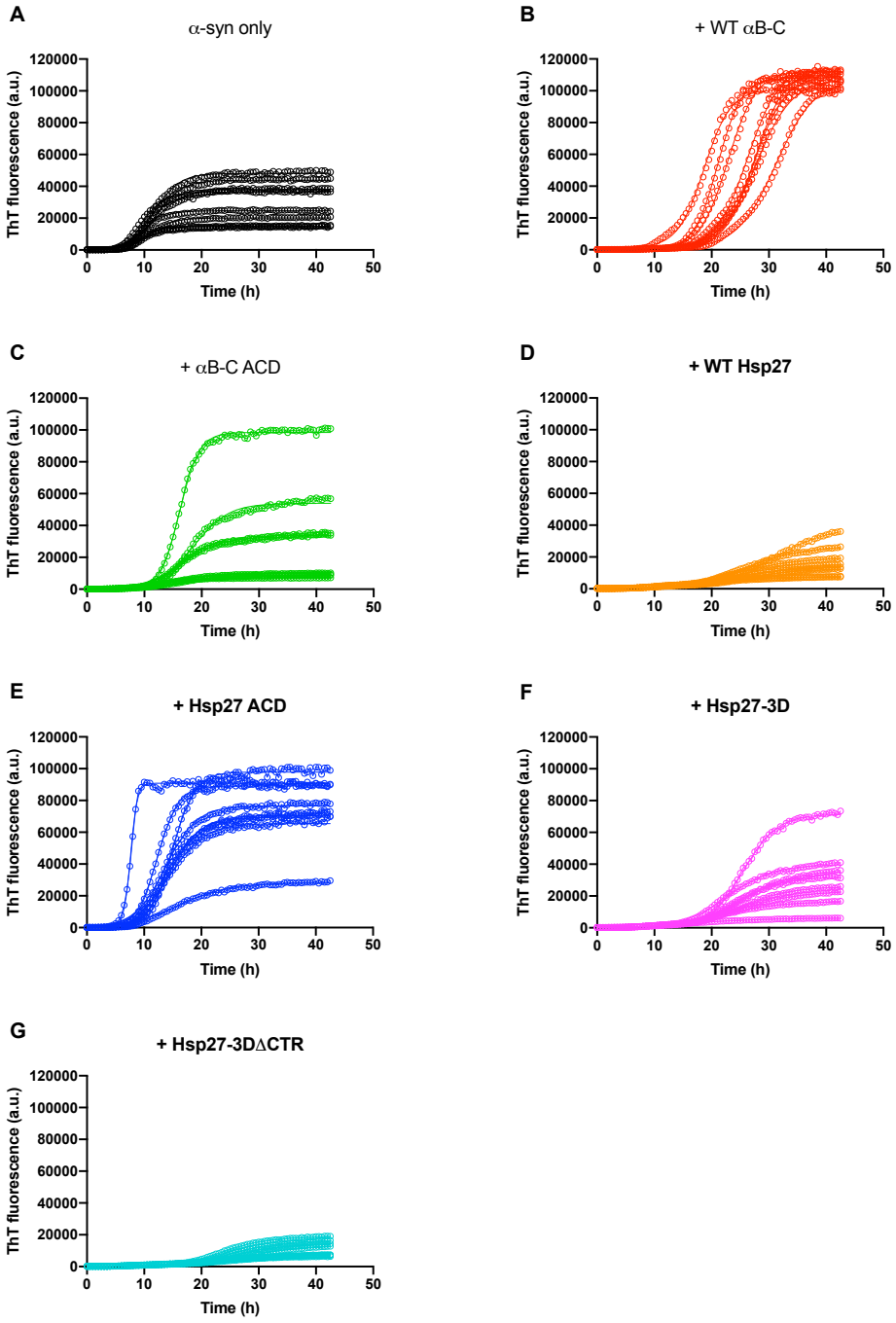
3.5 Conclusions

A variety of classes of HSPs have been shown to form stable associations with amyloid fibrils[262], suggesting that this phenomenon may play a cytoprotective role. The expression levels of sHSPs are increased in the mammalian brain during ageing[242], and sHSPs are known to associate with senile plaques and Lewy bodies[103–105]. These factors necessitate a detailed understanding of how sHSPs interact with amyloid fibrils and what the consequences of these interactions are *in vitro*. Using two distinct disease-associated proteins that form fibrils we observed that the ACDs of αB-C and Hsp27 were less effective at delaying amyloid fibril nucleation and elongation than full-length and NTR+ACD constructs. Only the full-length and NTR+ACD constructs were able to significantly delay amyloid fibril nucleation and disaggregate pre-formed apoC-II fibrils. Importantly, we show that sequences within the NTR of Hsp27 and the terminal regions of αB-C are required for the association of these sHSPs with pre-formed amyloid fibrils, and their ability to induce disaggregation. The CTR of Hsp27 appears to play an important role in mediating the association of fibrils into larger aggregates. There is growing evidence that the sequestration of small protein aggregates into much larger aggregates, called aggresomes, is cytoprotective[263]. The formation of an aggresome limits the cytotoxicity of aggregates spatially, while also reducing their reactive surface area. There is also evidence that aggresome formation can enable asymmetric inheritance of protein aggregates in dividing cells[263]. Our work demonstrates that the terminal regions of sHSPs are important for this potentially cytoprotective role *in vivo*.

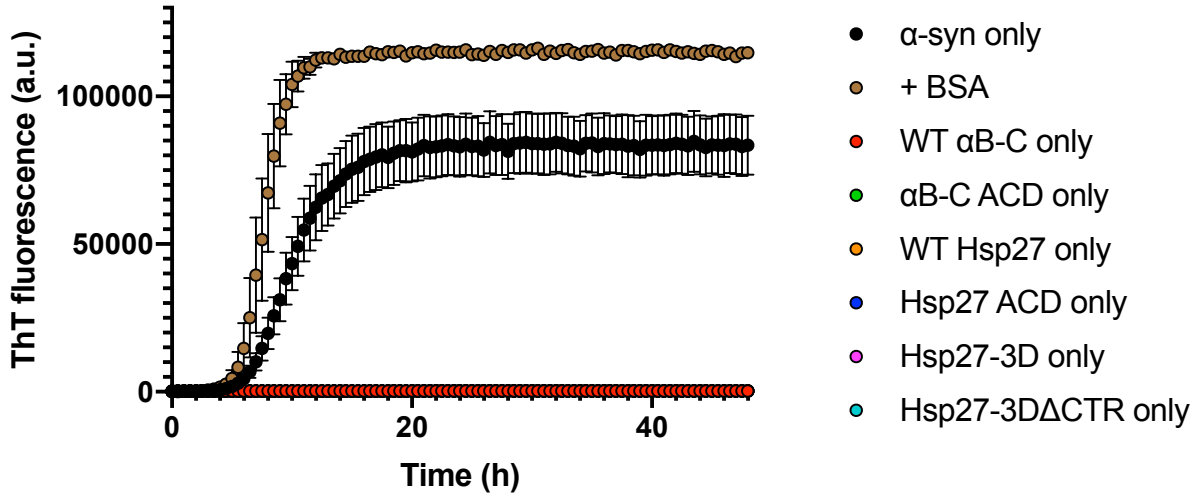
Overall, the results of this study show that sHSPs interact with various species formed during the aggregation of a protein into amyloid fibrils and that they do so via multiple distinct binding sites involving the N- and C-terminal regions, as well as the ACD. Thus, the ACD alone is not sufficient for all of the chaperone activities exhibited by the full-length protein. This work expands our understanding of the roles of the N- and C-terminal regions of human sHSPs in interacting with proteins that form amyloid. This increased understanding of the mechanisms and consequences of sHSP interactions with

amyloid fibrils has important implications in the pathogenesis and progression of diseases associated with amyloid deposition.

3.6 Supplementary information



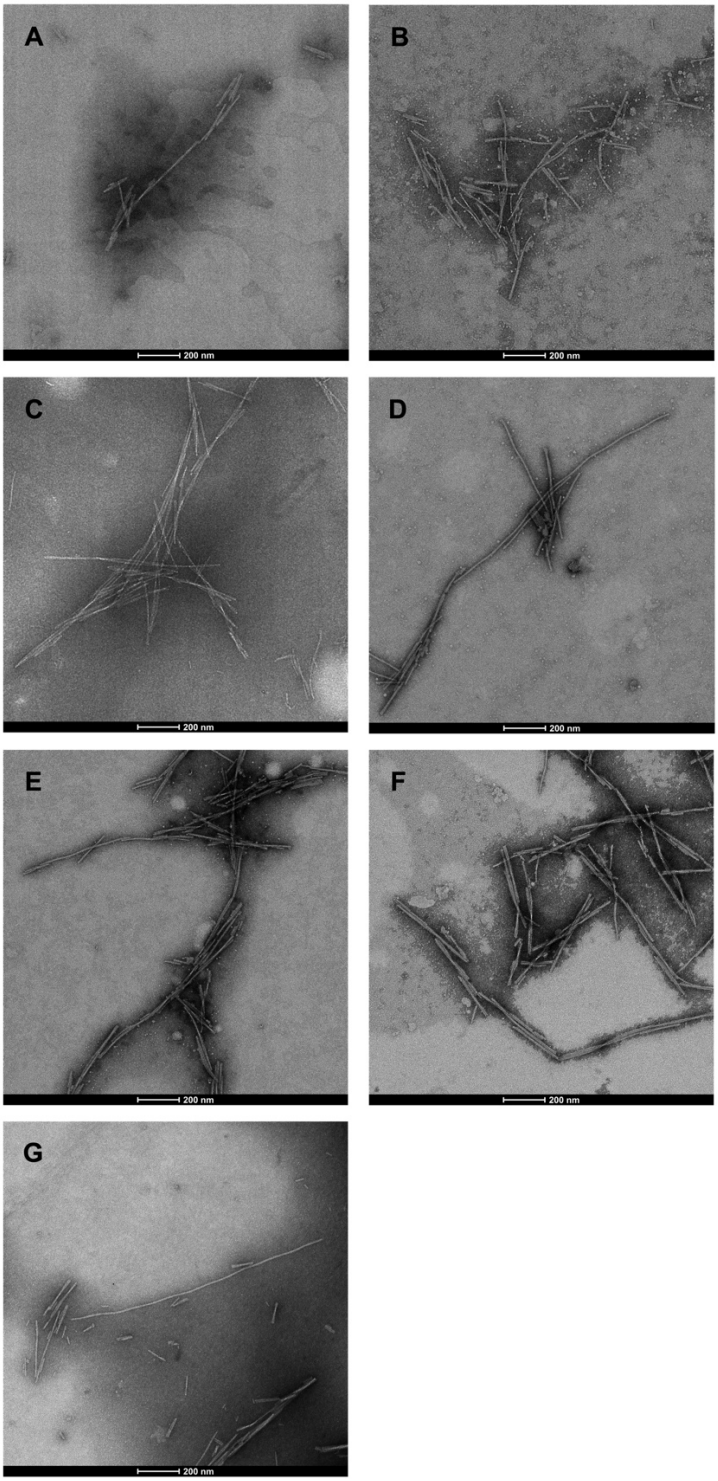
Supplementary Figure 3.1. Raw ThT kinetics data (n = 8) of unseeded α-syn alone (200 μM) (A) or with WT αB-C (B), αB-C ACD (C), WT Hsp27 (D), Hsp27 ACD (E), Hsp27-3D (F) or Hsp27-3DΔCTR (G). sHSP concentration was 10 μM. Fits to the raw data were obtained using a 4-parameter sigmoid Boltzmann curve using GraphPad in prism version 8.



Supplementary Figure 3.2. ThT assay of α-syn incubated at 200 µM alone (black), + 10 µM BSA (brown) and 10 µM of each sHSP construct incubated alone at 37°C with 700 rpm shaking as indicated. Data are presented as mean ± SEM, where n = 8.

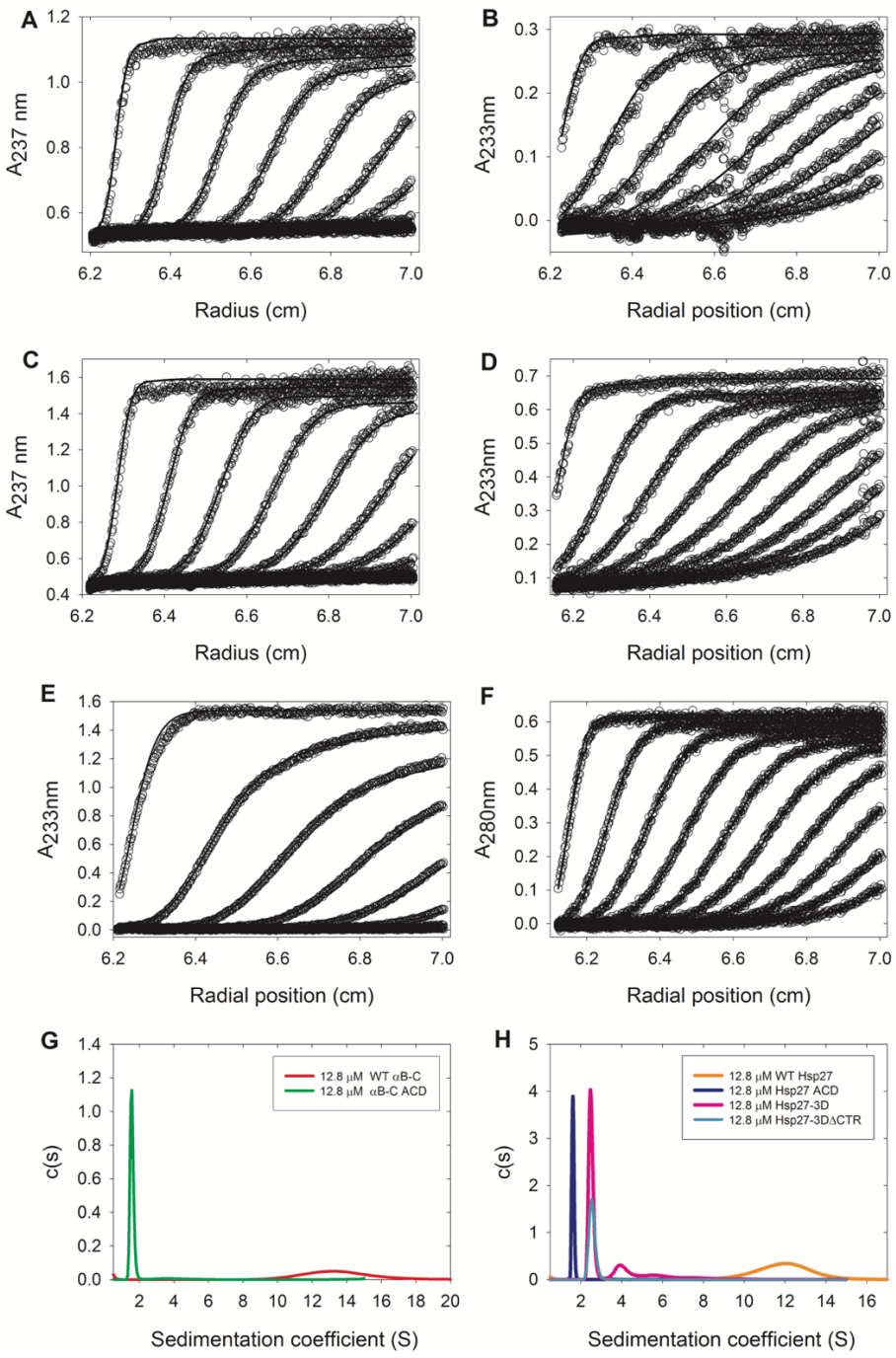
Supplementary Table 3.1 One-way ANOVA test results of T_{lag} and T_{50} parameters derived from results of unseeded α-syn amyloid formation kinetics in the presence or absence of the various sHSP constructs.

	T_{lag}			T_{50}		
Tukey's multiple comparisons test	Mean difference (h)	Significance summary	Adjusted P Value	Mean difference (h)	Significance summary	Adjusted P Value
α-syn only vs. + WT αB-C	-13.64	****	<0.0001	-14.67	****	<0.0001
α-syn only vs. + αB-C ACD	-3.163	ns	0.4776	-5.385	**	0.0086
α-syn only vs. + WT Hsp27	-6.883	**	0.0022	-13.69	****	<0.0001
α-syn only vs. + Hsp27 ACD	-2.025	ns	0.8792	-2.803	ns	0.4663
α-syn only vs. + Hsp27-3D	-8.316	***	0.0001	-12.78	****	<0.0001
α-syn only vs. + Hsp27-3DΔCTR	-7.411	***	0.0008	-13.73	****	<0.0001
+ WT αB-C vs. + αB-C ACD	10.47	****	<0.0001	9.285	****	<0.0001
+ WT αB-C vs. + WT Hsp27	6.754	**	0.0028	0.9763	ns	0.9934
+ WT αB-C vs. + Hsp27 ACD	11.61	****	<0.0001	11.87	****	<0.0001
+ WT αB-C vs. + Hsp27-3D	5.322	*	0.0336	1.886	ns	0.8469
+ WT αB-C vs. + Hsp27-3DΔCTR	6.227	**	0.0073	0.935	ns	0.9948
+ αB-C ACD vs. + WT Hsp27	-3.721	ns	0.2848	-8.309	****	<0.0001
+ αB-C ACD vs. + Hsp27 ACD	1.137	ns	0.9926	2.581	ns	0.5646
+ αB-C ACD vs. + Hsp27-3D	-5.153	*	0.0437	-7.399	***	0.0001
+ αB-C ACD vs. + Hsp27-3DΔCTR	-4.248	ns	0.1552	-8.35	****	<0.0001
+ WT Hsp27 vs. + Hsp27 ACD	4.858	ns	0.0679	10.89	****	<0.0001
+ WT Hsp27 vs. + Hsp27-3D	-1.433	ns	0.9754	0.91	ns	0.9955
+ WT Hsp27 vs. + Hsp27-3DΔCTR	-0.5272	ns	>0.9999	-0.04125	ns	>0.9999
+ Hsp27 ACD vs. + Hsp27-3D	-6.291	**	0.0065	-9.98	****	<0.0001
+ Hsp27 ACD vs. + Hsp27-3DΔCTR	-5.385	*	0.0304	-10.93	****	<0.0001
+ Hsp27-3D vs. + Hsp27-3DΔCTR	0.9054	ns	0.9979	-0.9512	ns	0.9943



Supplementary Figure 3.3. Transmission electron microscopy of unseeded α-syn fibrils formed at 200 μM alone (A) or in the presence of 10 μM of WT αB-C (B), αB-C ACD (C), WT Hsp27 (D), Hsp27 ACD (E), Hsp27-3D (F) or Hsp27-3DΔCTR (G) for 48 hours at 37°C with constant agitation as described in the methods section. The fibrils were diluted by a factor of 10 with

dH_2O and applied to carbon coated Formvar 300 mesh copper grids and visualised using a Talos L120C TEM. The scale bars represent 200 nm.



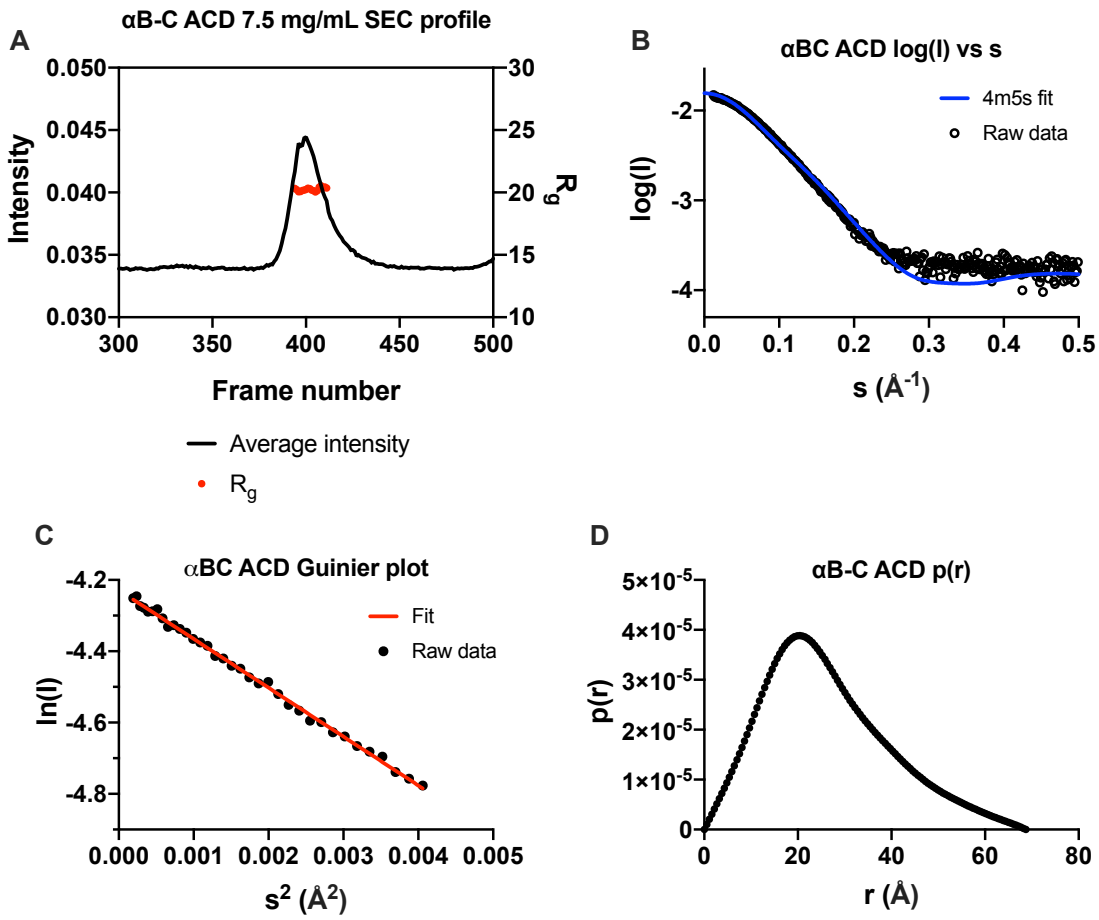
Supplementary Figure 3.4. SV-AUC analysis of sHSP constructs. Raw SV-AUC data (circles) and fits obtained (lines) of WT αB-C (A) obtained at a rotor speed of 40000 rpm, αB-C ACD (B) obtained at a rotor speed of 50000 rpm, WT Hsp27 (C) obtained at a rotor speed of 40000 rpm and Hsp27 ACD (D) Hsp27-3D (E) and Hsp27-3DΔCTR (F) obtained at a rotor speed of 50000 rpm. sHSP concentrations were 12.8 μM. G-H) The resulting size distributions obtained from fits to the raw data αB-C constructs (G) and Hsp27 constructs (H).

Supplementary Table 3.2 Weight-average sedimentation coefficients of sHSP constructs

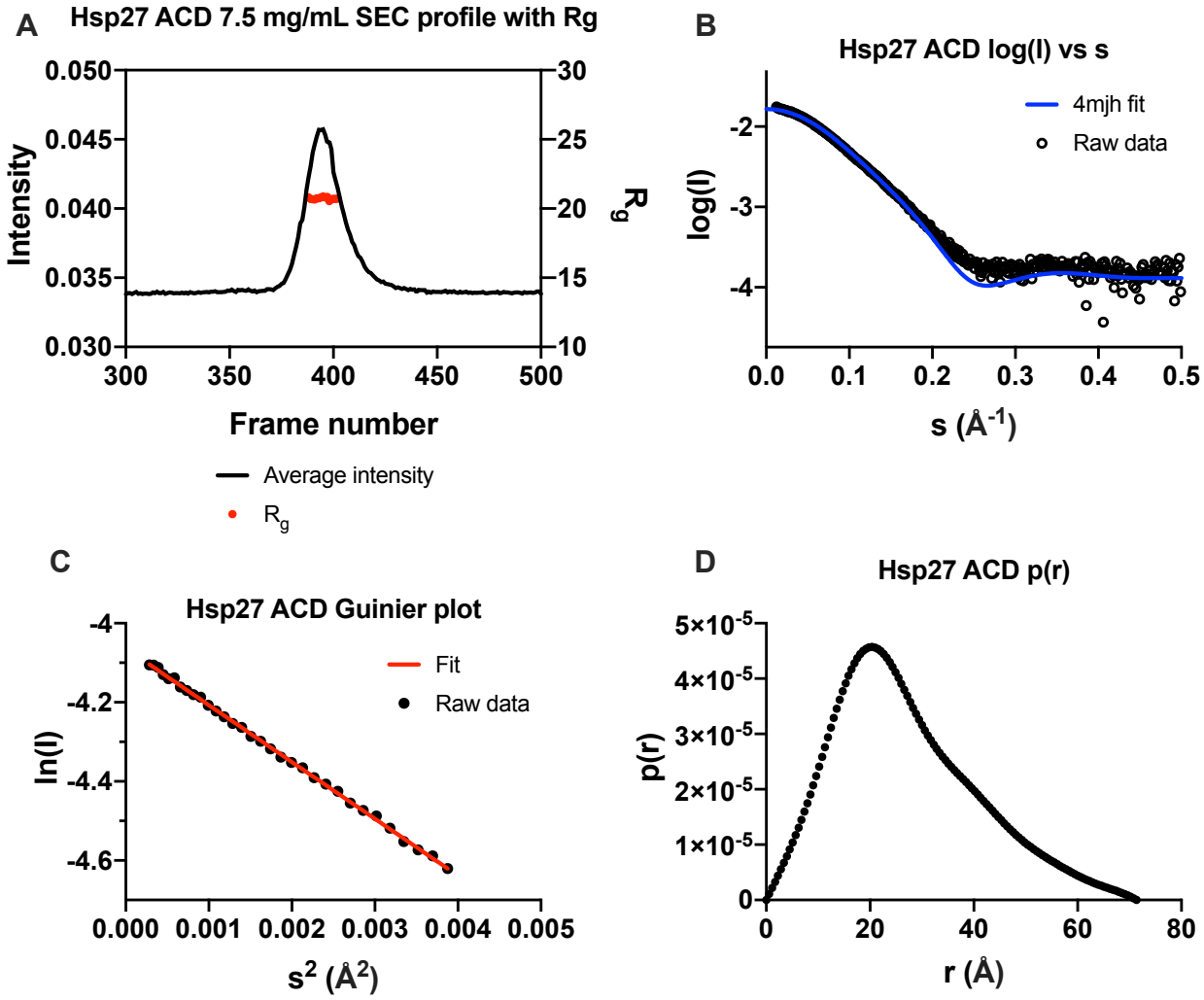
	Weight-average sedimentation coefficient (S)	Loading concentration (AU)
WT αB-C	12.76*	0.59
αB-C ACD	2.07**	0.30
WT Hsp27	11.95*	1.12
Hsp27 ACD	2.31**	0.58
Hsp27-3D	3.65**	1.56
Hsp27-3DΔCTR	2.58**	0.62

* Integral range 4-24 S

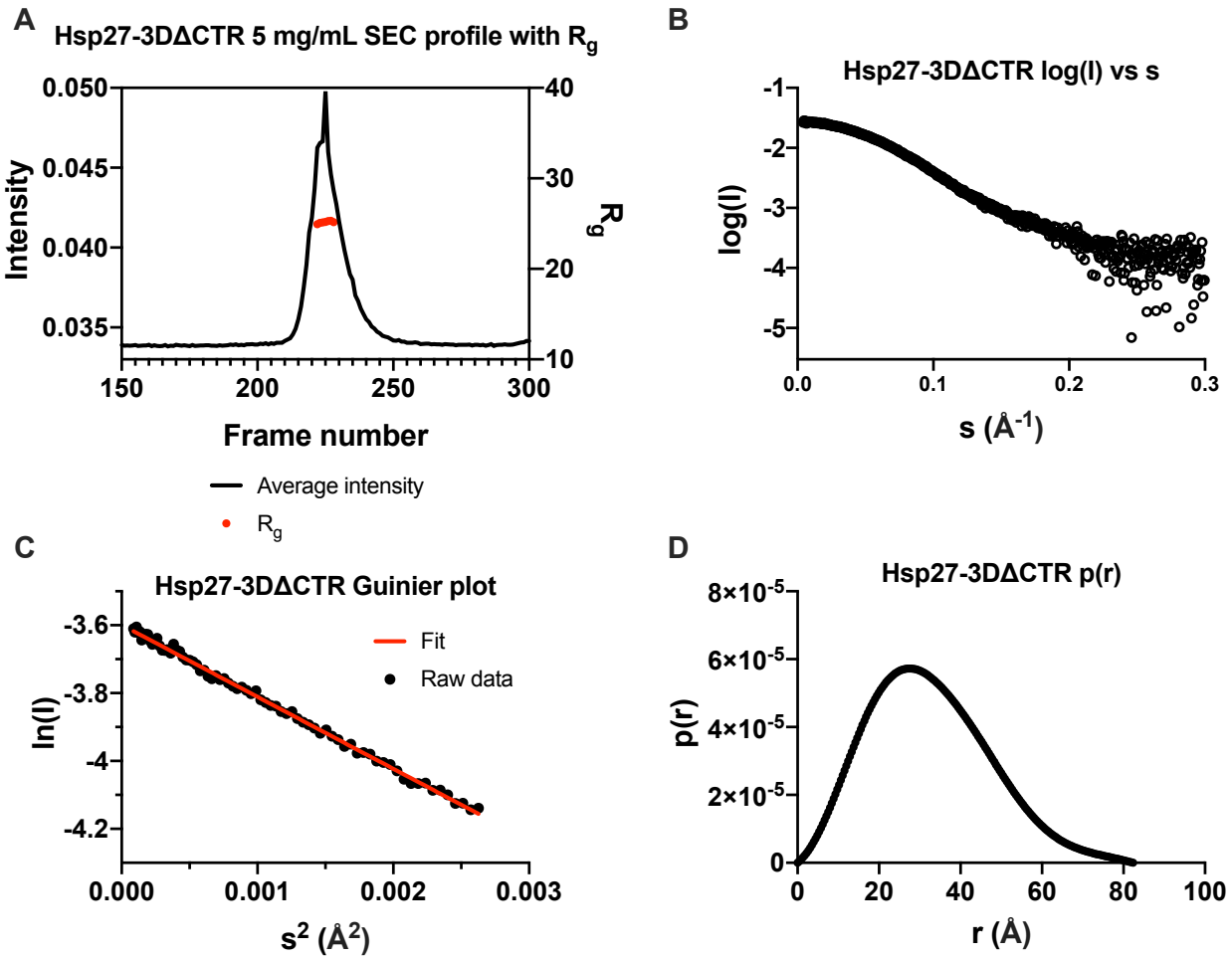
** Integral range 0.5-15 S



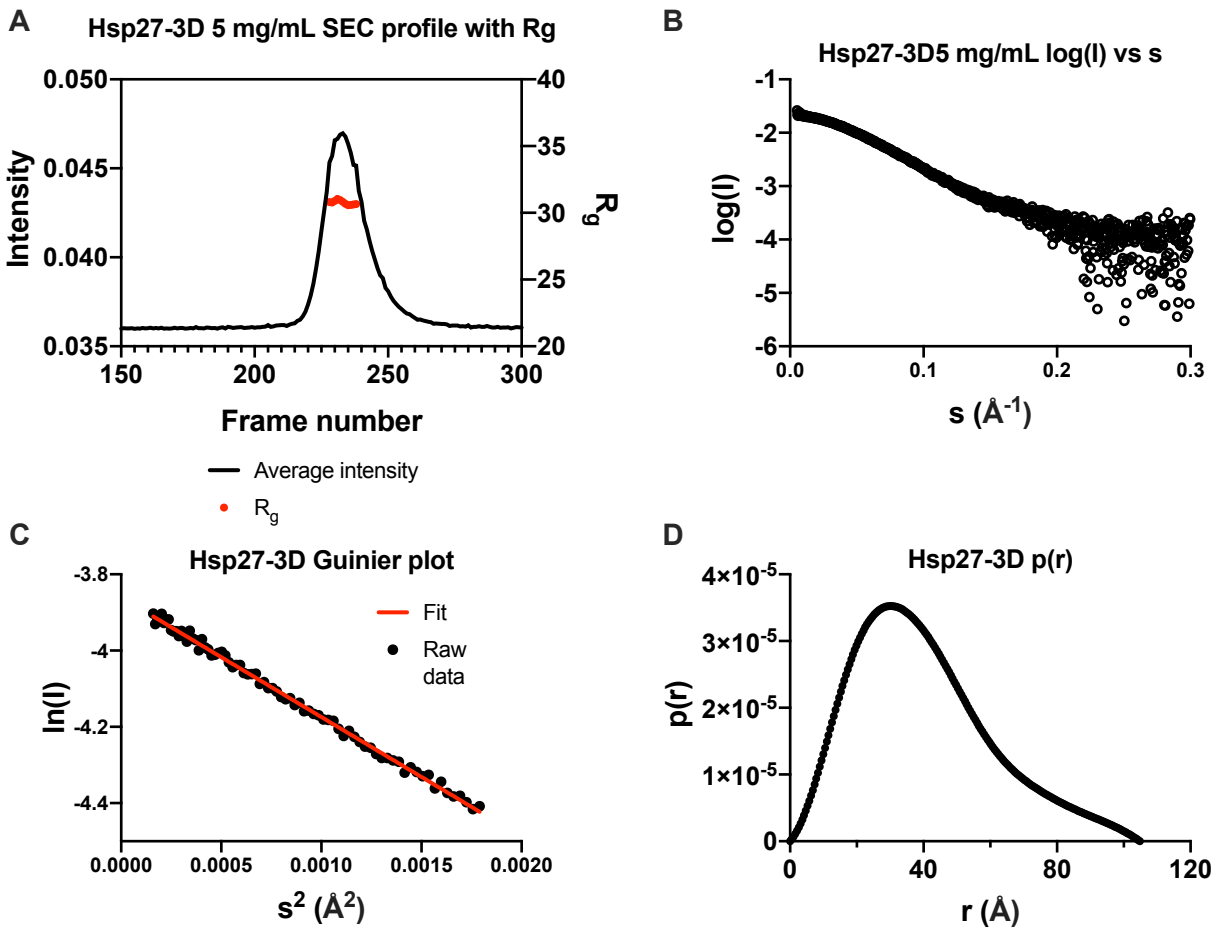
Supplementary Figure 3.5. SAXS analysis of αB-C ACD at a concentration of 755 μM, pH 8.0. 50 μL of αB-C ACD at 7.5 mg/mL (755 μM) was injected onto a Superdex 200 increase 5/150 size exclusion column and eluted at 0.45 mL/min A) UV absorbance at 280 nm (black line, left y-axis) as a function of the frame number following sample loading onto the column. The R_g (red circles, right y-axis) was calculated across the peak using chromixs in the ATSAS software. B) Radially averaged and buffer subtracted scattering intensity expressed as log(I) for αB-C ACD as a function of the scattering angle (s) (black circles). The theoretical scattering profile for the crystal structure of αB-C ACD (PDB: 4m5s) generated using CRYSOL is shown as a blue line for comparison. C) Guinier plot of αB-C ACD generated using primus in the ATSAS software package (raw data shown as black circles, and the linear fit to this data depicted as a red line). D) p(r) function of αB-C ACD generated using primus in the ATSAS software package.



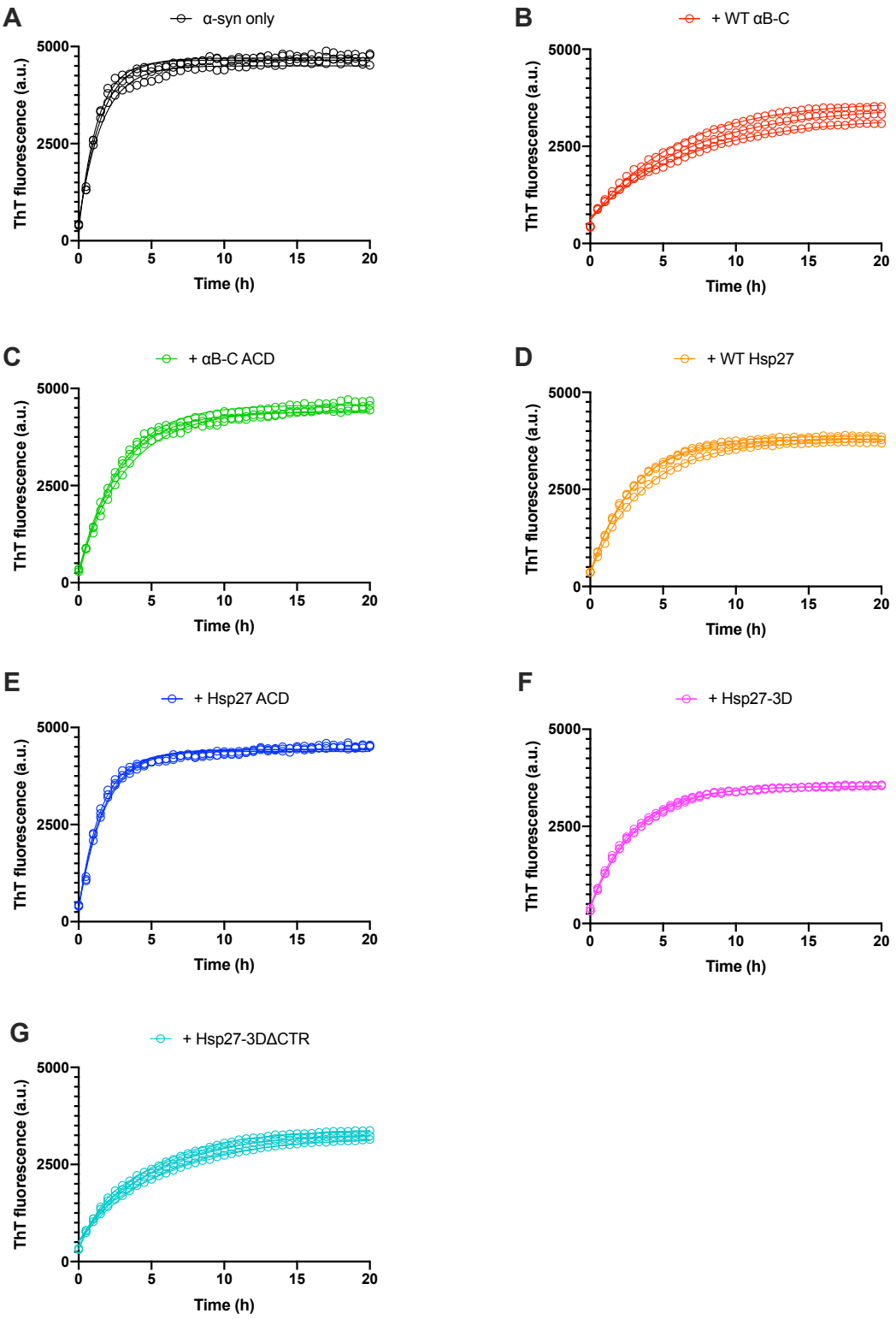
Supplementary Figure 3.6. SAXS analysis of Hsp27 ACD at a concentration of 7.5 mg/mL (726 μM), pH 8.0. 50 μL of Hsp27 ACD at 7.5 mg/mL was injected onto a Superdex 200 increase 5/150 size exclusion column and eluted at 0.45 mL/min A) UV absorbance at 280 nm (black line, left y-axis) as a function of the frame number following sample loading onto the column. The R_g (red circles, right y-axis) was calculated across the peak using chromixs in the ATSAS software. B) Radially averaged and buffer subtracted scattering intensity expressed as log(I) for Hsp27 ACD as a function of the scattering angle (s) (black circles). The theoretical scattering profile for the crystal structure of Hsp27 ACD (PDB: 4mjh) generated using CRYSOL is shown as a blue line for comparison. C) Guinier plot of Hsp27 ACD generated using primus in the ATSAS software package (raw data shown as black circles, and the linear fit to this data depicted as a red line). D) p(r) function of Hsp27 ACD generated using primus in the ATSAS software package.



Supplementary Figure 3.7. SAXS of Hsp27-3DΔCTR at a concentration of 5 mg/mL (253 μM), pH 8.0. 50 μL of Hsp27-3DΔCTR at 5 mg/mL was injected onto a Superdex 200 increase 5/150 size exclusion column and eluted at 0.45 mL/min A) UV absorbance at 280 nm (black line, left y-axis) as a function of the frame number following sample loading onto the column. The R_g (red circles, right y-axis) was calculated across the peak using chromixs in the ATSAS software. B) Radially averaged and buffer subtracted scattering intensity expressed as log(I) for Hsp27-3DΔCTR as a function of the scattering angle (s) (black circles). C) Guinier plot of Hsp27 ACD generated using primus in the ATSAS software package (raw data shown as black circles, and the linear fit to this data depicted as a red line). D) p(r) function of Hsp27-3DΔCTR generated using primus in the ATSAS software package.

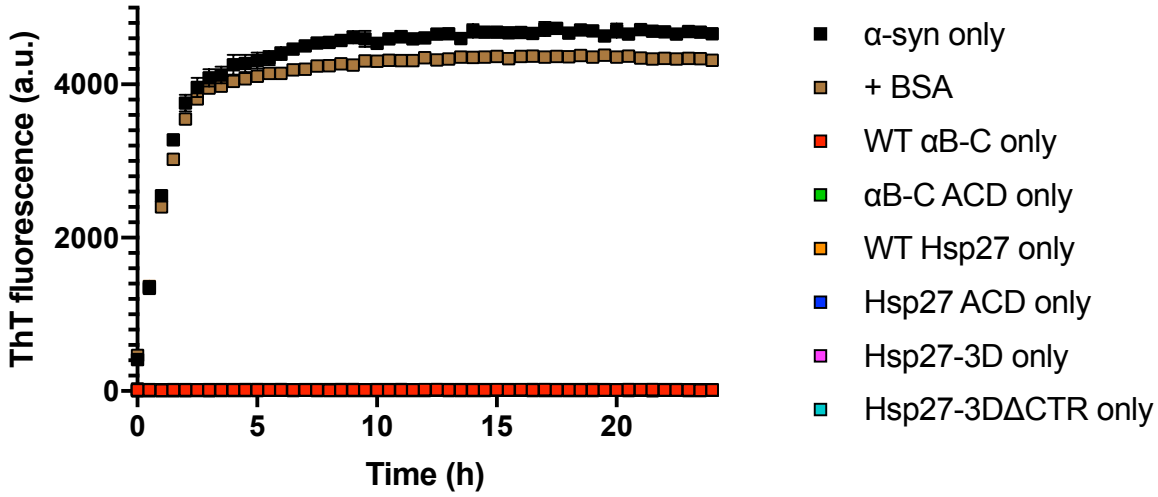


Supplementary Figure 3.8. SAXS of Hsp27-3D at a concentration of 5 mg/mL (220 µM), pH 8.0. 50 µL of Hsp27-3D at 5 mg/mL was injected onto a Superdex 200 increase 5/150 size exclusion column and eluted at 0.45 mL/min A) UV absorbance at 280 nm (black line, left y-axis) as a function of the frame number following sample loading onto the column. The R_g (red circles, right y-axis) was calculated across the peak using chromixs in the ATSAS software. B) Radially averaged and buffer subtracted scattering intensity expressed as log(I) for Hsp27-3D as a function of the scattering angle (s) (black circles). C) Guinier plot of Hsp27-3D generated using primus in the ATSAS software package (raw data shown as black circles, and the linear fit to this data depicted as a red line). D) p(r) function of Hsp27-3D generated using primus in the ATSAS software package.

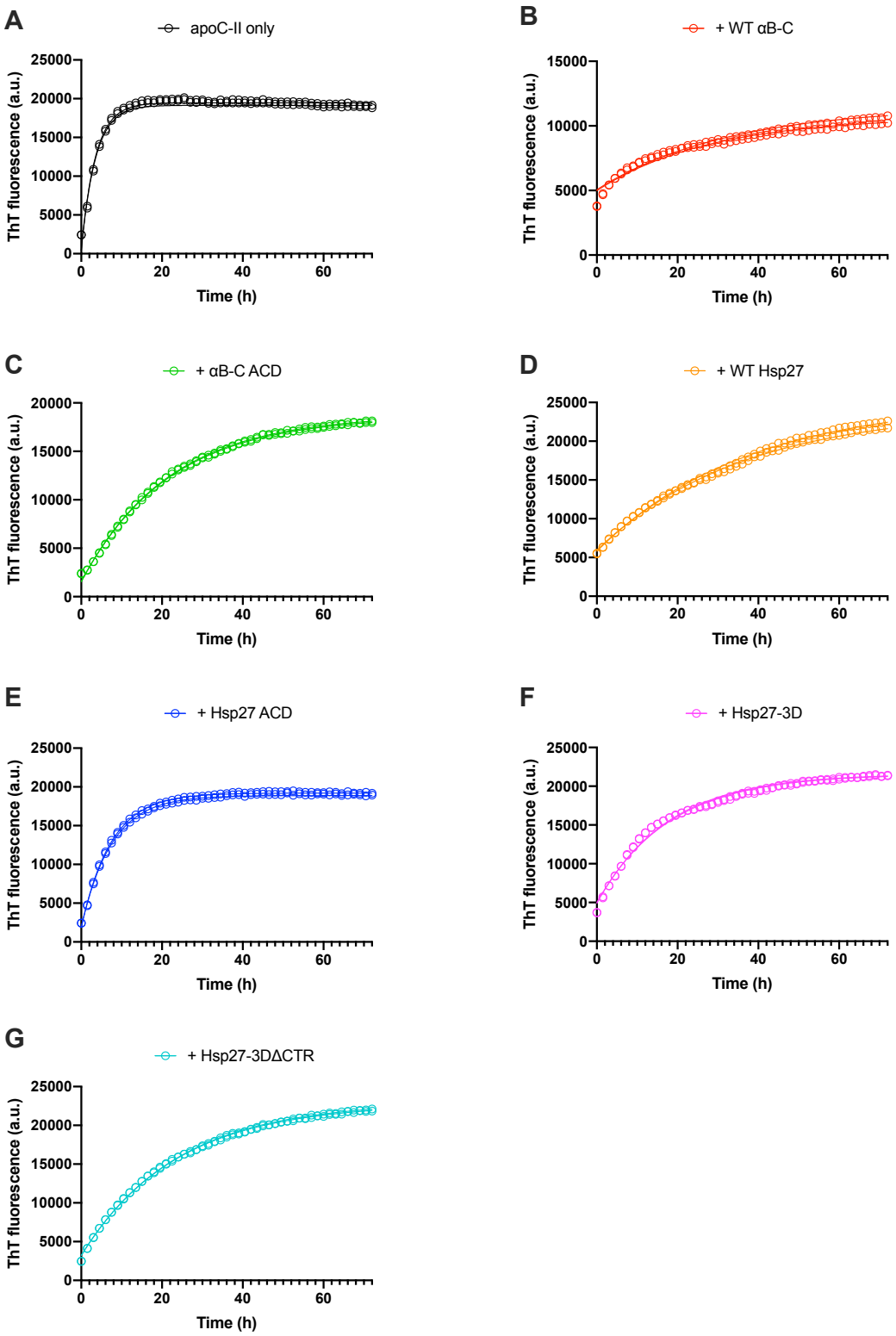


Supplementary Figure 3.9. Raw ThT kinetics data (n = 3, circles) and derived fits (lines) of (A) seeded α-syn alone (200 μM with 5% total seed concentration) or with WT αB-C (B) , αB-C ACD (C), WT Hsp27 (D), Hsp27 ACD (E), Hsp27-3D (F) or Hsp27-

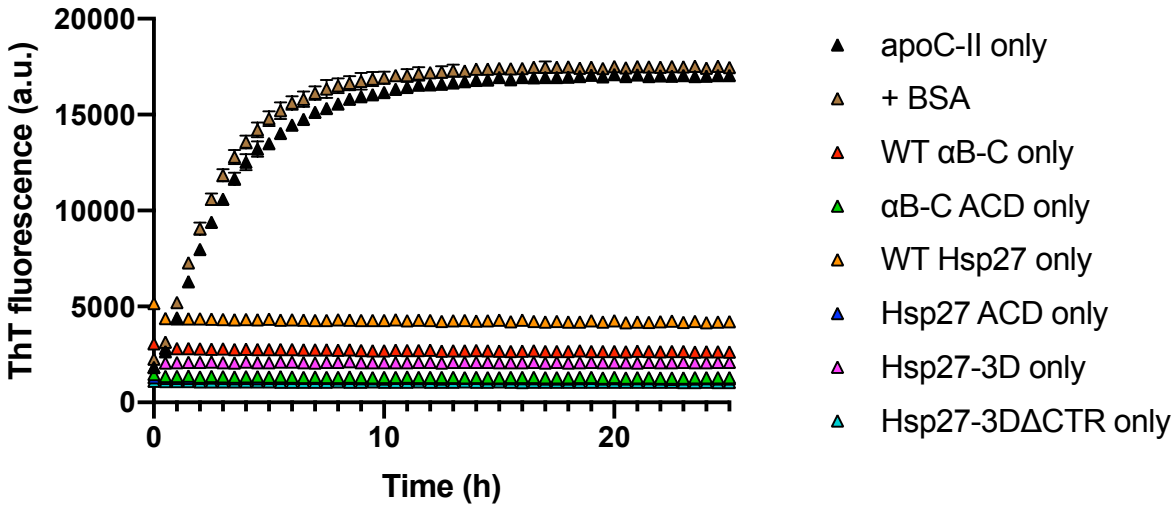
3DΔCTR (G). sHSP concentration was 50 μM. Fits were derived using a one-phase association model in GraphPad in Prism version 8.



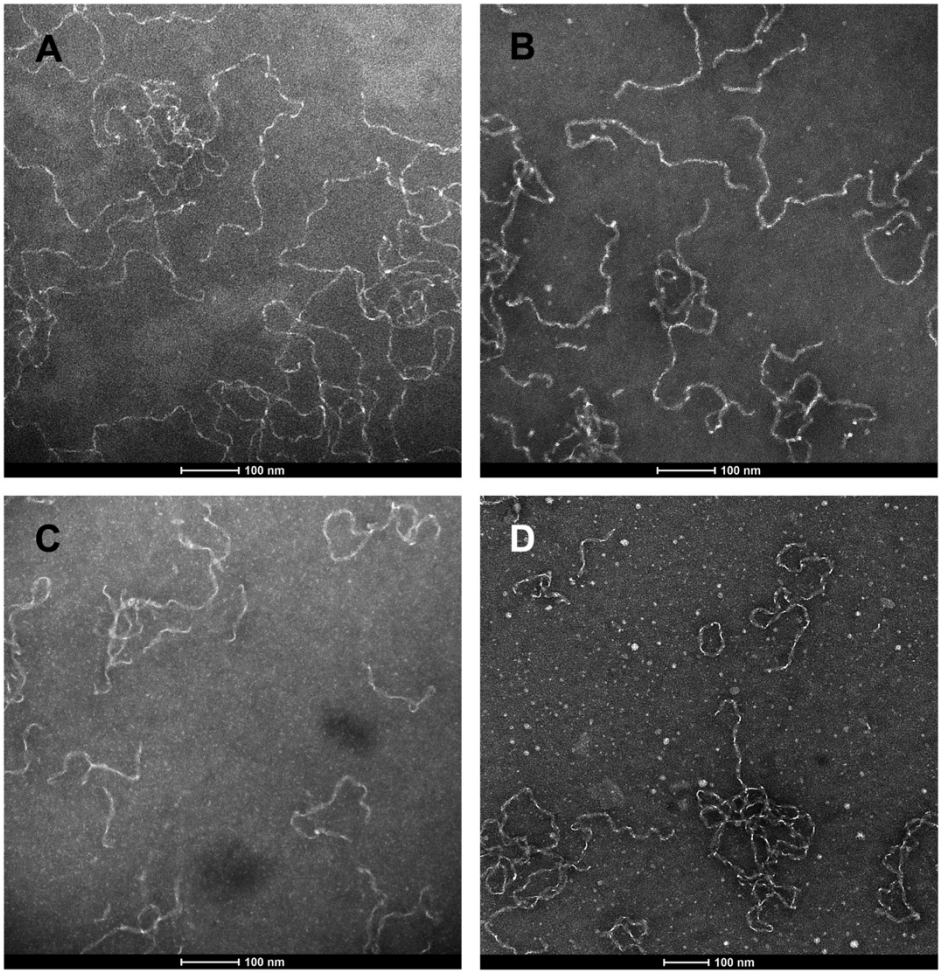
Supplementary Figure 3.10. ThT assay of 200 µM α-syn with 5% (of total α-syn concentration) seeds incubated alone (black), + 50 µM BSA (brown) and 50 µM of each sHSP incubated alone at 45°C without shaking as indicated. Data are presented as mean ± SEM, where n = 3.



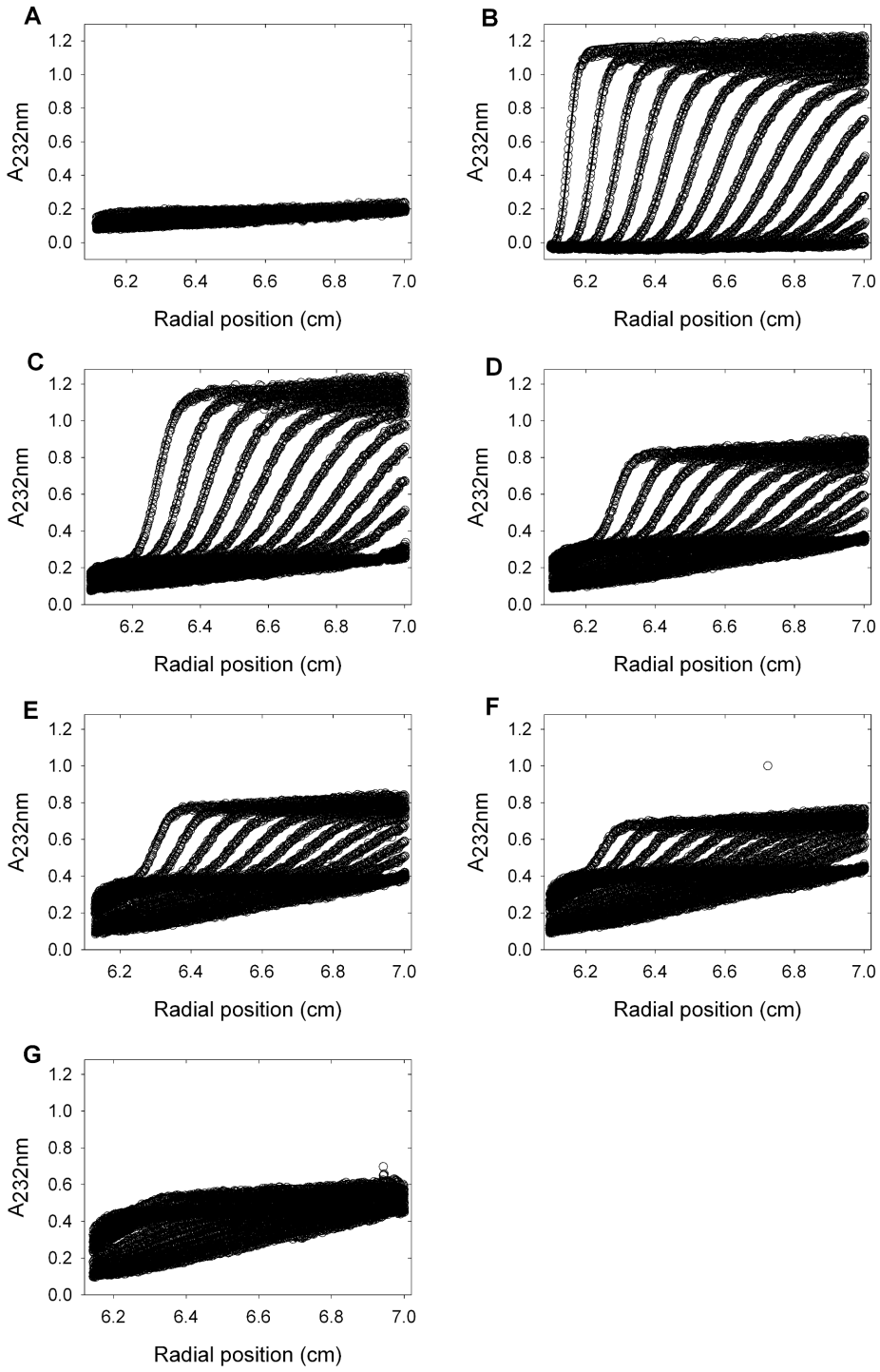
Supplementary Figure 3.11. Raw ThT kinetics data (n = 2, circles) and derived fits (lines) of (A) unseeded apoC-II alone (56 μM) or with WT αB-C (B) , αB-C ACD (C), WT Hsp27 (D), Hsp27 ACD (E), Hsp27-3D (F) or Hsp27-3DΔCTR (G). sHSP concentration was 12.8 μM. Fits were derived using a one-phase association model in GraphPad in Prism version 8.



Supplementary Figure 3.12. ThT assay of apoC-II incubated at 56 µM alone (black), + 12.8 µM BSA (brown) and 12.8 µM of each sHSP construct incubated alone at 30°C as indicated. Data are presented as mean ± SEM, where n = 2.

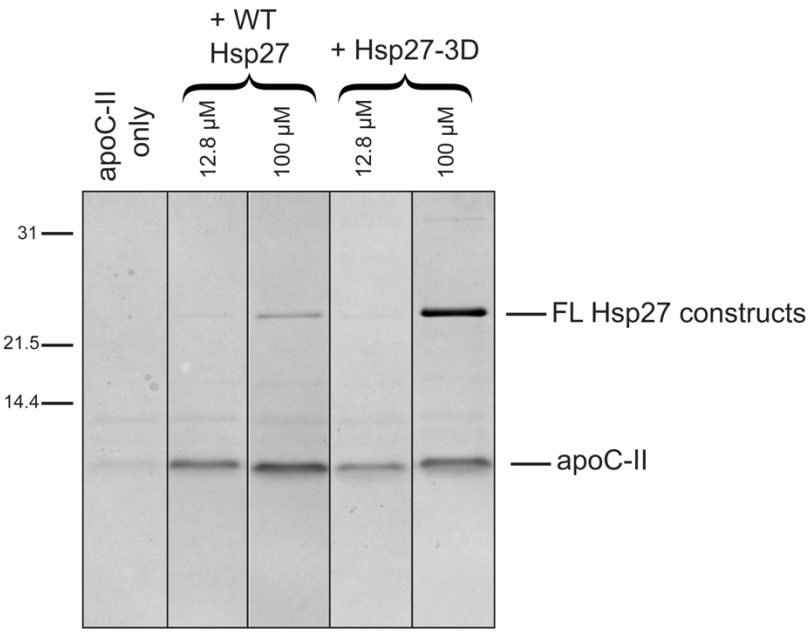


Supplementary Figure 3.13. Transmission electron microscopy of unseeded apoC-II fibrils formed at 56 μM alone (A) or in the presence of 12.8 μM of WT αB-C (B), αB-C ACD (C) or Hsp27-3D (D) for 168 hours at 30°C without agitation as described in the methods section. The fibrils were diluted by a factor of 4 with dH_2O and applied to carbon coated Formvar 300 mesh copper grids and visualised using a Talos L120C TEM. The scale bars represent 100 nm.

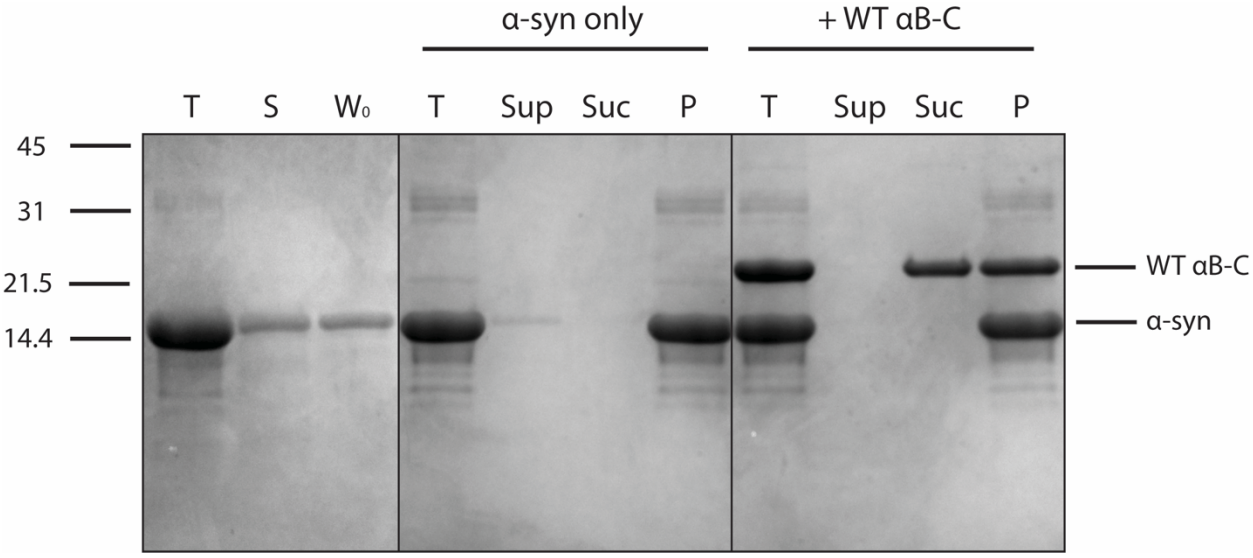


Supplementary Figure 3.14. Raw SV-AUC data (circles) and fits (lines) obtained using a c(s) distribution with regularization by maximum entropy of pre-formed apoC-II fibrils (56 µM) incubated with WT αB-C (12.8 µM) for 0-20 hours. A rotor speed of 40000 rpm was used. A) ApoC-II preformed fibrils incubated alone. B) WT αB-C incubated alone. Pre-formed apoC-II fibrils incubated with WT αB-C for 0 hours (C), 2 hours (D), 4 hours (E), 8 hours (F) or 20 hours (G). For clarity, in panel (A) every tenth scan is shown (corresponding to a time interval of 1 hour and 13 minutes) and in panel (B) all of the first 16 scans are

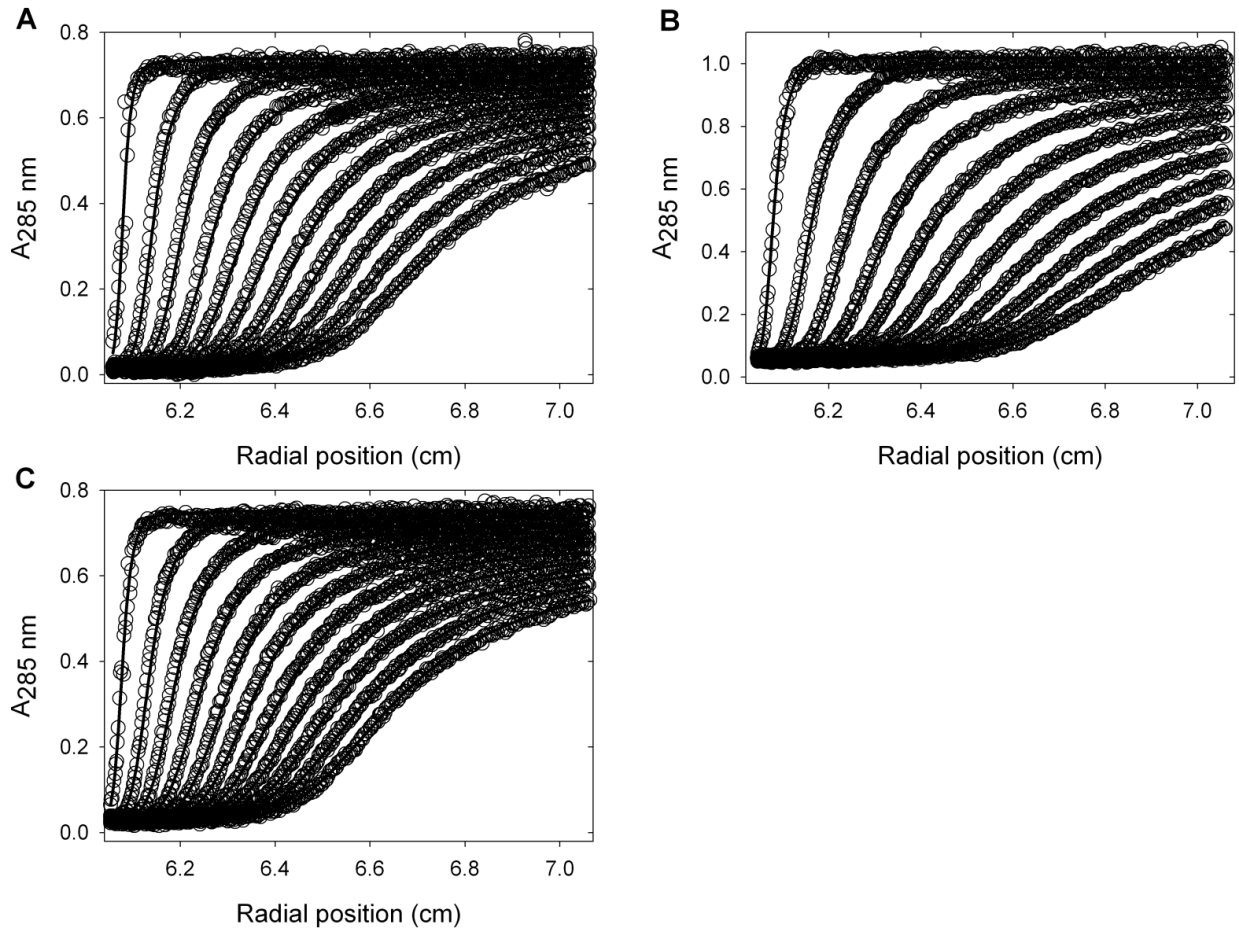
shown (corresponding to a time interval of 8 minutes). For clarity in panels (C-G), the first 11 scans are shown and subsequently every tenth scan is shown.



Supplementary Figure 3.15. SDS-PAGE analysis of the supernatant fractions obtained from a pelleting assay of pre-formed apoC-II fibrils (56 µM) incubated for 72 hours at 30 °C alone or with 12.8 µM or 100 µM WT Hsp27 or Hsp27-3D as indicated.



Supplementary Figure 3.16. α-Syn fibrils were formed at 200 μM for 48 hours, 37°C with constant agitation at 700 rpm. These fibrils were then pelleted at 18,000 x g for 10 mins at room temperature. The supernatant (S) was collected and the pelleted was resuspended in an equal volume. The fibrils were then pelleted again under identical conditions and the wash (W_0) was collected. The remaining fibrils were separated into two tubes and WT αB-C was added to a final concentration of 50 μM to one of the tubes and an equal volume of buffer to the other. The fibrils were then incubated at 37°C for 24 hours and then pelleted through a 20% (w/v) sucrose layer as described in the methods section. The supernatant (Sup), sucrose (Suc), and pellet (P) layers were then analysed by SDS-PAGE alongside a fraction obtained prior to centrifugation (T). The position of molecular weight markers are indicated on the left with units of kDa and the position of α-syn and WT αB-C are indicated on the right.

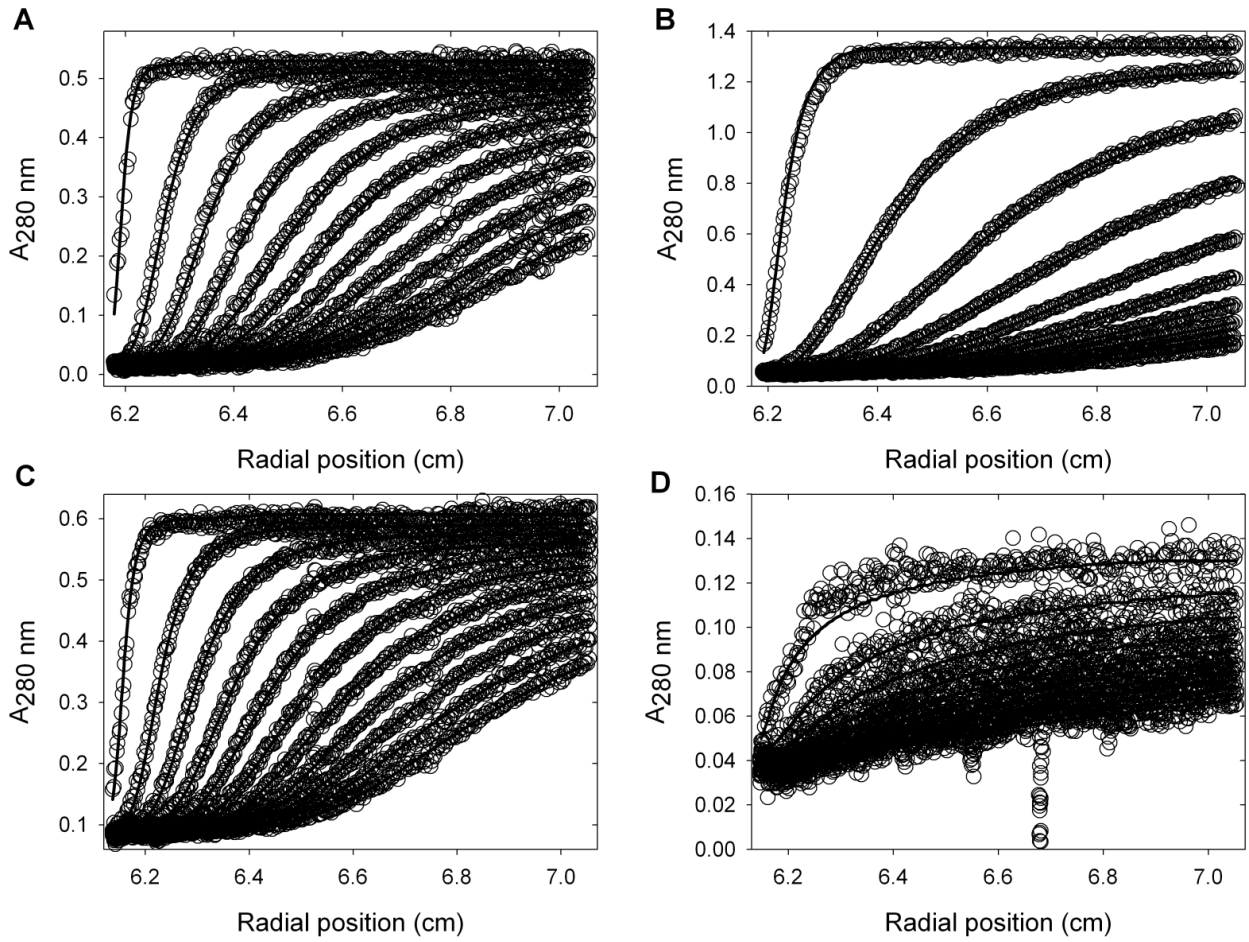


Supplementary Figure 3.17. Raw SV-AUC data (circles) and fits (lines) obtained using a c(s) distribution with a worm-like chain model with Tikhonov-Phillips regularization by second derivative of pre-formed apoC-II fibrils (56 µM) incubated with 12.8 µM WT αB-C or αB-C ACD for 72 hours. A rotor speed of 8000 rpm was used. Pre-formed apoC-II fibrils incubated alone (A), with 12.8 µM WT αB-C (B) or with 12.8 µM αB-C ACD (C). For clarity, every tenth scan is shown in (A-C), corresponding to a time interval of 49 minutes.

Supplementary Table 3.3 Weight-average fibril sedimentation coefficients of pre-formed apoC-II fibrils incubated with αB-C constructs.

	Weight-average sedimentation coefficient (S)*	Loading concentration (AU)
56 μM apoC-II only	141.0	0.74
+ 12.8 μM WT αB-C	188.3	0.98
+ 12.8 μM αB-C_{CD}	129.7	0.73

* Weight average sedimentation coefficient over integral range 20-700 S

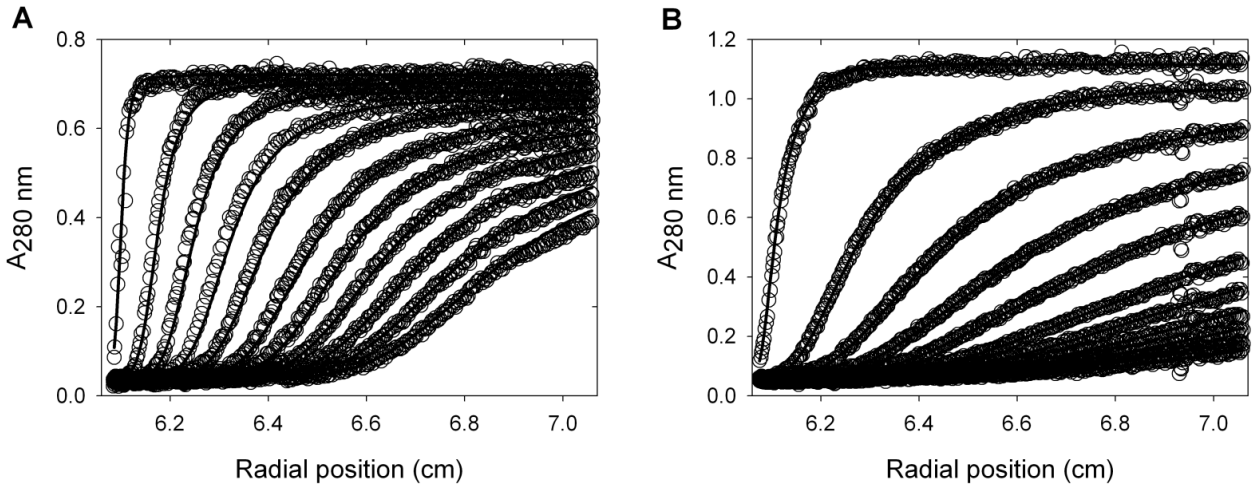


Supplementary Figure 3.18. Raw SV-AUC data (circles) and fits (lines) obtained using a c(s) distribution with a worm-like chain model with Tikhonov-Phillips regularization by second derivative of pre-formed apoC-II fibrils (56 µM) incubated with 12.8 µM Hsp27 constructs for 72 hours. A rotor speed of 8000 rpm was used. Pre-formed apoC-II fibrils incubated alone (A), with 12.8 µM WT Hsp27 (B), with 12.8 µM Hsp27 ACD (C) or with 12.8 µM Hsp27-3D (D). For clarity, every seventh scan is shown in (A-D), corresponding to a time interval of 31 minutes.

Supplementary Table 3.4 Weight-average fibril sedimentation coefficients of pre-formed apoC-II fibrils incubated with Hsp27 constructs.

	Weight average sedimentation coefficient (S)*	Loading concentration (AU)
56 µM apoC-II only	154.5	0.52
+ 12.8 µM WT Hsp27	381.8	1.31
+ 12.8 µM $Hsp27_{CD}$	146.6	0.53
+ 12.8 µM Hsp27-3D	379.5	0.10

*Integral range 1-1000 S



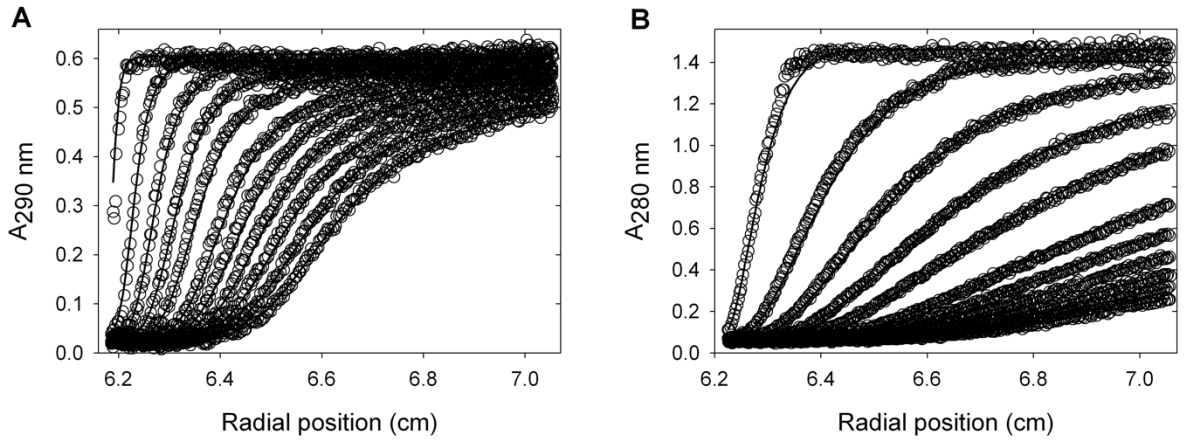
Supplementary Figure 3.19. Raw SV-AUC data (circles) and fits (lines) obtained a c(s) distribution with a worm-like chain model with Tikhonov-Phillips regularization by second derivative of pre-formed apoC-II fibrils (56 µM) incubated alone (A) or with 6.4 µM Hsp27-3D (B) for 72 hours. A rotor speed of 8000 rpm was used. For clarity, every seventh scan is shown in (A-B), corresponding to a time interval of 32 minutes.

Supplementary Table 3.5 Weight-average fibril sedimentation coefficients of pre-formed apoC-II fibrils incubated with Hsp27-3D.

	Weight average sedimentation coefficient (S)	Loading concentration (AU)
56 µM apoC-II only	142.6*	0.70
+ 6.4 µM Hsp27-3D	384.0**	1.09

*Integral range 20-700 S

**Integral range 20-2000 S

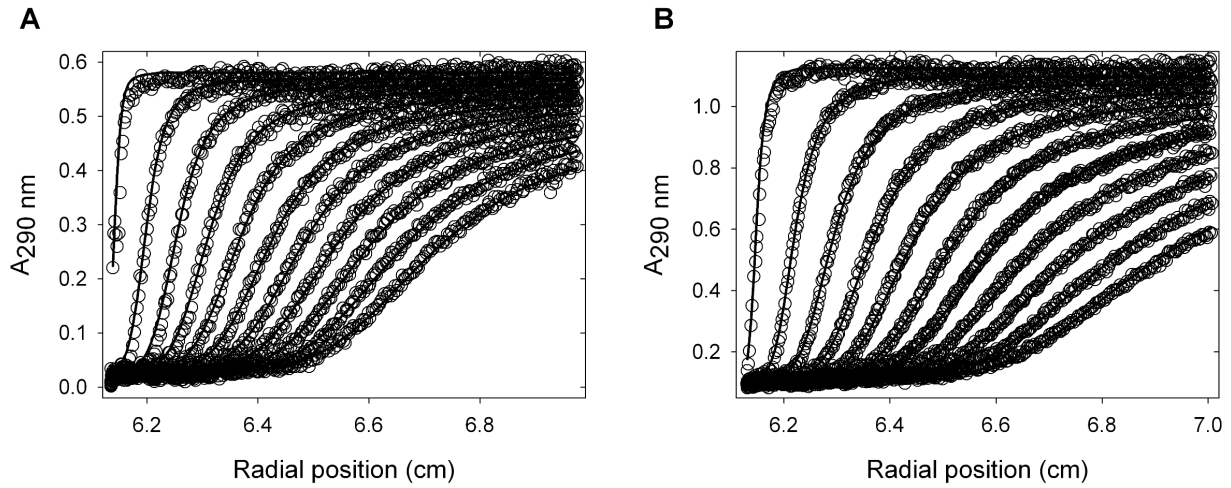


Supplementary Figure 3.20. Raw SV-AUC data (circles) and fits (lines) obtained a c(s) distribution with a worm-like chain model with Tikhonov-Phillips regularization by second derivative of pre-formed apoC-II fibrils (56 µM) incubated alone (A) or with 12.8 µM WT Hsp27 (B) for 0 hours. A rotor speed of 8000 rpm was used. For clarity, every seventh scan is shown in (A-B), corresponding to a time interval of 20 minutes.

Supplementary Table 3.6 Weight-average fibril sedimentation coefficients of pre-formed apoC-II fibrils incubated with WT Hsp27 for 0 hours.

	Weight average sedimentation coefficient (S)	Loading concentration (signal)
56 µM apoC-II only	125.3*	0.59
+ 12.8 µM WT Hsp27 for 0 hours	341.5*	1.44

*Integral range 20-1000 S

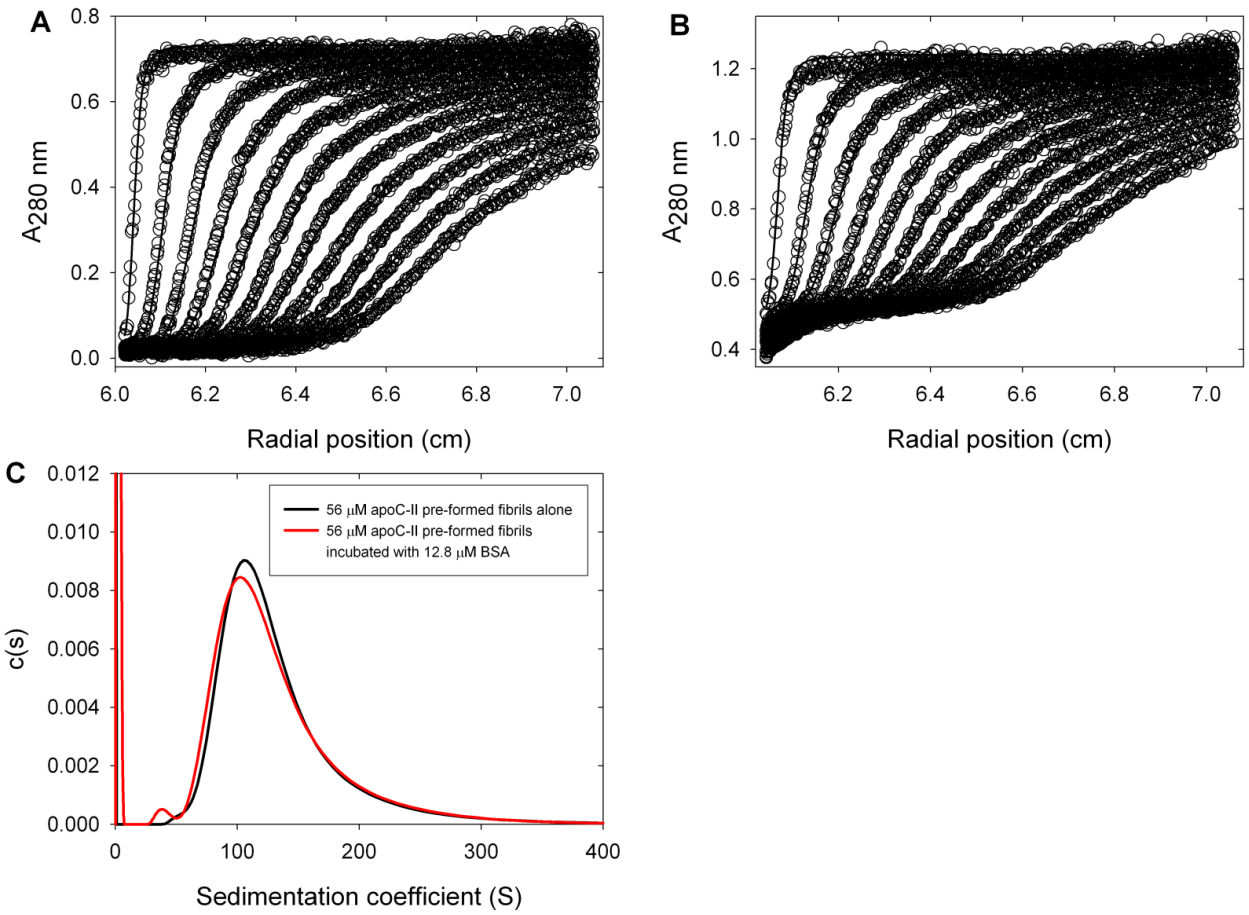


Supplementary Figure 3.21. Raw SV-AUC data (circles) and fits (lines) obtained a c(s) distribution with a worm-like chain model with Tikhonov-Phillips regularization by second derivative of pre-formed apoC-II fibrils (56 µM) incubated alone (A) or with 12.8 µM Hsp27-3DΔCTR (B) for 72 hours. A rotor speed of 8000 rpm was used. For clarity, every seventh scan is shown in (A-B), corresponding to a time interval of 27 minutes.

Supplementary Table 3.7 Weight-average fibril sedimentation coefficients of pre-formed apoC-II fibrils incubated with Hsp27-3DΔCTR.

	Weight average sedimentation coefficient (S)	Loading concentration (signal)
56 µM apoC-II only	121.8*	0.56
+ 12.8 µM Hsp27-3DΔCTR	159.0*	1.0

*Integral range 20-500 S

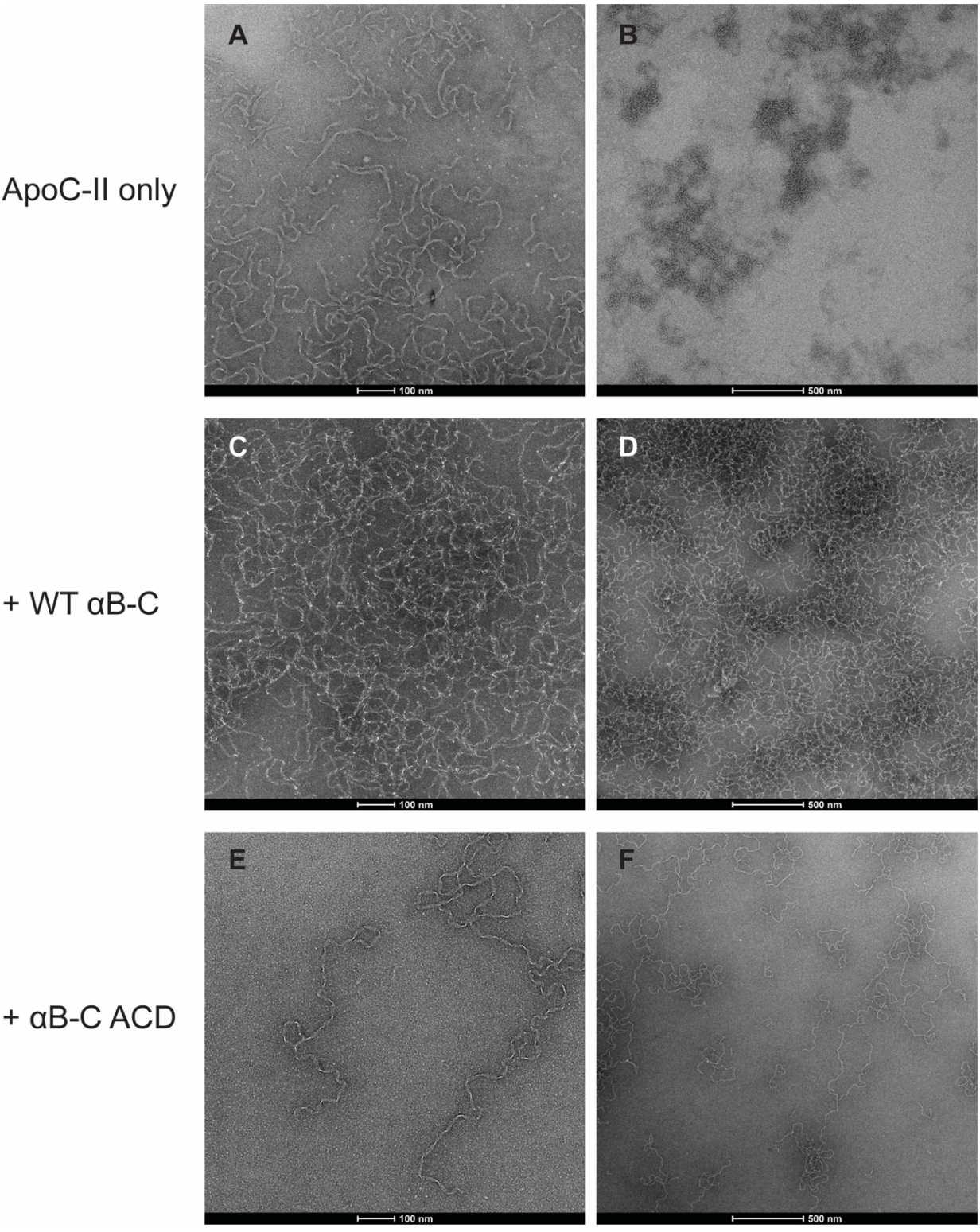


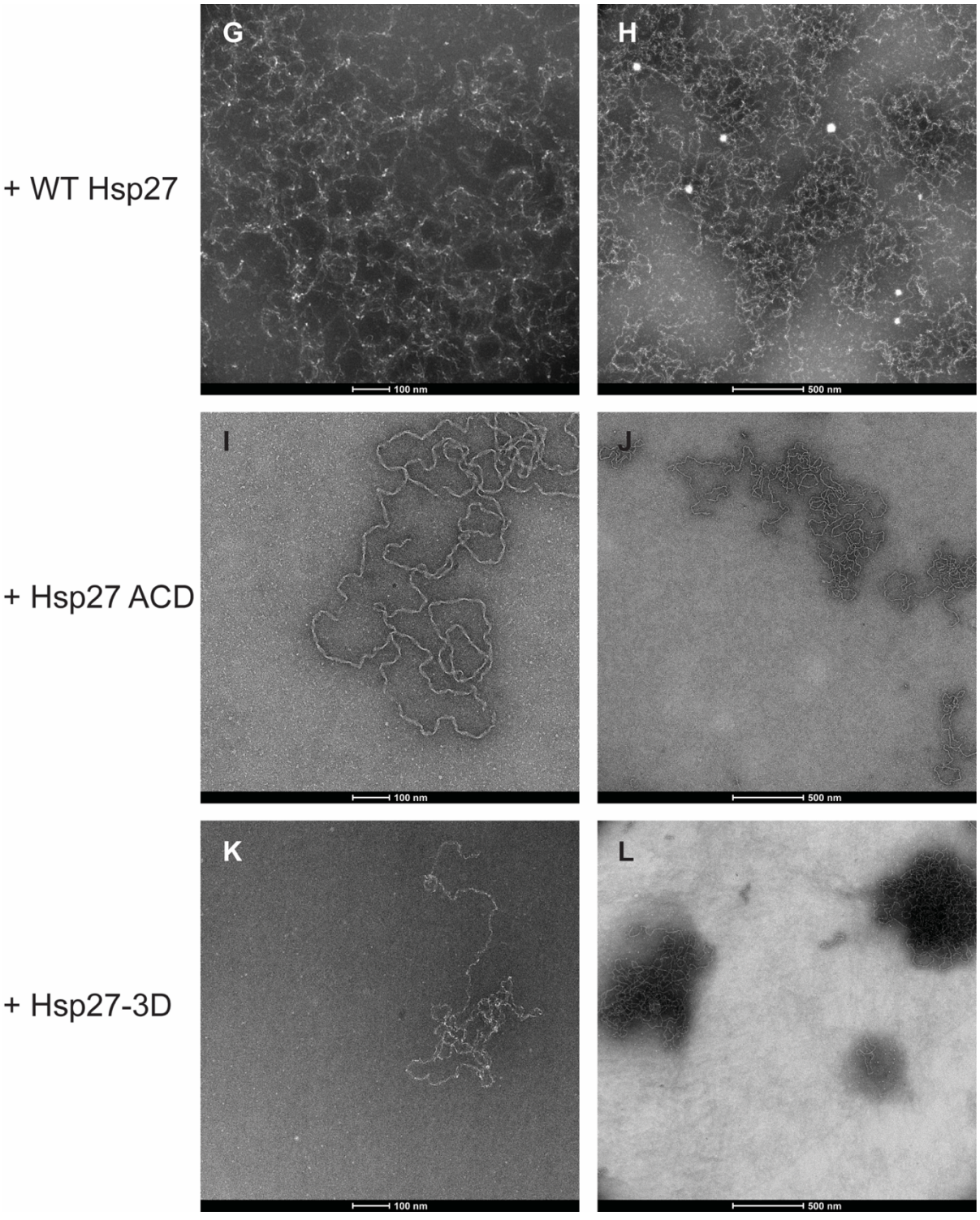
Supplementary Figure 3.22. SV-AUC data (circles) and fits (lines) obtained using a c(s) distribution with a worm-like chain model with Tikhonov-Phillips regularization by second derivative of pre-formed apoC-II fibrils (56 μM) incubated alone (A) or with 12.8 μM BSA (B) for 72 hours. A rotor speed of 8000 rpm was used. C) Sedimentation coefficient distributions c(s) derived from fits to the data shown in A and B for apoC-II fibrils incubated alone (black) and apoC-II incubated with BSA (red). For clarity, every seventh scan is shown in (A-B), corresponding to a time interval of 31 minutes.

Supplementary Table 3.8 Weight-average fibril sedimentation coefficients of pre-formed apoC-II fibrils incubated with BSA.

	Weight-average sedimentation coefficient (S)*	Loading concentration (AU)
56 µM apoC-II fibrils incubated alone	136.5	0.72
56 µM apoC-II fibrils incubated with 12.8 µM BSA	137.3	0.73

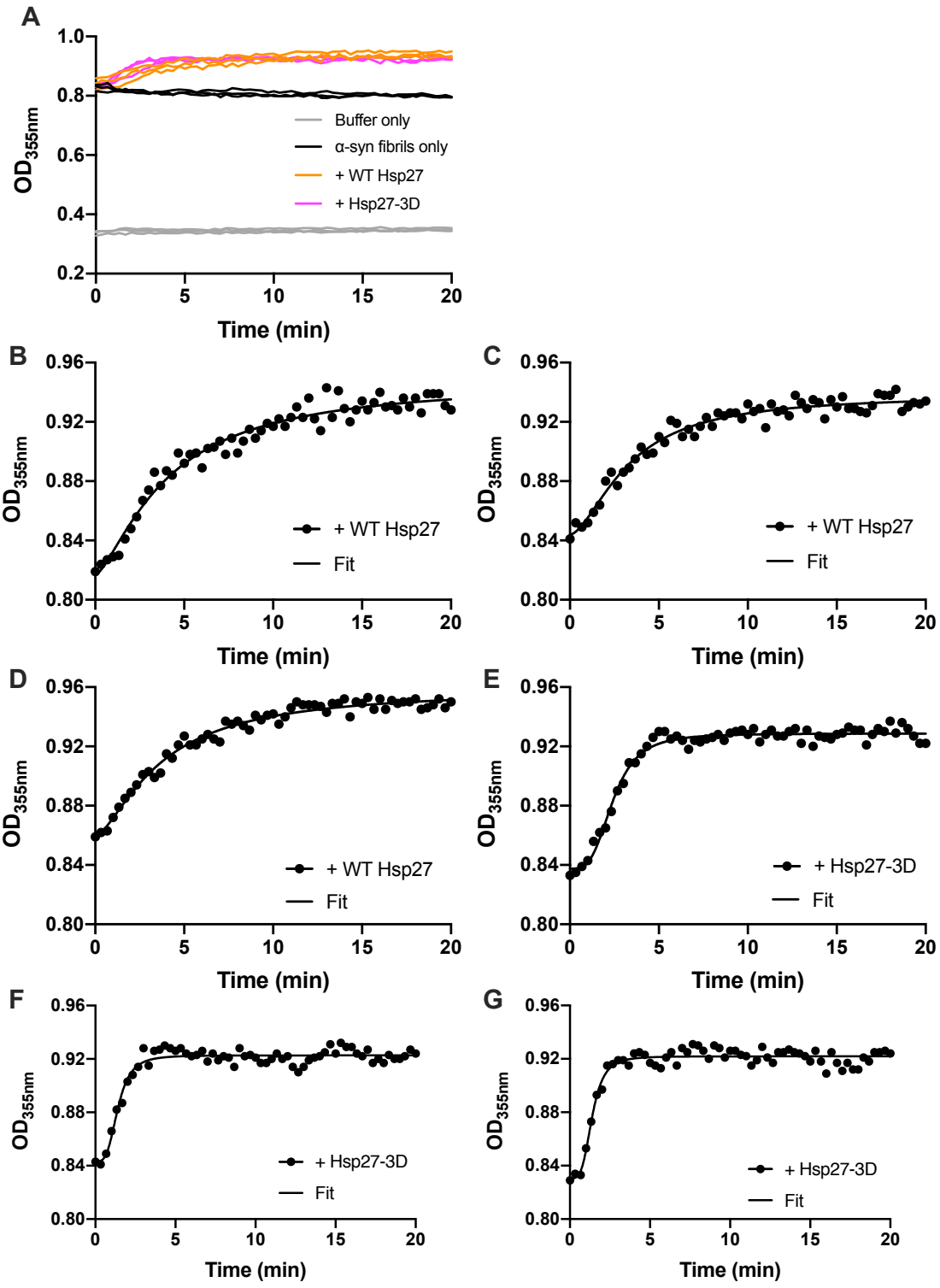
* Integral range 40-700 S


ApoC-II only
+ WT αB-C
+ αB-C ACD
A
B
C
D
E
F
100 nm
500 nm
100 nm
500 nm
100 nm
500 nm



Supplementary Figure 3.23. Transmission electron microscopy of pre-formed apoC-II fibrils (56 μM) incubated alone (A-B) or in the presence of 12.8 μM of WT αB-C (C-D), αB-C ACD (E-F), WT Hsp27 (G-H), Hsp27 ACD (I-J) or Hsp27-3D (K-L) for a further 72 hours at 30°C. The fibrils were diluted by a factor of 5 with dH_2O and applied to carbon coated Formvar 300 mesh

copper grids and visualised using a Talos L120C TEM. The scale bars represent 100 nm for the left panels and 500 nm for the panels on the right.

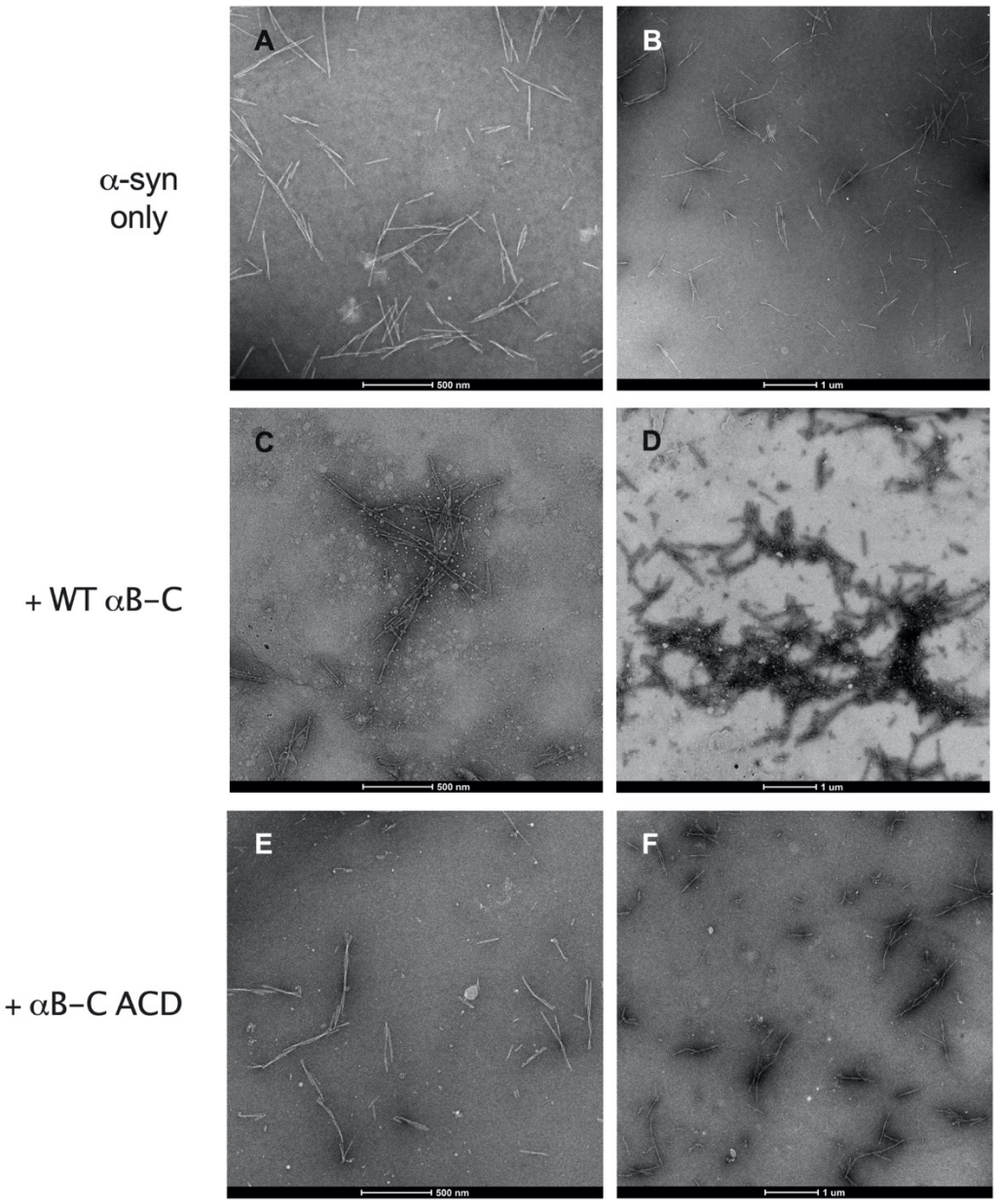


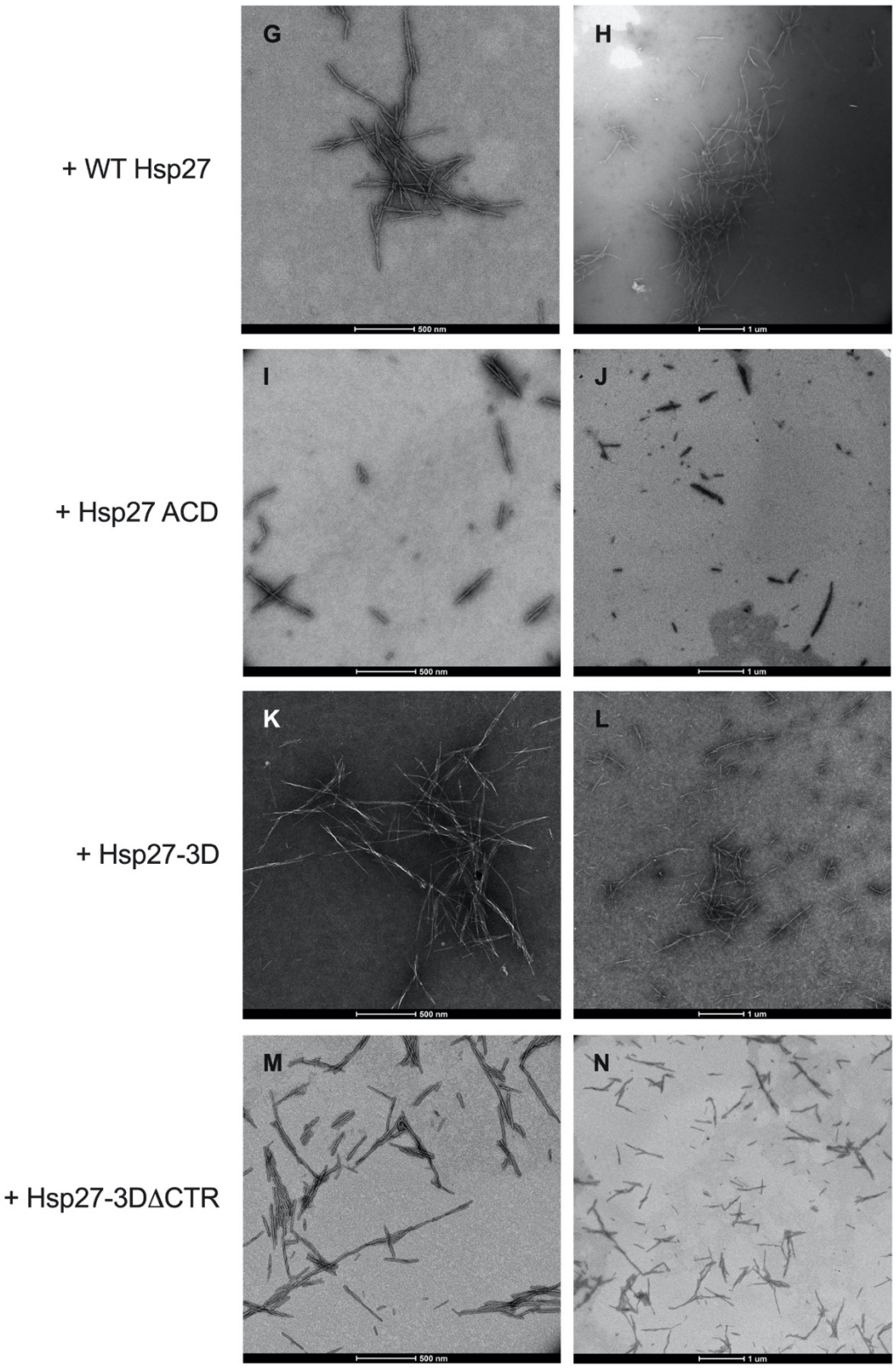
Supplementary Figure 3.24. A) Raw OD data (n = 3) obtained for α-syn fibrils incubated alone (black), and with WT Hsp27 (orange) and Hsp27-3D (magenta). Also shown is the OD of buffer incubated alone (grey). B-D) Individual traces of raw OD data for each replicate of fibrils incubated with WT Hsp27 along with fits to the data obtained using a 4-parameter sigmoidal

Hill-plot. E-F) Individual traces of raw OD data for each replicate of fibrils incubated with Hsp27-3D along with fits to the data obtained using a 4-parameter sigmoidal Hill-plot.

Supplementary Table 3.9 Time to half maximal change in turbidity (T_{50}) for each replicate and average T_{50} for α-syn fibrils incubated with FL Hsp27 constructs.

	T_{50} (min)	Error	T_{50} average (min)
+ Hsp27-3D 1	1.38	0.06	1.73 ± 0.34
+ Hsp27-3D 2	1.40	0.07	
+ Hsp27-3D 3	2.41	0.07	
+ WT Hsp27 1	3.68	0.19	3.69 ± 0.22
+ WT Hsp27 2	3.31	0.21	
+ WT Hsp27 3	4.06	0.30	


α-syn only
+ WT αB–C
+ αB–C ACD
A
B
C
D
E
F
500 nm
1 um
500 nm
1 um
500 nm
1 um



Supplementary Figure 3.25. Transmission electron microscopy of pre-formed α-syn fibrils (200 μM) incubated alone (A-B) or in the presence of 10 μM of WT αB-C (C-D), αB-C ACD (E-F), WT Hsp27 (G-H), Hsp27 ACD (I-J), Hsp27-3D (K-L) or Hsp27-3DΔCTR (M-N) for a further 24 hours at 37°C. The fibrils were diluted by a factor of 10 with dH_2O and applied to carbon

coated Formvar 300 mesh copper grids and visualised using a Talos L120C TEM. The scale bars represent 500 nm for the left panels and 1 μm for the panels on the right.

Chapter 4: The role of the ACD in inhibiting amyloid fibril elongation

4.1 Abstract

Small heat-shock proteins (sHSPs) are ubiquitously expressed molecular chaperones that protect the proteome against proteostasis failure. Human sHSPs populate a polydisperse ensemble of oligomers that readily exchange subunits. This polydispersity renders sHSPs refractory to biophysical characterization by X-ray diffraction and cryo-EM, however the central, highly conserved α-crystallin domain (ACD) can be crystallized. The ACD adopts a β-sandwich fold and forms antiparallel dimers via an extended β-strand, creating a shared β-sheet between the two subunits. sHSP oligomers are widely regarded to act as storage forms of these chaperone-active, exchangeable dimers. Indeed, ACD dimers have been shown to be chaperone-active. However, the exchange of sHSP monomers from oligomers has been observed, and the chaperone function(s) of the monomers are largely unknown. We and others[314,316] have begun to characterize the ACD monomer via NMR and sedimentation velocity analytical ultracentrifugation.

In this chapter, we investigated the interaction of the αB-C ACD with apolipoprotein C-II and α-synuclein amyloid fibrils using NMR. Significant resonance broadening was observed in the presence of amyloid fibrils, indicative of an ACD-fibril interaction. Substantially more signal broadening was observed in the presence of short, fragmented fibrils relative to an equal mass of long fibrils, demonstrating that the ACD interacts preferentially with fibril ends. Furthermore, resonances corresponding to the ACD monomer were broadened to a greater extent than those corresponding to the dimer. This indicates that the primary fibril-interacting species is monomeric and implicates the intra-dimer interface as an interactive site. These findings are supported by our mutagenesis studies in which disulfide cross-linked ACD dimers were less effective at inhibiting amyloid fibril elongation and naturally occurring fibril end-to-end joining than non-covalent dimers. Our results provide further evidence for the dynamic nature of sHSP assemblies and the importance of this dynamism for substrate binding and chaperone function.

4.2 Introduction

In Chapter 3, the roles of the three sHSP regions in inhibiting amyloid fibril formation were identified and can be summarised as follows. The NTR of sHSPs plays an important role in inhibiting fibril nucleation and elongation, and in mediating interactions with pre-existing fibrils and promoting fibril dissociation. The ACD may play a minor role in inhibiting fibril nucleation, but mainly appeared to inhibit the elongation phase of fibril formation and did not form strong interactions with pre-existing fibrils or promote their disaggregation. Though the CTR did not appear to be important for inhibiting fibril nucleation or elongation, it was implicated in fibril binding, and was shown to be important for the lateral association of fibrils into larger aggregates that occurs after the sHSP binds to fibrils. We have continued to investigate the mechanisms of action of full-length sHSPs in this chapter, however the major focus of this chapter was to improve our understanding of the mechanisms of action of the ACD.

Previous studies have focused on the interactions of the ACD with substrates prior to their aggregation into either amorphous aggregates or amyloid fibrils[254,279,281,295]. Our results presented in Chapter 3 suggest that the ACD may exert some of its chaperone function by transiently interacting with amyloid fibrils. Our ability to analyse the sedimentation coefficient distributions of apoC-II fibrils via AUC enables us to determine the effects of the ACD on fibril elongation and on the sizes of pre-formed fibrils. An initial observation that we did not elaborate on in Chapter 3 was that upon incubation of pre-formed apoC-II fibrils with the ACDs of both αB-C and Hsp27, the weight-average fibril sedimentation coefficient was reduced. This result indicates that the lengths of the fibrils are reduced upon incubation with the two ACD constructs. The magnitude of this effect was small, but highly reproducible. We demonstrated that the ACDs did not dissociate monomeric apoC-II from the fibrils and that the ACDs also did not stably interact with the fibrils or induce fibril lateral-lateral association. Consequently, we inferred that the small reduction in the lengths of the fibrils could be due to an interaction between the ACD constructs and the fibrils. An explanation for our observations will be provided in this chapter.

Another initial observation presented in Chapter 3 was that the ACD of αB-C often inhibited amyloid fibril formation more effectively than the ACD of Hsp27. With ~50% sequence identity and 82%

sequence similarity across the ACD (Fig. 4.1), the mechanisms of action of both proteins would be expected to be highly similar. One noteworthy difference between the two ACD constructs is the intra-dimer disulfide in Hsp27 ACD. This disulfide covalently links the two subunits, presumably preventing any dimer-monomer exchange. In all of the experiments in Chapter 3, the pair of cysteine residues were in the oxidised (disulfide-linked) state. Reduction of the disulfide bridge and comparative studies of the chaperone activity of the reduced and oxidised form of the ACD would help to identify the mechanism of action of the ACDs. These experiments will be presented in this chapter.

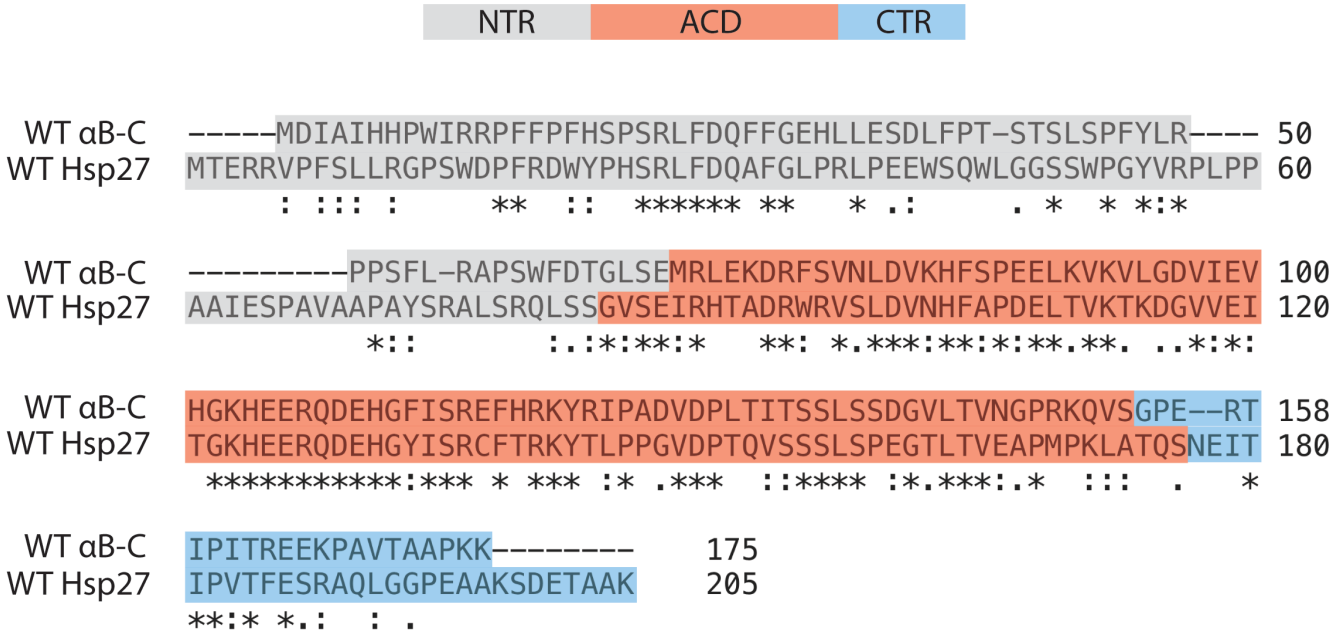


Figure 4.1. Pairwise sequence comparison of the amino acid sequences of WT αB-C and WT Hsp27. The three sHSP regions are colour-coded as follows: NTR, grey; ACD, red; CTR, blue. Identical residues are denoted by "*", highly similar residues are denoted by ":" and similar residues are denoted by ".". The pairwise comparison was generated using Clustal Omega[365]. The percentage sequence identity across all three domains is ~40% and the percentage sequence similarity is ~67%.

4.3 Results

4.3.1 The α-crystallin domain of αB-crystallin halts apoC-II amyloid fibril growth and end-to-end joining

In Chapter 3 we showed that the ACD of αB-C inhibits the spontaneous formation of apoC-II amyloid fibrils. Here we investigated the effects of adding WT αB-C or αB-C ACD at several time points during the formation of apoC-II amyloid fibrils. The addition of WT αB-C appeared to halt amyloid fibril formation

by apoC-II with relatively equal efficacy at all time points (Fig. 4.2 A), as we have previously observed[258]. In contrast, the addition of αB-C ACD at the beginning of apoC-II fibril formation, rather than halting fibril formation, slowed the rate of elongation producing a sigmoidal curve with a T_{50} of ~ 26 hours (Fig. 4.2 B). Though αB-C ACD was less effective than WT αB-C when added at earlier timepoints, at later timepoints both constructs inhibited further fibril elongation with relatively similar efficacies (Fig. 4.2). Some of these samples were subjected to SV-AUC analysis at two timepoints: 4.5 hours after the start of the assay and 72 hours after the start of the assay (Supplementary Fig. 4.1, Supplementary Tables 4.1 and 4.2). A rotor speed of 8000 rpm was used in order to obtain size distributions of the fibrillar material[327]. By integrating the signal observed in the c(s) distribution, the relative proportions of sedimenting material can be compared between samples and across the two timepoints. This analysis confirmed that after the addition of WT αB-C at any timepoint, fibril formation was almost entirely halted. For αB-C ACD, a smaller change in the sedimenting signal was observed between the 5 and 72 hour timepoints when αB-C ACD was added 4.5 hours compared to when it was added at 0 hours, in agreement with the results of the ThT assay.

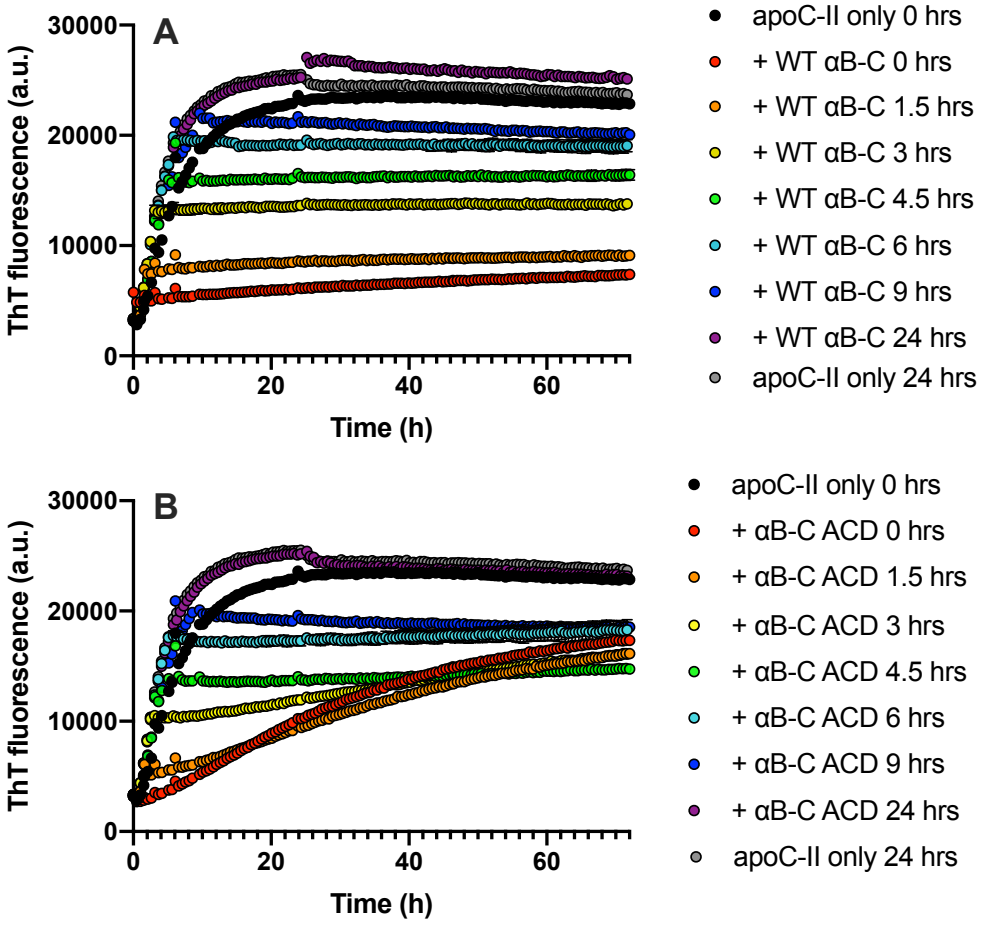


Figure 4.2. WT αB-C and αB-C ACD inhibit apoC-II fibril formation when added during the elongation phase. WT αB-C (A) or αB-C ACD (B) were added to a final concentration of 12.8 μM at 0, 1.5, 3, 4.5, 6, 9 or 24 hours after fibril formation by 56 μM apoC-II was initiated as indicated. Equal volumes of buffer were added at 0 or 24 hours to apoC-II alone as a control. Data are presented as mean ± SEM where n = 2.

Next we added WT αB-C or αB-C ACD at 0 hours and allowed fibrils to form for 168 hours before subjecting the samples to SV-AUC in order to determine whether the presence of WT αB-C or αB-C ACD result in a reduction in the lengths of the fibrils over longer incubations. Fibrils formed in the absence of sHSPs had a broad size distribution with a peak of ~112 S (Fig. 4.3 A, Table 4.1). TEM was used to confirm the twisted ribbon fibrillar morphology of the fibrils (Fig. 4.3 B-C). The size distribution of the fibrils formed in the presence of WT αB-C was left-shifted relative to those formed alone (Fig. 4.3 D, Table 4.1), indicating that the fibrils were shorter than those formed alone. This was confirmed using TEM (Fig. 4.3 E-F). Interestingly, fibrils formed in the presence of αB-C ACD were found to have the

smallest size distribution (Fig. 4.3 G, Table 4.1), and the short lengths of these fibrils were confirmed using TEM (Fig. 4.3 H-I). Therefore, both chaperones inhibit the formation of fibrils and αB-C ACD restricted the elongation of the fibrils more effectively than WT αB-C.

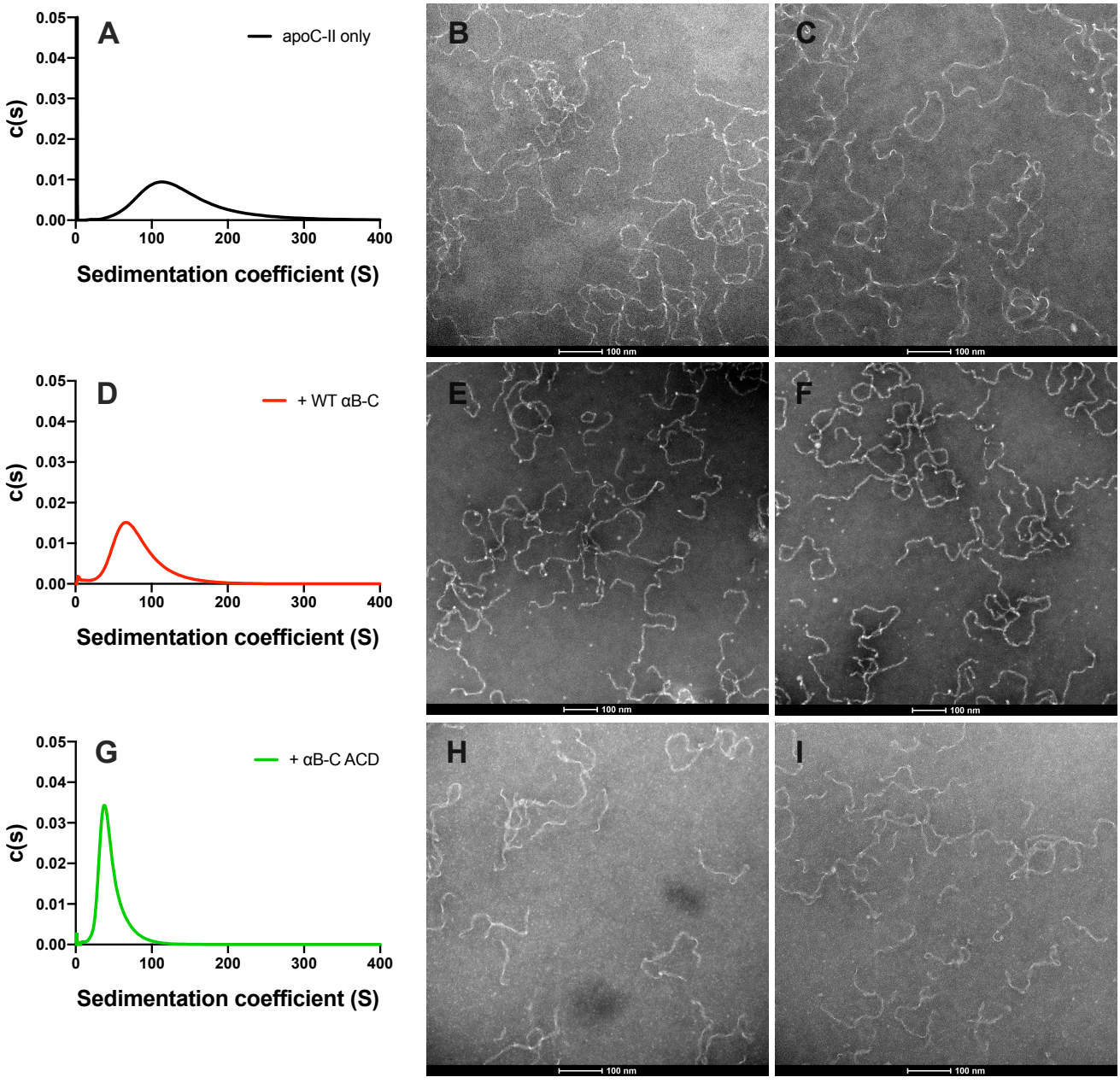


Figure 4.3. Analysis of the lengths of apoC-II fibrils formed in the presence of WT αB-C or αB-C ACD. ApoC-II fibrils (56 μM) were formed alone (A-C), in the presence of 12.8 μM WT αB-C (D-F) or 12.8 μM αB-C ACD (G-I) for 168 hours at 30°C. Fibril sizes were analysed by SV-AUC (A, D, G) using a detection wavelength of 280 nm and transmission EM. Two representative images are shown for each of: apoC-II fibrils formed alone (B-C), in the presence of WT αB-C (E-F) or αB-C ACD (H-I).

Table 4.1 Weight-average fibril sedimentation coefficient alone or in the presence of αB-C constructs

	Weight average sedimentation coefficient (S)*	Sedimentation coefficient distribution peak position (S)	Weight-average fibril mass (kDa)**	Loading concentration (signal)
56 μM apoC-II only	143.1	112	38200	1.05
+ 12.8 μM WT αB-C	83.1	67	10100	0.96
+ 12.8 μM $\alpha B\text{-}C_{CD}$	48.1	38	2800	0.95

* Integral range 5-500 S

** Estimate based on worm-like chain model[327]

Mature apoC-II fibrils can be fragmented by sonication to generate smaller fibrils[85]. As a result of the flexibility of the fibrils, these short fibrils can rejoin via an end-to-end interaction, to form longer fibrils again after a period of incubation. MacRaild *et al.* developed a model relating the sedimentation coefficient of apoC-II fibrils to their MW[327], shown in Fig. 4.4 A-B, which we have subsequently used to estimate weight-average fibril MW. Given that αB-C ACD was a highly effective inhibitor of the elongation of apoC-II fibrils, we tested the ability of this sHSP construct to inhibit apoC-II fibril end-to-end joining using SV-AUC. ApoC-II fibrils were sonicated and various concentrations of αB-C ACD were added to the fibrils which were then analysed by AUC immediately (Fig. 4.4 C), and again after 72 hours of incubation (Fig. 4.4 D). The raw SV-AUC data were fit using least-squares boundary modelling[328] to derive apparent sedimentation coefficient distributions (ls-g*(s)) (methods section 2.2.17). At t_0, fragmented fibrils incubated in the presence of αB-C ACD were found to have considerably smaller size distributions than the fibril fragments incubated alone (Fig. 4.4 C, Table 4.2). We repeated the experiment using fragmented apoC-II fibrils incubated alone at 10°C and found that the size distributions of fragmented fibrils at t_0 was reduced relative to that at 20°C (Fig. 4.4 E, Table 4.2), suggesting that the rejoining process can be slowed down at a reduced temperature. Furthermore, we analysed the earlier and later sedimentation boundaries separately, and this analysis indicated that the

size of fragmented apoC-II fibrils incubated alone increased during the SV experiment (Fig. 4.4 F, Table 4.2), which takes approximately 8 hours. Therefore, the differences observed at t_0 between fragmented fibrils incubated alone and those incubated in the presence of αB-C ACD likely arises from fibril rejoining that occurs on a faster timescale than our measurements enable us to detect. At increasing concentrations of αB-C ACD, the size distributions of the fragmented fibrils were progressively left-shifted, indicating concentration-dependent inhibition of fibril rejoining (Fig. 4.4 C-D). At t_0, a concentration of αB-C ACD as low as 0.8 μM was relatively as effective as 12.8 μM, indicating saturation of the effect on fibril rejoining at sub-stoichiometric ratios (Fig. 4.4 C). Furthermore, concentrations of αB-C ACD from 0.8-12.8 uM were able to inhibit the rejoining of apoC-II fibrils for at least 72 hours (Fig. 4.4 D). 0.05 μM of αB-C ACD inhibited rejoining to some extent but was noticeably less effective. To confirm that the inhibition of fibril end-to-end joining was specific for αB-C ACD, we tested the abilities of three non-chaperone control proteins to inhibit apoC-II fibril rejoining: BSA, ovalbumin and lysozyme. No significant change in the weight-average fibril sedimentation coefficients were observed in the presence of any of these control proteins relative to apoC-II fibril fragments incubated alone (Supplementary Fig. 4.2). Since fibril rejoining arises from an interaction between two fibril ends, we hypothesized that αB-C ACD may interact with apoC-II fibrils at their ends in order to inhibit this process. In Chapter 3 we demonstrated that αB-C ACD does not colocalize to pre-formed apoC-II fibrils. We were also unable to co-precipitate apoC-II fibrils with a 6 x His-tagged αB-C ACD construct in the presence of nickel-NTA resin, even under conditions where the ratio of αB-C ACD:apoC-II fibril ends would be expected to be far greater than 1 (Fig. 4.5). Therefore, we hypothesized that the effect of αB-C ACD on apoC-II fibril rejoining may arise from a transient interaction with the fibrils. To test this we used NMR, a powerful technique for investigating transient protein-protein interactions.

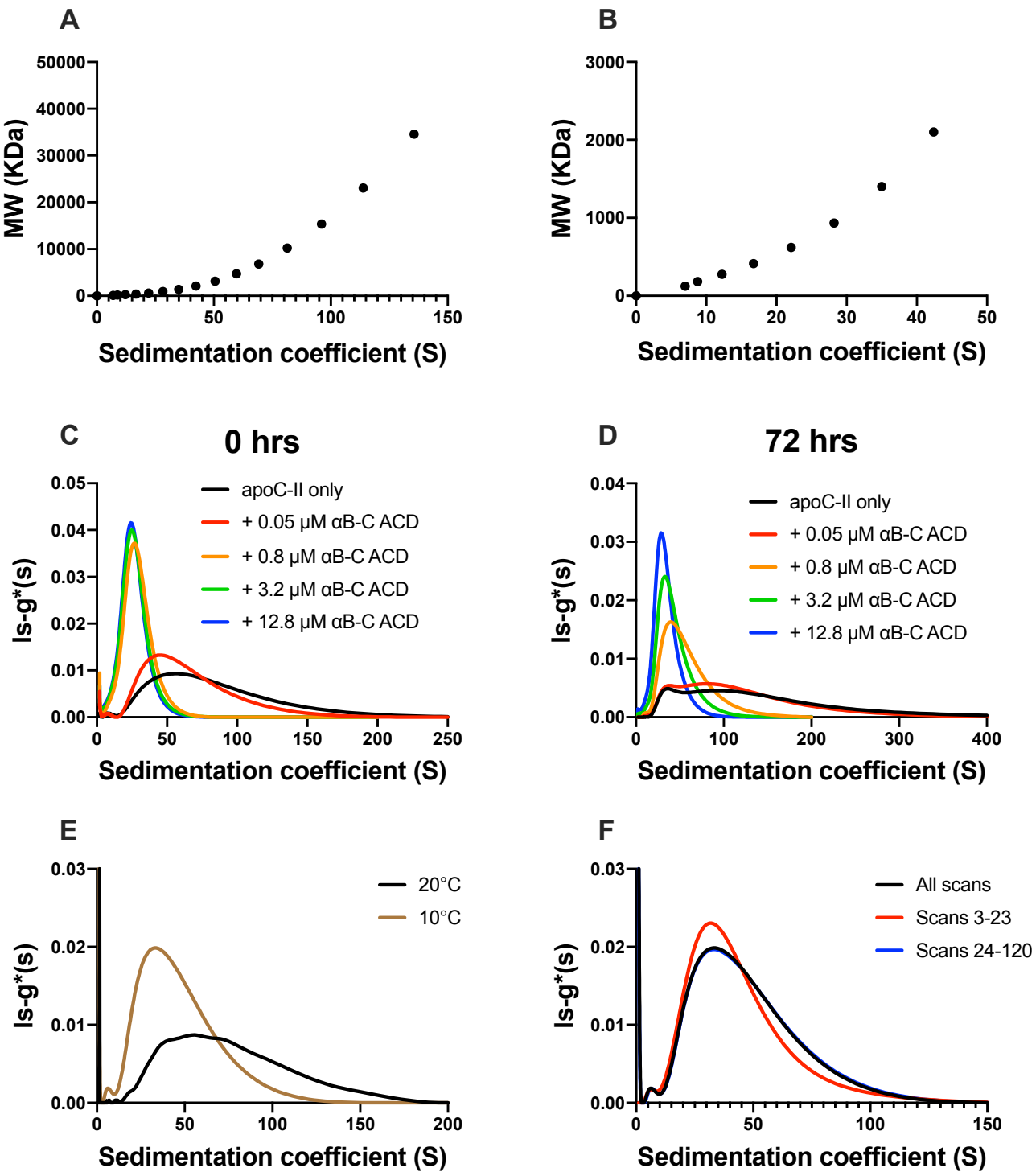


Figure 4.4. αB-C ACD inhibits apoC-II fibril end-to-end joining at sub-stoichiometric molar ratios. A and B) The relationship between the weight-average fibril sedimentation coefficient and weight-average fibril molecular mass as described by MacRaild *et al.*[327] for flexible wormlike chains over the sedimentation coefficient range 0 – 150 S (A) and 0 – 50 S (B). C and D) ApoC-II fibrils (56 μM) were formed for 168 hours at 30°C and fragmented by sonication. Immediately after fragmentation,

αB-C ACD was added to a final concentration of 0.05 (red), 0.8 (orange), 3.2 (green) or 12.8 (blue) μM as indicated. Fibril sizes were then analysed by SV-AUC immediately (C) or after a further 72 hour incubation at 30°C (D) using detection wavelengths of 275 nm. ApoC-II fibril fragments incubated alone are shown in black. Raw data were fit using the SEDFIT software and the wormlike chain model depicted in (A-B). E) ApoC-II fibrils (56 μM) were formed for 168 hours at 30°C and fragmented by sonication. Immediately after fragmentation, the fibrils were analysed by SV-AUC at 20°C (black) or 10°C (brown) using detection wavelengths of 280 nm. F) Various ranges of sedimentation scans (3-120, black; 3-23, red or 24-120, blue) were fit as described above for the fibril fragments analysed at 10°C shown in (E).

Table 4.2 Sedimentation velocity analysis of apoC-II fibril fragments at 20°C and 10°C

	Scans analysed	Weight average sedimentation coefficient (S)
ApoC-II fibril fragments at 20°C	3-120	83.2*
ApoC-II fibril fragments at 10°C	3-120	48.0**
ApoC-II fibril fragments at 10°C	3-23	44.3**
ApoC-II fibril fragments at 10°C	24-120	48.6**

*Integral range 10-500 S

**Integral range 10-200 S

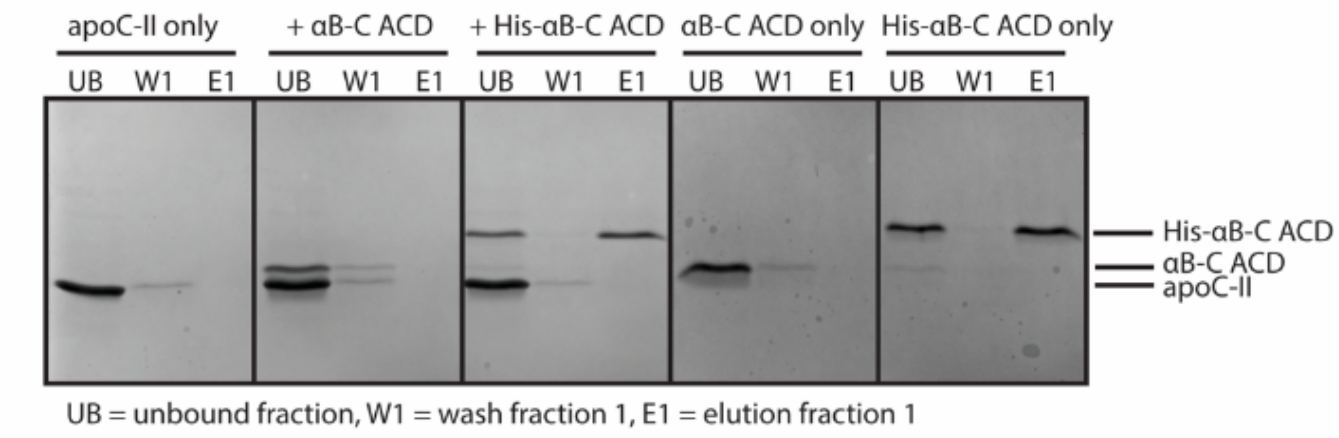


Figure 4.5. ApoC-II fibrils are not co-precipitated with 6 x His-tagged αB-C ACD using nickel-NTA resin. ApoC-II fibrils (56 μM) were incubated alone, or in the presence of 12.8 μM αB-C ACD or 6 x His-tagged αB-C ACD and nickel-NTA resin. Resin was purified from the mixture by centrifugation at 1000 x rpm (74 x g). The unbound fraction was collected, and resin was washed twice by centrifugation. Bound proteins were eluted from the resin using 500 mM imidazole and a further centrifugation step. The unbound, first wash fractions and first elution fractions were analysed by SDS-PAGE. Also shown are control samples of 6 x His-tagged αB-C ACD or untagged αB-C ACD incubated with nickel-NTA resin alone and analysed in an identical manner.

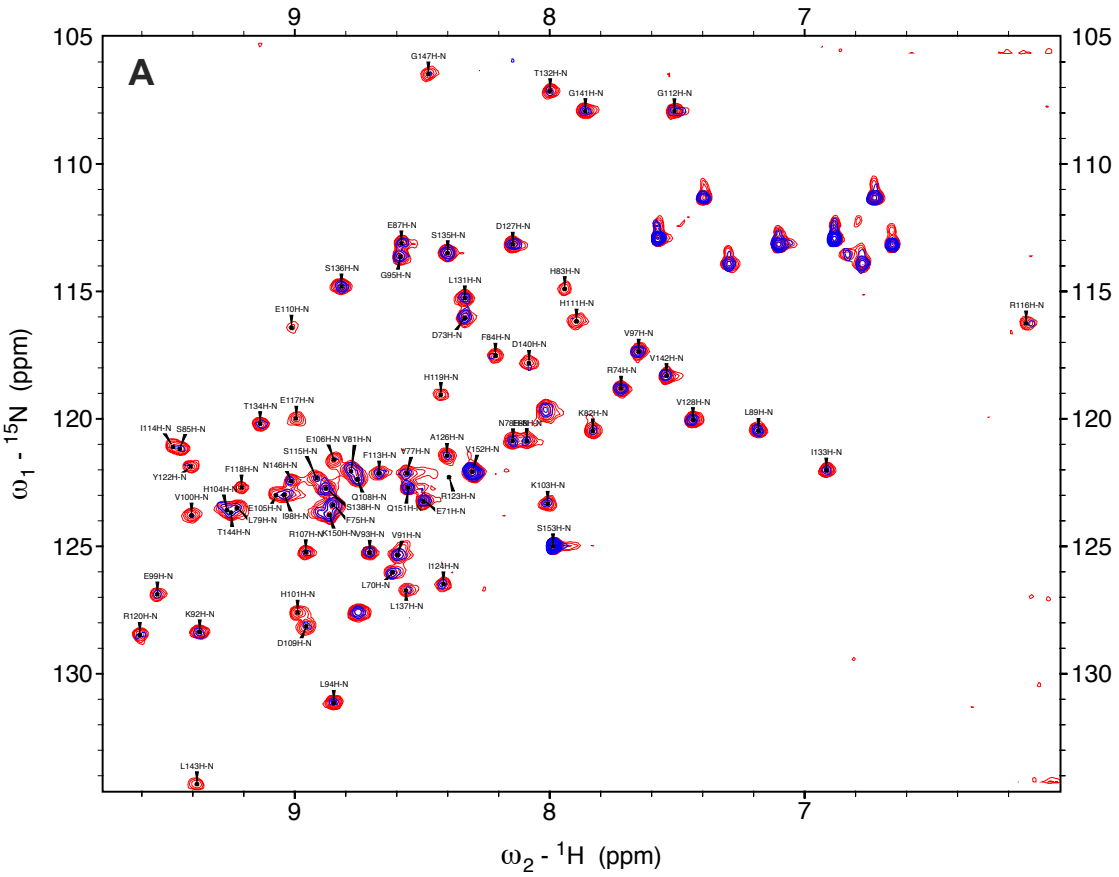
4.3.2 The ACD of αB-C transiently interacts with the ends of amyloid fibrils

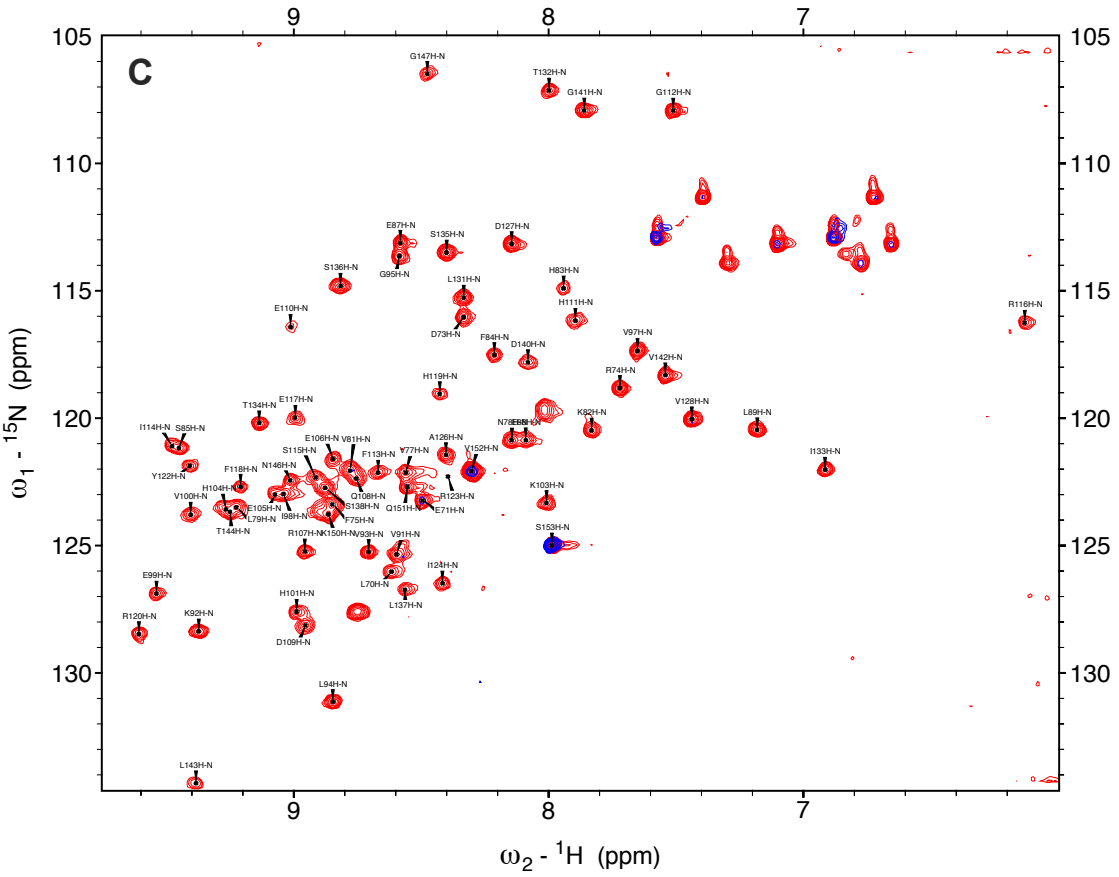
To investigate a transient interaction between αB-C ACD and fibrils using NMR we exploited the small MW of αB-C ACD and the large MW of apoC-II fibrils. When a small molecule such as αB-C ACD binds a large MW molecule such as an amyloid fibril, its rate of molecular tumbling is reduced, leading to markedly enhanced nuclear spin transverse relaxation rates (R_2), and consequently a loss of signal intensity. Thus, the fibril-bound form of a small MW protein is expected to be "NMR invisible" using standard solution-NMR techniques. We used spectral assignments of αB-C ACD kindly provided by Associate Professor Justin Benesch (University of Oxford) via personal communication. When ^{15}N-labelled αB-C ACD was incubated in the presence of apoC-II fibrils, the signal intensity of peaks corresponding to αB-C ACD was reduced relative to αB-C ACD incubated alone (Fig. 4.6 A), however no large peak shifts were observed. This signal broadening observed in the presence of the fibrils is indicative of an interaction between the fibrils and αB-C ACD. However, the concentration of fibrils used was relatively high (10 mg/mL). Therefore, to rule out non-specific effects that could be induced by an increase in sample viscosity due to the concentration of apoC-II, we also recorded a ^{15}N HSQC spectra of αB-C ACD incubated in the presence of 10 mg/mL BSA (Fig. 4.6 B). Unlike the sample containing fibrils, no significant peak broadening was observed, indicating that αB-C ACD does not interact with BSA, and that small changes in sample viscosity arising from high protein concentrations do not cause a loss of signal intensity. To test the hypothesis that αB-C ACD interacts specifically with apoC-II fibril ends, it was necessary to perform another HSQC in which the total concentration of fibrils was identical, but the concentration of fibril ends was increased, i.e. with the same mass of shorter fibrils. To do this, the sample containing αB-C ACD and pre-formed apoC-II fibrils was sonicated to fragment the fibrils and a further HSQC was recorded (Fig. 4.6 C).

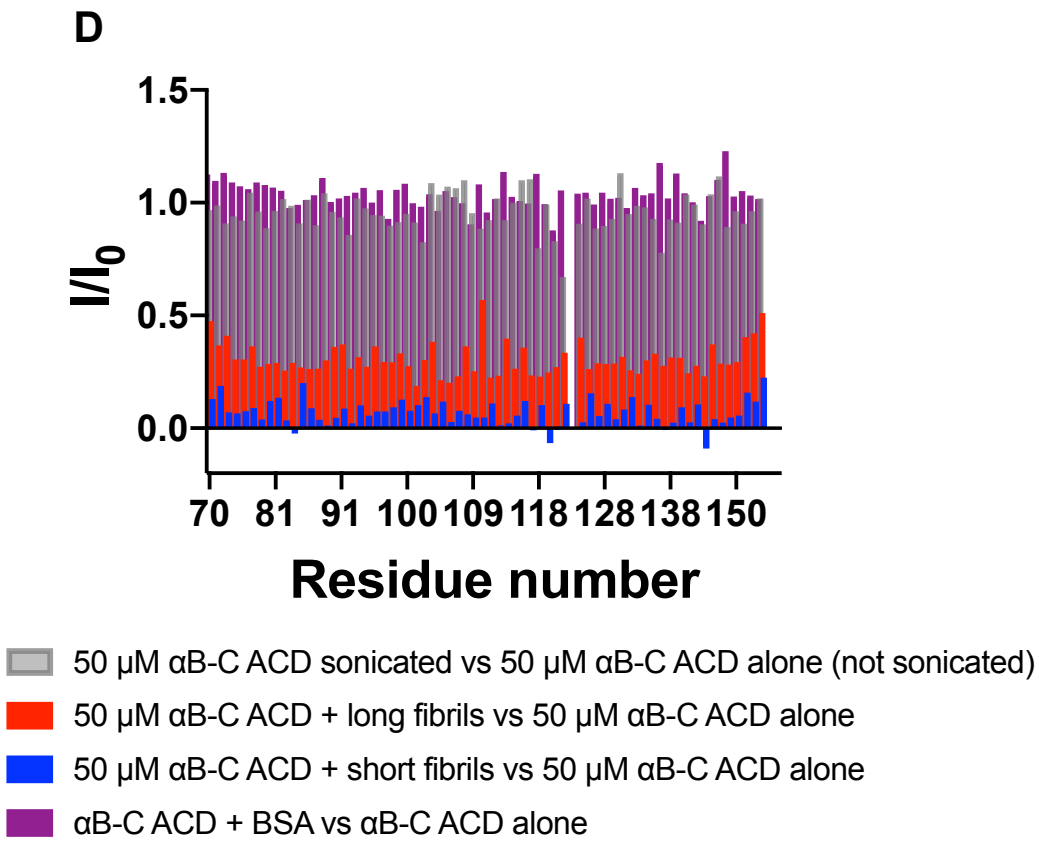
We used the wormlike chain model relating the sedimentation coefficient of apoC-II fibrils to their MW (Fig. 4.4 A-B) to estimate the average fibril MW, and the concentration of fibril ends for the fibrils prior to sonication and for the fragmented fibrils. Non-fragmented fibrils exhibit a size distribution with a weight-average sedimentation coefficient of ~130 S. As an approximation, we calculate that this corresponds to a weight average fibril mass of ~31 MDa (Fig. 4.4 A) with approximately 3500 subunits per weight average fibril and, thus, a concentration of fibril ends of ~0.6 μM. After sonication, the weight-average sedimentation coefficient of the fibrils is reduced to ~26 S, corresponding to a MW of 830 kDa (Fig. 4.4 B), ~90 subunits per weight-average fibril and a concentration of fibril ends of approximately 24 μM. Therefore, in this experiment, in which the concentration of αB-C ACD was 50 μM, we could not achieve a 1:1 molar ratio of αB-C ACD:fibril ends, but we could alter the ratio by at least one order of magnitude in order to test this hypothesis.

After sonication, the peaks corresponding to αB-C ACD were broadened to such an extent as to be almost entirely NMR-invisible, with the exception of peaks corresponding to highly dynamic regions of αB-C ACD such as loops, glutamine and asparagine side chains, and the N- and C-termini. To confirm that the process of sonication did not affect the signal intensity of peaks corresponding to αB-C ACD, a spectrum was recorded on a separate sample of αB-C ACD alone after sonication (Supplementary Fig. 4.3). I/I_0 ratios were calculated for all assigned peaks across the spectrum for all samples relative to αB-C ACD alone (Fig. 4.6 D). For each sample, the mean I/I_0 ratio (relative to αB-C ACD alone prior to sonication) and the standard deviation (SD) observed across all residues were also computed in order to make comparisons between samples. Sonication alone or the presence of BSA did not affect the signal intensity of αB-C ACD, with I/I_0 ratios of 0.96 ± 0.08 and 1.04 ± 0.06 for these samples, respectively (Fig. 4.6 D). Incubation with long apoC-II fibrils resulted in I/I_0 ratios of 0.31 ± 0.07, indicating an interaction between the fibrils and αB-C ACD (Fig. 4.6 D). However, after fragmentation of the fibrils, the I/I_0 ratios were further reduced to 0.07 ± 0.06 (Fig. 4.6 D). The differential I/I_0 ratios observed for the same sample before and after fibril fragmentation indicates that a larger population of αB-C ACD interacts with the shorter fibrils relative to the longer fibrils within the NMR timescale of this experiment. Quantitatively, the extent of signal broadening observed in the presence of the long and short fibrils is dependent on

the kinetics of exchange between αB-C ACD and the fibrils, which we cannot determine from these data. Therefore, αB-C ACD exhibits a preference for binding fibrils ends as opposed to the surface of the fibril, but these data do not rule out an additional, interaction of αB-C ACD with the fibril surface. We also analysed the chemical shift perturbation of each assigned peak in the presence of long apoC-II fibrils (Fig. 4.6 E). This was not done for the sample in the presence of the short fibrils due to a low signal to noise ratio. No large shifts were observed; however, some residues were found to have chemical shift perturbations (CSPs) greater than 1 standard deviation (SD) from the mean CSP which was calculated across all residues (Fig. 4.6 E). Of these, six out of nine were located in the β5 strand, the loop between strands β5 and β6/7, and the β6/7 strand. This region corresponds to the dimer interface. One of the other residues with a CSP > 1 SD from the mean was F84, whose side chain extends towards β6/7 in the crystal structure. All nine residues with CSPs greater than 1 SD from the mean were mapped onto the crystal structure in Fig. 4.6 F. This entire experiment was replicated independently, yielding similar results, which are shown in Supplementary Fig. 4.4).


A
B
ω_1 - ^{15}N (ppm)
ω_2 - ^{1}H (ppm)
9
8
7
105
110
115
120
125
130


C
9
8
7
105
110
115
120
125
130
ω1 - 15N (ppm)
ω2 - 1H (ppm)
G147H-N
T132H-N
G141H-N
G112H-N
E87H-N
S135H-N
D127H-N
G95H-N
S136H-N
H83H-N
L131H-N
H111H-N
E110H-N
R116H-N
D73H-N
F84H-N
D140H-N
V97H-N
V142H-N
R74H-N
H119H-N
T134H-N
E117H-N
V128H-N
L89H-N
K82H-N
I114H-N
S85H-N
I133H-N
E106H-N
V81H-N
A126H-N
S115H-N
F113H-N
V77H-N
Y152H-N
Y122H-N
F118H-N
N146H-N
K103H-N
H104H-N
V100H-N
Q108H-N
R123H-N
E105H-N
S138H-N
Q151H-N
E71H-N
I98H-N
L79H-N
F75H-N
T144H-N
S153H-N
R107H-N
K150H-N
Y93H-N
V91H-N
I124H-N
E99H-N
L70H-N
H101H-N
L137H-N
R120H-N
K92H-N
D109H-N
L94H-N
L143H-N


D
1.5
1.0
0.5
0.0
I/I0
70 81 91 100 109 118 128 138 150
Residue number
50 μM αB-C ACD sonicated vs 50 μM αB-C ACD alone (not sonicated)
50 μM αB-C ACD + long fibrils vs 50 μM αB-C ACD alone
50 μM αB-C ACD + short fibrils vs 50 μM αB-C ACD alone
αB-C ACD + BSA vs αB-C ACD alone

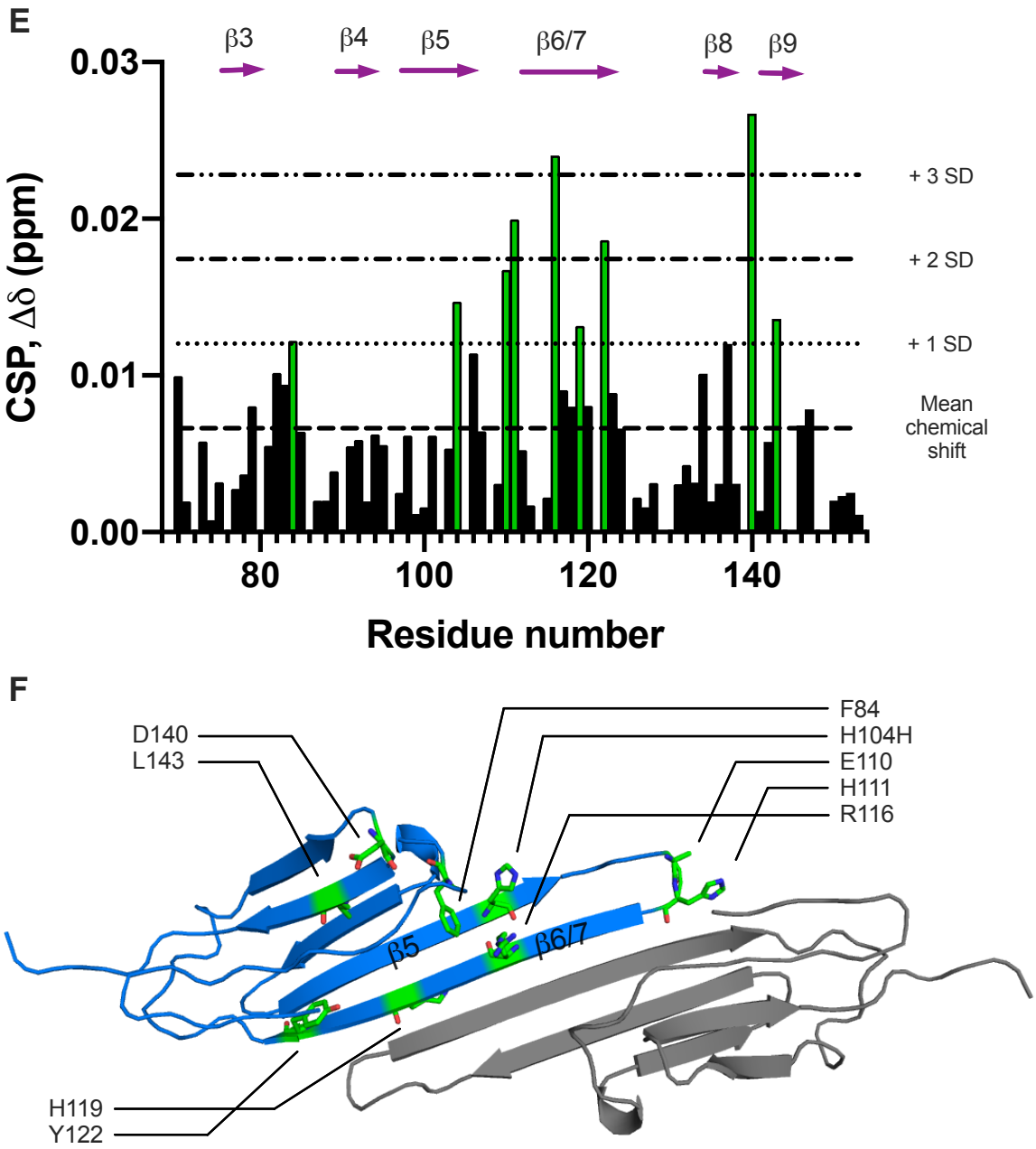


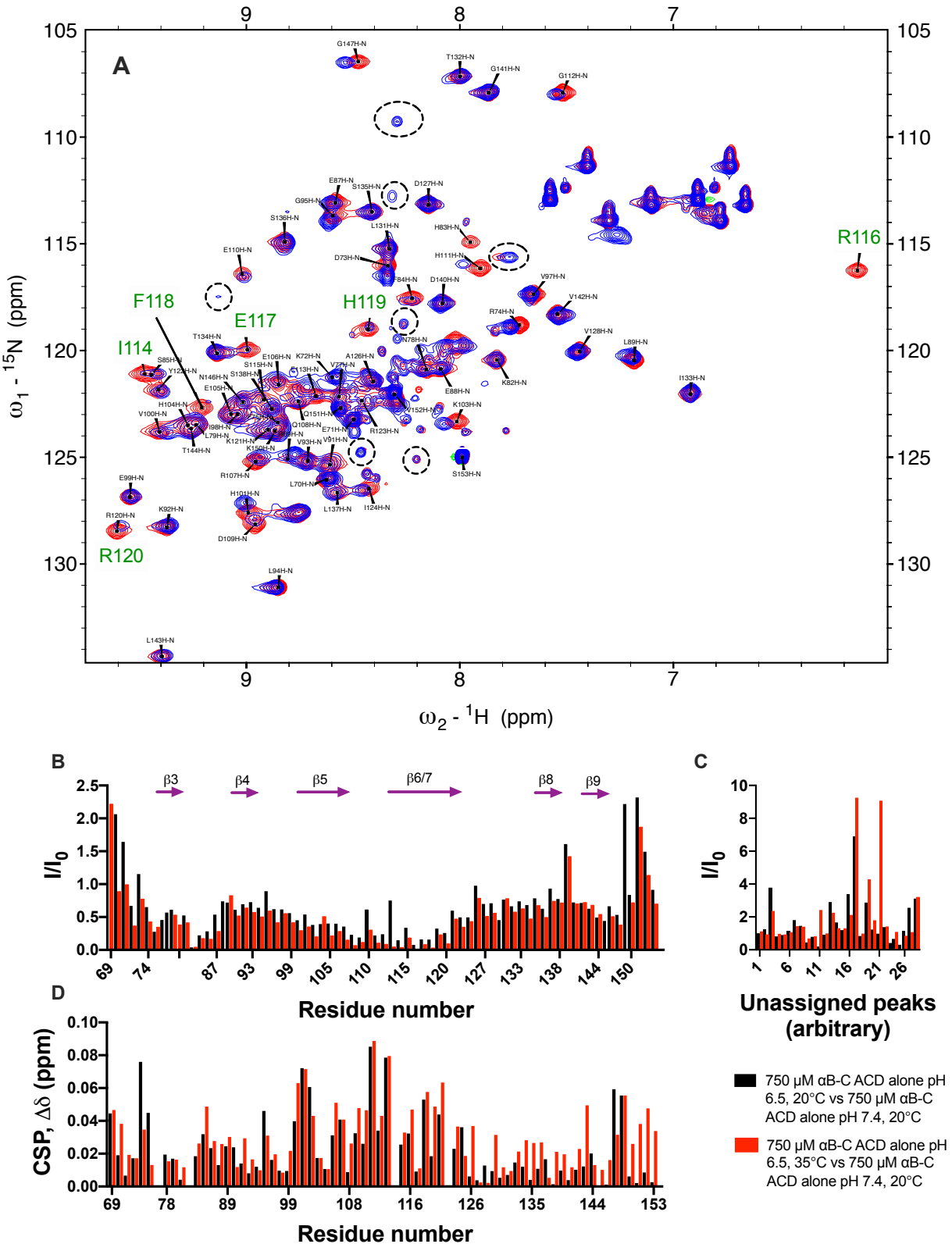
Figure 4.6. αB-C ACD interacts preferentially with the ends of apoC-II fibrils. ^{15}N HSQCs of αB-C ACD alone (red) overlaid with αB-C ACD in the presence of 10 mg/mL of long apoC-II fibrils (blue, A), 10 mg/mL BSA (blue, B), or 10 mg/mL short apoC-II fibrils (blue, C). D) The raw intensities of each assigned peak in each spectra were divided by the raw intensities of the peaks in the control spectra: 50 μM αB-C ACD alone to generate I/I_0 ratios for each assigned peak: αB-C ACD alone sonicated vs αB-C ACD alone prior to sonication (grey), αB-C ACD + 10 BSA vs αB-C ACD alone (purple), αB-C ACD + 10 mg/mL long apoC-II fibrils vs αB-C ACD alone (red) and αB-C ACD + 10 mg/mL short apoC-II fibrils vs αB-C ACD alone (blue). E) CSP analysis of each

assigned peak in the presence of 10 mg/mL of long apoC-II fibrils relative to αB-C ACD alone. The mean CSP and the SD was calculated across all assigned peaks. The mean, and ± 1, 2 and 3 SD from the mean was plotted as lines as indicated. Residues with CSPs > 1 SD from the mean CSP were plotted in green. F) The crystal structure of the αB-C ACD dimer (PDB: 4m5s) is shown with one subunit in blue and one in grey. Residues with CSPs > 1 SD from the mean CSP were mapped onto one subunit of the dimer in green and shown as lines.

4.3.3 Detection of αB-C ACD dimer-monomer exchange at pH 7.4

In the experiments presented in section 4.3.2, a low concentration of 50 μM αB-C ACD was used, and as a result, the signal to noise ratio was low. To more accurately identify any small peak shifts, or regions of the protein with enhanced peak broadening we altered the ratio of αB-C ACD and apoC-II fibril fragments: 750 μM αB-C ACD, and 2 mg/mL apoC-II fibril fragments. Initially, we recorded a ^{15}N HSQC of the ACD alone. At this concentration of αB-C ACD, at least 20 additional peaks can be observed that are barely visible at lower concentrations (Fig. 4.7 A). In this spectrum, and in subsequent spectra shown in this chapter, low contour levels have been used in order to show these minor peaks. In some instances, this gives the appearance of poor phasing in the ^{1}H dimension for some resonances that are not entirely symmetrical, however all spectra were phased as best as possible. We hypothesized that these peaks may correspond to a minor population of ACD monomer, which is expected to be partially unfolded[314]. We used three approaches to test this hypothesis. Firstly, a reduction in pH has been previously reported to increase the dissociation constant (K_d) of a similar construct of αB-C ACD, thereby increasing the population of ACD monomer[316]. Rajagopal *et al*. estimated the K_d to be 2 μM at pH 7.5 and 30 μM at pH 6.5[316] using ITC, however the raw data was not shown. Assuming these estimates to be close to the true values, at 750 μM, the concentration of monomer can be estimated to be ~50 μM, and therefore could be detectable by NMR. At pH 6.5, the concentration of monomer would be expected to increase to nearly 190 μM. Thus, if the unknown peaks correspond to the ACD monomer, their signal intensity should increase upon reducing the pH from 7.5 to 6.5. Indeed, Rajagopal *et al*. observed extra peaks at pH 6.5 that were not visible at pH 7.5[316]. The authors determined that the new peaks arise from peak doubling due to monomer-dimer exchange on the slow-intermediate NMR timescale, and assigned some of these peaks at pH 6.5[316]. Here, we observed many similar spectral changes as well as additional unassigned peaks at pH 6.5 relative to pH 7.4. In general, and in accordance with the results presented

by Rajagopal *et al.*[316], the signals arising from the assigned peaks were weakened, while the unassigned peaks were enhanced in intensity by reducing the pH from 7.4 to 6.5 (Fig. 4.7 B-C). In particular, peaks corresponding to residues located at the dimer interface (e.g.: I114, R116, E117, F118, H119 and R120, Fig. 4.7 A) become extremely weak at the reduced pH, suggesting that the conformation and/or conformational exchange of these residues are altered. An additional ^{15}N HSQC was recorded at on a sample containing 750 μM αB-C ACD at pH 6.5, 35°C. We again analysed the intensity ratios of the assigned and unknown peaks observed here relative to their intensities at pH 7.4, 20°C (Fig. 4.7 B-C). Residues 83, 114, and 116-118 were found to have I/I_0 ratios below 1 SD from the mean I/I_0 ratio calculated across all residues at both pH 6.5, 20°C and pH 6.5, 35°C relative to pH 7.4, 20°C (Fig. 4.7 B). These residues were mapped onto the structure of the dimer in Fig. 4.7 E. Residues 114-118 are located at the dimer interface β6/7 strand. The sidechain of H83 is located in close proximity to the positively charged R116 in the dimer structure. A disruption to the dimer interface, which may be caused by a reduction in pH, could reposition R116 such that the chemical environment of H83 is significantly altered and this may account for the observed reduction in I/I_0 for residue 83. Alternatively, protonation of the imidazole ring of H83 could result in a repulsive interaction with R116 and contribute to the pH-dependent dimer-to-monomer transition. CSPs were also calculated for the assigned residues at pH 6.5 (both at 25°C and 30°C) relative to pH 7.4 (Fig. 4.7 D). Only minor CSPs were observed, generally located at the β5 strand, the loop between strands β5 and β6/7, and the β6/7 strand. To verify that the appearance of the unassigned peaks were not due to minor contaminants or degraded protein, we have independently replicated these spectra on multiple preparations of ^{15}N αB-C ACD. In these replicated spectra, the appearance of unassigned peaks in the same positions are repeatedly observed. Furthermore, the assigned peaks corresponding to the dimer interface undergo the most significant peak broadening and although the CSPs are extremely small, the larger observed changes cluster to the β5 strand, the loop between strands β5 and β6/7, and the β6/7 strand. One example of these replicated spectra, the intensity ratio analysis and CSP analysis are shown in Supplementary Fig. 4.5.


A
R116
F118
E117
H119
I114
R120
ω_1 - ^{15}N (ppm)
ω_2 - ^{1}H (ppm)
B
β3
β4
β5
β6/7
β8
β9
I/I$_0$
Residue number
C
I/I$_0$
Unassigned peaks (arbitrary)
D
CSP, Δδ (ppm)
Residue number
750 μM αB-C ACD alone pH 6.5, 20°C vs 750 μM αB-C ACD alone pH 7.4, 20°C
750 μM αB-C ACD alone pH 6.5, 35°C vs 750 μM αB-C ACD alone pH 7.4, 20°C

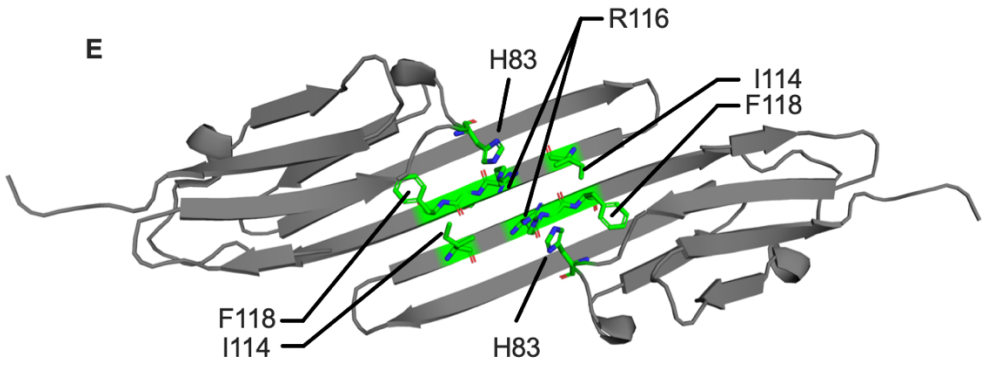


Figure 4.7. A reduction in pH perturbs the equilibrium between the major and minor state of αB-C ACD. A) ^{15}N HSQC of 750 μM αB-C ACD alone at pH 7.4 (red) and 6.5 (blue), both at 20°C. A selection of unassigned peaks are circled with a dashed line, however there are approximately 28 unassigned peaks in total. A selection of assigned peaks that were noticeably broadened at pH 6.5 relative to pH 7.4 are labelled in green. B) The raw intensities of each assigned peak in the spectra at pH 6.5, 20°C (black) and of an additional spectra collected at 35°C (red) was divided by the raw intensity of each assigned peak in the spectra at 7.4, 20°C to generate I/I_0 ratios for each assigned peak. C) Additional observed peaks that were not assigned were selected based on the spectra obtained at pH 7.4, 20°C. The raw intensities of each of these peaks in the spectra obtained at pH 6.5, 20°C (black) and pH 6.5, 35°C (red) was divided by the raw intensity of each unknown peak in the spectra at pH 7.4, 20°C (where it was possible to select peaks) to generate I/I_0 ratios for each unknown peak. D) CSP analysis of each assigned peak for αB-C ACD alone at pH 6.5, 20°C (black) and at pH 6.5, 30°C (red) vs pH 7.4, 20°C. E) The crystal structure of the αB-C ACD dimer (PDB: 4m5s) is shown with both subunits in grey. The mean and standard deviation for the I/I_0 ratios shown in (B) were calculated for both of pH 6.5, 20°C vs pH 7.4, 20°C and pH 6.5, 35°C vs pH 7.4, 20°C. Assigned peaks with I/I_0 ratios below 1 standard deviation from the mean I/I_0 in both of these comparisons were mapped onto the crystal structure of both of the subunits in green and shown using the stick representation.

To further interrogate the possibility that αB-C ACD transitions between a major population of dimer and a minor population of monomer at pH 7.4, we recorded an additional ^{15}N HSQC at pH 5.9 and also used SV-AUC across the pH range 7.4 - 6.0 (Fig. 4.8). At pH 5.9, some peaks corresponding to residues distal to the dimer interface could be identified, however many peaks were substantially broadened and/or shifted towards the centre of the spectrum (Fig. 4.8 A). A small number of peak shifts could be identified based on previously published spectra[316], however the majority could not be identified. Although the dimer dissociation constant for αB-C ACD has not been definitively determined in solution,

it is likely to be in the low μM to high nM range at pH 7.4 and has not been reported at pH 6.0. Consequently, accurate determination of the dimer dissociation constant in solution both at pH7.4 and pH 6.0 is an important future direction for this work. To further demonstrate that the minor peaks we observe, which increase in intensity at low pH, correspond to the αB-C ACD monomer we also collected spectra at a protein concentration closer to the expected dimer dissociation constant (25 μM) at both pH 7.4 and pH 6.0 (Supplementary Fig. 4.6). This spectrum was also collected using a separate preparation of ^{15}N αB-C ACD. Analysis of these spectra revealed similar changes to those observed at 750 μM, pH 5.9 relative to 750 μM at pH 7.4. Peaks corresponding to the C-terminal end of β5, the loop between β5 and β6/7 and the β6/7 strand were generally not observable/identifiable at pH 6.0, while peaks corresponding to residues distal to the dimer interface could be identified based on spectra obtained at pH 7.4. An overlay of the spectra acquired at 750 μM, pH 5.9 and at 25 μM, pH 6.0 is shown in Supplementary Fig. 4.7. This overlay demonstrates that the majority of the unassigned peaks we observe at 750 μM are also observable at a concentration likely to be closer to the K_d of the dimer interface. This provides further evidence that the unassigned peaks arise from the αB-C ACD monomer. SV-AUC was also performed at a protein concentration close to the expected K_d for dimer dissociation (12.8 μM). This demonstrated a pH-dependent decrease in the sedimentation coefficient distribution from pH 7.4 – 6.0 (Fig. 4.8 B), consistent with an increase in the proportion of monomer existing at pH 6.0 relative to pH 7.4. Additionally, the sedimentation coefficient distribution of αB-C ACD E117C, which forms a disulfide cross-linked dimer, at pH 7.4 was found to be right-shifted relative to αB-C ACD at the same pH. This indicates that while αB-C ACD is predominantly dimeric at pH 7.4 and 12.8 μM, some monomer-dimer exchange contributes to the lower sedimentation coefficient observed relative to the disulfide cross-linked αB-C ACD E117C dimer. We also used SV-AUC to demonstrate that disulfide cross-linking at the dimer interface prevents dimer dissociation (Fig. 4.8 C). At pH 7.4 and in the absence of TCEP, αB-C ACD E117C forms a dimer with a weight-average sedimentation coefficient of 1.87 S. The reducing agent TCEP allows monomer-dimer exchange, resulting in a broader distribution shifted towards lower S values, however at pH 7.4 the peak corresponding to αB-C ACD E117C dimer is predominant (Fig. 4.8 C). At pH 6.0, αB-C ACD E117C can only undergo monomer-dimer exchange in the presence of TCEP. Under these conditions, a single asymmetric peak was observed in the c(s)

distribution with a peak position close to 1 S, indicating that the monomeric form of αB-C ACD E117C is predominantly populated.

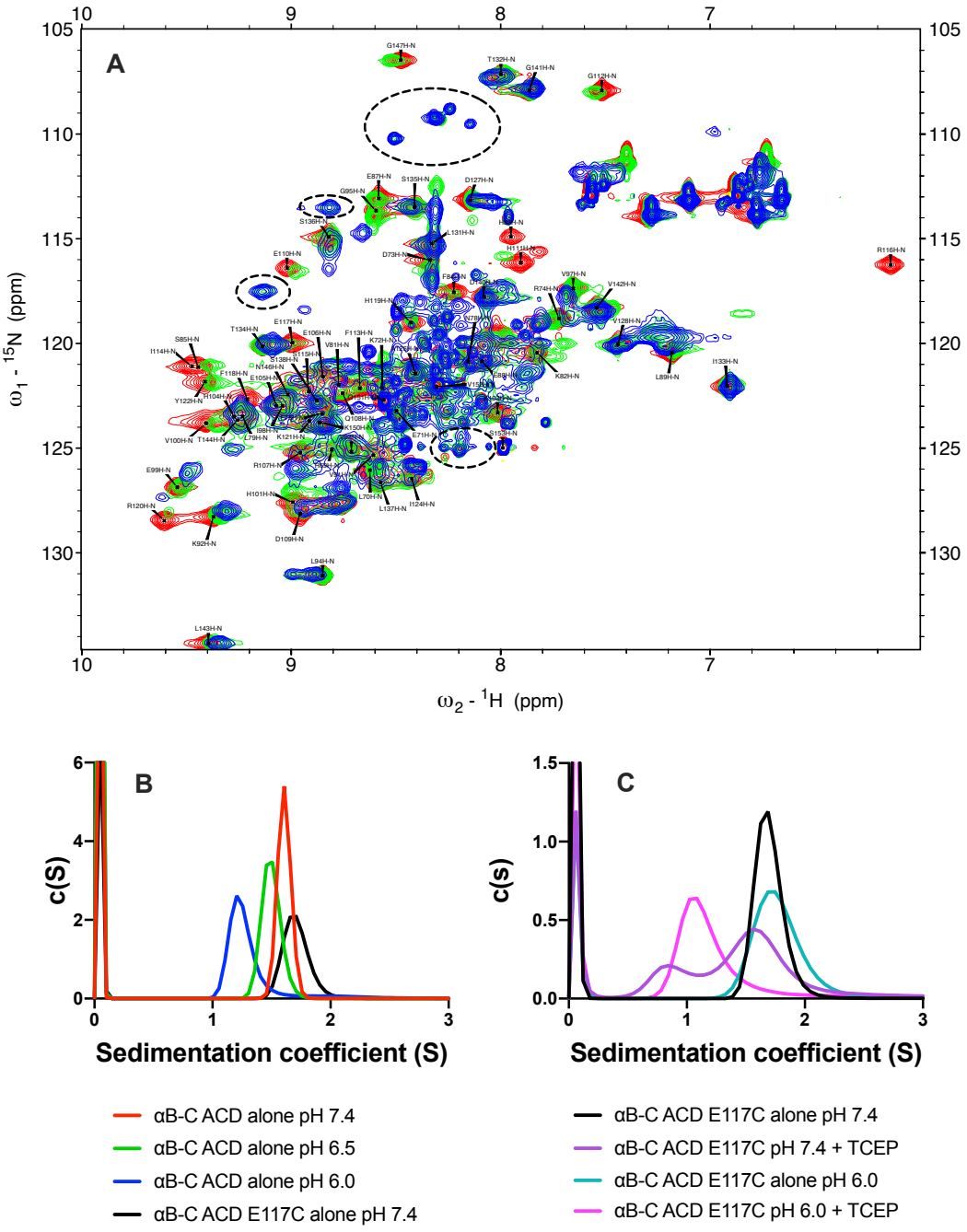
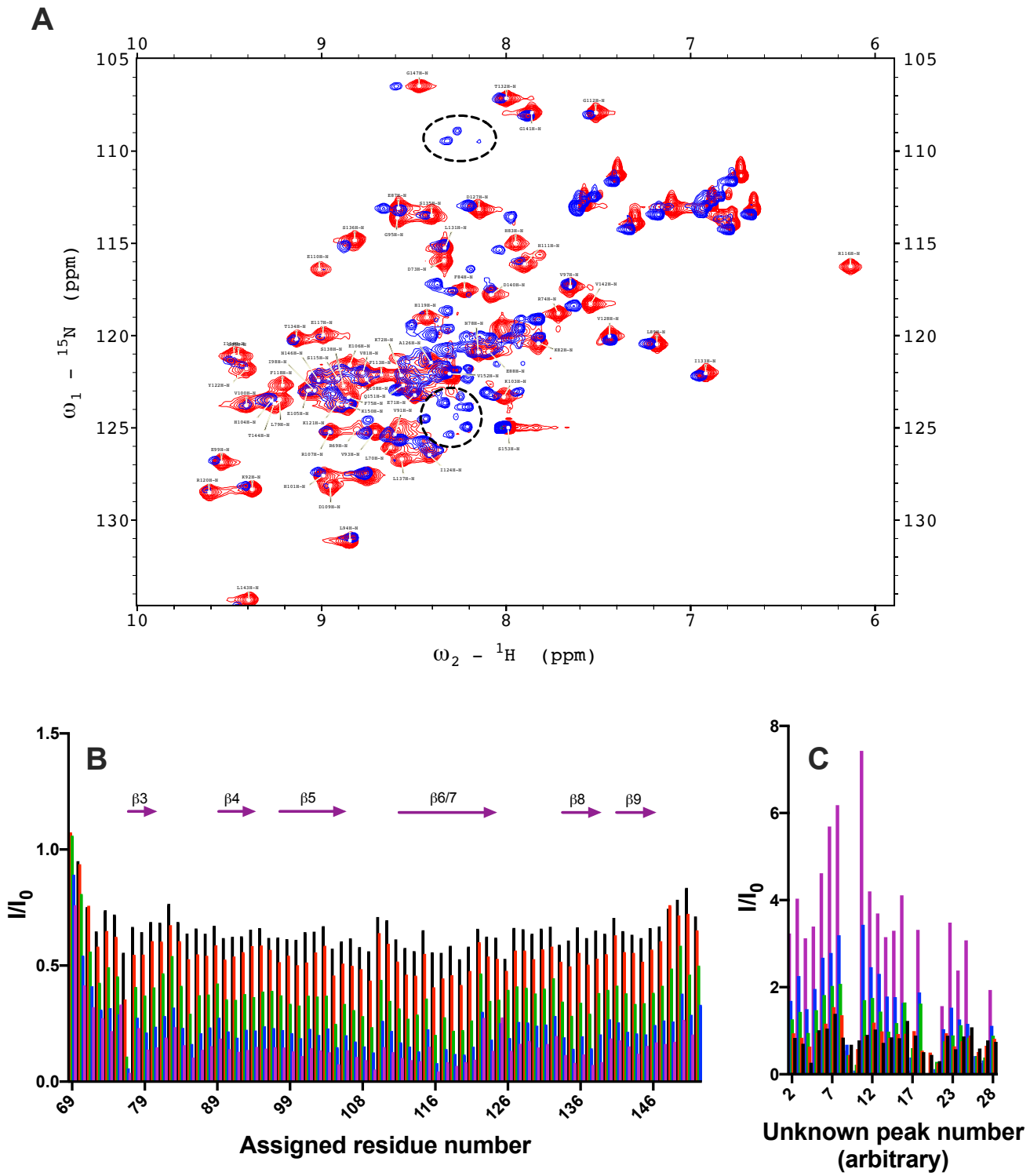


Figure 4.8. αB-C ACD transitions between monomer and dimer over the pH range 6.0 – 7.4. A) ^{15}N HSQC spectra acquired on a 750 μM sample of αB-C ACD at pH 7.4 (red), pH 6.5 (green) or pH 5.9 (blue). Some of the unassigned peaks that increase in

intensity as the pH is reduced are circled with a dashed line. B) Sedimentation coefficient distributions obtained via SV-AUC of 12.8 μM αB-C ACD at pH 7.4 (red), pH 6.5 (green), pH 6.0 (blue) or αB-C ACD E117C at pH 7.4 (black) using a detection wavelength of 225 nm. C) Sedimentation coefficient distributions obtained via SV-AUC of 12.8 μM αB-C ACD E117C at pH 7.4 (black), pH 7.4 + 2 mM TCEP (purple), pH 6.0 (cyan) or pH 6.0 + 2 mM TCEP (magenta).


A
ω_1 – ^{15}N (ppm)
ω_2 – ^{1}H (ppm)
B
β3
β4
β5
β6/7
β8
β9
I/I$_0$
Assigned residue number
C
I/I$_0$
Unknown peak number (arbitrary)
400 μM αB-C ACD, 50 mM GuHCl vs 400 μM αB-C ACD alone
400 μM αB-C ACD, 100 mM GuHCl vs 400 μM αB-C ACD alone
400 μM αB-C ACD, 200 mM GuHCl vs 400 μM αB-C ACD alone
400 μM αB-C ACD, 300 mM GuHCl vs 400 μM αB-C ACD alone
400 μM αB-C ACD, 400 mM GuHCl vs 400 μM αB-C ACD alone

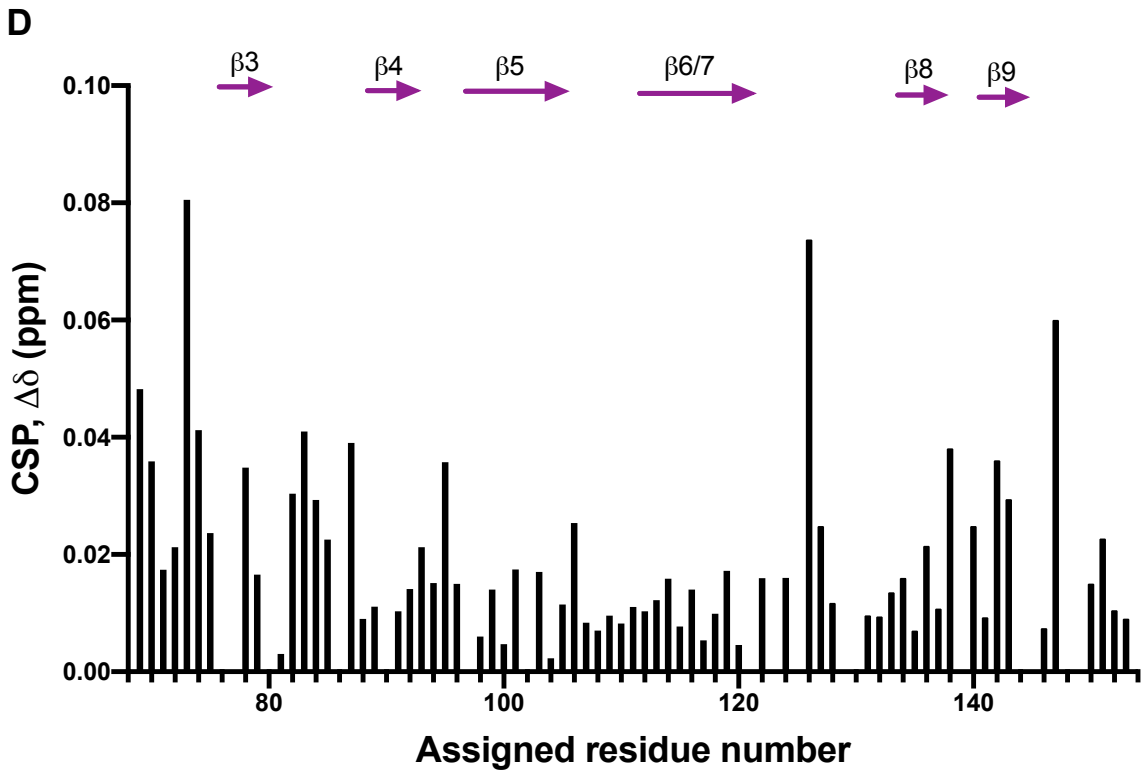


Figure 4.9. Titrating GuHCl perturbs the equilibrium between the minor and major state of αB-C ACD. A) Overlay of ^{15}N HSQCs of 400 μM αB-C ACD alone at pH 7.4 (red) with 400 μM αB-C ACD alone, 400 mM GuHCl, at pH 7.4 (blue). Some examples of unassigned peaks observed with increasing GuHCl concentration are circled with a dashed line. B) GuHCl was titrated into a sample of 400 μM αB-C ACD. The raw intensities of each assigned peak in the spectra at each titration concentration of GuHCl were divided by the raw intensity of each assigned peak in the spectra at 0mM GuHCl to generate I/I_0 ratios for each assigned peak. C) Additional unassigned peaks observed at higher GuHCl concentrations were selected and the raw intensities of these peaks were divided by the raw intensities of the peaks at 0 mM GuHCl (where possible) to generate I/I_0 ratios for each unassigned peak. D) Chemical shift perturbation (CSP) analysis of each assigned peak in the presence of 100 mM GuHCl relative to αB-C ACD alone.

Our next approach was to titrate αB-C ACD with the chaotrope, GuHCl from 0 mM to 400 mM. Our rationale for this experiment was based on recently published work in which Alderson *et al*. used Carr-Purcell-Meiboom-Gill (CPMG) relaxation dispersion NMR and high-pressure NMR to show that the Hsp27 ACD partially unfolds upon dimer dissociation[314]. Furthermore, the unfolding that occurs upon dimer dissociation was localised to the dimer interface[314]. The authors speculated that localised unfolding at the intradimer interface occurs in closely related human sHSPs, including αB-C. We

therefore sought to investigate spectral changes induced by low concentrations of GuHCl to determine whether partial unfolding induced by GuHCl produces similar spectral changes to those observed by lowering the pH. Titration of GuHCl from 0 - 400 mM resulted in a relative enhancement of the unassigned peaks and a reduction in the intensity of the assigned dimer peaks with increasing GuHCl concentrations (Fig. 4.9 A-C). An overlay of αB-C ACD at 0 mM GuHCl with αB-C ACD at 400 mM GuHCl demonstrates the appearance of new, unassigned peaks in similar positions to those observed in experiments performed at pH 6.5 and pH 6.0 (Fig. 4.9 A, Fig. 4.7 A, Fig. 4.8 A). Across the entire series of GuHCl titrations, the I/I_0 ratios for assigned peaks located near the dimer interface were marginally lower than those observed across the rest of the spectrum (Fig. 4.9 B), also in agreement with the I/I_0 ratios obtained at pH 6.5 vs pH 7.4 (Fig. 4.7 B). CSPs were calculated across all residues at 100 mM GuHCl relative to 0 mM (Fig. 4.9 D). However, shifts of greater than 0.04 ppm were mainly localised to solvent-exposed loops rather than the dimer interface, likely indicating that the chaotrope interferes with the hydrogen bonding network formed at the surface of the protein in the absence of GuHCl.

Lastly, we determined the ^{15}N nuclear spin transverse relaxation rates (R_2) of both the assigned and unassigned peaks at 750 μM, pH 7.4. The assigned peaks had relatively high R_2 rates (~20-30 s^{-1}) for a protein expected to form a dimer of ~20 kDa (Fig. 4.10 A). In particular, residues 82-83 and several residues at and near the dimer interface had R_2 rates of > 25 s^{-1} (Fig. 4.10 A) suggesting that these residues undergo chemical exchange on the micro to millisecond timescale that enhances their R_2 values. The unassigned peaks in the HSQC spectra had far lower R_2 values (Fig. 4.10 B), similar to the reported R_2 values for ubiquitin, a small, dynamic protein with a MW of 8.6 kDa[366,367]. This indicates that the unknown peaks may arise from a flexible protein of a similar size, properties that could be expected of the ACD monomer (~10 kDa). Although we have not unambiguously determined the identity of these peaks, these three data sets (and the work presented by Rajagopal *et al.*[316]) strongly support our hypothesis that they correspond to an alternate conformation of the ACD, and that this conformation is most likely monomeric and flexible.

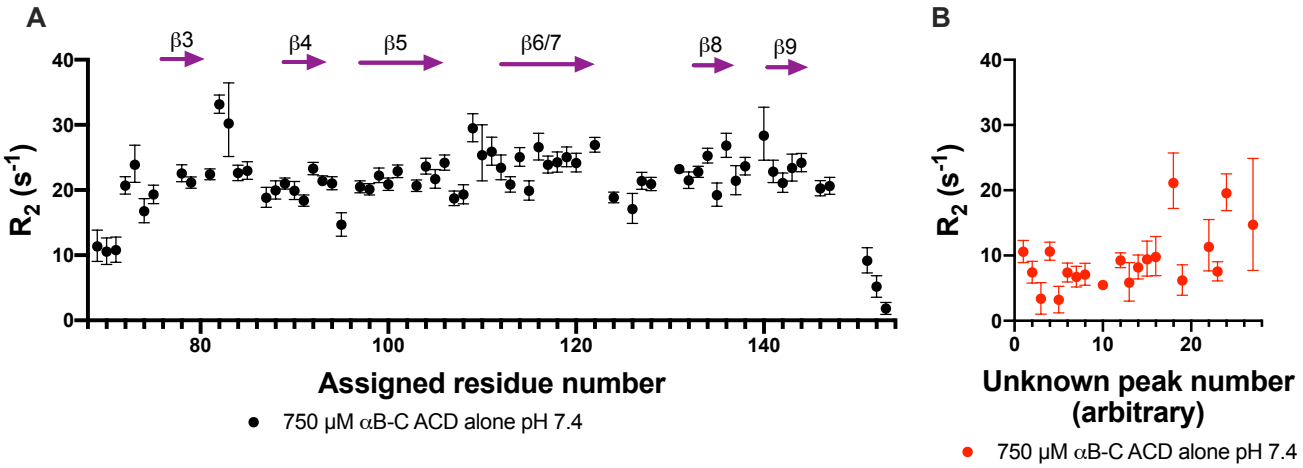
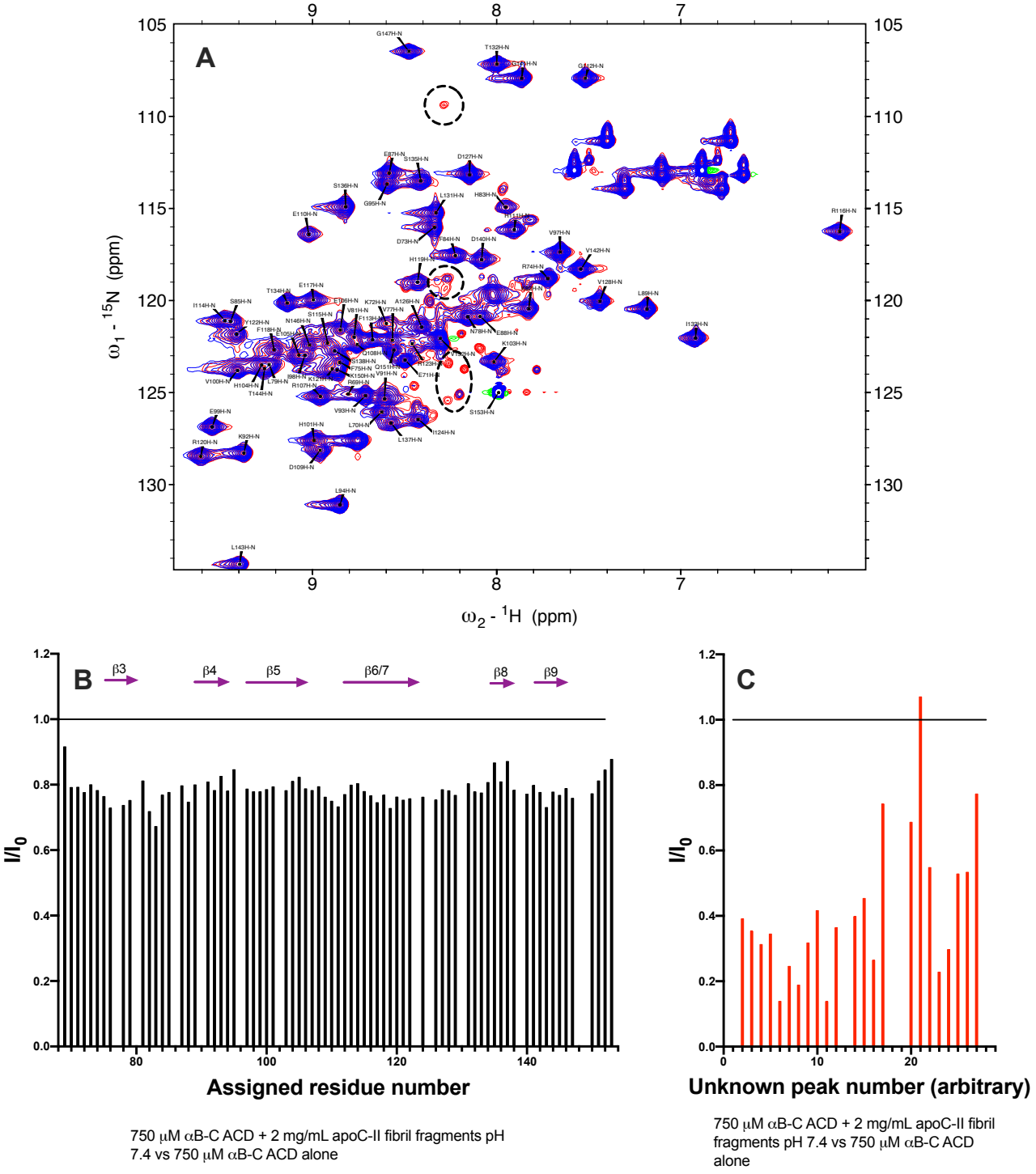


Figure 4.10. Nuclear spin transverse relaxation rates for (A) assigned peaks and (B) unassigned peaks in the spectra observed for a sample containing 750 μM αB-C ACD, pH 7.4, 25°C. Relaxation delays of 17 ms to 136 ms were used to obtain nuclear spin relaxation decay curves. ^{15}N relaxation parameters were determined by fitting the raw decay data to a single exponential decay (methods section 2.2.21.5) using the software GraphPad in Prism version 8. Error bars represent the 95% confidence interval.

4.3.4 The αB-C ACD monomer binds apoC-II fibrils

After these initial experiments, we then added apoC-II fibrils fragmented by sonication to a final concentration of 2 mg/mL. We observed that the assigned peaks corresponding to the ACD dimer were modestly broadened (I/I_0 = 0.78 ± 0.05) relative to the ACD alone (Fig. 4.11 A-B), consistent with our initial observations of peak broadening for the 50 μM sample of αB-C ACD in the presence of 10 mg/mL apoC-II fibrils (Fig. 4.6). However, the majority of unassigned peaks corresponding to the monomer were broadened to a greater extent (I/I_0 = 0.42 ± 0.23) than the assigned dimer peaks (Fig. 4.11 A and C), indicating that the species corresponding to these peaks may be the primary fibril-interacting species. CSPs were calculated for the assigned residues in the presence of apoC-II fibrils, however only one CSP > 0.004 ppm was detected (Fig. 4.11 D). Thus, under these conditions no significant resonance changes were observed for the assigned peaks. These experiments have been independently replicated at two different αB-C ACD concentrations (100 μM and 250 μM) using a different preparation of ^{15}N αB-C ACD and two different apoC-II preparations. Although fewer unassigned peaks are observed at these

concentrations, an identical trend is observed: the unassigned peaks are broadened to a greater extent than the assigned peaks. This data is shown in Supplementary Fig. 4.8 and Supplementary Fig. 4.9.



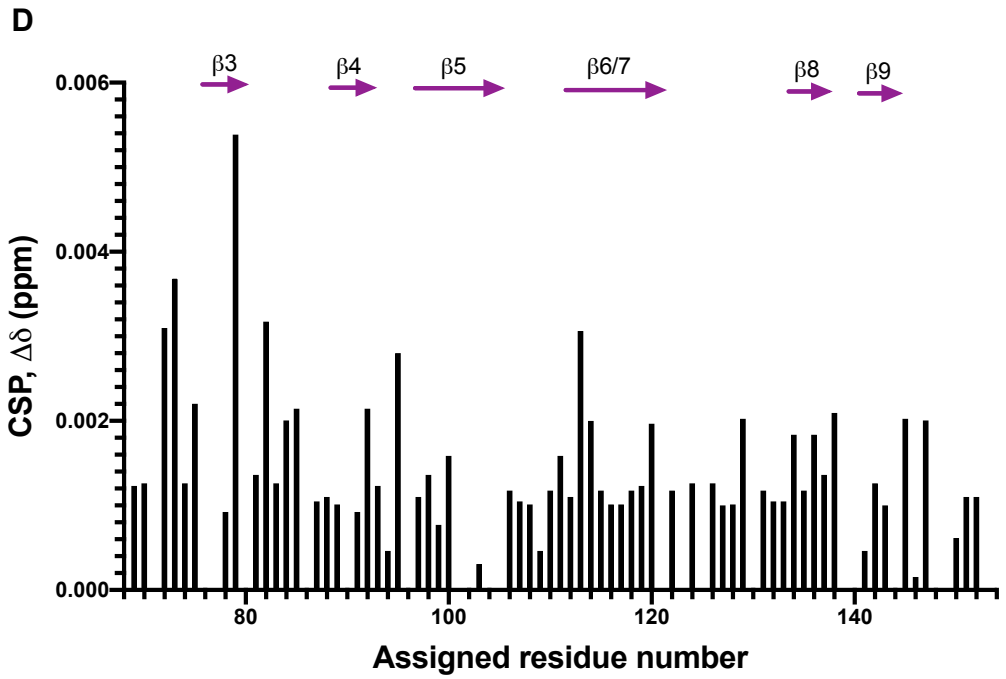
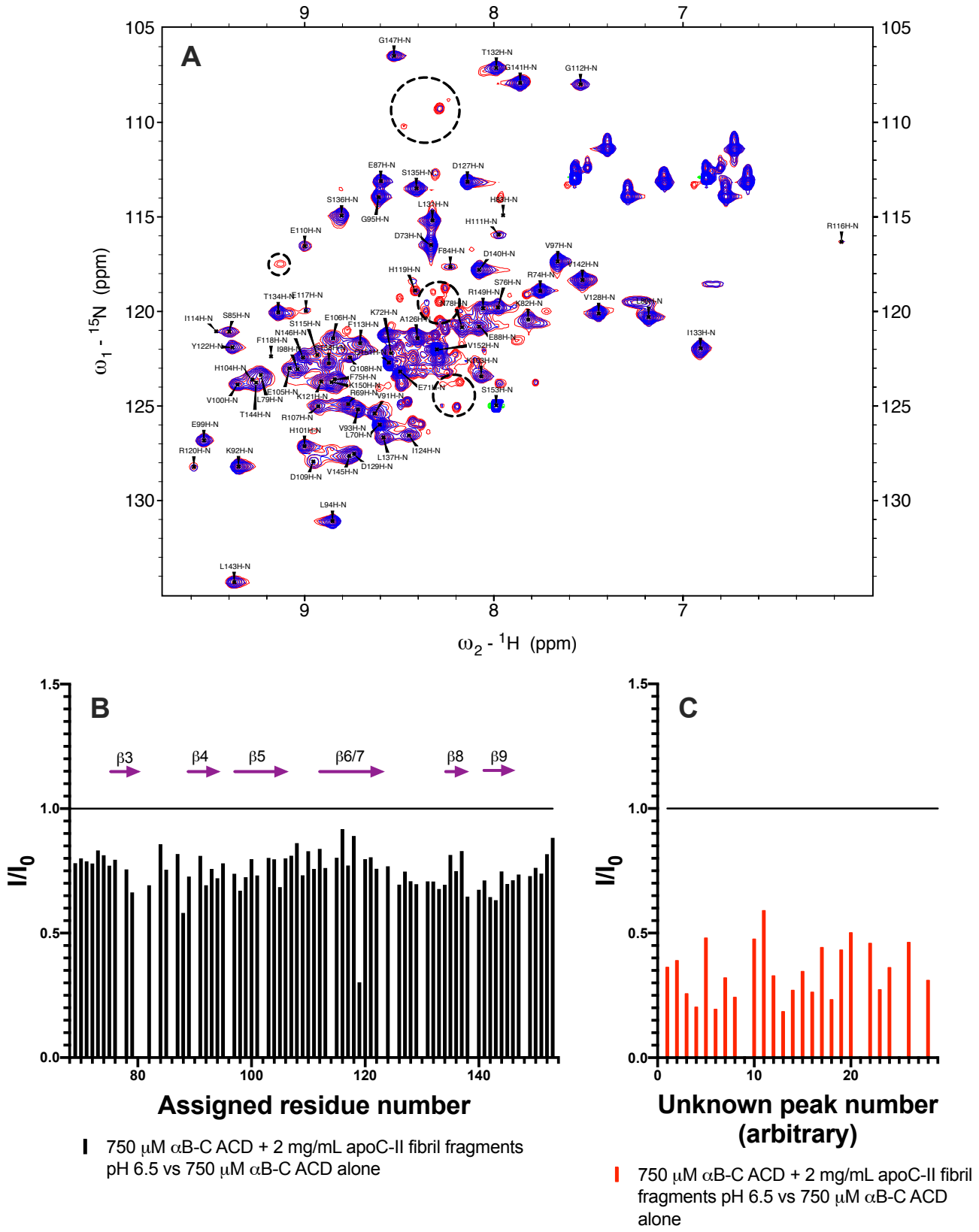


Figure 4.11. In the presence of apoC-II fibrils, peaks corresponding to the minor state are broadened to a greater extent than the peaks corresponding to the major state. A) ^{15}N HSQC of 750 μM αB-C ACD alone at pH 7.4 (red) and in the presence of 2 mg/mL apoC-II fibril fragments (blue). A selection of unassigned peaks are circled with a dashed line. B) The raw intensities of the assigned peaks in the presence of fibril fragments were divided by the raw intensities of the assigned peaks in the αB-C ACD alone sample to generate I/I_0 ratios for the assigned peaks. C) The raw intensities of the unassigned peaks in the presence of fibril fragments were divided by the raw intensities of the unassigned peaks in the αB-C ACD alone sample to generate I/I_0 ratios for the unassigned peaks. In (B) and (C) an I/I_0 ratio of 1 is indicated by a black line. D) Chemical shift perturbation analysis of each assigned peak in the presence of 2 mg/mL of fragmented apoC-II fibrils relative to αB-C ACD alone at pH 7.4.

To further test the hypothesis that the minor state is the primary fibril-interacting species, a further two ^{15}N HSQCs were collected, one in the absence and one in the presence of apoC-II fibrils, at pH 6.5. Consistent with our earlier observations, at the reduced pH, the intensity of the unassigned peaks was enhanced, and as many as 50 additional peaks can be identified (Fig. 4.12 A). Again, in the presence of the fibril fragments, the assigned dimer peaks are broadened to some extent ($I/I_0 = 0.75 \pm 0.09$), while the unassigned peaks are broadened to a greater extent ($I/I_0 = 0.35 \pm 0.11$) (Fig. 4.12 B-C). Only extremely small CSPs (> 0.006 ppm) were observed, mainly localised to β6/7 and the preceding loop near the dimer interface (Fig. 4.12 D). The enhanced signal broadening observed for the unassigned

peaks relative to the assigned peaks support our hypothesis that the species giving rise to the unassigned peaks, which we propose to be the monomer, interacts with the fibrils.


A
B
C
ω_1 - ^{15}N (ppm)
ω_2 - ^{1}H (ppm)
β3
β4
β5
β6/7
β8
β9
I/I$_0$
Assigned residue number
Unknown peak number (arbitrary)
750 μM αB-C ACD + 2 mg/mL apoC-II fibril fragments pH 6.5 vs 750 μM αB-C ACD alone
750 μM αB-C ACD + 2 mg/mL apoC-II fibril fragments pH 6.5 vs 750 μM αB-C ACD alone

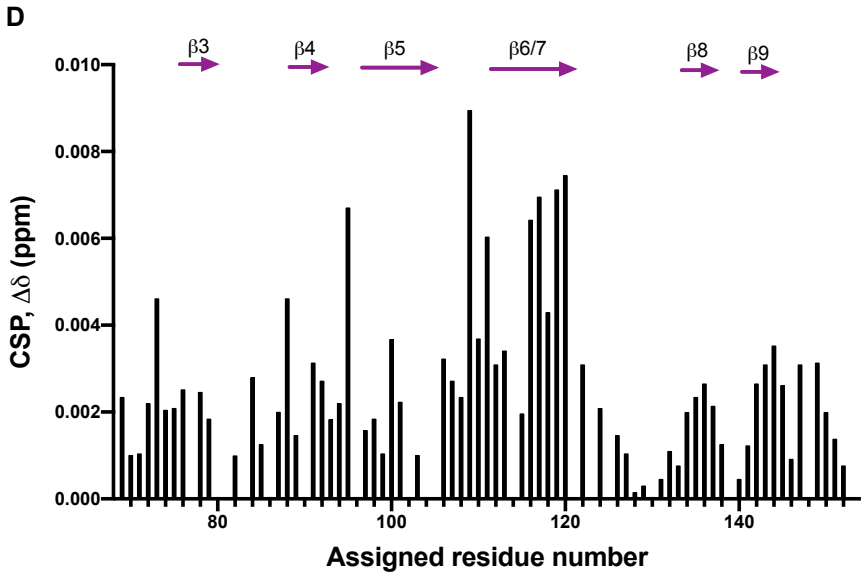
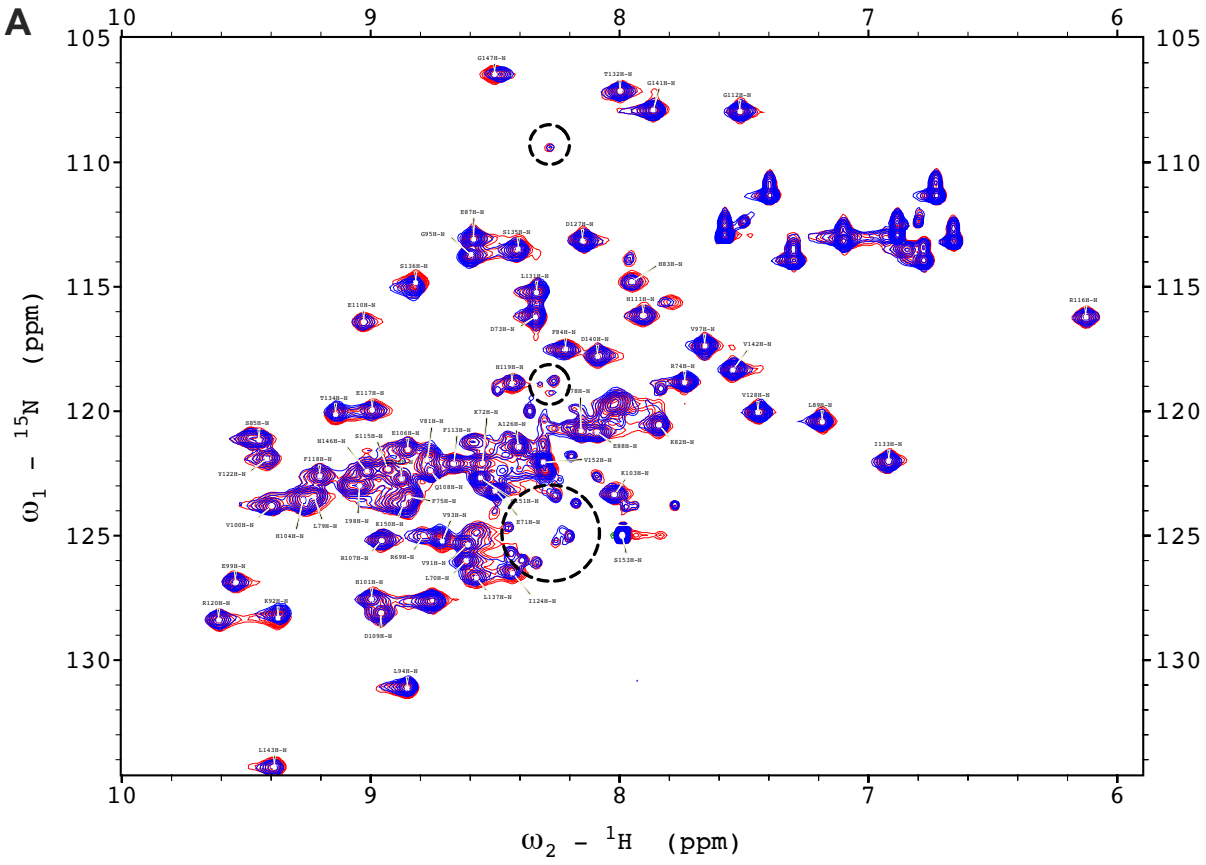


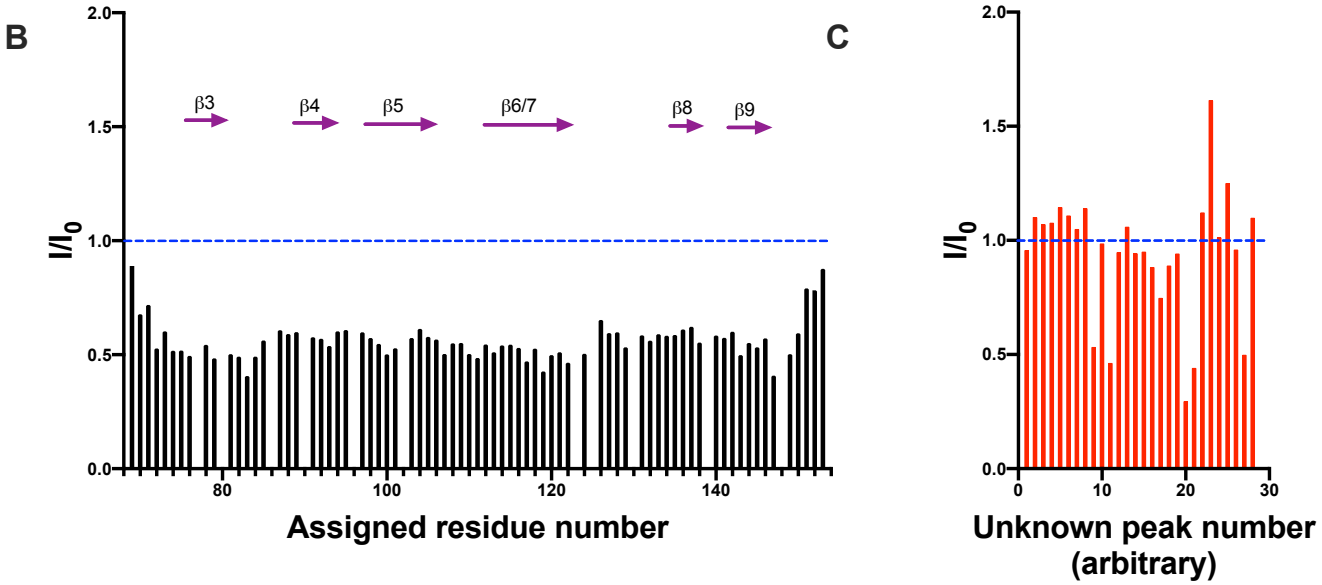
Figure 4.12. In the presence of apoC-II fibrils at pH 6.5, peaks corresponding to the minor state are broadened to a greater extent than the peaks corresponding to the major state. A) ^{15}N HSQC of 750 μM αB-C ACD alone at pH 6.5 (red) and in the presence of 2 mg/mL apoC-II fibril fragments (blue). B) The raw intensities of the assigned peaks in the presence of fibril fragments were divided by the raw intensities of the assigned peaks in the αB-C ACD alone sample to generate I/I_0 ratios for the assigned peaks. C) The raw intensities of the unassigned peaks in the presence of fibril fragments were divided by the raw intensities of the unassigned peaks in the αB-C ACD alone sample to generate I/I_0 ratios for the unassigned peaks. D) Chemical shift perturbation analysis of each assigned peak in the presence of 2 mg/mL of fragmented apoC-II fibrils relative to αB-C ACD alone at pH 6.5.

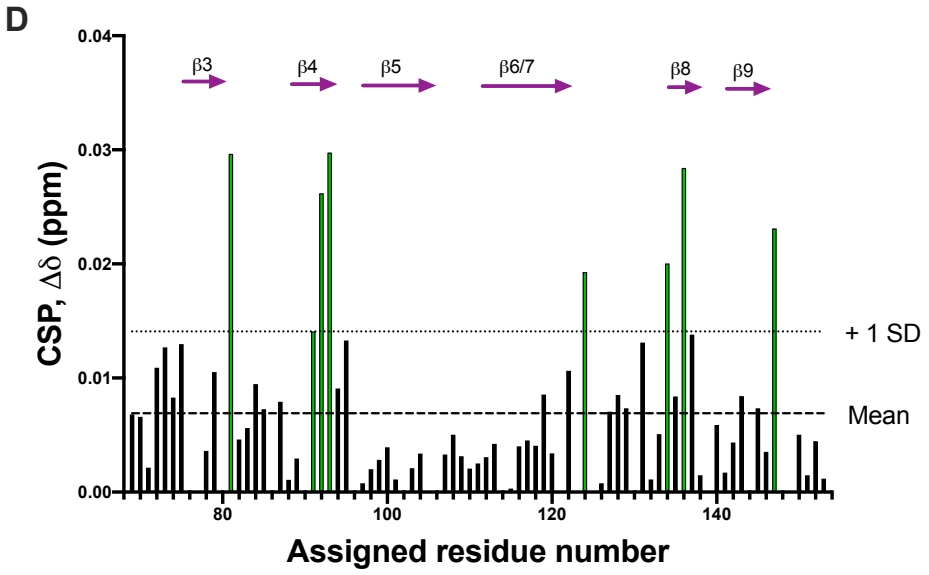
4.3.5 αB-C ACD interacts with monomeric and fibrillar α-syn via distinct binding sites

We next collected two additional ^{15}N HSQCs on a 500 μM sample of αB-C ACD at pH 7.4 alone or in the presence of 1000 μM of monomeric α-syn. Initially, the rationale for this experiment was to closely reproduce previously published results in which ^{15}N HSQCs were collected for αB-C ACD alone and in the presence of a 2:1 molar ratio of monomeric α-syn[281]. In general, we observed similar small peak shifts for the assigned residues that Liu *et al.* highlighted, K92, V93, I124, T134, S135, S136 (Fig. 4.13 A, D and E)[281]. Furthermore, additional unassigned peaks are readily observed in their spectra although these are not mentioned in their analysis. These unassigned peaks are generally in similar positions to those observed in our spectra (Fig. 4.13 A). To our knowledge, the additional peaks have not yet been assigned, which is likely due to the fact that the signal intensity for these peaks is extremely weak

relative to the assigned peaks. Analysis of the intensity ratios of the assigned and unassigned peaks revealed an interesting trend: in general, the assigned peaks were broadened ($I/I_0 = 0.56 \pm 0.09$) to a greater extent than the unassigned peaks ($I/I_0 = 0.94 \pm 0.28$), with a few notable exceptions (Fig. 4.13 B-C). This trend suggests that the species corresponding to the minor state may not interact with monomeric α-syn. The generalised peak broadening most likely signifies that the dimer of αB-C ACD binds transiently with soluble α-syn monomer. Based on the results of their ^{15}N HSQCs, Liu *et al.* proposed that the interaction interface between αB-C ACD and monomeric α-syn is located at the β4/8 hydrophobic groove[281] and not the interface of the dimer. Here we have mapped residues with the largest CSPs (> mean CSP calculated cross all residues + 1 SD) onto the structure of the αB-C ACD dimer in Fig. 4.13 E. From this analysis it is evident that residues with relatively larger CSPs are mainly localised to the β4/8 groove. Therefore, our results are generally consistent with the results Liu *et al.* presented in their work.


A
10
9
8
7
6
105
110
115
120
125
130
ω_1 – ^{15}N (ppm)
ω_2 – ^{1}H (ppm)


B
C
β3
β4
β5
β6/7
β8
β9
I/I0
Assigned residue number
Unknown peak number
(arbitrary)


D
β3
β4
β5
β6/7
β8
β9
CSP, Δδ (ppm)
+ 1 SD
Mean
Assigned residue number

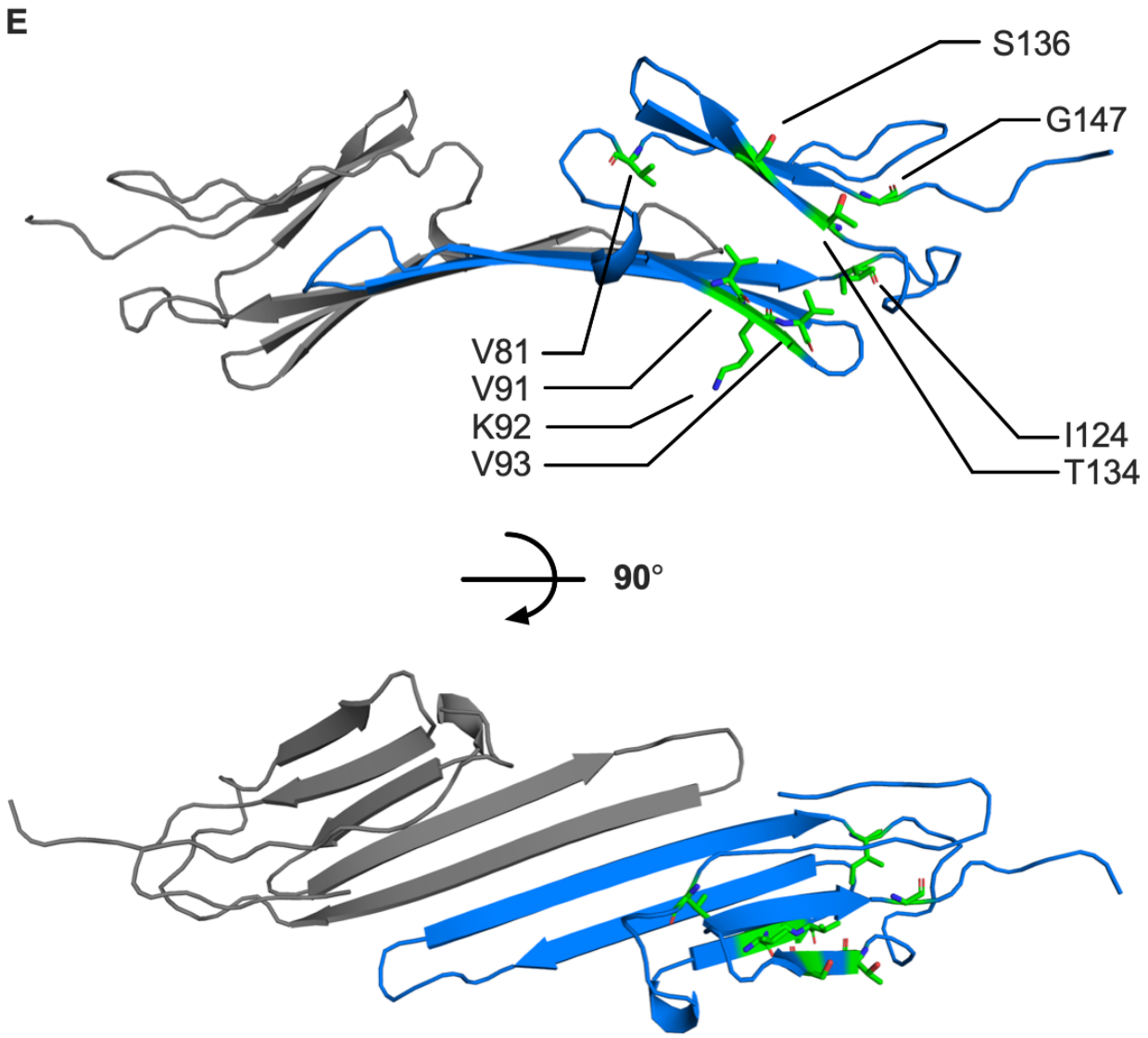
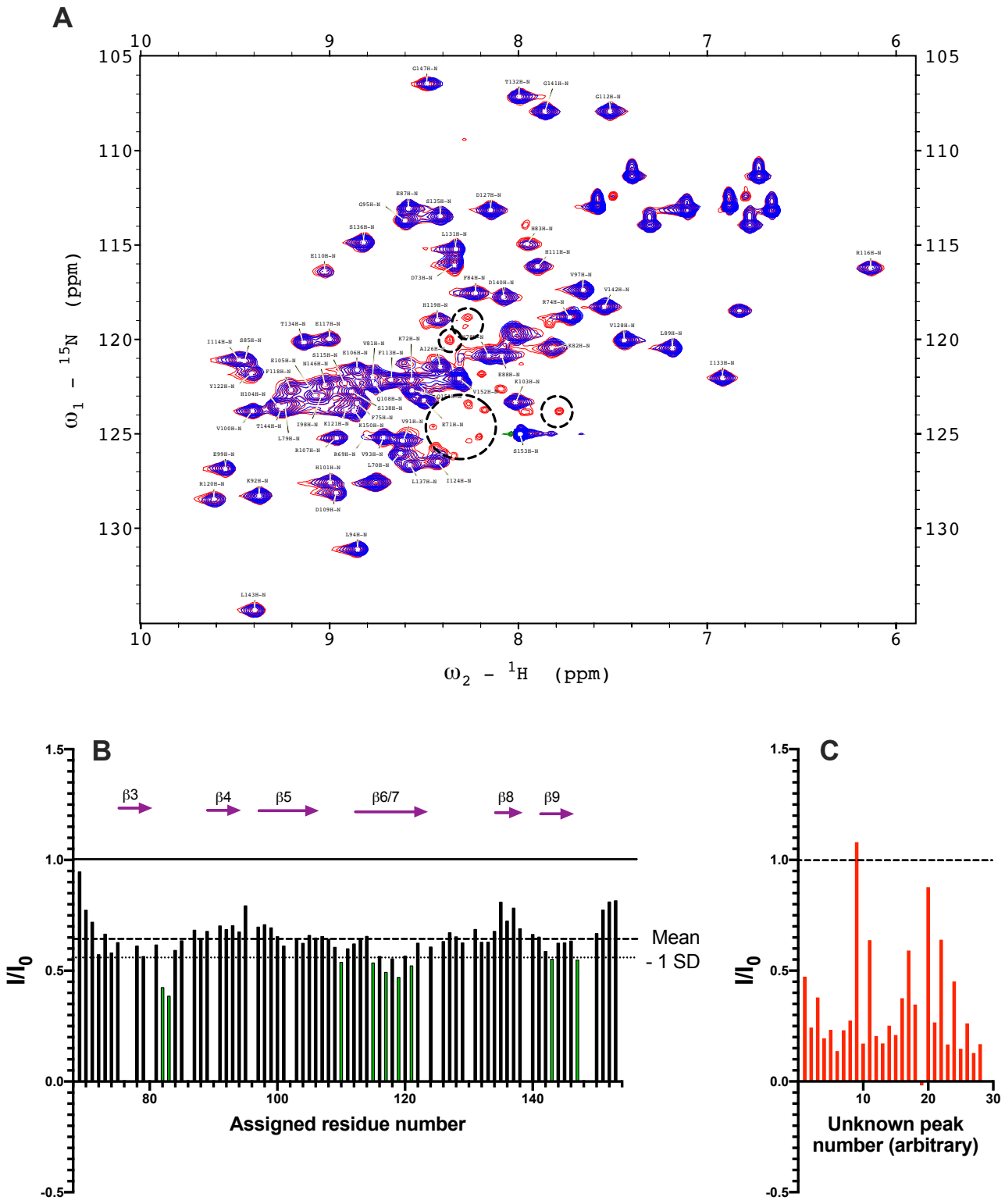


Figure 4.13. In the presence of monomeric α-syn, peaks corresponding to the major state are broadened to a greater extent than the peaks corresponding to the minor state. A) ^{15}N HSQC of 500 μM αB-C ACD alone at pH 7.4 (red) and in the presence of 1000 μM α-syn monomer (blue). A selection of unassigned peaks is circled with a dashed line. B) The raw intensities of the assigned peaks in the presence of α-syn were divided by the raw intensities of the assigned peaks in the αB-C ACD alone sample to generate I/I_0 ratios for the assigned peaks. C) The raw intensities of the unassigned peaks in the presence of α-syn were divided by the raw intensities of the unassigned peaks in the αB-C ACD alone sample to generate I/I_0 ratios for the unassigned peaks. In (B) and (C) a dashed blue line indicates an I/I_0 ratio of 1. D) CSP analysis for the assigned peaks in the presence of α-syn monomer relative to αB-C ACD alone. A dashed black line indicates the mean CSP calculated across all

residues and a dotted black line indicates the mean CSP + 1 SD. E) The crystal structure of the αB-C ACD dimer (PDB: 4m5s) is shown with one subunit in blue and one in grey. Residues with CSPs > the mean CSP + 1 SD were mapped onto one of the subunits of the crystal structure of the dimer in green and shown as lines.

To determine whether the interaction of αB-C ACD with α-syn fibrils was similar to its interaction with monomeric α-syn, we collected a further two ^{15}N HSQCs of 500 μM sample of αB-C ACD at pH 7.4 alone or in the presence of 1000 μM of fibrillar α-syn (Fig. 4.14 A). Here we also sonicated the α-syn fibrils to increase the abundance of fibril ends in a manner similar to that done for the apoC-II fibrils in the previous experiments. Interestingly, unlike the sample containing monomeric α-syn, the peaks corresponding to the minor state were generally broadened ($I/I_0 = 0.33 \pm 0.24$) to a greater extent than the peaks corresponding to the major state ($I/I_0 = 0.64 \pm 0.10$) (Fig. 4.14 B-C). This trend is similar to the trend observed in the experiments containing apoC-II fibrils, indicating that the minor state of αB-C ACD interacts with both types of fibrils. However, in the presence of fibrillar α-syn, the assigned resonances were generally broadened to a greater extent than for apoC-II. Analysis of the I/I_0 ratios for the assigned peaks in the presence of α-syn fibrils revealed that residues at the dimer interface were broadened marginally more than the other assigned peaks (with I/I_0 ratios < mean I/I_0 ratio – 1 SD) (Fig. 4.14 B). These residues were mapped to the structure of the ACD dimer in Fig. 4.14 D. We also calculated CSPs for all of the assigned peaks (Fig. 4.14 E). This revealed small CSPs of approximately 0.01 – 0.02 ppm at the dimer interface, but additional CSPs were identified in the loops between strands β2 and β3 and between β3 and β4, suggesting this region may also be important for interacting with α-syn fibrils. As this experiment has only been undertaken once, it is important to further validate these results by replicating this experiment at a lower pH, at which the minor peaks are more readily observed.


A
B
C
β3
β4
β5
β6/7
β8
β9
Mean
- 1 SD
I/I0
Assigned residue number
Unknown peak
number (arbitrary)

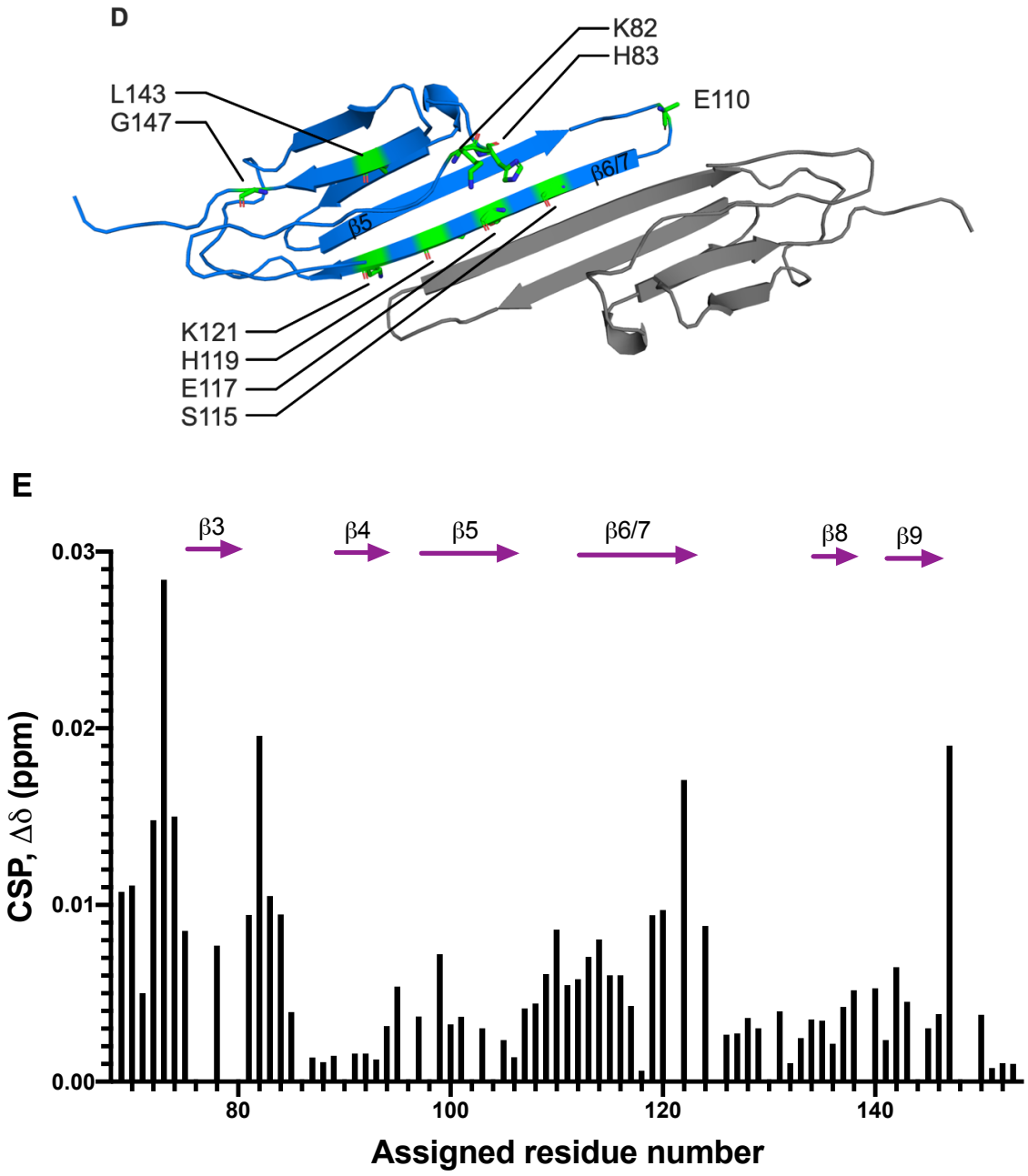


Figure 4.14. In the presence of fibrillar α-syn, peaks corresponding to the minor state are broadened to a greater extent than the peaks corresponding to the major state. A) ^{15}N HSQC of 500 μM αB-C ACD alone at pH 7.4 (red) and in the presence of 1000 μM α-syn fibril fragments (blue). A selection of unassigned peaks are circled with dashed lines. B) The raw intensities of the assigned peaks in the presence of fibril fragments were divided by the raw intensities of the assigned peaks in the αB-C ACD alone sample to generate I/I_0 ratios for the assigned peaks. A solid black line indicates an I/I_0 ratios of 1, a dashed black line indicates the mean I/I_0 ratio calculated across all residues and a dotted black line indicates the mean I/I_0 – 1 SD. Residues with I/I_0 ratios < the mean – 1 SD are coloured green. C) The raw intensities of the unassigned peaks in the presence of fibril fragments were divided by the raw intensities of the unassigned peaks in the αB-C ACD alone sample to generate I/I_0 ratios

for the unassigned peaks. A dashed black line indicates an I/I_0 ratio of 1. D) The crystal structure of the αB-C ACD dimer (PDB: 4m5s) is shown with one subunit in blue and one in grey. Residues with I/I_0 ratios calculated to be < the mean – 1 SD were plotted onto the structure of one of the subunits of the dimer in green and represented as lines. E) CSP analysis of each assigned peak in the presence of 1000 μM α-syn fibril fragments relative to αB-C ACD alone.

Across all of the experiments at the higher αB-C ACD concentrations, numerical, albeit arbitrary, values were assigned to each minor peak, in order to compare the trends in the intensity ratios across multiple experiments. The unassigned peaks were subsequently clustered according to three variables: (1) whether their signals were enhanced by a reduction in pH from 7.4 to 6.5, (2) whether their signals were broadened in the presence of monomeric α-syn and (3) whether their signals were broadened in the presence of both apoC-II and α-syn fibrils. For these variables, the following I/I_0 thresholds were chosen: (1) 1.2, (2) 0.75 and (3) 0.4. Thirteen of the unassigned peaks were broadened in the presence of both fibril types and of these, seven were enhanced by a reduction in pH (Fig. 4.15). Six of the unassigned peaks were also below the threshold set for peak broadening in the presence of monomeric α-syn, however none of these were broadened in the presence of both fibril types (Fig. 4.15), which supports the hypothesis that αB-C ACD interacts differently with fibrils relative to monomeric α-syn. It is important to note however, that the majority of the assigned peaks were also below the 0.75 I/I_0 threshold set for peak broadening in the presence of monomeric α-syn (Fig. 4.13 B). Therefore, our two main observations are that a conserved sub-set of unassigned peaks are specifically broadened in the presence of fibrils, and a separate sub-set of unassigned peaks are broadened to a similar extent as the majority of the assigned peaks in the presence of monomeric α-syn.

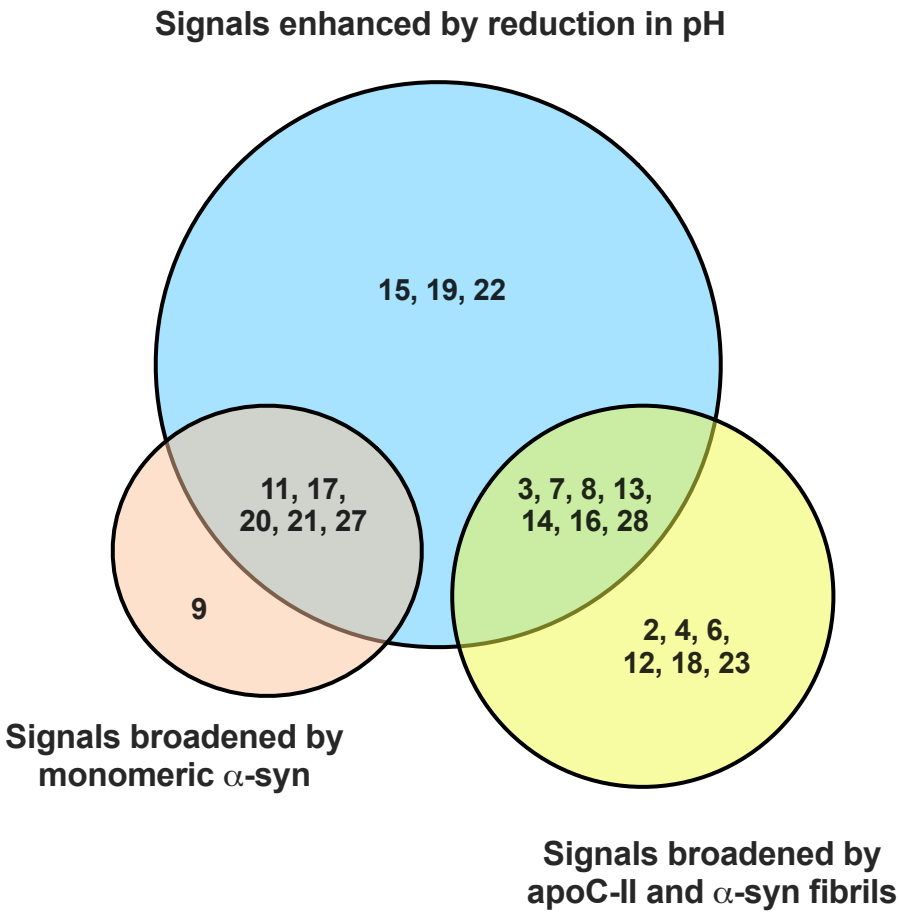
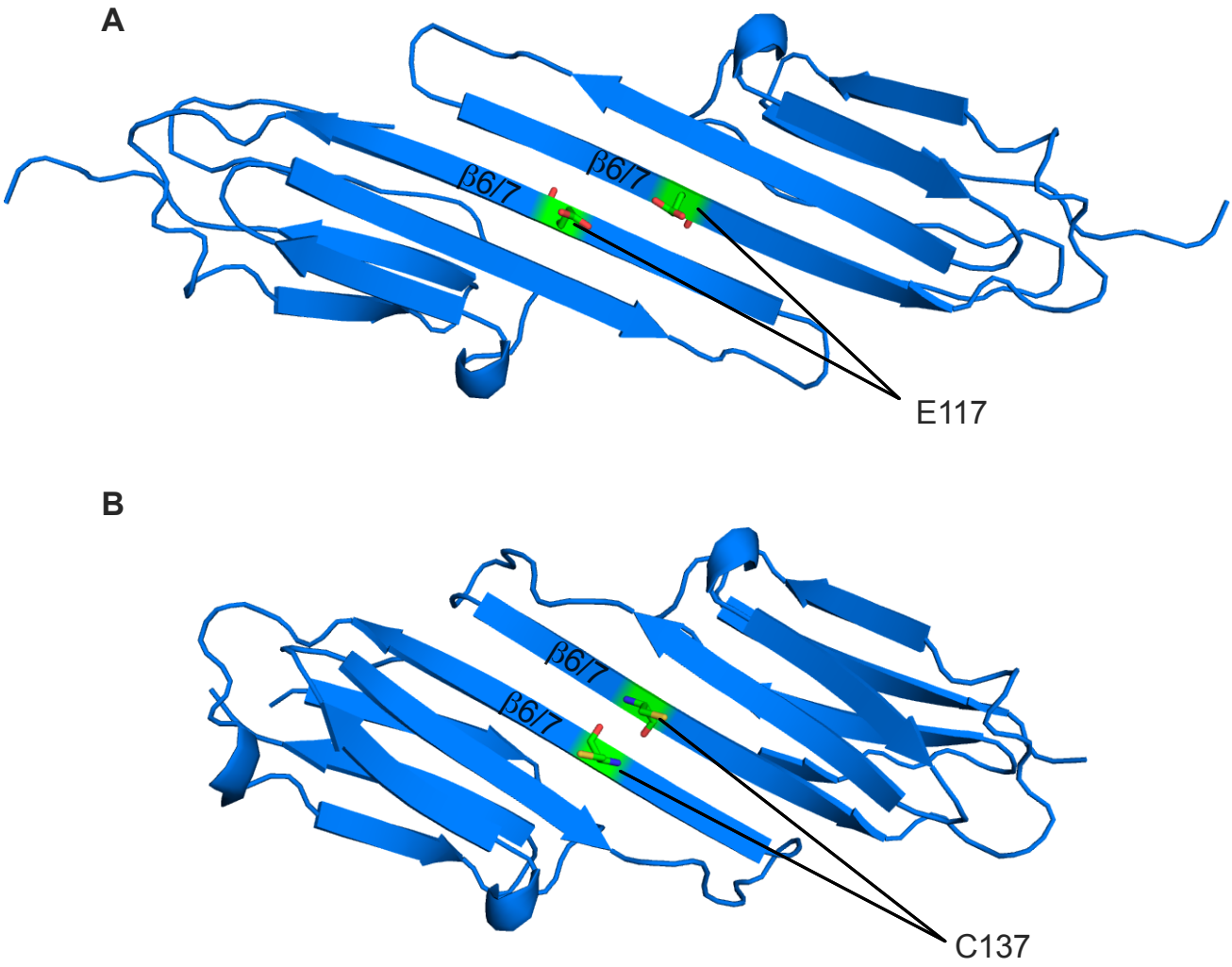


Figure 4.15. Meta-analysis of the intensity ratio trends of unassigned peaks across multiple experiments represented as a Venn diagram. Intensity ratios (I/I_0) were calculated for each unassigned peak across the experiments shown in Figures 4.7, 4.11, 4.12, 4.13 and 4.14. The intensity ratios were then analysed according to three variables: (1) enhancement of signal intensity at pH 6.5 relative to 7.4 (blue), (2) broadening in the presence of monomeric α-syn (green) and (3) broadening in the presence of both apoC-II and α-syn fibrils (purple). For the first variable, the mean I/I_0 ratio of each unassigned peak was calculated across two experiments: pH 6.5 vs pH 7.4 at 20°C, and pH 6.5, 30°C vs pH 7.4, 20°C. The threshold for signal enhancement was set as $I/I_0 \geq 1.2$. For the second variable, the threshold for signal broadening was set as $I/I0 < 0.75$. For the third variable, the threshold for signal broadening was set as $I/I_0 < 0.4$ in both experiments.

4.3.6 αB-C ACD and Hsp27 ACD dimers can be cross-linked via an inter-subunit disulfide bridge

The results of the ^{15}N HSQC experiments performed in the presence of both fibril types suggest that the minor state of αB-C ACD interacts with fibrils. Based on the data presented in Figures 4.7 – 4.10, we hypothesized that the minor state corresponds to the ACD monomer. As an alternative way of testing

this hypothesis, we turned to a closely related sHSP, Hsp27, which has been shown to form disulfide cross-linked dimers via an intermolecular disulfide bridge. This interchain disulfide bridge is formed via a conserved cysteine residue, C137 which is located at the centre of the dimer interface β6/7 strand and opposite the same residue in the other subunit (Fig. 4.16 B). This disulfide bridge can be reduced in the presence of reducing agents such as TCEP (Fig. 4.16 C), and we additionally purified C137S constructs of WT Hsp27 and Hsp27 ACD in order to eliminate non-specific effects that could arise due to the presence of TCEP (Fig. 4.16 C, H-M). We confirmed that all our unmutated Hsp27 constructs, including the full-length but primarily dimeric construct for Hsp27 (Hsp27-3D) and the construct lacking the CTR (Hsp27-3DΔCTR) form disulfide-linked dimers and that the C137S mutants do not, using SDS-PAGE and MS (Fig. 4.16). Furthermore, we mutated the corresponding interface residue (Fig. 4.16 A, C-G) in both full-length αB-C and αB-C ACD from a glutamate to a cysteine residue and confirmed that these E117C mutants can form disulfide cross-linked dimers using SDS-PAGE under reducing and non-reducing conditions and MS (Fig. 4.16). CD spectroscopy was used to confirm that the point mutations did not significantly alter the secondary structure of the sHSP constructs (Supplementary Fig. 4.10).


A
β6/7
β6/7
E117
B
β6/7
β6/7
C137

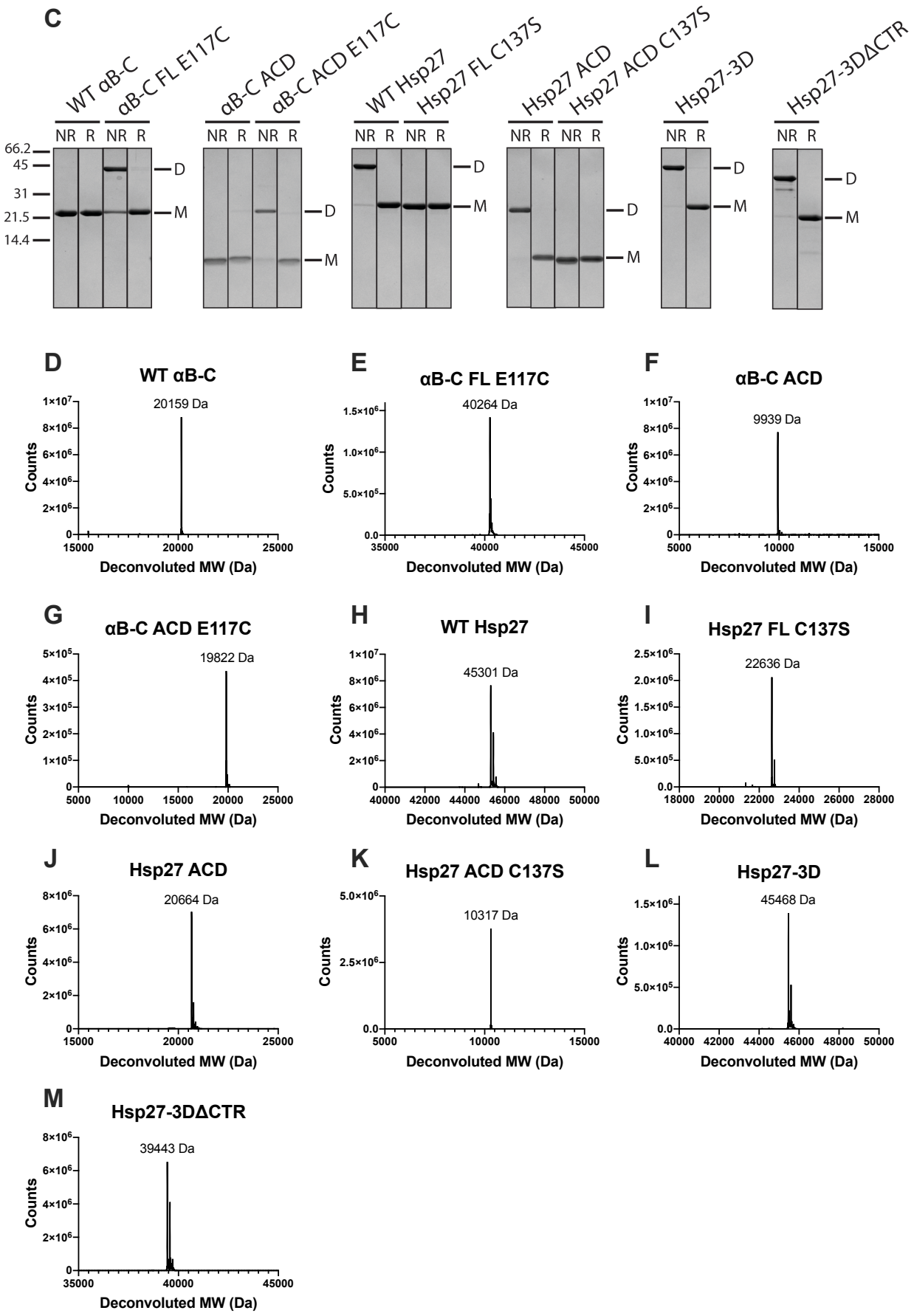
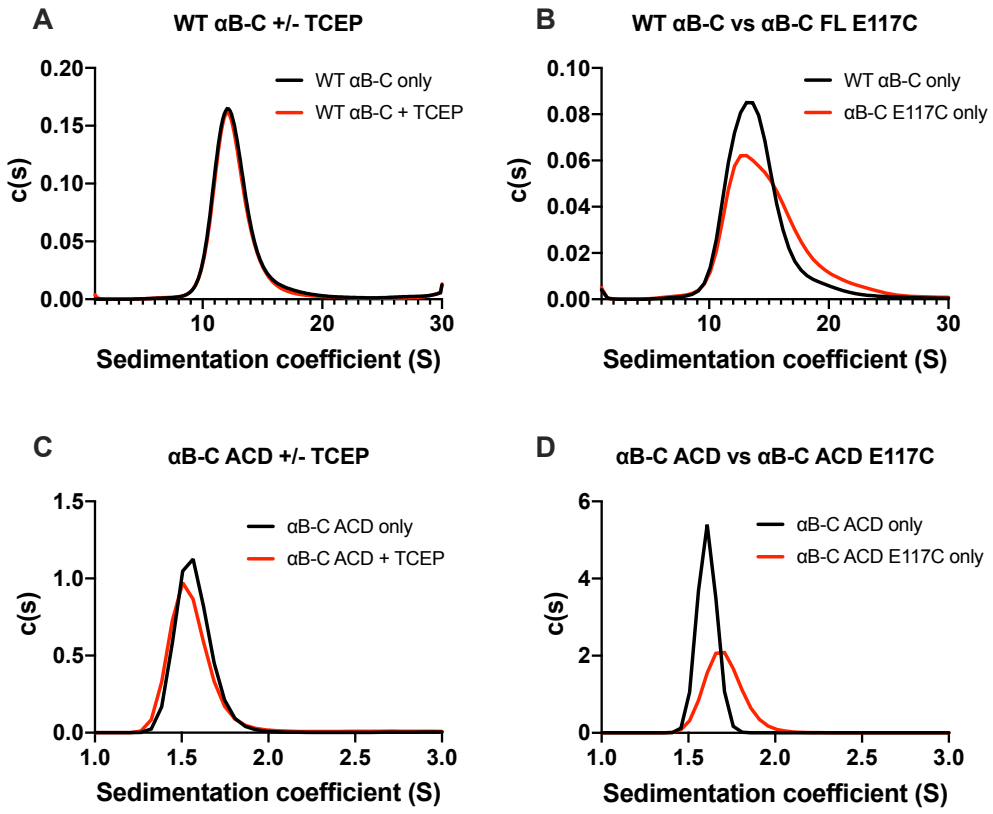

C
WT αB-C
αB-C FL E117C
αB-C ACD
αB-C ACD E117C
WT Hsp27
Hsp27 FL C137S
Hsp27 ACD
Hsp27 ACD C137S
Hsp27-3D
Hsp27-3DΔCTR
NR R NR R
66.2
45
31
21.5
14.4
D
M
D
WT αB-C
20159 Da
E
αB-C FL E117C
40264 Da
F
αB-C ACD
9939 Da
G
αB-C ACD E117C
19822 Da
H
WT Hsp27
45301 Da
I
Hsp27 FL C137S
22636 Da
J
Hsp27 ACD
20664 Da
K
Hsp27 ACD C137S
10317 Da
L
Hsp27-3D
45468 Da
M
Hsp27-3DΔCTR
39443 Da
Counts
Deconvoluted MW (Da)

Figure 4.16. sHSP constructs containing cysteine residues at the intra-dimer interface form disulfide linked dimers *in vitro*. A) Crystal structure of the αB-C ACD dimer (PDB: 4m5s) with the position of residue E117 indicated as green lines in each subunit of the dimer. B) Crystal structure of the Hsp27 ACD dimer with the position of the residue C137 indicated in green lines in each subunit of the dimer. C) SDS-PAGE analysis of the indicated sHSP construct under non-reducing conditions (NR) or reducing conditions (R) as indicated. The position and mass in kDa of MW markers is indicated on the left. The positions of disulfide-linked dimers (D) or non-linked monomers (M) is indicated to the right of each panel. FL denotes that the sHSP construct is the full-length construct. D-M) Deconvoluted masses of WT αB-C (D), αB-C FL E117C (E), αB-C ACD (F), αB-C ACD E117C (G), WT Hsp27 (H), Hsp27 FL C137S (I), Hsp27 ACD (J), Hsp27 ACD C137S (K) Hsp27-3D (L), Hsp27-3DΔCTR (M). Above each mass spectra are the deconvoluted masses for the main peak in Da.

In section 4.3.3, the monomer-dimer equilibrium of αB-C ACD across the pH range 6.0 - 7.4 was demonstrated using NMR and SV-AUC. It was also shown that even at pH 7.4, αB-C ACD likely undergoes some monomer-dimer exchange because the sedimentation coefficient of this peak was left-shifted relative to the peak for αB-C ACD E117C under non-reducing conditions at the same pH (Fig. 4.8 B). SDS-PAGE under reducing conditions and MS under denaturing conditions enabled detection of monomers of the Hsp27 constructs. However, we sought to determine whether reduction or mutation of the disulfide bridge also enhances monomer-dimer exchange in solution and thereby affects their sedimentation properties. The presence of TCEP did not affect the sedimentation coefficient of WT αB-C or αB-C ACD (Fig. 4.17 A, C). This is consistent with our expectations based on the fact that αB-C lacks cysteine residues. The E117C mutation resulted in a small increase in the weight-average sedimentation coefficient for both full-length αB-C and αB-C ACD (Fig. 4.17 B, D). Therefore, this non-native mutation perturbs the equilibrium of WT αB-C oligomers and may also inhibit the monomer-dimer exchange of αB-C ACD. For WT Hsp27, a broad sedimentation coefficient distribution was obtained regardless of the presence of TCEP (Fig. 4.17 E) or the C137S mutation (Fig. 4.17 F), however a slight peak shift towards lower S values was obtained under conditions where the disulfide is absent. This finding is consistent with previous observations that reduction alone does not result in large alterations to the oligomeric size of WT Hsp27[314]. For Hsp27 ACD, a small but reproducible shift towards lower S values was obtained in the presence of TCEP (Fig. 4.17 G). This shift was enhanced when the concentration of Hsp27 ACD was reduced at the same concentration of TCEP (Fig. 4.17 G). However, this effect was not reproduced

at the much higher protein concentrations required for SEC-SAXS (7.5 mg/mL, compare data presented in Supplementary Fig. 3.6 and Supplementary Fig. 4.11). This is likely due to the equilibrium being shifted towards dimers at the significantly higher protein concentrations required for SAXS analysis. The effect was also not reproduced to the same extent for the Hsp27 ACD C137S mutation (Fig. 4.17 H). We only observed a much smaller, albeit reproducible, reduction in the weight-average sedimentation coefficient indicating that the cysteine to serine mutation may perturb the dimer-monomer dynamics. Using native MS, Alderson *et al*. observed both Hsp27 ACD C137S monomers and dimers whereas only dimers were detected for Hsp27 ACD[314]. However, monomers may be more easily detectable using gas-phase measurements than solution-phase measurements. Further work will be needed to interrogate the dimer-monomer transition of Hsp27 ACD and Hsp27 ACD C137S under various solution conditions. We also assessed the effects of TCEP on the sedimentation properties of Hsp27-3D, the full-length but primarily dimeric construct for Hsp27. Interestingly, in the presence of TCEP, SV-AUC demonstrated that the equilibrium between Hsp27-3D dimers and larger oligomers was shifted towards larger oligomers (Fig. 4.17 I). This effect was also confirmed via SEC-SAXS (compare data presented in Supplementary Fig. 3.8 with data presented in Supplementary Fig. 4.12). Removal of the disulfide bridge may destabilise the Hsp27-3D dimer in such a way that other intermolecular contacts are formed, perhaps via the NTR or CTR. Such interactions may be important in stabilising the monomeric form of Hsp27-3D since the monomer has been proposed to be unstable[314]. However, for the Hsp27-3D construct lacking the CTR (Hsp27-3DΔCTR), no change in the sedimentation coefficient was observed in the presence of TCEP (Fig. 4.17 J). Overall these results suggest that by reducing the intra-dimer disulfide in Hsp27, monomers are able to form to a greater extent than in the absence of reducing agents, however the NTR and the CTR may form inter-subunit interactions within or between sHSP dimers to prevent monomerization as was recently proposed by Clouser *et al*.[290], since the Hsp27 ACD monomer is likely to be prone to aggregation[314].


A
WT αB-C +/- TCEP
WT αB-C only
WT αB-C + TCEP
c(s)
0.20
0.15
0.10
0.05
0.00
10
20
30
Sedimentation coefficient (S)
B
WT αB-C vs αB-C FL E117C
WT αB-C only
αB-C E117C only
c(s)
0.10
0.08
0.06
0.04
0.02
0.00
10
20
30
Sedimentation coefficient (S)
C
αB-C ACD +/- TCEP
αB-C ACD only
αB-C ACD + TCEP
c(s)
1.5
1.0
0.5
0.0
1.0
1.5
2.0
2.5
3.0
Sedimentation coefficient (S)
D
αB-C ACD vs αB-C ACD E117C
αB-C ACD only
αB-C ACD E117C only
c(s)
6
4
2
0
1.0
1.5
2.0
2.5
3.0
Sedimentation coefficient (S)

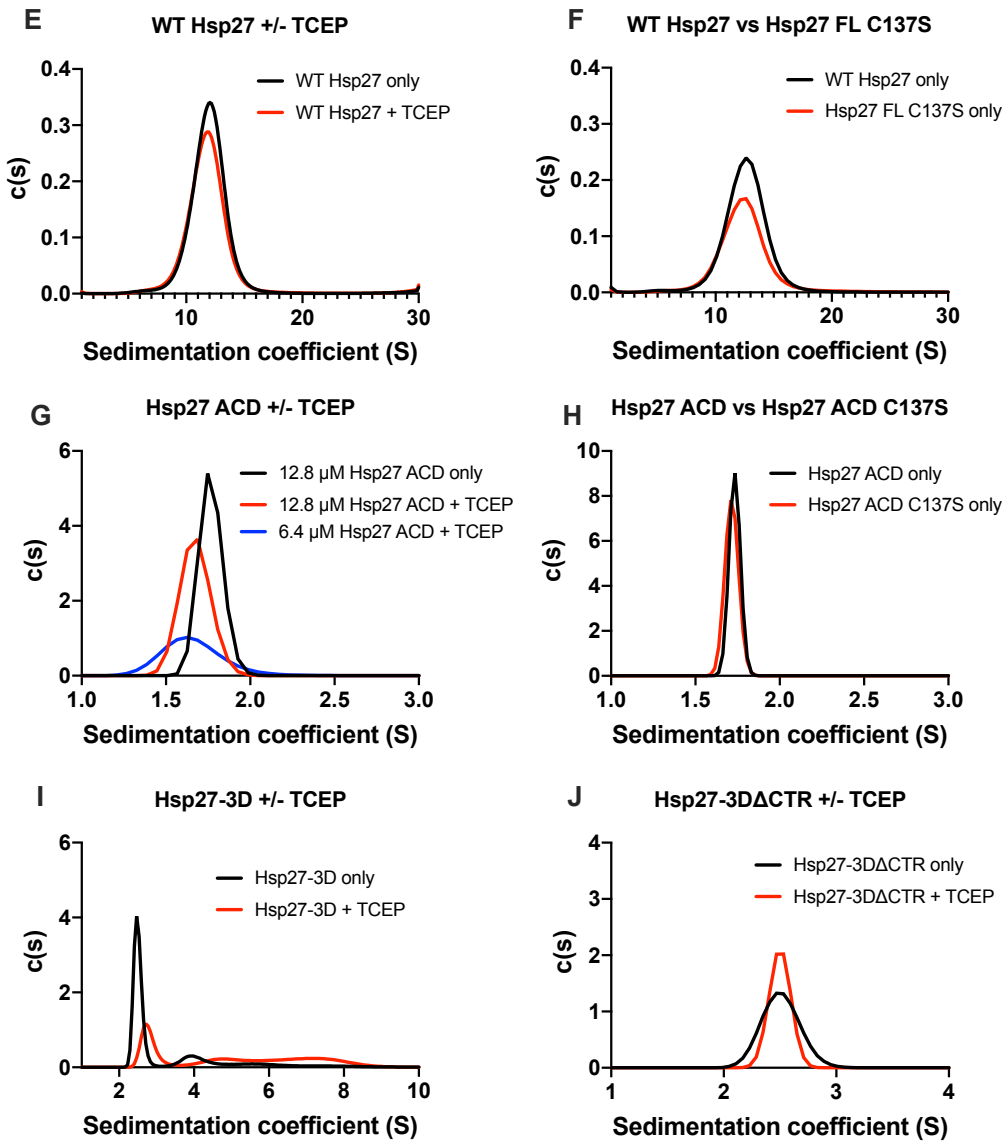


Figure 4.17. SV-AUC analysis of sHSP constructs under reducing or non-reducing conditions. sHSP concentration was 12.8 μM unless specified otherwise. Sedimentation coefficient distributions obtained via SV-AUC of (A) WT αB-C alone (black) or in the presence of 2 mM TCEP (red), (B) WT αB-C alone (black) or αB-C E117C (red), (C) αB-C ACD alone (black) or in the presence of 2 mM TCEP (red), (D) αB-C ACD alone (black) or αB-C ACD E117C (red), (E) WT Hsp27 alone (black) or in the presence of 2 mM TCEP (red), (F) WT Hsp27 alone (black) or Hsp27 C137S (red), (G) Hsp27 ACD alone (black), in the presence of 2 mM TCEP (red) or at a concentration of 6.4 μM in the presence of 2 mM TCEP (blue), (H) Hsp27 ACD alone (black) or Hsp27 ACD C137S (red), (I) Hsp27-3D alone (black) or in the presence of 2 mM TCEP (red), (J) Hsp27-3DΔCTR alone (black) or in the presence of 2 mM TCEP (red). Note that for the purposes of direct comparison, the data presented in (D) is replicated from Fig. 4.8 B. Detection wavelengths were: 237 (A and D), 233 nm (B, C, E) and 228 nm (F). The wavelengths used were as follows: 238 nm (A, B, E and F), 234 nm (C and I), 226 nm (D), 229 nm (G), 233 nm (H) and 277 nm (J).

4.3.7 Disulfide cross-linking regulates the chaperone activity of αB-C ACD and Hsp27 ACD

Next, we assayed the ability of each of these constructs to inhibit amyloid fibril formation by apoC-II using ThT assays (Fig. 4.18). The effect of removing the intra-dimer disulfide via the reducing agent TCEP or via mutagenesis was tested for each sHSP construct. TCEP alone had a minimal effect on the kinetics of apoC-II aggregation. For full-length αB-C, the least effective construct was αB-C E117C in the absence of TCEP (Fig. 4.18 A). All of the constructs lacking the intra-dimer disulfide were more effective (WT αB-C +/- TCEP and αB-C E117C + TCEP). αB-C E117C + TCEP appeared to be more effective than WT αB-C +/- TCEP. For αB-C ACD, the least effective construct was αB-C E117C in the absence of TCEP. All the other constructs inhibited apoC-II fibril formation with similar efficacies (Fig. 4.18 B). For the full-length Hsp27 constructs, WT Hsp27 in the absence of TCEP was the least effective while all other combinations inhibited apoC-II fibril formation with relatively similar activities (Fig. 4.18 C). Lastly, Hsp27 ACD was less effective than Hsp27 ACD C137S +/- TCEP and Hsp27 ACD + TCEP (Fig. 4.18 D). These results were also replicated using the reducing agent DTT rather than TCEP (Supplementary Fig. 4.13). Thus, for each sHSP tested, removal of the intra-dimer disulfide improved the ability of the sHSP construct to inhibit apoC-II fibril formation (Fig. 4.18 A-D).

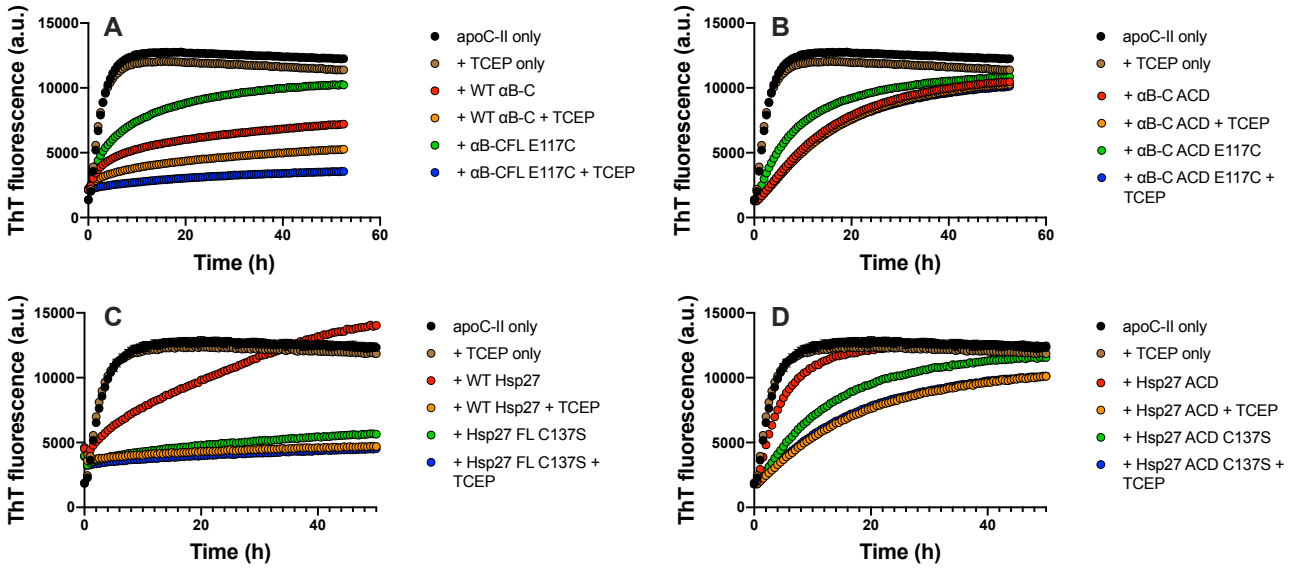


Figure 4.18. Disulfide cross-linked dimers are less effective inhibitors of apoC-II aggregation than non-linked sHSP constructs. ThT assay to monitor the fibril formation of apoC-II (56 μM) incubated alone (black), in the presence of 2 mM TCEP (brown), or in the presence of 12.8 μM: WT sHSP (red), WT sHSP + 2 mM TCEP (orange), the E117C (A and B) or C137S (C and D) mutants of the indicated sHSP (green) and the E117C (A and B) or C137S (C and D) mutants + 2 mM TCEP (blue). Data are presented as mean ± SEM where n = 2.

To determine whether the trends observed in the ThT assays in Figure 4.18 correlated with the lengths of apoC-II fibrils formed we again used SV-AUC. Samples were formed under identical conditions and subjected to SV-AUC analysis (Fig. 4.19). The results of the AUC were in excellent agreement with the results of the ThT assay. All disulfide-linked constructs restricted the elongation of apoC-II fibrils to a lesser extent than non-linked constructs (via TCEP reduction or mutagenesis) (Fig. 4.19 A-D). Similar to the ThT assay, αB-C FL E117C + TCEP was more effective than WT αB-C +/- TCEP, as indicated by a reduction in the proportion of sedimenting signal and a reduction in the weight-average sedimentation coefficient (Fig. 4.19 A). For all the other sHSP constructs, the disulfide-linked constructs were less effective than the non-linked constructs, which displayed relatively similar efficacies (Fig. 4.19 B-D).

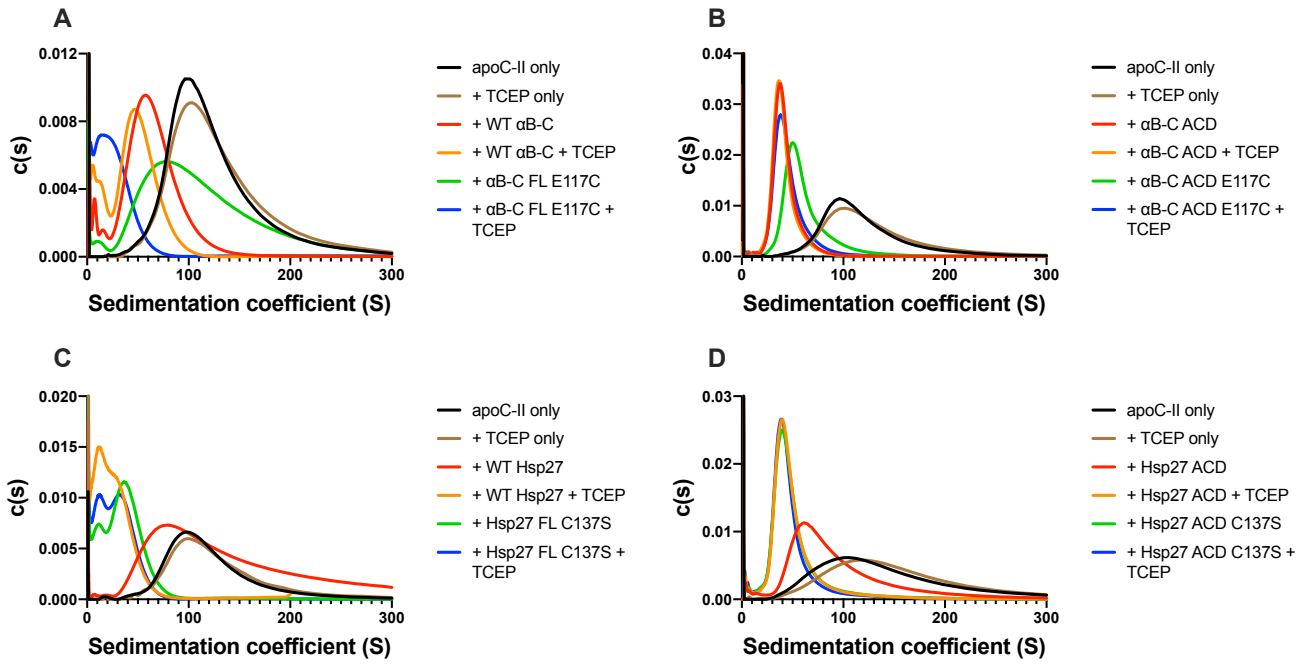


Figure 4.19. Disulfide cross-linked dimers are less effective inhibitors of apoC-II fibril elongation than non-linked sHSP constructs. SV-AUC analysis of apoC-II (56 μM) fibrils formed for 168 hours, 30°C alone (black), in the presence of 2 mM TCEP (brown), or in the presence of 12.8 μM: WT sHSP (red), WT sHSP + 2 mM TCEP (orange), the E117C (A and B) or C137S (C and D) mutants of the indicated sHSP (green) and the E117C (A and B) or C137S (C and D) mutants + 2 mM TCEP (blue). Detection wavelengths were: 285 nm (A and B), 290 nm (C) or 280 nm (D).

Lastly, we analysed whether the disulfide-linked constructs were less effective inhibitors of apoC-II fibril end-to-end joining than non-linked constructs, again using SV-AUC. Fragmented fibrils were incubated with various sHSP constructs in the presence or absence of TCEP and analysed by SV-AUC as soon as possible after fragmentation (Fig. 4.20). The presence of TCEP alone did not affect the size of fragmented apoC-II fibrils. TCEP also did not affect the size of fragmented apoC-II fibrils incubated with either of the αB-C constructs (Fig. 4.20 A-B). However, the presence of TCEP in combination with WT Hsp27 (Fig. 4.20 C) or Hsp27 ACD (Fig. 4.20 D) resulted in smaller fibril sedimentation coefficient distributions, indicating that reduction of the intra-dimer disulfide improved the ability of Hsp27 constructs to inhibit fibril end-to-end joining. The ability of Hsp27 ACD C137S +/- TCEP was also tested (Fig. 4.20 E). The fibril sedimentation coefficient distributions were left shifted relative to those obtained for apoC-II + Hsp27 ACD, but similar to that obtained for apoC-II + Hsp27 ACD + TCEP (Fig. 4.20 D). Thus, removal of the intra-dimer disulfide consistently enhanced the ability of Hsp27 constructs to inhibit apoC-II fibril elongation and end-to-end joining. We also tested the ability of the full-length but dimeric construct of Hsp27 (Hsp27-3D) to inhibit end-to-end joining under reducing or non-reducing conditions at two different concentrations. As we have previously observed with non-fragmented fibrils, at the higher concentration (12.8 μM), non-reduced Hsp27-3D binds fibrils and induces the tangling of fibrils into much larger aggregates such that a significant proportion of apoC-II fibrils are too large for SV-AUC analysis (Fig. 4.20 F and Chapter 3 Fig. 3.6 E). However, under reducing conditions, Hsp27-3D was observed to inhibit fibril end-to-end joining almost as effectively as the ACD-only constructs (Fig. 4.20 F). This trend was also observed at the lower Hsp27-3D concentration (Fig. 4.20 G). This indicates that full-length sHSPs may interact with apoC-II in at least two distinct ways, one in which fibril tangling is promoted, and one in which the fibril ends are blocked. Our results suggest that by reducing the intra-

dimer disulfide, the mode of interaction of Hsp27-3D with fibrils is switched from an interaction that primarily drives fibril tangling, to an interaction that primarily inhibits fibril rejoining.

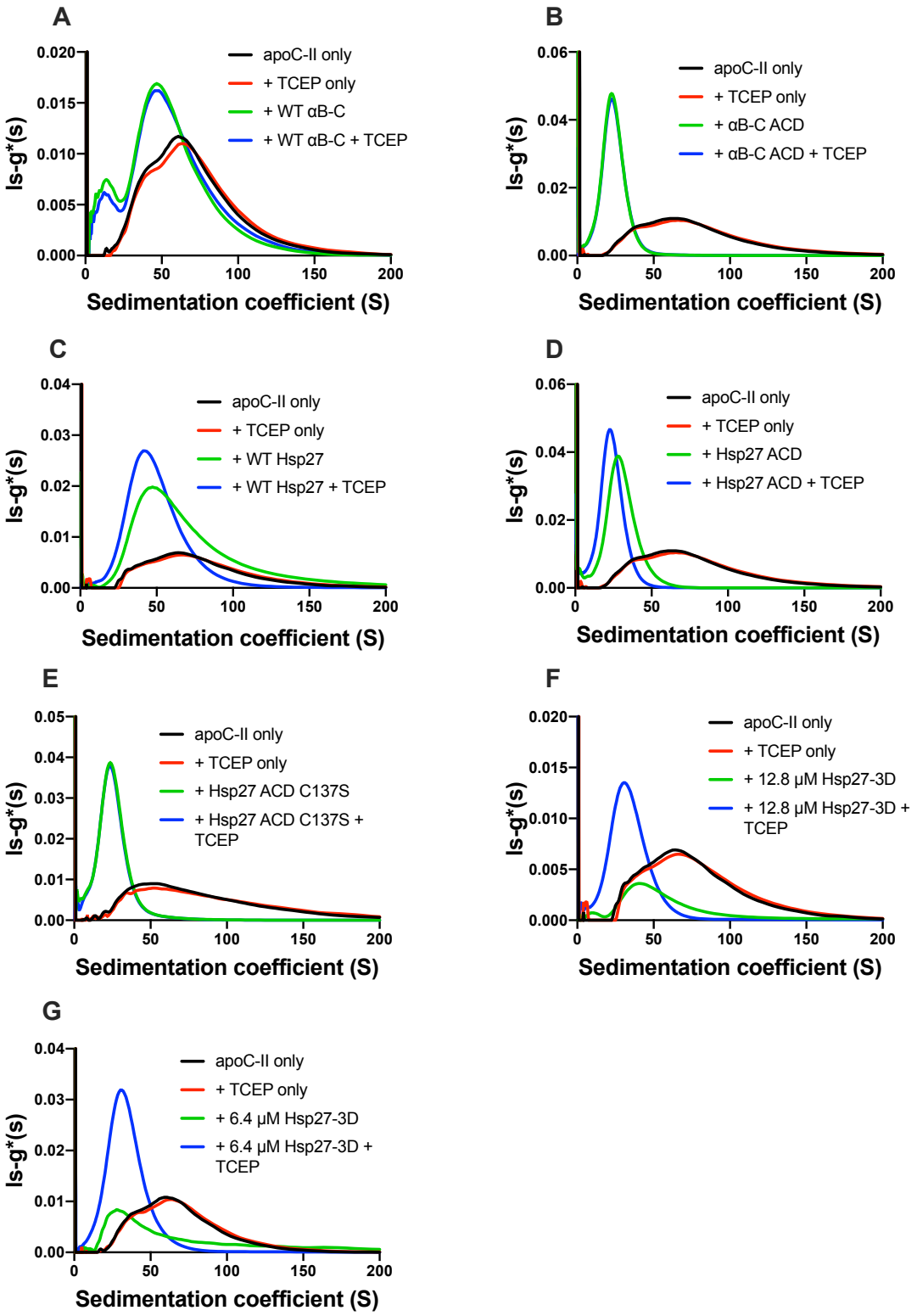


Figure 4.20. Disulfide cross-linked dimers are less effective inhibitors of apoC-II fibril end-to-end joining than non-linked sHSP constructs. SV-AUC analysis of fragmented apoC-II fibrils (56 μM) incubated alone (black), + 2 mM TCEP (red), + 12.8 μM of (A) WT αB-C, (B) αB-CACD, (C) WT Hsp27, (D) Hsp27 ACD, (E) Hsp27 ACD C137S or (F) Hsp27-3D (green) or + 12.8 μM of (A) WT αB-C, (B) αB-CACD, (C) WT Hsp27, (D) Hsp27 ACD, (E) Hsp27 ACD C137S or (F) Hsp27-3D + 2 mM TCEP (blue). Detection wavelengths were: 285 nm (A), 280 nm (B, D and E), 288 nm (C and F). (G) SV-AUC analysis of fragmented apoC-II fibrils (56 μM) incubated alone (black), + 2 mM TCEP (red), + 6.4 μM Hsp27-3D (green) or + 6.4 μM Hsp27-3D + 2 mM TCEP (blue). A detection wavelength of 285 nm was used.

Lastly, we investigated whether the presence of an intra-dimer disulfide affects the chaperone activity of αB-C and Hsp27 constructs against α-syn amyloid formation using a ThT assay and a pelleting assay (Fig. 4.21). DTT and TCEP were found to affect the kinetics of α-syn amyloid formation, therefore we avoided the use of reducing agents in these assays. For the Hsp27 constructs, the observed trend was identical to that of apoC-II: disulfide-linked constructs were less effective inhibitors of amyloid formation than non-disulfide linked constructs (Fig. 4.21 C-D). Consequently, the mechanism(s) by which the Hsp27 constructs inhibit apoC-II and α-syn amyloid formation may be similar, however further characterisation of the interactions between Hsp27 and apoC-II and α-syn would be needed to test this hypothesis.

For the inhibition of α-syn amyloid formation by αB-C, the relationship between the presence of the intra-dimer disulfide was opposite to that observed for Hsp27 (Fig. 4.21 A-B). The E117C αB-C constructs, which form disulfide-linked dimers (Fig. 4.16) were more effective than the unmutated constructs (Fig. 4.21 A-B). These data suggest that the mechanism(s) by which αB-C inhibits α-syn and apoC-II amyloid formation may differ. One possible explanation for this observation is that dimeric forms of αB-C interact with monomeric α-syn to a greater extent than monomeric forms of αB-C (as suggested by our NMR data, Figs. 4.13 - 4.15). Alternatively, as indicated by our pelleting assay (Fig. 4.21 E), both the unmutated αB-C ACD and αB-C ACD E117C are found in the pellet fraction at the end of an incubation with α-syn under conditions that induce the fibril formation of α-syn. In contrast, neither the unmutated Hsp27 ACD or Hsp27 ACD C137S were found in the pellet fraction. This observation signifies a difference in the mode of interaction between these ACD-only constructs and α-syn (either in its

monomeric or fibrillar form), and a difference in the mode of interaction may account for the differential effects of the disulfide bridge on the chaperone activity of these proteins. Further experiments are needed to determine the sHSP-α-syn interactions that cause these differences.

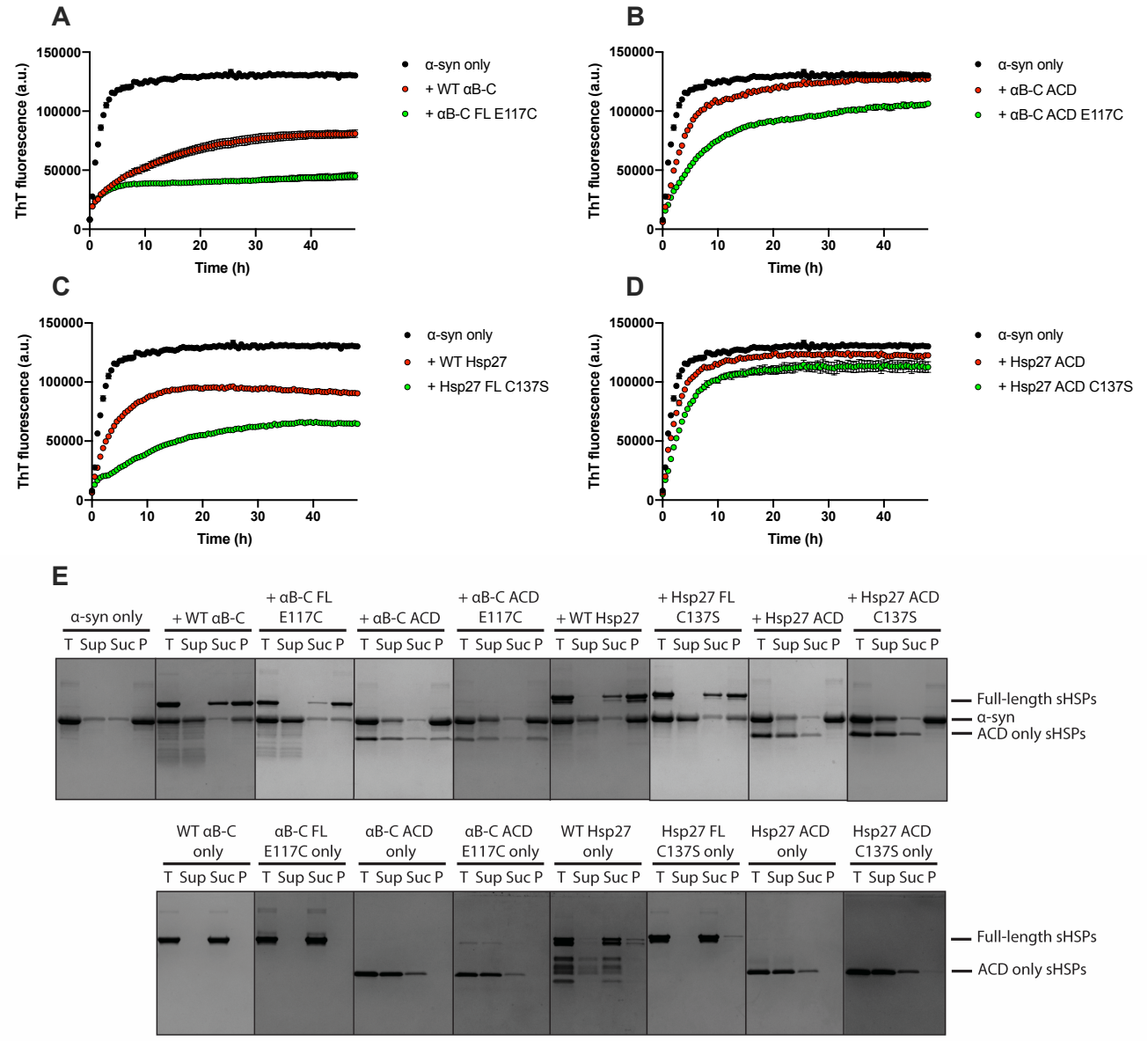


Figure 4.21. Disulfide linked αB-C constructs are more effective inhibitors of α-syn aggregation, while disulfide cross-linked Hsp27 dimers are less effective. A-D) α-syn seeded amyloid formation (5% total seeds) at 45°C alone (black) or in the presence of WT αB-C (red, A), αB-C FL E117C (green, A), αB-C ACD (red, B), αB-C ACD E117C (green, B), WT Hsp27 (red, C),

Hsp27 FL C137S (green, C), Hsp27 ACD (red, D) or Hsp27 ACD C137S (green, D). Data are presented as mean ± SEM where n = 3. E) SDS-PAGE results of a pelleting assay performed at the end of the aggregation timecourse shown in (A-D) in the absence or presence of the various sHSP constructs as indicated. Also shown are control samples of each sHSP incubated alone under identical conditions and analysed by centrifugation and SDS-PAGE in the same way.

4.4 Discussion

The results presented in this chapter expand our understanding of how the ACD of αB-C, and to a lesser extent Hsp27, interact with amyloid fibrils to inhibit their assembly. The capacity of the ACD-only constructs to inhibit amyloid fibril nucleation was primarily investigated in Chapter 3. In this chapter, ACD-only constructs were found to inhibit amyloid fibril elongation and end to end joining, and αB-C ACD was particularly effective at this. The underlying mechanisms and interactions will be discussed herein.

The first findings presented in this chapter were that αB-C constructs inhibited apoC-II fibril formation even when added during elongation. Interestingly, for αB-C ACD, the chaperone activity appeared to be enhanced when it was added during elongation rather than if it was added at the initiation of fibril formation. The later parts of this chapter demonstrate that αB-C ACD mainly exerts its chaperone function against apoC-II fibril formation by interacting with fibril ends. Therefore, by adding αB-C ACD at t_0, many short fibrils may form, resulting in a large population of fibril ends, whereas if αB-C ACD is added at later timepoints there are likely to be fewer individual fibrils, but they will be longer. A larger population of fibril ends will template further amyloid formation via the addition of monomers to fibril ends faster than a smaller population of fibril ends. Since the concentration of αB-C ACD is constant, the apparent increase in the chaperone activity of αB-C ACD when added at later timepoints could be due to a reduced abundance of fibril ends at a given αB-C ACD concentration.

Another intriguing observation was that both WT αB-C and αB-C ACD restricted the elongation of apoC-II fibrils, but that αB-C ACD was more effective than WT αB-C. However, in Chapter 3 we showed that WT αB-C forms strong interactions with apoC-II fibrils. This interaction would increase their apparent mass at a given fibril length. In contrast αB-C ACD does not form strong interactions with fibrils, thus the

derived weight-average fibril lengths would be expected to more accurately represent the true fibril lengths. A second factor that must be considered is our observation that the interaction of WT αB-C with apoC-II fibrils can induce the tangling of fibrils to some extent. Fibril tangling also increases the sedimentation coefficient of the fibrils, thereby increasing their apparent fibril length. However, it is possible that αB-C ACD truly restricts the elongation of apoC-II fibrils more effectively than WT αB-C. In Chapter 3, evidence was presented in support of the hypothesis that smaller conformers of sHSPs, such as monomers and dimers, are the primary fibril-interacting species. WT αB-C forms oligomers, which may need to dissociate extensively in order to bind elongating apoC-II fibrils, whereas αB-C ACD forms dimers that do not need to dissociate to the same extent. Therefore, the rate of oligomer dissociation of WT αB-C may determine the extent to which WT αB-C can inhibit the relatively fast elongation of apoC-II fibrils. In our fibril fragmentation SV-AUC experiments, we found that the reduced form of Hsp27-3D was more effective than the reduced form of WT Hsp27 at inhibiting fibril end-to-end joining. This could indicate that the smaller dissociated forms of sHSPs are more effective at inhibiting fibril elongation than larger oligomeric forms.

Though we could not detect a strong interaction of αB-C ACD with apoC-II fibrils, our fibril rejoining experiments and our NMR experiments indicate a transient interaction of αB-C ACD with the fibrils at their ends. αB-C ACD was highly effective at inhibiting the naturally occurring end-to-end joining of apoC-II fibrils even at sub-stoichiometric molar ratios. The reduced signal intensities of αB-C ACD in the presence of short relative to long fibrils demonstrated that αB-C ACD exhibits at least some preference for binding to fibril ends rather than the surface of the fibril. However, we also observed signal broadening in the presence of long apoC-II fibrils. Therefore, αB-C ACD likely also interacts with the surface of the fibril with a weaker affinity. Alternatively, it interacts only with fibril ends and the signal broadening observed in the presence of the long apoC-II fibrils arises from slow-intermediate exchange on the NMR timescale. An interaction between αB-C ACD and fibril ends was proposed by Mainz *et al.* based on the observation that a construct lacking the NTR inhibited seeded Aβ(1-40) amyloid formation as effectively as WT αB-C[295], however no direct evidence for this hypothesis was presented. Small CSPs were also observed for αB-C ACD in the presence of Aβ(1-40), and many were localised to the β4/8 edge. However, the CSPs observed were only marginally higher than those observed across all residues.

Furthermore, many residues were missing from their analysis, particularly in β5 and β6/7. The authors proposed that the β strands located at the edges of the ACD β-sandwich are structurally similar to the ends of fibrils and could therefore interact with fibrils ends. Our CSPs observed in the presence of long apoC-II fibrils supports their fibril-capping hypothesis, but additionally suggests that the β6/7 strand could be important for the fibril-capping interaction.

At high enough αB-C ACD concentrations, additional unassigned peaks were visible in our ^{15}N HSQCs. We used several approaches, including SV-AUC and NMR across the pH range 5.9-7.4, titration of GuHCl, and estimation of transverse nuclear relaxation rates to determine whether these peaks arise from monomeric αB-C ACD in equilibrium with αB-C ACD dimer. This multi-faceted analysis strongly indicated that the unassigned peaks arise from the αB-C ACD monomer. Destabilisation of the αB-C ACD dimer in a pH-dependent manner may be due to histidine residues located at and near the dimer interface. Rajagopal *et al.* noted that αB-C ACD has a relatively high abundance of histidine residues[316]. These histidine residues are primarily located at the dimer interface or make contacts with residues at the interface. The authors estimated pK_A values for four out of five of the histidine residue side chains based on the chemical shifts of the imidazole ring nuclei. Two histidines had estimated pK_A values within the pH range of 6.0 and 8.0. Therefore, ionisation or partial ionisation of these histidine residues may occur under physiological conditions. This ionisation may be enough to destabilise the dimer interface and shift the equilibrium from ACD dimer to ACD monomer. Substitution of H104 located within the β5 strand near the dimer interface for glutamine or lysine was also found to destabilise the αB-C ACD dimer even at pH 7.5[316].

Whether monomeric forms of αB-C are significantly populated both *in vitro* and *in vivo* remains an open research question. The exchange of monomers from full-length αB-C oligomers was first suggested by Aquilina *et al.* based on the detection of both odd- and even-numbered αB-C oligomers via native MS[282]. Importantly, the abundance of odd-numbered oligomers was found to increase with decreasing pH[286], a finding that compliments one of the key findings presented in this chapter. Models for odd-numbered oligomers have also been proposed based on cryo-electron microscopy data[304]. Dimers and monomers of αB-C ACD were both detected in the gas-phase using native MS, while only dimers were detected for

αB-C ACD E117C[279]. Yet, the detection of full-length αB-C monomers via techniques other than native MS is challenging because αB-C assembles primarily into oligomers at typical concentrations required for biophysical analyses. Consequently, there is little information, at present, regarding the structure of an isolated, full-length αB-C monomer. However, the Hsp27 ACD monomer has recently been characterised in solution using ^{15}N relaxation dispersion NMR. Alderson *et al.* stabilised the partially unfolded Hsp27 ACD monomer using high pressure, low pH and relatively low protein concentrations[314]. In general, the ^{15}N HSQC signals of Hsp27 ACD obtained at pH 4.5 were less dispersed than the signals obtained at pH 7.0, consistent with our observations using αB-C ACD at pH 6.5 relative to pH 7.4. The guanidine titration experiment presented in this thesis also yielded similar results. Taken together, we hypothesize that, like the Hsp27 ACD monomer, the αB-C ACD monomer is less folded than an ACD subunit within the dimer.

The estimated ^{15}N transverse relaxation rates for αB-C ACD presented here were comparable with those reported by Rajagopal *et al.* for αB-C ACD (data not shown[316]) and Alderson *et al.* for Hsp27 ACD (Supplementary information[314]). Notably, resonances with R_2 rates higher than 25 s^{-1} were found to be mainly localised to the loop preceding β6/7, the β6/7 strand, and residues located within two loops in close proximity to the dimer interface. Rajagopal *et al.* obtained CPMG relaxation dispersion curves for approximately 16 resonances, many of which were again located in the loop between β5 and β6/7 and the β6/7 strand[316]. These two-state transitions indicate that these residues undergo chemical exchange between the major (observed) population and a minor population. A meta-analysis of all existing structures of the αB-C ACD in the PDB reveal that the loop connecting β5 and β6/7 exists either in the "loop up" or "loop down" conformation (Rajagopal *et al.*[316]). Though major conclusions should not be drawn simply from this observation, it supports the hypothesis that this loop may be dynamic and therefore undergoing chemical exchange. Conformational exchange at the loop could be transferred to the β6/7 strand to destabilise the interface. Collectively our data, and this previously published work, support conformational exchange occurring at the dimer interface and that the unknown peaks arise from the conformationally flexible ACD monomer, however we have not yet assigned the peaks.

In the next part of this chapter we investigated the involvement of the assigned and unassigned peaks in interacting with apoC-II and α-syn fibrils, and monomeric α-syn. In general, a specific subset of the

unassigned peaks were broadened in the presence of both types of fibrils, while a different subset of unassigned peaks were broadened in the presence of the α-syn monomer. The assigned, dimer peaks were also broadened to a similar extent in the presence of α-syn monomer. This analysis suggests that αB-C ACD interacts with both fibril types via a similar mechanism, while the interaction with monomeric α-syn appears to involve different peaks in the spectra that arise either from the dimer or the monomer. Clearly further work needs to be conducted to better understand the interaction of αB-C ACD with monomeric α-syn, however the CSPs we observed for αB-C ACD in the presence of monomeric α-syn generally agree with previously published results[281]. Liu *et al.* proposed that αB-C ACD interacts with α-syn via the β4/β8 hydrophobic groove, which is distal to the intradimer interface. This hydrophobic groove is also known to bind a conserved IXI/V motif contained within the CTR of sHSPs. Th IXI/V motif binds diagonally between the two β strands in either orientation[280], and this site of the ACD is proposed to bind substrate peptides in a similar manner. Based on CSPs observed using NMR, Freilich *et al.* found that tau binds to the β4/β8 hydrophobic groove in Hsp27 ACD[300], and Liu *et al.* proposed that the α-syn monomer competes with the CTR motif for binding to the β4/β8 site in αB-C ACD[281].

ThT assays demonstrated that the disulfide cross-linked dimeric αB-C ACD construct (E117C construct) more effectively inhibited seeded α-syn fibril assembly than the unmutated construct that can exchange between monomer and dimer. This finding supports the hypothesis that ACD dimers significantly contribute to the chaperone activity of αB-C ACD against α-syn amyloid formation, perhaps by binding and stabilising monomeric α-syn. Disulfide formation restricts αB-C ACD E117C to the antiparallel II (AP_{II}) register within the dimer and prevents it from accessing the AP_I or AP_{II} registers[279], and this may account for its increased chaperone activity against α-syn relative to αB-C ACD, which forms dimers that can access all three registers[277,279,280]. Another consideration is that although our NMR experiments indicated that the minor species of αB-C ACD appears to interact with both apoC-II and α-syn fibrils, the fibrillar core differs structurally between these two fibril types. ApoC-II forms fibrils consisting of one protofilament of two β-sheets stacked vertically (Fig. 1.2), while α-syn fibrils are larger, typically consisting of two protofilaments, each with four or five β-sheets (Fig. 1.6). Additionally, based on molecular models of apoC-II[35] and α-syn fibrils[74,147], it is likely that the β-strands in apoC-II fibrils are longer than those found in α-syn fibrils. Furthermore, these models suggest that the fibrillar core of α-

syn is surrounded by longer flexible N- and C-terminal regions than that of apoC-II fibrils. αB-C ACD may form stronger interactions with the ends of apoC-II fibrils because the β-strands are longer, more accessible or have higher structural similarity to the intra-dimer interface of αB-C ACD. Given that αB-C ACD appears to transiently interact with soluble and fibrillar α-syn and also become stably associated with growing α-syn fibrils it is challenging to discern all of the intermolecular interactions that account for the chaperone activity of αB-C ACD against this particular substrate. As apoC-II is too unstable we were also unable to investigate the effects of monomeric apoC-II on the assigned and unassigned peaks using NMR. An intriguing further direction for this research would be to examine the effects of various disease-relevant substrates on the chemical shifts and signal intensities of both the assigned and unassigned peaks to determine whether our observations are specific for α-syn or conserved for other substrates.

For Hsp27 ACD, the cross-linked construct was less effective than the C137S construct at inhibiting seeded α-syn fibril formation. In this assay, the least effective construct was Hsp27 ACD, followed by Hsp27 ACD C137S and αB-C ACD (which displayed similar chaperone capacities), and the most effective was αB-C ACD E117C. Therefore, despite the high sequence identity and structural similarity of these proteins (Fig. 4.1, Fig. 4.22), some additional factors besides the disulfide cross-linking contribute to the differential activities of the two sHSPs. Fig. 4.22 shows the spatial distribution of poorly conserved residues between αB-C ACD and Hsp27 ACD. It is evident that within the ACD, the residues within the β-strands are highly conserved, while residues in the loops connecting the β-strands are less conserved. The key exception is a cluster of three residues at the dimer interface, one of which corresponds to C137 in Hsp27 ACD. This observation suggests that differences in the chaperone activity of αB-C ACD relative to Hsp27 ACD could be attributed to either the dimer interface, as we have investigated in this work, or these loop regions, or both. These two regions of lower sequence conservation could cause differences in the affinity of the two ACD-only constructs for monomeric α-syn or fibrillar α-syn. Another explanation for the differences in chaperone activity between αB-C ACD and Hsp27 ACD is our observation that both αB-C ACD constructs form associations with elongating α-syn fibrils whereas neither Hsp27 ACD construct does. Further work would be required to better understand these

interactions. For the remainder of this chapter, we will focus on the interactions of αB-C ACD, and to a lesser extent Hsp27 ACD, with amyloid fibrils.

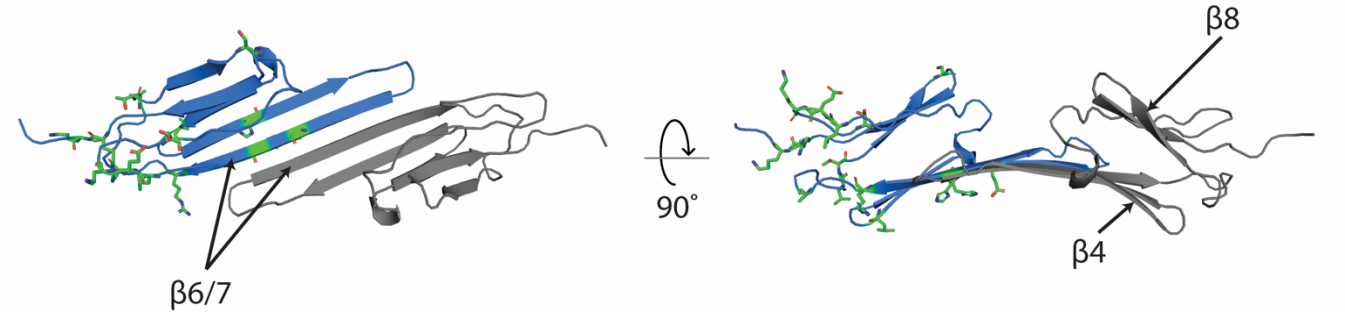


Figure 4.22. Representation of poorly conserved residues between αB-C ACD and Hsp27 ACD. Residues classified as poorly conserved were mapped onto one subunit of the structure of αB-C ACD (PDB: 4M5S) in green and shown using the stick representation in PyMOL. The positions of the dimer interface β6/7 strand and the β4/8 outer groove are indicated.

The final experiments presented in this chapter demonstrate that disulfide cross-linking impaired the chaperone activity of both αB-C and Hsp27 constructs against amyloid fibril elongation and rejoining by apoC-II. The similarities observed between αB-C ACD and Hsp27 ACD against apoC-II amyloid formation suggest a similar mechanism by which the ACD constructs interact with apoC-II fibrils, and in particular, with fibril ends. The observation that disulfide cross-linked constructs were always less effective inhibitors of fibril formation than non-covalent constructs supports our hypothesis that the β6/7 strand may be an interactive site that binds the ends of apoC-II amyloid fibrils. Importantly, the effects of disulfide cross-linking at this interface on the chaperone activity of the sHSP constructs were conserved for both the ACD-only constructs and for the full-length constructs. However, our SV-AUC data demonstrate that WT αB-C and WT Hsp27 both assemble into oligomers regardless of disulfide cross-linking. How then does removal of the intra-dimer disulfide enhance the chaperone activity of an oligomeric, WT sHSP? One possibility is that removal of the disulfide cross-link enhances the exchange of monomers from oligomers, increasing the accessibility of the β6/7 strand, as has been proposed based on native MS[284,286]. Another explanation is that an interaction between the β6/7 strand and elongating amyloid fibrils need not arise solely from monomeric forms of sHSPs. In odd-numbered sHSP oligomers, at least one intra-dimer interface would be accessible for interactions with substrate proteins, including growing fibrils. The specific sub-structure of the oligomer would then define the accessibility of the β6/7

strand. We suggest that this site may be a generic amyloid fibril binding site, since our NMR experiment indicated that the αB-C ACD monomer is also likely to be important for interacting with α-syn fibrils. Additionally, Hsp27 ACD C137S was found to be more effective against seeded α-syn fibril assembly than Hsp27 ACD and for apoC-II, disulfide cross-linked ACDs were always less effective than non-linked constructs. Some existing literature supports our fibril-capping hypothesis. Firstly, Alderson *et al.* found that reduced Hsp27 was a more effective chaperone than oxidised Hsp27 against several substrates[314]. Second, the β6/7 strand of αB-C was identified as a substrate interaction site by Ghosh *et al.* using protein pin arrays[368]. Third, Mainz *et al.* proposed that the β3/4/8 strands of αB-C ACD are interaction sites with Aβ(1-40) fibrils on the basis that small CSPs were detected in these regions in the presence of Aβ(1-40). In their work, small CSPs were also detected for two residues in the β6/7 strand however the majority of residues in the β6/7 strand were excluded from their analysis. Lastly, NMR of Hsp27 ACD in the presence of tau also revealed CSPs at both the β4/8 hydrophobic groove, as well as the β6/7 strand and the loop between β5 and β6/7[300]. Therefore, based on our results and the work of others, the β4/8 hydrophobic groove may be an important interaction site for some substrates, for example monomeric α-syn, however the β6/7 strand appears to also be an important interaction site for amyloid fibrils.

While we observed a great deal of similarity between αB-C ACD and Hsp27 ACD in terms of their chaperone activity and substrate interactions, some significant differences were observed. Firstly, Hsp27 ACD was found to be less effective than αB-C ACD E117C at inhibiting apoC-II fibril elongation and fibril rejoining. One possible explanation is that αB-C ACD E117C does not form disulfide linked dimers to the same extent as Hsp27 ACD (as was suggested by SDS-PAGE under non-reducing conditions). If this is true, the enhanced chaperone activity of αB-C ACD E117C relative to Hsp27 ACD could be due to an increased availability of ACD monomers for fibril binding. An alternative explanation is that the presence or absence of the inter-subunit disulfide bridge does not completely explain the difference in the chaperone activity of these two proteins. This could be the case if the ACD possesses other interfaces for interacting either with fibrils or with other intermediates of the fibril formation pathway. Our NMR experiments in the presence of both fibril types provide substantial evidence that the β6/7 strand that becomes accessible in the monomeric state may be an important interactive surface for amyloid fibrils. However, it is important to note that in one experiment we also detected minor CSPs in loops flanking

the β3 strand. This strand (β3) or the flanking loops may also serve as an interaction site with amyloid fibril ends. Based on the crystal structures of both αB-C ACD and Hsp27 ACD, this strand is partially accessible in the dimeric state, but potentially more accessible in our construct for αB-C ACD. Close inspection of the two crystal structures demonstrate that the β3 strand in αB-C ACD is slightly more solvent exposed than the β3 strand in Hsp27 ACD (Fig. 4.23). Importantly, in the crystal structure of Hsp27 ACD, residues in the β2 strand appear to make weak interactions with residues in the loop between β5 and β6/7 of the other subunit in the dimer. Thus, the β3 strand of Hsp27 ACD may be relatively more occluded than the same strand in αB-C ACD. In the monomeric state, the interactions between residues in β2 and the loop at the interface would be lost. Monomerisation may contribute to β3 becoming more solvent exposed and accessible for substrates. Again, in αB-C ACD, the β3 strand may be inherently more accessible even in the dimeric state and contribute to the differential chaperone activity observed between αB-C ACD E117C and Hsp27 ACD. However, it is also important to consider that our R_2 measurements suggest that the β2 strand of αB-C ACD is dynamic and may therefore only form transiently in solution. This is in agreement with Alderson *et al*., who observed similar reduced R_2 values for the β2 strand of Hsp27 ACD[369]. Therefore, the accessibility of the β3 strand in both ACDs may depend on how dynamic the β2 strand is and how transiently it interacts with the adjacent β3 strand and/or residues within the other subunit in the dimer. Another observation is that the β3 strand in Hsp27 ACD (95-WRVSLD-100) is less hydrophobic than the β3 strand in αB-C ACD (75-FSVNLD-80), an additional factor which may contribute to differences in substrate binding between the two proteins. Further experiments are needed to determine the importance of this region of the ACD in interacting with substrates, including amyloid fibrils, since our results primarily point to the dimer interface as an important substrate binding site. A further, more complex explanation is that all four of the β strands at the edges of the ACD (β3, β4, β6/7 and β8) are sites available for interacting with fibril ends due to the structural similarities between these strands and the cross-β fibril structure. This would mean that the overall chaperone activity of the two different ACD constructs would depend on both the accessibility of these edge strands, and the affinities of these strands for fibril ends, which of course may differ across the different strands and between the two different ACDs. It is worth noting that the β6/7 strand and the β3 strand are longer than the β4 or β8 strands. In a systematic, computational analysis of all β-strand-to-β-strand protein-protein interactions in the PDB, higher affinity interactions were generally

formed between longer β-strands[370]. Thus, the longer β6/7 and β3 strands may form stronger interactions with fibril ends; however, this is purely speculative and would require substantial further work. An important future direction for this work would be to characterise the interactions of the Hsp27 ACD (and Hsp27 ACD C137S) with apoC-II and α-syn fibrils via NMR.

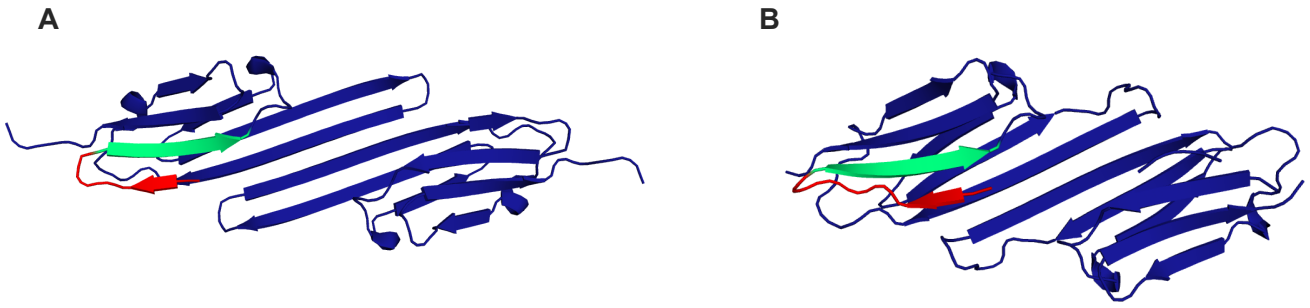


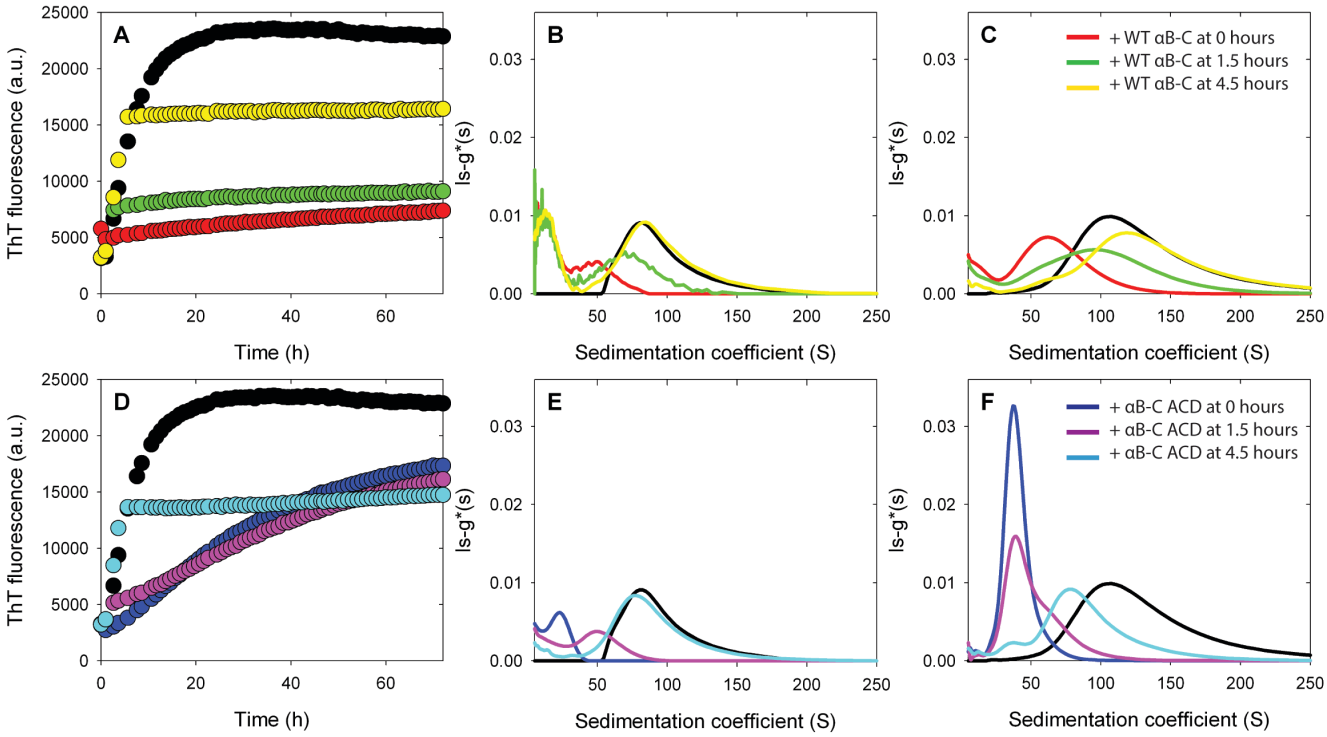
Figure 4.23. Crystal structures of αB-C ACD (A, PDB: 4m5s) and Hsp27 ACD (B, PDB: 4mjh). In each structure, the β3 strand of one protomer is coloured green and the preceding loop and β2 strand is coloured red.

4.5 Conclusions

In this chapter we have focused on the interactions of the ACD-only constructs with apoC-II and α-syn fibrils. This was primarily due to our ability to identify the interaction sites of these constructs using NMR. Due to the large size of WT αB-C and WT Hsp27, only a small number of dynamic residues in the CTR can be observed using solution-state NMR. Collectively our data indicate that full-length sHSP constructs likely interact with fibrils via binding sites in both the NTR and ACD, and also potentially within the CTR. To examine and fully characterise all of these interactions via NMR would be an enormous undertaking, likely involving solid-state NMR and is thus beyond the scope of this thesis. However, our ThT assays and our SV-AUC analysis of apoC-II fibrils in the presence of the various sHSPs demonstrates that our findings regarding the ACD-only constructs are relevant in the context of the full-length proteins. For example, both Hsp27 ACD and WT Hsp27 inhibit apoC-II fibril elongation, however WT Hsp27 additionally forms strong interactions with apoC-II fibrils to increase their sedimentation coefficient. A potentially useful albeit challenging future direction for this work could involve

investigating the interaction of Hsp27-3DΔCTR with amyloid fibrils using NMR. This would enable the NTR – fibril interaction to be investigated in the absence of the CTR interactions.

4.6 Supplementary information



Supplementary Figure 4.1. ApoC-II fibril formation kinetics and fibril size distributions with αB-C constructs added during elongation. A) ApoC-II fibril formation alone (black) or with 12.8 μM WT αB-C added at 0 (red), 1.5 (green) or 4.5 (yellow) hours after the initiation of fibril formation. B and C) ApoC-II fibril size distributions measured at 5 hours (B) and 72 hours (C) after the beginning of fibril assembly for fibrils formed alone (black) or with 12.8 μM WT αB-C added at 0 (red), 1.5 (green) or 4.5 (yellow) hours after the initiation of fibril formation. D) ApoC-II fibril formation alone (black) or with 12.8 μM αB-C ACD added at 0 (blue), 1.5 (purple) or 4.5 (cyan) hours after the initiation of fibril formation. E and F) ApoC-II fibril size distributions measured at 5 hours (E) and 72 hours (F) after the beginning of fibril assembly for fibrils formed alone (black) or with 12.8 μM αB-C ACD added at 0 (blue), 1.5 (purple) or 4.5 (cyan) hours after the initiation of fibril formation. For the purposes of comparison, the apoC-II fibril formation kinetics shown in (A) and (D) are the same as those depicted in Fig. 4.1.

Supplementary Table 4.1 ApoC-II fibril size distributions with αB-C constructs added during fibril formation obtained at 5 hours after the initiation of fibril assembly

	Weight average sedimentation coefficient at 5 hours (S)*	Loading concentration (signal)
56 µM apoC-II only	96.2	0.46
+ 12.8 µM WT αB-C at 0 hrs	26.0	0.37
+ 12.8 µM WT αB-C at 1.5 hrs	47.5	0.46
+ 12.8 µM WT αB-C at 4.5 hrs	74.5	0.74
+ 12.8 µM αB-C ACD at 0 hrs	16.0	0.18
+ 12.8 µM αB-C ACD at 1.5 hrs	39.8	0.22
+ 12.8 µM αB-C ACD at 4.5 hrs	86.8	0.51

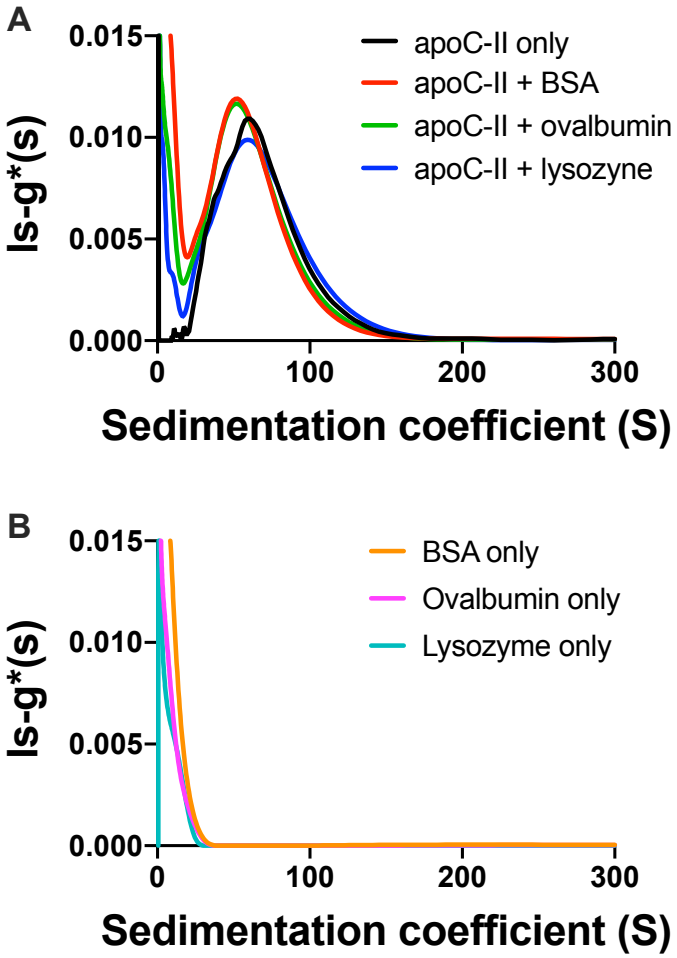
* Integral range 1-500 S

Supplementary Table 4.2 ApoC-II fibril size distributions with αB-C constructs added during fibril formation obtained at 72 hours after the initiation of fibril assembly

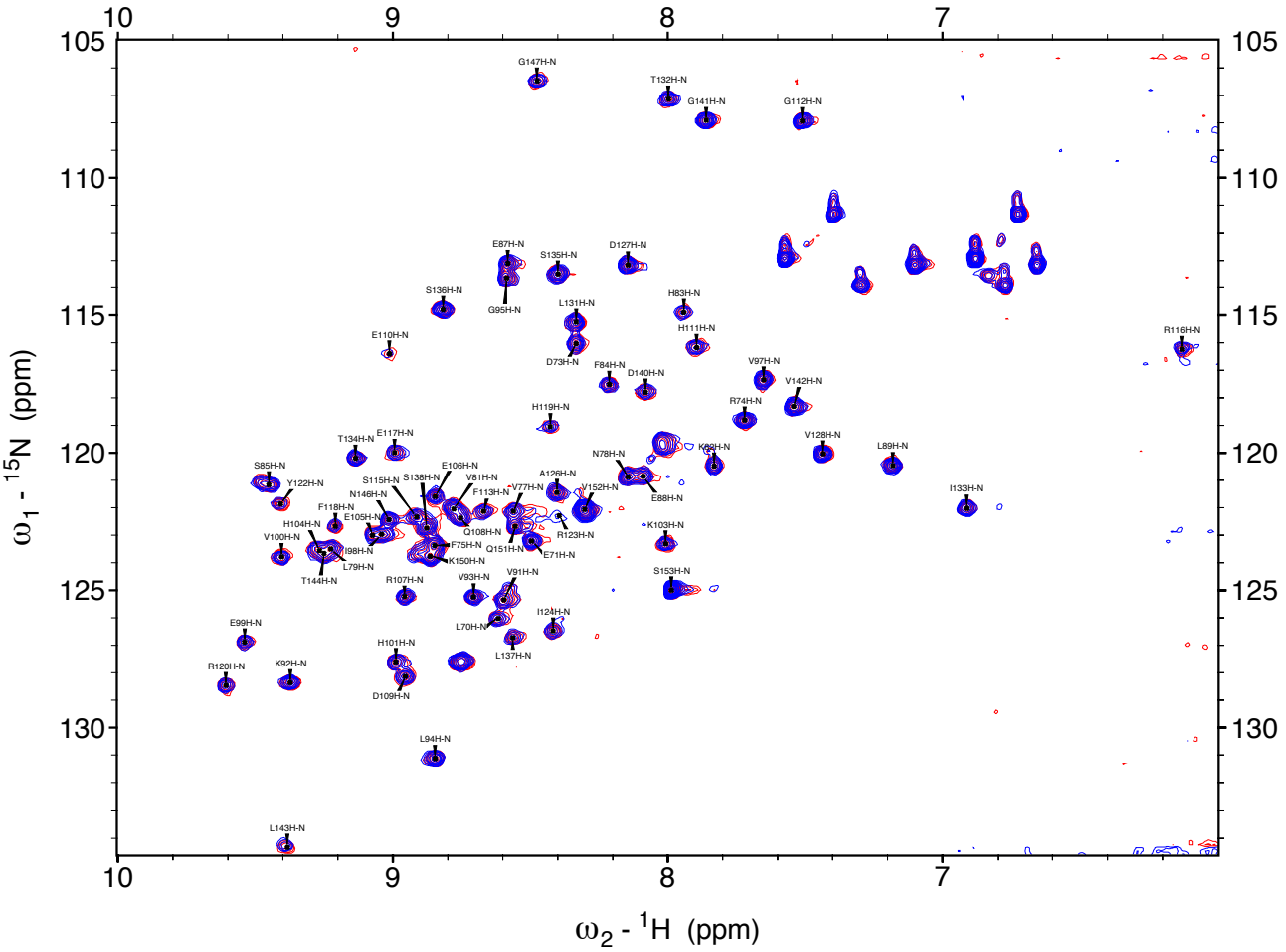
	Weight average sedimentation coefficient at 72 hours (S)*	Loading concentration (signal)
56 µM apoC-II only	137.1	0.91
+ 12.8 µM WT αB-C at 0 hrs	70.7	0.42
+ 12.8 µM WT αB-C at 1.5 hrs	103.7	0.55
+ 12.8 µM WT αB-C at 4.5 hrs	143.0	0.79
+ 12.8 µM αB-C ACD at 0	42.1	0.65

hrs		
+ 12.8 µM αB-C ACD at 1.5 hrs	55.2	0.54
+ 12.8 µM αB-C ACD at 4.5 hrs	92.1	0.58

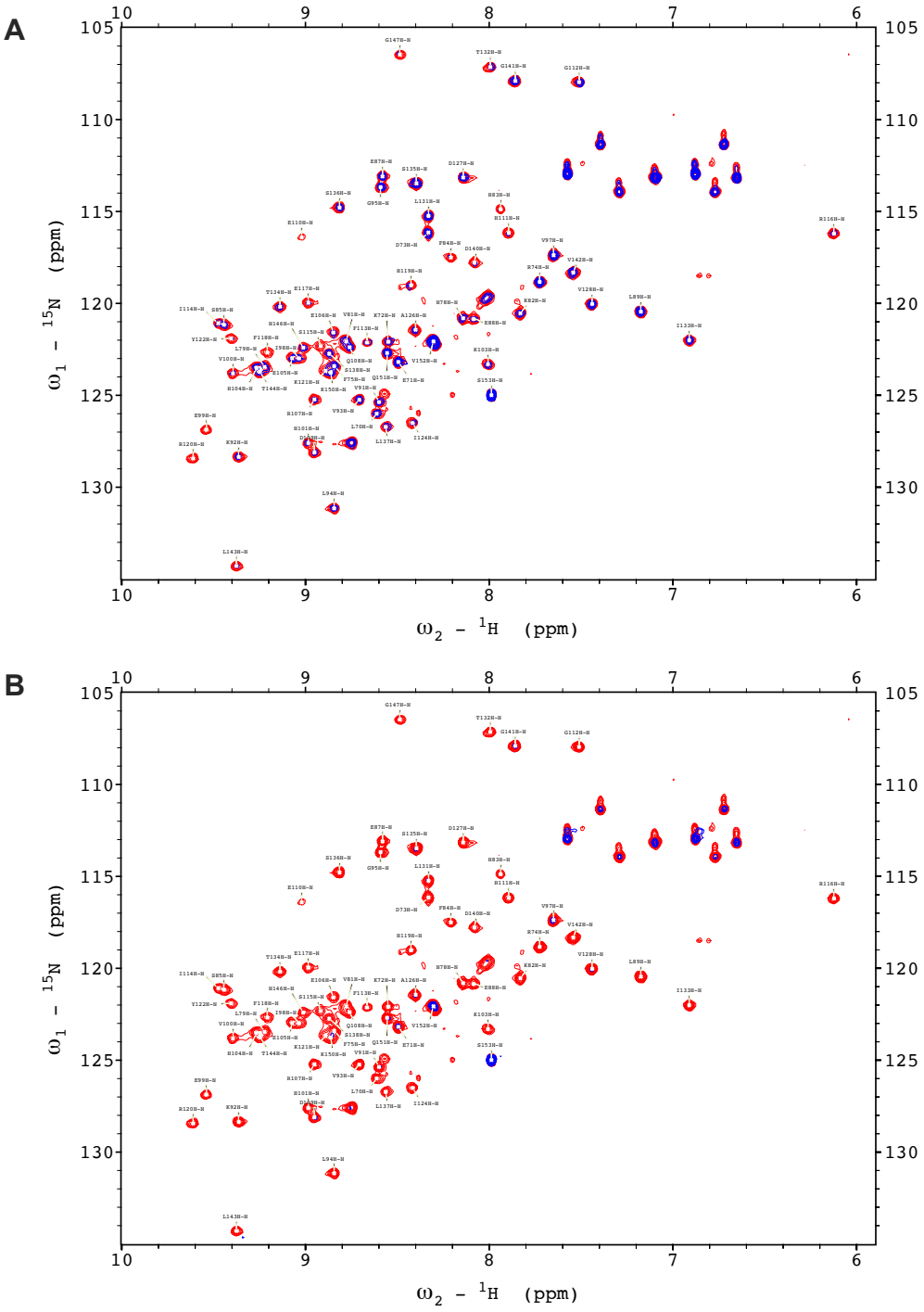
* Integral range 20-500 S

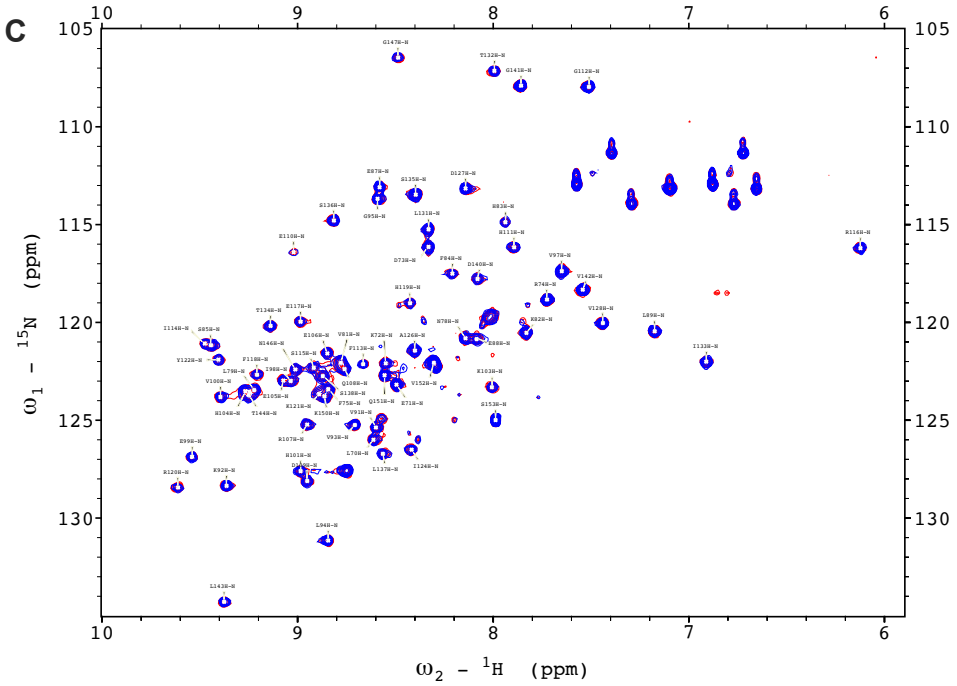


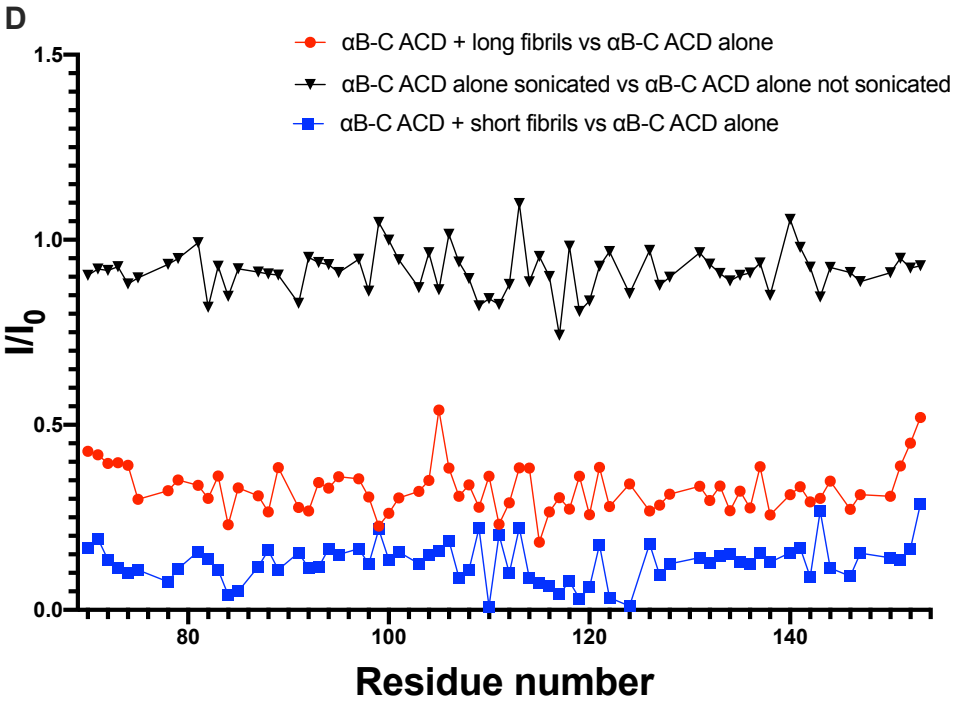
Supplementary Figure 4.2. SV-AUC of apoC-II fibril fragments incubated with BSA, ovalbumin or lysozyme. A) ApoC-II fibrils (56 μM) were sonicated as per methods section 2.2.12 and incubated alone (black) or in the presence of BSA (red), ovalbumin (green) or lysozyme (blue) (12.8 μM). The fibrils were analysed by SV-AUC as soon as possible after the addition of the control proteins. B) Also shown is SV-AUC analysis of each of the control proteins: BSA (orange), ovalbumin (magenta) and lysozyme (cyan) incubated alone at 12.8 μM.

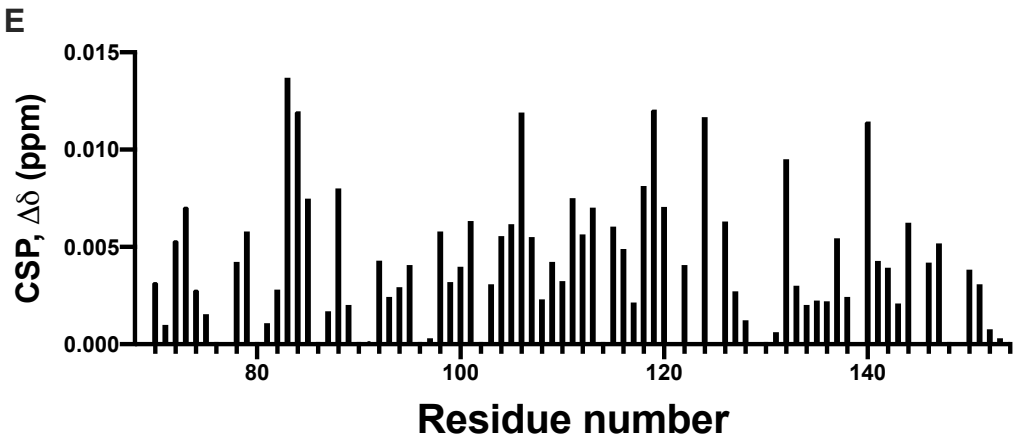


Supplementary Figure 4.3. ^{15}N HSQC overlay of 50 μM αB-C ACD alone in 50 mM sodium phosphate, pH 7.4, 0.02% sodium azide before (red) and after (blue) sonication as described in methods section 2.2.12.

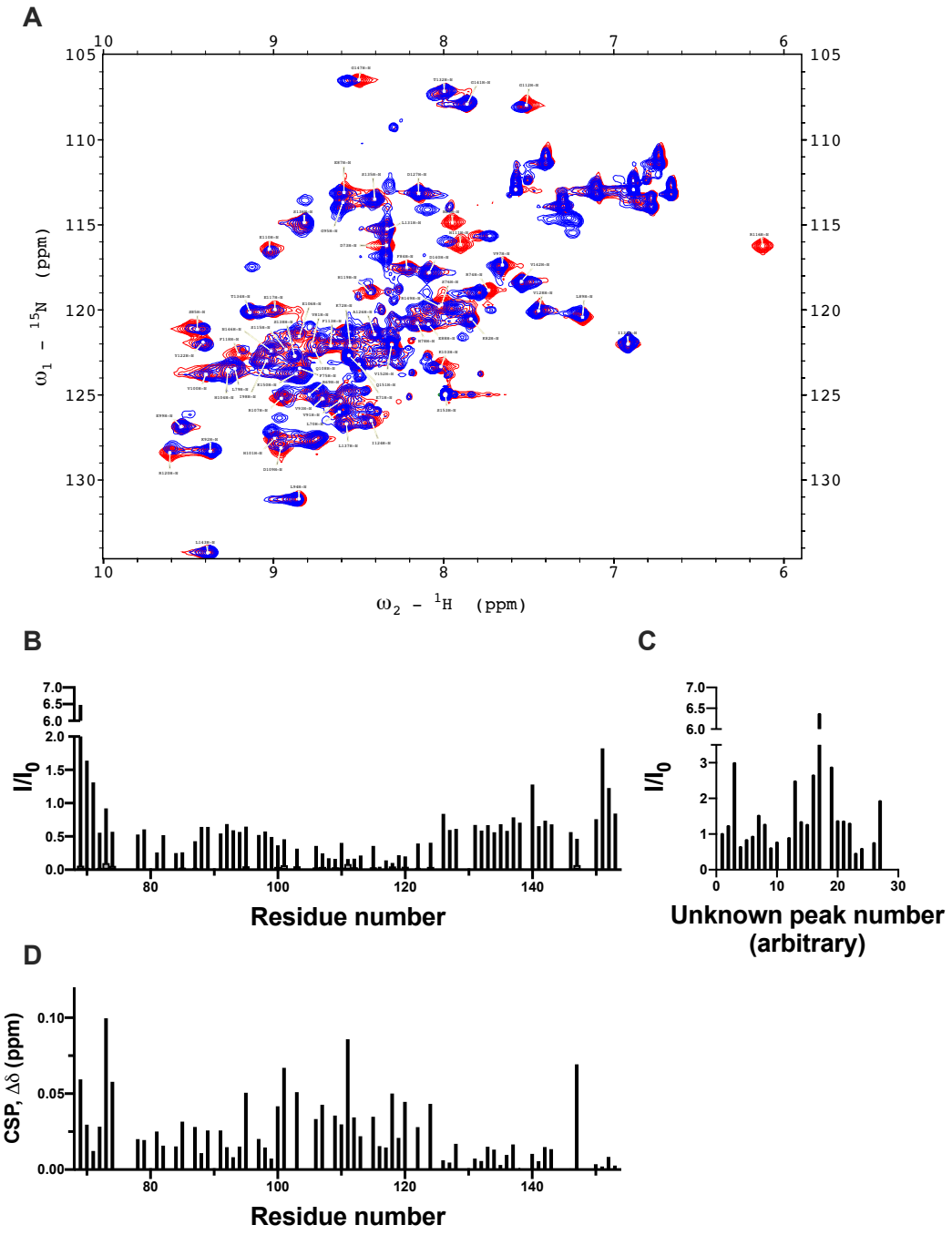

A
B
10
9
8
7
6
105
110
115
120
125
130
ω_1 – ^{15}N (ppm)
ω_2 – ^{1}H (ppm)


C
ω_1 – ^{15}N (ppm)
ω_2 – ^{1}H (ppm)

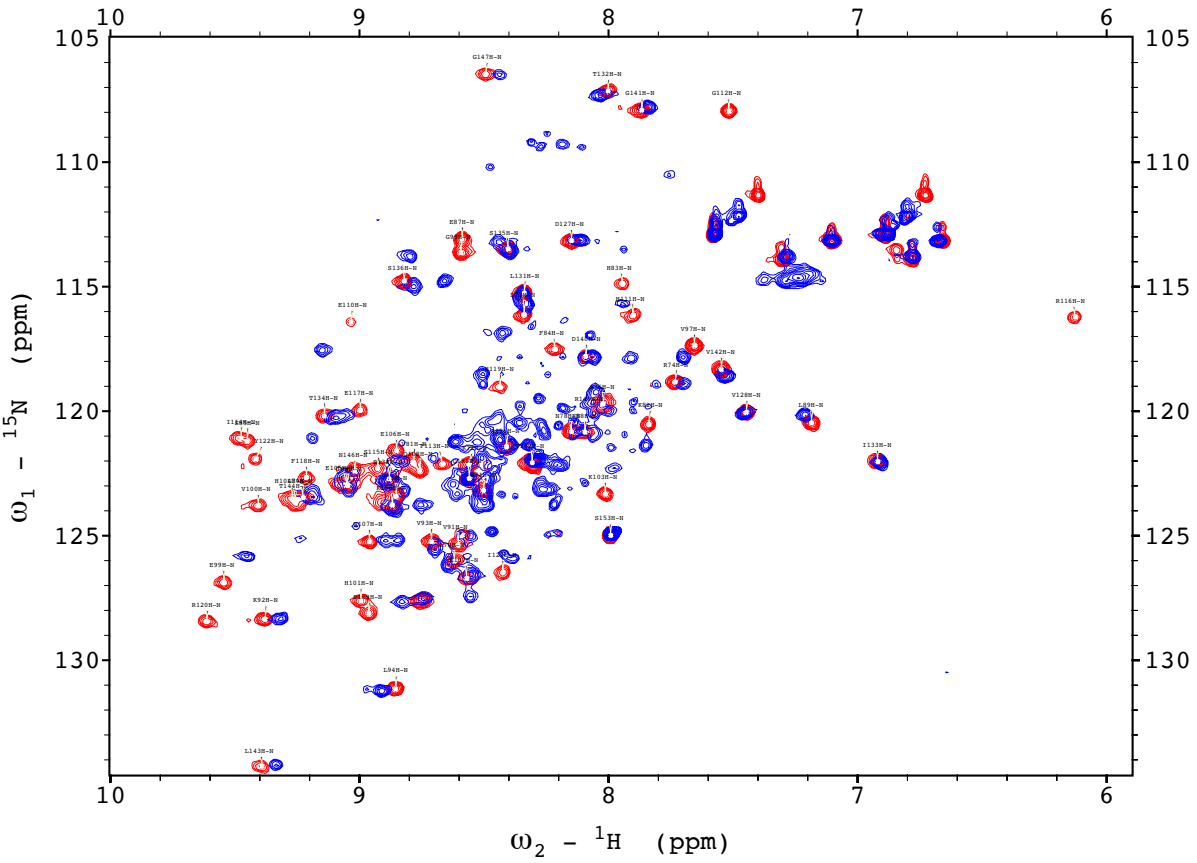

D
αB-C ACD + long fibrils vs αB-C ACD alone
αB-C ACD alone sonicated vs αB-C ACD alone not sonicated
αB-C ACD + short fibrils vs αB-C ACD alone
I/I0
Residue number



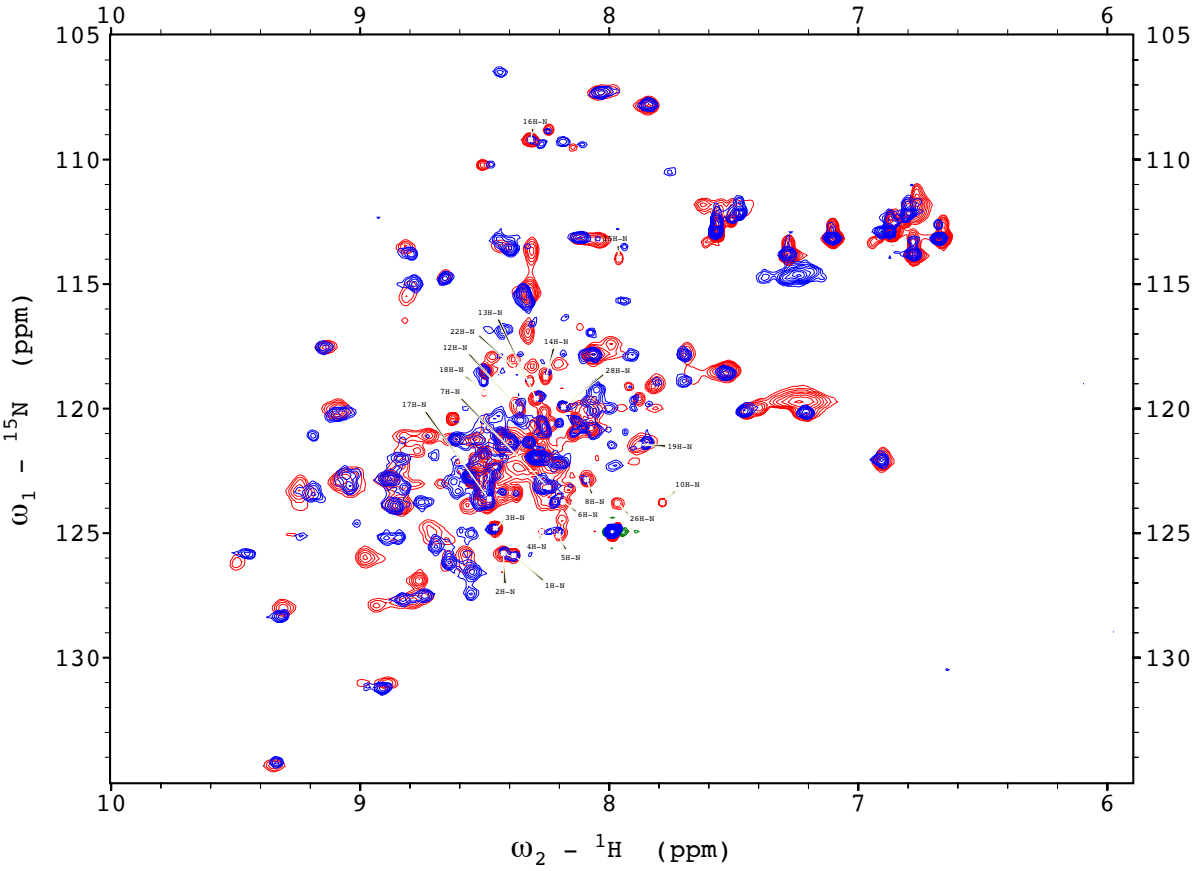
Supplementary Figure 4.4. A) ^{15}N HSQC overlay of 50 μM αB-C ACD in 50 mM sodium phosphate, pH 7.4, 0.02% sodium azide alone (red) and in the presence of apoC-II fibrils (10 mg/mL) (blue). B) ^{15}N HSQC overlay of 50 μM αB-C ACD in 50 mM sodium phosphate, pH 7.4, 0.02% sodium azide alone (red) and in the presence of sonicated apoC-II fibrils (10 mg/mL) (blue). C) ^{15}N HSQC overlay of 50 μM αB-C ACD alone in 50 mM sodium phosphate, pH 7.4, 0.02% sodium azide before (red) and after sonication (blue). Sonication was performed as described in methods section 2.2.12. D) The raw intensities of each assigned peak in each spectra were divided by the raw intensities of the peaks in the control spectra: 50 μM αB-C ACD alone to generate I/I_0 ratios for each assigned peak: αB-C ACD alone sonicated vs αB-C ACD alone prior to sonication (black), αB-C ACD + 10 mg/mL long apoC-II fibrils vs αB-C ACD alone (red) and αB-C ACD + 10 mg/mL short apoC-II fibrils vs αB-C ACD alone (blue). E) Chemical shift perturbation (CSP) analysis of each assigned peak in the presence of long (non-sonicated) apoC-II fibrils relative to αB-C ACD alone.



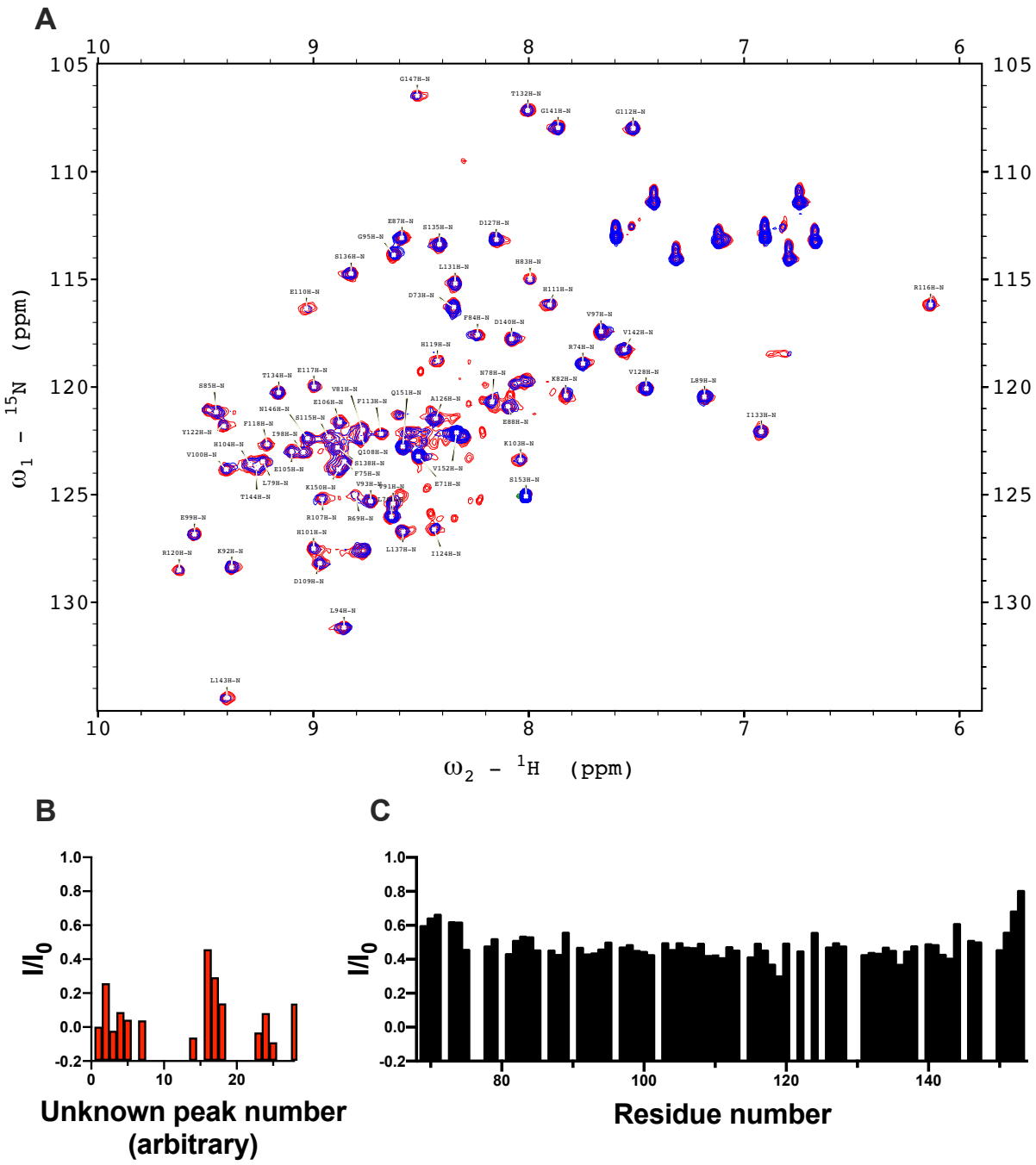
Supplementary Figure 4.5. A) ^{15}N HSQC of 750 μM αB-C ACD alone at pH 7.4 (red) and 6.5 (blue), both at 20°C. B) The raw intensities of each assigned peak in the spectra at pH 6.5, 20°C was divided by the raw intensity of each assigned peak in the spectra at 7.4, 20°C to generate I/I$_0$ ratios for each assigned peak. C) Additional observed peaks that were not assigned were selected based on the spectra obtained at pH 7.4, 20°C. The raw intensities of each of these peaks in the spectra obtained at pH 6.5, 20°C was divided by the raw intensity of each unknown peak in the spectra at pH 7.4, 20°C (where it was possible to select peaks) to generate I/I$_0$ ratios for each unknown peak. D) CSP analysis of each assigned peak for αB-C ACD alone at pH 6.5, 20°C vs pH 7.4, 20°C.



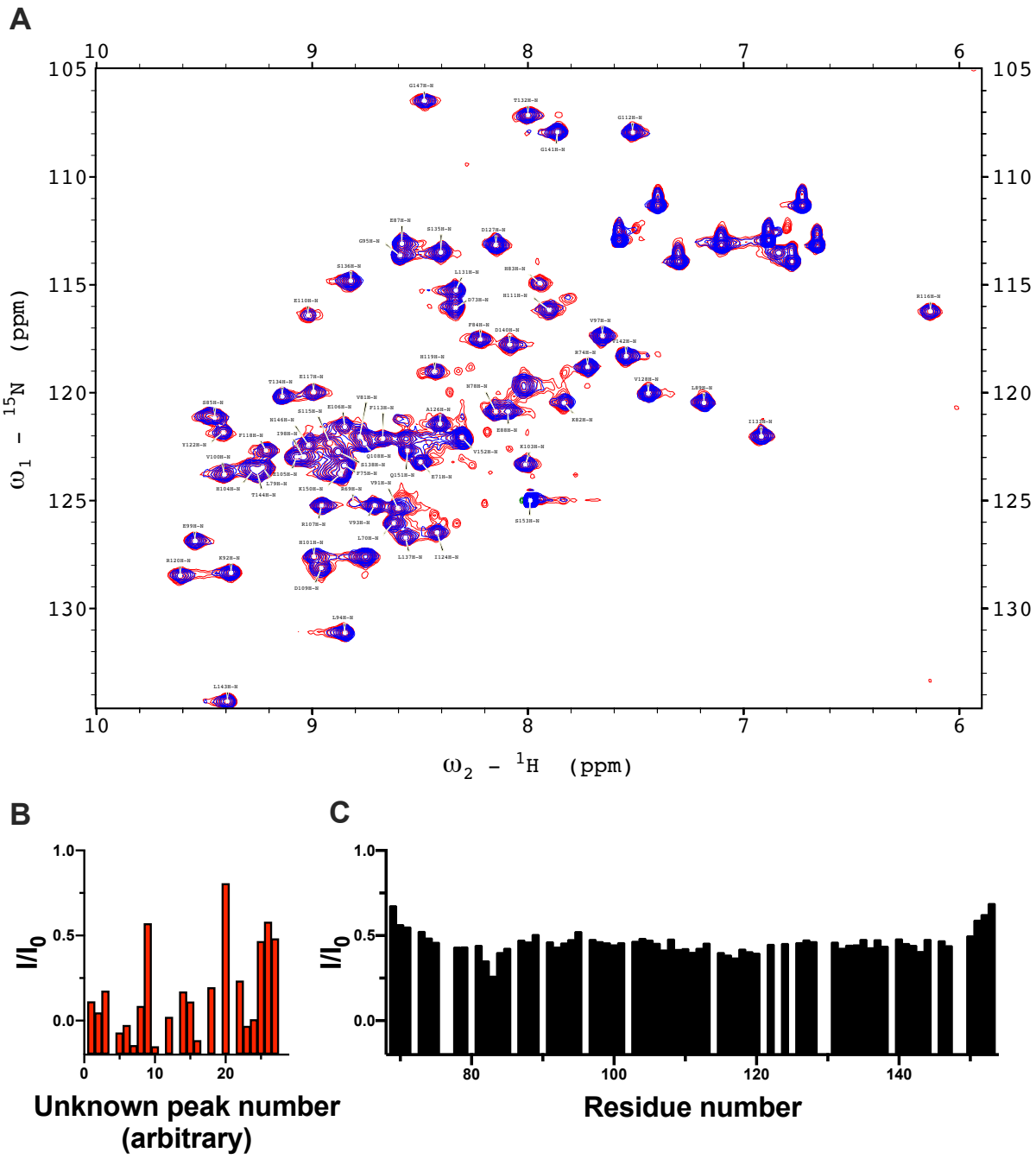
Supplementary Figure 4.6. A) ^{15}N HSQC of 25 μM αB-C ACD alone at pH 7.4 (red) and 6.0 (blue), both at 20°C.



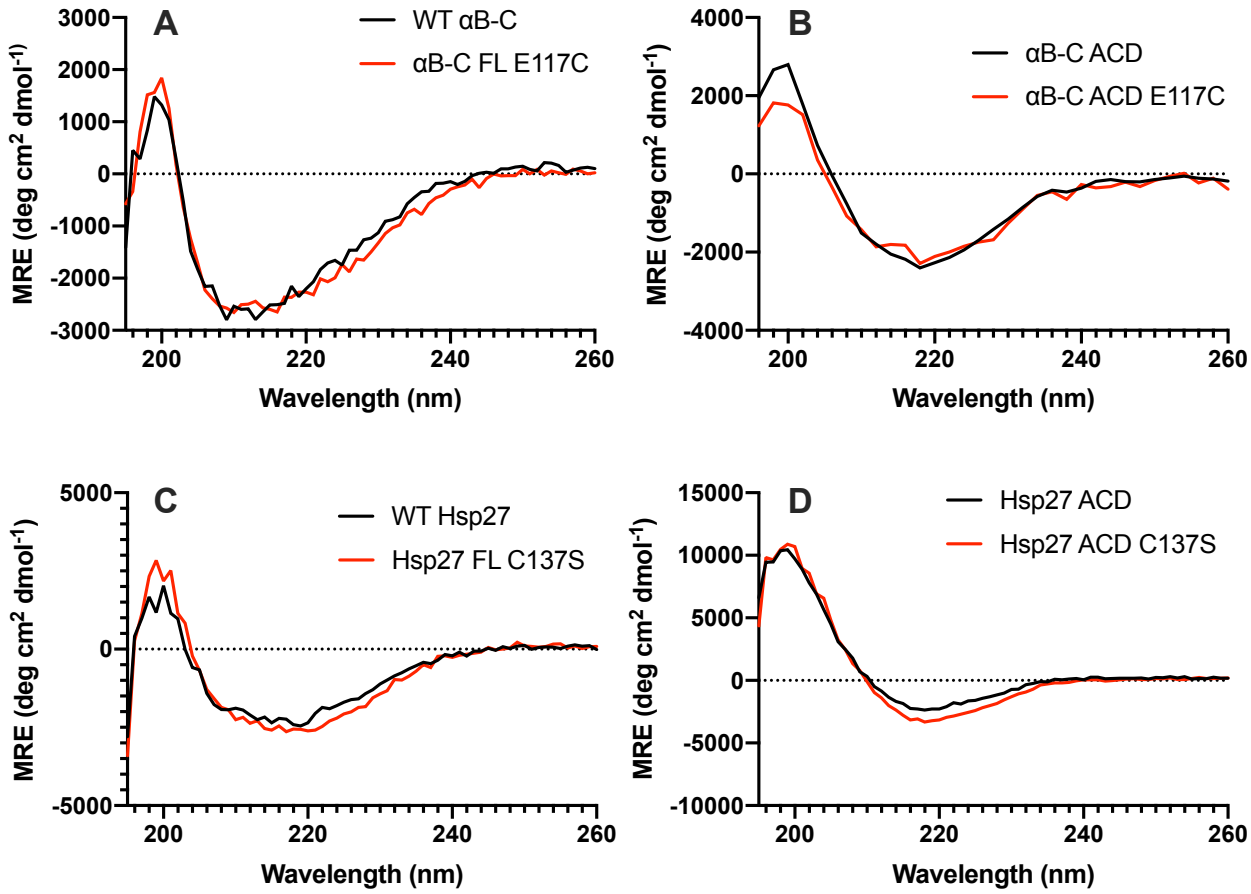
Supplementary Figure 4.7. A) ^{15}N HSQC of 750 μM αB-C ACD alone at pH 5.9 (red) and at 25 μM, pH 6.0 (blue), both at 20°C. Note that in this figure, in order to allow a qualitative comparison of the spectra, the contour levels for the two spectra differ due to the large differences in protein concentration. Unassigned peaks that were observed at 750 μM αB-C ACD alone at pH 5.9 are labelled.



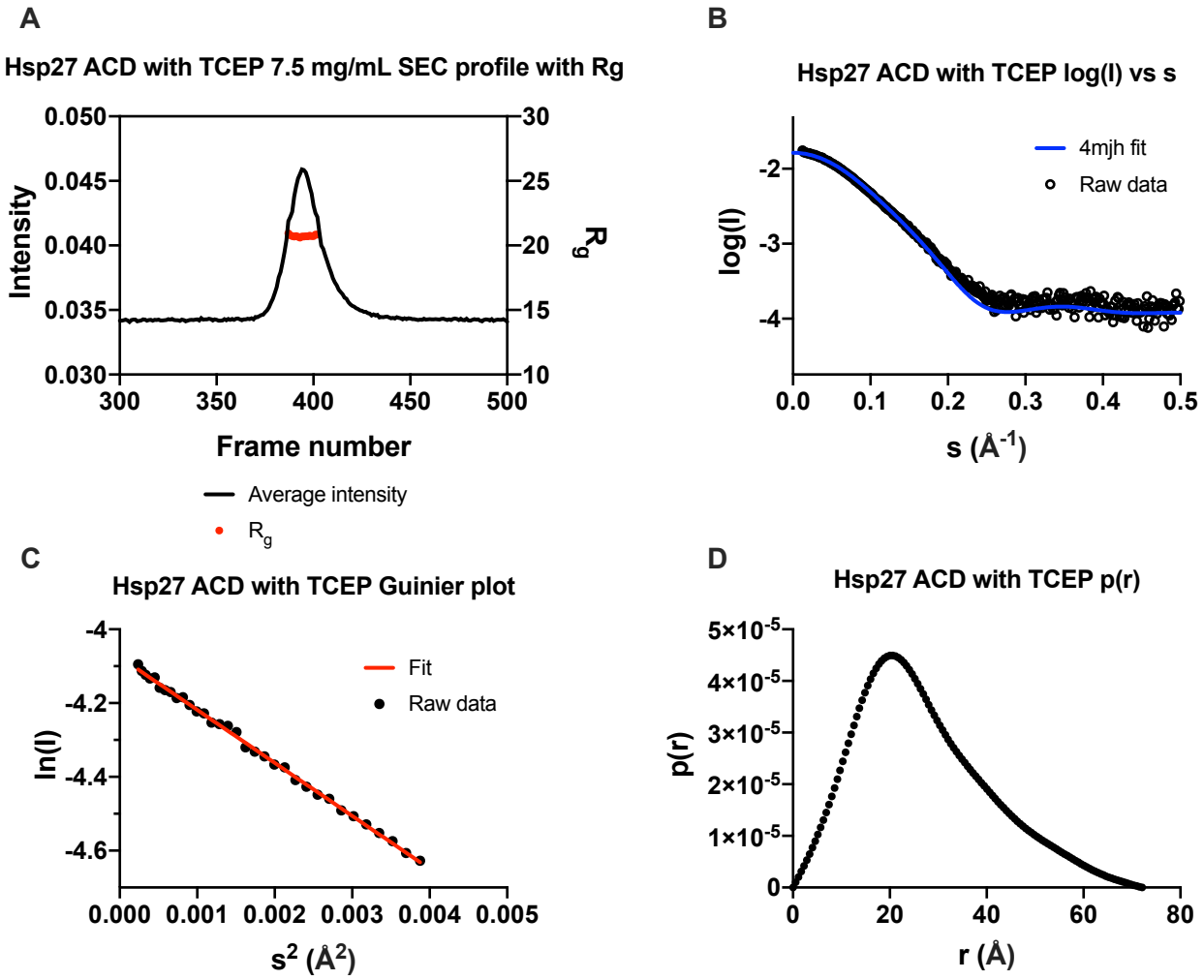
Supplementary Figure 4.8. A) ^{15}N HSQC of 100 μM αB-C ACD alone at pH 7.4 (red) and in the presence of 10 mg/mL fragmented apoC-II fibrils (blue), both at 20°C. The raw intensity of each unassigned (B) and assigned (C) peak in the spectra obtained in the presence of fibrils (where it was possible to select peaks) was divided by the raw intensity of the same peak in the absence of fibrils to generate I/I_0 ratios.



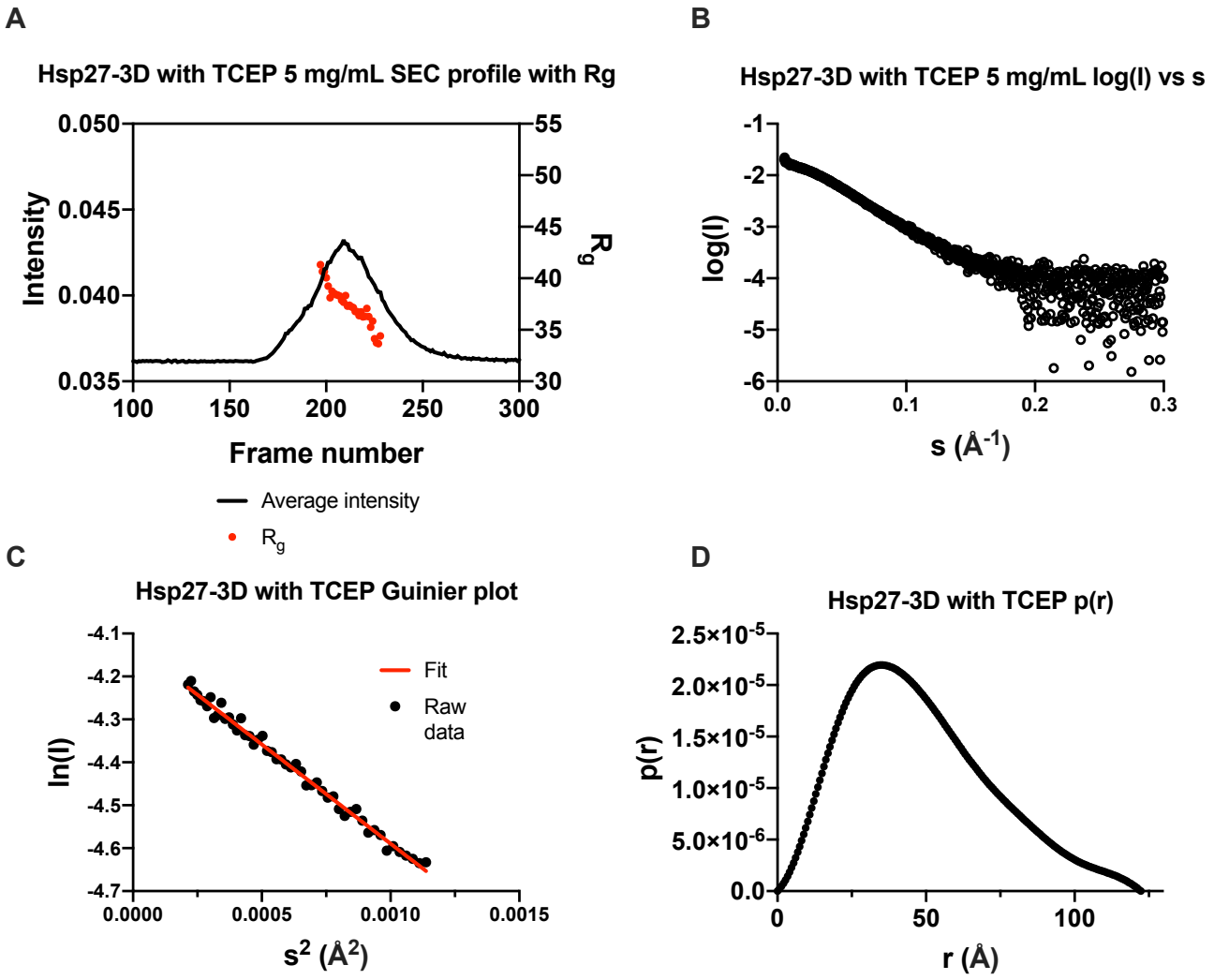
Supplementary Figure 4.9. A) ^{15}N HSQC of 250 μM αB-C ACD alone at pH 7.4 (red) and in the presence of 10 mg/mL fragmented apoC-II fibrils (blue), both at 20°C. The raw intensity of each unassigned (B) and assigned (C) peak in the spectra obtained in the presence of fibrils (where it was possible to select peaks) was divided by the raw intensity of the same peak in the absence of fibrils to generate I/I$_0$ ratios.



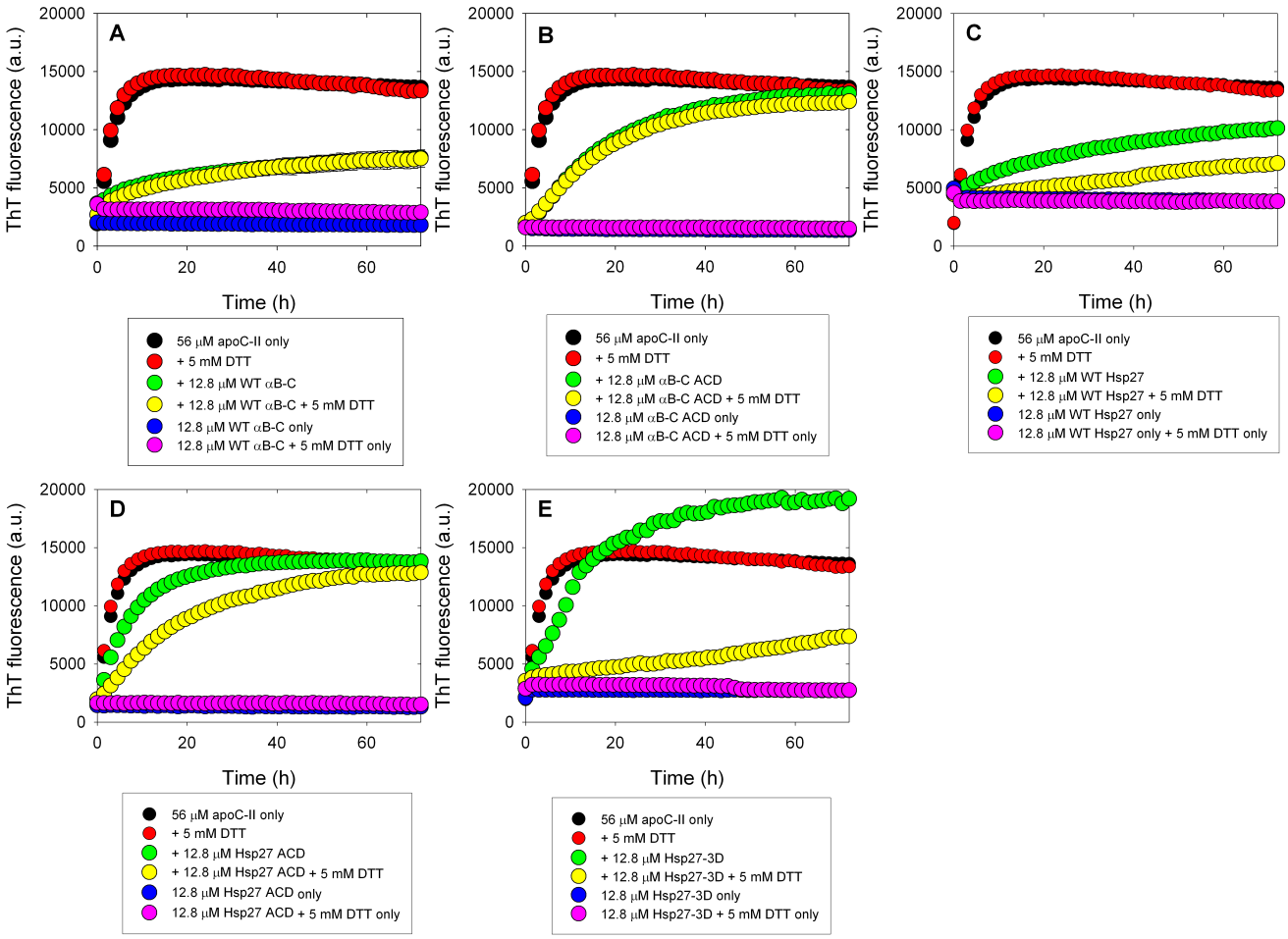
Supplementary Figure 4.10. CD spectroscopy of WT and mutated sHSP constructs. A) WT αB-C (black) and αB-C E117C (red). B) αB-C ACD (black) and αB-C ACD E117C (red). C) WT Hsp27 (black) and Hsp27 C137S (red). D) Hsp27 ACD (black) and Hsp27 ACD C137S (red). All proteins were analysed at a concentration of 0.2 mg/mL in 0.1 M sodium phosphate, pH 7.4.



Supplementary Figure 4.11. SAXS analysis of Hsp27 ACD at a concentration of 750 μM, pH 8.0 in the presence of 2 mM TCEP. 50 μL of Hsp27 ACD at 750 μM was injected onto a Superdex 200 increase 5/150 size exclusion column and eluted at 0.45 mL/min A) UV absorbance at 280 nm (black line, left y-axis) as a function of the frame number following sample loading onto the column. The R_g (red circles, right y-axis) was calculated across the peak using chromixs in the ATSAS software. B) Radially averaged and buffer subtracted scattering intensity expressed as log(I) for Hsp27 ACD as a function of the scattering angle (s) (black circles). The theoretical scattering profile for the crystal structure of Hsp27 ACD (PDB: 4mjh) generated using CRYSOL is shown as a blue line for comparison. C) Guinier plot of Hsp27 ACD generated using primus in the ATSAS software package (raw data shown as black circles, and the linear fit to this data depicted as a red line). D) p(r) function of Hsp27 ACD generated using primus in the ATSAS software package.



Supplementary Figure 4.12. SAXS analysis of Hsp27-3D at a concentration of 220 μM, pH 8.0 in the presence of 2 mM TCEP. 50 μL of Hsp27-3D at 220 μM was injected onto a Superdex 200 increase 5/150 size exclusion column and eluted at 0.45 mL/min A) UV absorbance at 280 nm (black line, left y-axis) as a function of the frame number following sample loading onto the column. The R_g (red circles, right y-axis) was calculated across the peak using chromixs in the ATSAS software. B) Radially averaged and buffer subtracted scattering intensity expressed as log(I) for Hsp27-3D as a function of the scattering angle (s) (black circles). C) Guinier plot of Hsp27-3D generated using primus in the ATSAS software package (raw data shown as black circles, and the linear fit to this data depicted as a red line). D) p(r) function of Hsp27-3D generated using primus in the ATSAS software package.



Supplementary Figure 4.13. ThT fibril formation kinetics of apoC-II (56 μM) alone (black), + 5 mM DTT (red), + 12.8 μM of the following sHSPs constructs: A, WT αB-C; B, αB-C ACD; C, WT Hsp27; D, Hsp27 ACD or E, Hsp27-3D in the absence (green) or presence (yellow) of 5 mM DTT. Samples were incubated at 30°C in 0.1 M sodium phosphate, pH 7.4 + 0.1% sodium azide with 10 μM ThT for 72 hours. Also shown are the indicated sHSP constructs incubated alone (blue) or in the presence of DTT only (magenta) under identical conditions.

Chapter 5: General Discussion

5.1 Rationale for this study

Maintaining proteostasis is essential for life at the cellular and organismal level. sHSPs are a major family of HSPs conserved across all forms of life. As ATP-independent molecular chaperones, they play numerous central housekeeping roles but are particularly important in the maintenance of proteostasis. Not only do sHSPs inhibit amyloid fibril formation by a variety of disease-related and model substrates, but they are also found co-localised to amyloid deposits isolated from patients with a range of neurodegenerative conditions. Consequently, there is substantial scientific interest in the mechanisms of action of these chaperone proteins. Of particular interest for this thesis, are the mechanisms and functional and/or pathological significance of the interactions of these proteins with pre-existing amyloid fibrils. Though sHSPs have been a popular research area in the field of proteostasis, their interactions with amyloid fibrils is an underrepresented area of study. We sought to address this knowledge gap using apoC-II, which is an amyloid system our lab has extensively characterised over the past two decades.

ApoC-II is an excellent system for studying amyloid formation *in vitro*. This is due to the particularly reproducible kinetics of aggregation and our ability to use SV-AUC to characterise the size distributions of the fibrils. These two properties distinguish apoC-II from many other amyloidogenic proteins. In addition to this, apoC-II has been found colocalised to amyloid plaques *in vivo*[155,156], and mutations in apoC-II have recently been found to cause renal amyloidosis[59,60]. Therefore, we used apoC-II to conduct a comprehensive comparison of the chaperone activities of an array of sHSP constructs with modified quaternary structures and quaternary dynamics. The interactions of sHSPs with their substrates and the effects of these interactions have been thoroughly investigated over the past two decades. Our work is distinguished from the majority of these existing studies because we not only investigated the capacity of these chaperones to inhibit amyloid formation, but also their capacity to interact with fibrils and the effects of these interactions on the fibrils. Importantly, our major findings were replicated for another amyloid-forming substrate, α-syn, which forms amyloid fibrils in Parkinson's disease.

5.2 sHSPs inhibit amyloid fibril formation using multiple substrate interactive sites

A major aim of this work was to compare the chaperone activity of an array of sHSPs with modified structures and various truncations. We and others have demonstrated the way these mutations/truncations effect the quaternary structure of the two sHSPs studied here[271,277,279,289]. All of the sHSP constructs tested displayed chaperone activity against both apoC-II and α-syn fibril formation. Crucially, this means that the ACD-only constructs of both αB-C and Hsp27 retain some chaperone activity. However, in all of our assays, the ACD-only constructs were less effective than constructs also containing the NTR. By employing a CTR deletion mutant, we show that inhibition of the nucleation stage of amyloid fibril assembly is mainly encoded by the NTR. These findings are consistent with the observation that the Hsp27 ACD and a Hsp27 construct containing the ACD and CTR were both relatively less effective chaperones against tau amyloid formation[300]. Only WT Hsp27 was found to delay the onset of aggregation, which indicates that the NTR is important for inhibiting the nucleation phase of amyloid formation by tau[300]. The inhibition of the nucleation phase of tau amyloid formation by full-length Hsp27 was also independently verified by Baughman *et al.*[291]. In Chapter 4, we demonstrated that the inhibition of apoC-II and α-syn fibril elongation by Hsp27 ACD was enhanced by removal of the intra-dimer disulfide, implicating the intra-dimer interface as another substrate binding site. For αB-C ACD the effect of intra-dimer disulfide formation depended upon the substrate tested. Against apoC-II fibril formation, disulfide bond formation impaired the chaperone activity of αB-C ACD, whereas for α-syn it improved its chaperone activity. We speculate that αB-C ACD interacts with monomeric and fibrillar α-syn via different binding sites. For example, αB-C ACD may interact with the ends of α-syn fibrils via its intra-dimer interface, as we observed for apoC-II, whereas it may interact with monomeric α-syn via a different interface. Overall, our results indicate that the NTR of αB-C and Hsp27 confer some chaperone activity via one or more substrate binding sites and the ACD additionally confers chaperone activity via the intra-dimer interface and likely via at least one other interface that we have not identified. This other interface could be the hydrophobic β4/8 groove at the outside edge of the ACD, which other groups have identified as a substrate binding site in separate studies[281,300]. Alternatively, a substrate binding site for α-syn may be formed at the surface between the β3 strands of each of the subunits in the dimer. By cross-linking the ACD subunits together via an intra-dimer disulfide, the dynamics across

the dimer interface may be constrained such that the putative substrate binding site is stabilized relative to the same site in the WT ACD. Our NMR results support the notion that the β4/8 groove is an additional substrate binding site for α-syn however further work would be needed to confirm this. We hypothesize that the common structural feature of amyloid fibrils – the unpaired β-strands at their ends – represents a common structural feature that sHSPs can interact with. However, at other stages of protein aggregation pathways, substrates would not necessarily present common structural motifs, thus the ability of sHSPs to bind such diverse substrates is likely to be dependent upon structural heterogeneity, flexibility and the presence of multiple substrate binding sites.

5.3 N- and C-terminal regions of sHSPs and their interactions with amyloid fibrils

Asides from the transient interaction of ACD-only constructs with amyloid fibrils (preferentially at the fibril ends), sHSPs form strong interactions with amyloid fibrils and this was shown to be dependent on the NTR and CTR. We observed a similar extent of fibril binding by full-length oligomeric and full-length sub-oligomeric sHSP constructs, but a reduced extent of binding by the various truncated constructs. As an example, Hsp27-3D and WT Hsp27 both bound amyloid fibrils to a similar extent in our assays, while Hsp27-3DΔCTR displayed a reduced extent of fibril binding and Hsp27 ACD did not form strong interactions with fibrils. However, the rate of fibril binding appeared to be increased for sub-oligomeric sHSPs relative to oligomeric sHSPs. For example, Hsp27-3D appeared to bind fibrils faster than WT Hsp27. The dissociation of sHSP oligomers would increase the accessibility of substrate binding sites within the NTR and CTR, thereby increasing the rate at which sHSPs may bind to substrates. Since Hsp27-3D is primarily dimeric, it does not need to dissociate prior to substrate binding, whereas WT Hsp27 likely needs to dissociate to some extent. What is the physiological function of this specific association of sHSPs with fibrils? Our results suggest two potentially important reasons for this colocalization: 1) the dissociation of pre-existing amyloid fibrils, and 2) the lateral association of pre-existing aggregates mediated by sHSPs. This work is the first to demonstrate that sHSPs can actively dissociate pre-existing amyloid fibrils in the absence of other contributing factors such as dilution. We therefore extended previous work whereby WT αB-C was shown to enhance dilution-induced dissociation of apoC-II fibrils[258] and induce dissociation of β_2-m oligomers[247]. Intriguingly, the rate of fibril binding by WT αB-C correlated with the rate at which it dissociated apoC-II fibrils, indicating that

the process of fibril binding may be linked to the process of fibril dissociation. The data presented in this thesis demonstrates that the NTR is important for fibril binding, fibril dissociation and that the NTR and CTR are both required for fibril-fibril lateral association and tangling. However, we did not gain further mechanistic detail regarding these processes beyond this basic level of understanding. One way to further investigate the roles of the NTR and CTR would be to repeat experiments performed in this study using just the isolated NTR and CTR. A construct encoding only the ACD and CTR of αB-C could also be made. This would enable further comparison of the roles of the NTR and CTR between αB-C and Hsp27 and may also shed light on the role of the CTR in fibril binding and lateral fibril association. These important chaperone properties of sHSPs should also be further investigated *in vivo* because sHSPs are found co-localised to amyloid deposits *in vivo*. Whether sHSPs exert these chaperone functions *in vivo*, and whether such functions have a potential therapeutic benefit remains to be seen. There is one existing study in which a range of HSPs, including αB-C, were found to reduce the toxicity of existing oligomeric aggregates added to cell culture medium by forming strong interactions with the aggregates and promoting their assembly into larger species[262]. How the larger species are less cytotoxic is not well understood, however, the reduction in their surface area and diffusional mobility would reduce the ability of the aggregates to aberrantly interact with other cellular components. Additionally, the colocalization of Hsp27 to the surface of α-syn fibrils was demonstrated to reduce the hydrophobicity of the fibrils and also their cytotoxicity when exposed to cultured neuroblastoma cells[257]. αB-C is also found colocalised with insoluble proteinaceous aggregates containing desmin in desmin-related myopathy[221], with aggregates isolated from aged human muscle fibres[241], and with insoluble aggregates in *C. elegans* and *E. coli*. Therefore, it is tempting to speculate that the colocalization of sHSPs to protein aggregates is a generic function. However, the interactions of sHSPs with protein aggregates not involved in neurodegenerative conditions have not been as rigorously investigated *in vitro,* thus the specificity of the colocalization is currently unclear. Future studies should therefore investigate the colocalization of sHSPs to protein aggregates associated with systemic and tissue-specific proteopathies to determine how generalised such interactions are and whether sHSPs reduce the severity of these conditions. In recent years, ACD-only constructs of human sHSPs have become popular tools for studying sHSPs since these constructs form stable dimers for which high-resolution crystal structures exist (i.e. they simplify the complexity of sHSPs). However, our study shows that the ACD-only constructs

lack several important chaperone activities. Thus, this work highlights the importance of examining the full-length proteins as well as the ACD-only constructs in order to fully comprehend the chaperone properties of these proteins.

5.4 ACD interactions with amyloid fibrils

The ability of sHSPs to inhibit amyloid fibril formation at sub-stoichiometric concentrations has been speculated to arise from an interaction between sHSPs and fibril ends[295]. However, full-length sHSPs bind along the lengths of amyloid fibrils occasionally co-localising to the ends of the fibrils[258]. Therefore, a capping interaction at fibril ends is very difficult to discern from an interaction between the sHSP and the surface of the fibril. This study greatly benefitted from the use of apoC-II fibrils that undergo breaking and end-to-end rejoining, processes that can be quantitatively studied using AUC. Additionally, apoC-II fibrils do not undergo lateral fibril association to the same extent as many other amyloidogenic proteins. Furthermore, the interactions we identified between ACD-only constructs and apoC-II fibrils were found to be transient. These properties enabled us to determine whether the ACD binds fibril ends preferentially to the fibril surface using solution NMR. We are therefore the first to provide direct evidence that the ACD of αB-C binds fibril ends with some preference over the surface of the fibril; however, we have not determined the extent of the difference in affinity between fibril ends and the fibril surface. Such experiments were only possible for the ACD-only constructs since the full-length constructs additionally form strong interactions with fibrils at their surface via NTR and CTR-mediated interactions. This finding is important because fibril fragments/seeds are a major mediator of cytotoxicity *in vivo* due to their ability to propagate protein aggregation throughout and between cells. We show that the ACD-only constructs are able to interact with fibril ends to inhibit this process at sub-stoichiometric ratios. Fibril end-binding therefore represents a potent mechanism sHSPs use to inhibit the propagation of aggregates and the toxicity associated with this process. Our data suggests that the full-length constructs also bind fibril ends, however they additionally bind the fibril surface via their NTR and CTR. Therefore, full-length sHSPs use multiple modes of interaction with amyloid fibrils to reduce their cytotoxicity.

The data presented in Chapter 4 also supports the notion that the ACD monomer is the primary species that interacts with fibrils at their ends. This hypothesis was developed in conjunction with two important previously published works. Firstly, the pH-dependent dimer-monomer dissociation of αB-C ACD was well characterised by Rajagopal *et al.* using NMR[316]. With decreasing pH from 7.4 new peaks appear, generally in the unfolded region of the spectra. We were able to replicate some of these results and detect the additional peaks in the spectra even at pH 7.4. Based on the work of Alderson *et al.*, the ACD monomer is hypothesized to be partially unfolded[314], further supporting the notion that the additional peaks in the unfolded region of our spectra correspond to the ACD monomer. We found that the addition of either apoC-II fibrils or α-syn fibrils to the ACD resulted in specific loss of signal intensity for the ACD monomer peaks. This suggests that the monomer interacts with fibrils with a greater affinity than the dimer, and that the intra-dimer interface may be an interactive site. This hypothesis was supported by our mutagenesis studies in which disulfide cross-linking of ACD dimers generally impaired their chaperone activity. From a structural perspective, the intra-dimer interface is an ideal candidate for forming interactions with the ends of fibrils. The intra-dimer interface is the longest β-strand in the ACD. The plasticity of this interface has been demonstrated by the crystallization of αB-C ACD in 3 different registers[277,279,280] and also by a crystal structure of Hsp27 ACD in which the β4 strand forms an interface with the β6/7 strand[371]. These observations suggest that the β6/7 strand can form hydrogen bonding interactions with unpaired β-strands in a promiscuous manner, making it an excellent candidate for binding to fibril ends.

In addition to the transient interaction we observed between ACD-only constructs and amyloid fibrils, an intriguing observation was that αB-C ACD formed strong interactions with elongating α-syn fibrils, but not with mature fibrils. Consequently, αB-C ACD was only observed to associate with α-syn fibrils when the ACD was added before fibril assembly. Furthermore, this association with growing fibrils was also observed for αB-C ACD E117C but not for Hsp27 ACD or Hsp27 ACD C137S. Therefore, disulfide cross-linking did not appear to affect the association of the ACD-only constructs with the fibrils. This result demonstrates inherent albeit unidentified differences in the way these two ACD-only constructs interact with α-syn. We did not extensively examine whether this interaction is functionally significant, although α-syn seeds formed in the presence of αB-C ACD (i.e. seeds with αB-C ACD associated) were as effective

at seeding further α-syn fibril formation as seeds formed in the absence of αB-C ACD (data not shown). Therefore, once αB-C ACD is associated with α-syn fibrils, it displays a limited ability to inhibit further fibril growth The kinetics and/or reversibility of this association with elongating α-syn fibrils might underlie the differential chaperone activity of αB-C ACD E117C relative to αB-C ACD against α-syn fibril formation. We hypothesize that αB-C ACD interacts with a motif/structural feature of α-syn that is formed as α-syn becomes incorporated into growing fibrils, but which is minimally populated once the fibrils have reached equilibrium. Somehow, αB-C ACD remains associated with the α-syn as the fibrils continue to grow. However, once the fibrils are no longer elongating, this motif/structural feature of α-syn is not formed frequently enough for the ACD to become associated with the fibrils at levels detectable by SDS-PAGE. The structural details underlying the association of αB-C ACD with the elongating α-syn fibrils are not known. To determine how the ACD forms such interactions would be a challenging undertaking, however it is likely that the ACD can no longer function as a chaperone once associated with the fibrils. High resolution cryo-EM is likely the best technique for researchers wishing to understand this interaction further.

5.5 A model for the interactions of sHSPs with aggregation prone proteins

The pathway for amyloid fibril formation was presented in Chapter 1 (Fig 1.4). Based on the results of this thesis, we propose the following model describing how sHSPs modulate this pathway (Fig. 5.1). Nucleation processes appear to be inhibited mainly by the NTR, however some of the work in this thesis suggest that the ACD may also have a role in inhibition of nucleation. Similarly, the NTR was found to be important for inhibiting fibril elongation, though the ACD also displayed an ability to inhibit this stage of fibril formation. Our results suggest that the intra-dimer interface of the ACD is important for inhibiting fibril elongation, likely because of a capping interaction with fibril ends. Such an interaction would also inhibit secondary processes such as seeding. The NTR was found to be required for the dissociation of apoC-II amyloid fibrils. Under the conditions we tested, we didn't observe α-syn fibril dissociation induced by sHSPs. Further conditions may need to be tested, however the dissociation of α-syn fibrils may require additional factors such as ATP-dependent HSPs. For both types of fibrils, fibril binding was conferred by both the NTR and CTR while the CTR was found to be important for inducing lateral fibril association. In an earlier study a full-length sHSP construct was found to inhibit the dilution-induced

fragmentation of apoC-II fibrils[258] however the region of the protein responsible for this function is unknown. Overall, we observed a great deal of similarity between our results with apoC-II and our results with α-syn, but this does not rule out important differences in the way sHSPs interact with these two different substrates. Therefore, sHSPs display a broad array of chaperone functions, which are conferred by various regions of the protein. This model could be further refined by making additional constructs or different mutations to alter the quaternary structure of the sHSPs.

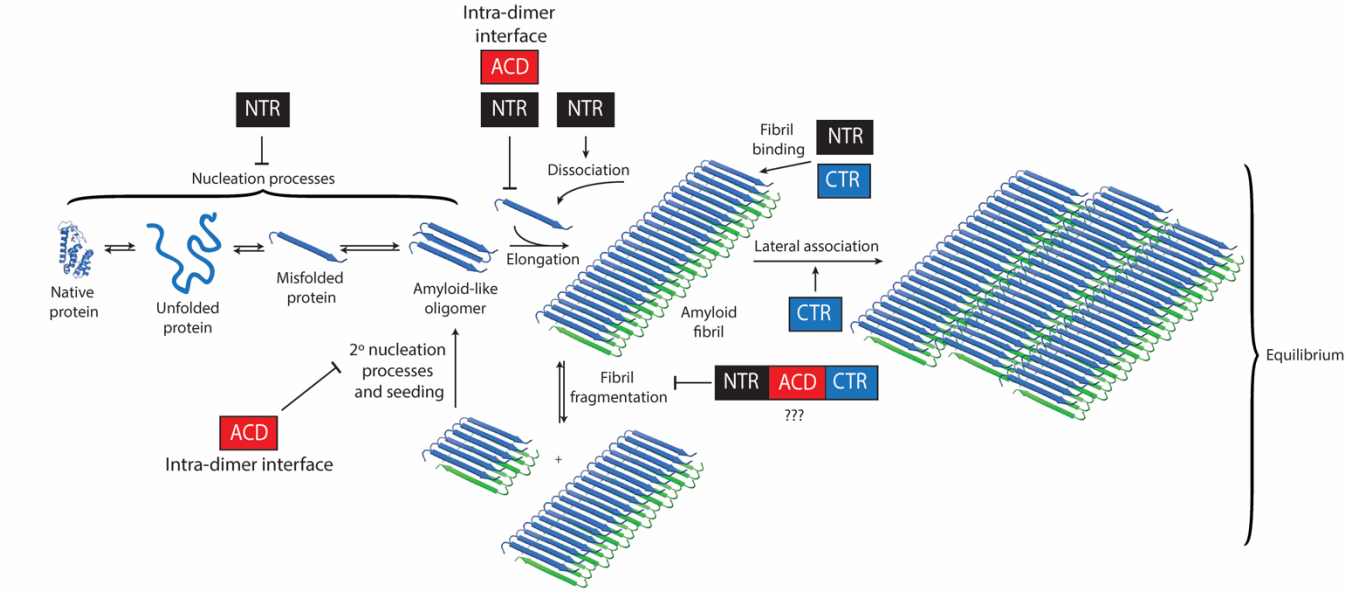


Figure 5.1. A model for the mechanisms used by sHSPs to inhibit amyloid formation and interact with pre-existing fibrils. sHSPs inhibit amyloid formation at various stages of the amyloid formation pathway. The regions of sHSPs responsible for these interactions are indicated with the NTR labelled black, ACD labelled red and CTR labelled blue. Binger *et al.* identified that full-length αB-C inhibits fibril fragmentation[258] however the region of the protein responsible for this function has not yet been identified.

5.6 Potential similarities between sHSPs and other ATP-independent molecular chaperones

Compared with the other major families of mammalian HSPs, sHSPs are more structurally heterogenous, with intrinsically disordered regions at their N- and C-termini. They are also ATP-independent and consequently classified as "holdase" rather than "foldase" chaperones. However, one mammalian chaperone that displays some similar structural and functional properties is clusterin. Clusterin is a secreted ATP-independent mammalian chaperone and is thus found in the extracellular milieu[372]. Like

sHSPs, the 3-dimensional structure of clusterin has not been solved, likely due to its long intrinsically disordered regions[373] and assembly into oligomers of varying sizes[374]. Clusterin inhibits the in vitro aggregation of an array of proteins that aggregate to form amyloid fibrils[375], and has also been found associated with amyloid deposits such as those found in AD[376]. Since clusterin is an extracellular protein the physiological role of this interaction is significant and should be further investigated *in vivo*. The potential effects of clusterin on the size distributions of pre-formed amyloid fibrils should be also investigated *in vitro*. A further similarity between clusterin and sHSPs is that factors that reduce the size of clusterin oligomers enhance its chaperone activity, suggesting that more dissociated forms of clusterin have an increased capacity to interact with substrate proteins[377]. Overall, this thesis demonstrates that the flexible regions of sHSPs play important chaperone roles and that the dissociation of sHSP oligomers may define the rate at which sHSPs can interact with substrate proteins due to the exposure of substrate binding sites that would otherwise be involved in sHSP-sHSP interactions. The dissociation of clusterin oligomers may likewise function to increase the accessibility of the intrinsically disordered regions of clusterin, the putative substrate binding sites. A sperate class of holdase chaperones are the recently identified protein domains called BRICHOS domains[378]. These are components of the proproteins of more than 30 genes but are proteolytically cleaved during protein maturation. Proproteins containing BRICHOS domains are all predicted to encode transmembrane regions with a propensity to form β-hairpin structures[379,380]. These β-hairpin structures can eventually result in the formation of amyloid. The BRICHOS domain is an ~100 residue, folded domain comprising two α-helices that enclose a five-stranded β-sheet[381]. BRICHOS is thought to prevent the transition of its substrate polypeptide from an unfolded conformation to a β-hairpin conformation, thus promoting the formation of the transmembrane helix[379,382]. In support of this hypothesis, BRICHOS domains were found to inhibit the nucleation phase of fibril formation by Aβ40 and Aβ42, maintaining these peptides in the soluble, unstructured form[383,384]. Thus, the chaperone activities of the BRICHOS domains are potentially similar to the those of the NTR/CTR of sHSPs in that they appear to act during the earliest stages of fibril assembly.

5.7 Why this study is important

The most important outcomes of this thesis are an enhanced understanding, *in vitro*, of the mechanisms of action of two human sHSPs, and especially an enhanced understanding of their interactions with amyloid fibrils. The work presented in this thesis represents *in vitro* studies, which have inherent limitations in terms of their relationship to the *in vivo* setting. Therefore, an important extension of this work would be to recapitulate important aspects of this study using cellular models or animal models. It is already known that sHSPs retain the ability to inhibit protein aggregation in cellular models, however more detailed analyses of the other chaperone functions of these proteins rely on robust intracellular models of amyloid formation. Some studies have explored the effects of culturing cells in the presence of sHSPs, amyloidogenic proteins, pre-formed fibrils and various combinations of these[257,262], however further developing cellular models that recapitulate *de novo* amyloid formation (in the absence of seeding with recombinant fibrils) has proven challenging.

Aspects of this study that would be particularly useful to examine *in vivo* would be how effectively the various constructs tested here affect intracellular α-syn aggregation and the resulting viability of these cells. Future research should also focus on whether sHSPs can dissociate (i.e. reverse) amyloid deposits *in vivo*, whether sHSPs induce the assembly of pre-existing fibrils into larger aggregates *in vivo*, whether these larger aggregates have a reduced cytotoxicity relative to smaller dispersed aggregates and how the various sHSP constructs tested here affect fibril lengths *in vivo*.

The methodologies we have used here to analyse the chaperone properties of sHSPs may be broadly applicable to researchers investigating other types of HSPs. The unique biophysical properties of apoC-II fibrils enabled us to identify new chaperone functions of sHSPs. A prime example from this work was our observation that ACD-only constructs inhibited apoC-II fibril end-to-end joining. It is unlikely that we would have been able to identify this chaperone function using α-syn fibrils, since they are generally too large for AUC analysis and α-syn fibril end rejoining is not well characterised.

5.8 Future Directions

There are many outstanding research questions, some of which have already been discussed earlier in this chapter. A major unexplored area of this work is investigating the interaction of Hsp27 ACD (in the reduced state or with the C137S mutation) with amyloid fibrils via NMR – as we did for αB-C ACD to determine whether the Hsp27 ACD monomer is also responsible for binding fibrils. Our mutagenesis studies suggest that this is the case, but we do not yet have direct evidence. Based on the work of Alderson *et al.*[314], it is likely that the Hsp27 ACD monomer is detectable at or near physiological pH as we observed for αB-C ACD. Therefore, similar experiments for Hsp27 ACD should be feasible. Of particular interest would be the interaction Hsp27 ACD with α-syn fibrils, to determine whether the Hsp27 ACD monomer peaks are also specifically broadened in the presence of fibrils relative to the dimer peaks. This would reinforce our hypothesis that the αB-C ACD monomer also interacts with α-syn fibrils.

Hsp27-3DΔCTR should be employed to further understand the involvement of the NTR in inhibiting amyloid fibril formation and in interacting with pre-formed fibrils. Since Hsp27-3DΔCTR exists in a relatively monodisperse dimeric state, and the NTR is not completely intrinsically disordered it may be possible to conduct substrate binding studies via NMR using this construct. Furthermore, the reduced fibril binding affinity we observed for this construct relative to full-length Hsp27 constructs may enable NMR studies of its interaction with fibrils, providing that the rates of fibril association/dissociation are amenable to solution NMR. Such studies may also enable characterization of the mechanism by which the NTR induces dissociation of apoC-II fibrils. In Chapter 3 we demonstrated that the rate of fibril binding by sHSPs containing the NTR correlated with the rate of fibril dissociation. Does fibril binding lead to fibril dissociation? Or do sHSPs cause dissociation by stabilizing the free monomer in equilibrium with the fibrils? Understanding the underlying mechanisms by which sHSPs induce apoC-II fibril dissociation could shed light on why they do not dissociate α-syn fibrils. Furthermore, an increased understanding of fibril dissociation induced by sHSPs could enable the development of therapeutics that enhance this effect or mimic this effect *in vivo* to help clear aggregates under conditions where the proteostasis network is overwhelmed.

Another major finding of this thesis was that against both substrates tested, reduction or removal of the intra-dimer disulfide improves the chaperone ability of all of the Hsp27 constructs we tested. Importantly, Hsp27 is a cytosolic protein, which therefore means that the intra-dimer disulfide would be expected to be in the reduced state *in vivo*. Nevertheless, the cysteine residue located at the intra-dimer interface is highly conserved in Hsp27 orthologs. Cysteine residues have an unusual pattern of conservation. Marino *et al.* found that, relative to other amino acids, cysteine residues are either very poorly conserved or very highly conserved[385]. Furthermore, cysteine residues spatially clustered together were also found to be more highly conserved than cysteine residues spatially isolated from other cysteine residues. Highly conserved cysteine residues are predicted to be located at functionally important sites, at catalytic sites or to be involved in stabilizing the structure of a protein through disulfide bond formation. Hsp27 is not known to possess catalytic activity, therefore it is likely that the cysteine residue located at the dimer interface is either functionally important or involved in stabilizing the structure of Hsp27 through disulfide bond formation. There is some existing evidence supporting both of these hypotheses. Firstly, Hsp27 can form disulfide cross-linked dimers intracellularly under conditions of oxidative stress[386,387]. Unsurprisingly, disulfide bond formation was shown to stabilize Hsp27 against urea-induced denaturation[387] and thermally induced changes in its quaternary structure[388]. Conversely, intra-dimer disulfide crosslinking of Hsp27 was found to either minimally impact its chaperone activity[387,389] or to decrease its chaperone activity, depending on the substrate tested[314,388]. These findings raise the question as to why the cysteine residue is so highly conserved. The answer to this question likely necessitates a broader understanding of the functions of Hsp27 in a cellular context. Asides from its function as a molecular chaperone, Hsp27 upregulates intracellular glutathione and increases the activity of enzymes involved in the pentose phosphate pathway such as glucose-6-phosphate dehydrogenase[390]. These functions increase the reductive capacity of the cell and decrease intracellular reactive oxygen species (ROS). Mutation of the conserved cysteine residue in Hsp27 reduced cellular resistance to conditions of oxidative stress such as exposure to hydrogen peroxide[386,389,390]. Moreover, the anti-apoptotic binding of Hsp27 to cytochrome c was found to be dependent on the lone cysteine residue of Hsp27[391]. Based on these studies it is plausible that under basal conditions in the absence of oxidative stress, Hsp27 chaperones various substrates in its oligomeric, dimeric or monomeric form. Against some substrates, for example amyloidogenic

substrates, the monomeric form appears to have an enhanced chaperone activity. A second function of Hsp27 is to serve as a sensor for the intracellular redox state and reduce intracellular ROS. Thus, under conditions of oxidative stress, the primary intracellular role of Hsp27 may be to inhibit apoptosis and/or maintain a reducing environment within the cell[390]. This is significant because there is a strong correlation between the accumulation of ROS and a reduction in life span[392,393]. Increased levels of oxidative stress are also evident in AD and PD brains[394,395]. A holistic understanding of the functional importance of the cysteine residue and its oxidized or reduced state relies on further *in vivo* studies, particularly those examining the chaperone activity and antioxidant properties of Hsp27 under various redox conditions.

5.9 Concluding remarks

The deposition of aggregation prone proteins as amyloid fibrils is a pathological hallmark of neurodegenerative and systemic diseases. The accumulation of these deposits signifies a failure of the proteostasis network to prevent protein misfolding and aggregation. To understand how the capacity of the proteostasis network becomes overwhelmed necessitates a detailed understanding of the mechanisms of action of all of the components of the network, including sHSPs. This thesis significantly advances our understanding of the mechanisms used by sHSPs to inhibit amyloid fibril formation. We also demonstrate the multiple ways sHSPs interact with pre-existing amyloid fibrils and present hypotheses as to the physiological role of these interactions. These hypotheses can be further investigated using cellular or animal models of amyloidoses to advance our understanding of the biological roles of sHSPs in the context of amyloidoses. If the results presented in this work are consistent with the functions of sHSPs *in vivo*, our findings could lead to the development of therapeutic approaches for enhancing these functions of sHSPs in order to treat and/or manage diseases associated with amyloid deposition.

References

(1) Wright, P. E.; Dyson, H. J. Intrinsically Unstructured Proteins: Re-Assessing the Protein Structure-Function Paradigm. *J. Mol. Biol.* **1999**, *293* (2), 321–331. https://doi.org/10.1006/jmbi.1999.3110.

(2) Anfinsen, C. B.; Haber, E.; Sela, M.; White, F. H. The Kinetics of Formation of Native Ribonuclease During Oxidation of the Reduced Polypeptide Chain. *Proc. Natl. Acad. Sci.* **1961**, *47* (9), 1309–1314. https://doi.org/10.1073/pnas.47.9.1309.

(3) Anfinsen, C. B. Principles That Govern the Folding of Protein Chains. *Science* **1973**, *181* (4096), 223–230. https://doi.org/10.1126/science.181.4096.223.

(4) Levinthal, C. Are There Pathways for Protein Folding? *J. Chim. Phys.* **1968**, *65*, 44–45. https://doi.org/10.1051/jcp/1968650044.

(5) Dill, K. A.; Chan, H. S. From Levinthal to Pathways to Funnels. *Nat. Struct. Mol. Biol.* **1997**, *4* (1), 10–19. https://doi.org/10.1038/nsb0197-10.

(6) Kauzmann, W. Some Factors in the Interpretation of Protein Denaturation11The Preparation of This Article Has Been Assisted by a Grant from the National Science Foundation. In *Advances in Protein Chemistry*; Anfinsen, C. B., Anson, M. L., Bailey, K., Edsall, J. T., Eds.; Academic Press, 1959; Vol. 14, pp 1–63. https://doi.org/10.1016/S0065-3233(08)60608-7.

(7) Sturtevant, J. M. Heat Capacity and Entropy Changes in Processes Involving Proteins. *Proc. Natl. Acad. Sci. U. S. A.* **1977**, *74* (6), 2236–2240.

(8) Pace, C. N.; Shirley, B. A.; McNutt, M.; Gajiwala, K. Forces Contributing to the Conformational Stability of Proteins. *FASEB J.* **1996**, *10* (1), 75–83. https://doi.org/10.1096/fasebj.10.1.8566551.

(9) Dobson, C. M. Protein Folding: A Perspective from Theory and Experiment. *Angew Chem Int Ed* **1998**, 26.

(10) Tsai, C.-J.; Kumar, S.; Ma, B.; Nussinov, R. Folding Funnels, Binding Funnels, and Protein Function. *Protein Sci.* **1999**, *8* (6), 1181–1190. https://doi.org/10.1110/ps.8.6.1181.

(11) Holtkamp, W.; Kokic, G.; Jäger, M.; Mittelstaet, J.; Komar, A. A.; Rodnina, M. V. Cotranslational Protein Folding on the Ribosome Monitored in Real Time. *Science* **2015**, *350* (6264), 1104–1107. https://doi.org/10.1126/science.aad0344.

(12) Hsu, S.-T. D.; Fucini, P.; Cabrita, L. D.; Launay, H.; Dobson, C. M.; Christodoulou, J. Structure and Dynamics of a Ribosome-Bound Nascent Chain by NMR Spectroscopy. *Proc. Natl. Acad. Sci.* 2007, *104* (42), 16516–16521. https://doi.org/10.1073/pnas.0704664104.

(13) Zipser, D.; Perrin, D. Complementation on Ribosomes. *Cold Spring Harb. Symp. Quant. Biol.* 1963, *28*, 533–537. https://doi.org/10.1101/SQB.1963.028.01.071.

(14) Kleizen, B.; Braakman, I. Protein Folding and Quality Control in the Endoplasmic Reticulum. *Curr. Opin. Cell Biol.* 2004, *16* (4), 343–349. https://doi.org/10.1016/j.ceb.2004.06.012.

(15) Voss, N. R.; Gerstein, M.; Steitz, T. A.; Moore, P. B. The Geometry of the Ribosomal Polypeptide Exit Tunnel. *J. Mol. Biol.* 2006, *360* (4), 893–906. https://doi.org/10.1016/j.jmb.2006.05.023.

(16) Ptitsyn, B. INTER-DOMAIN MOBILITY IN PROTEINS AND ITS PROBABLE FUNCTIONAL ROLE. *FEBS Lett.* 1978, *93* (1), 4.

(17) Jaenicke, R. Folding and Association of Proteins. *Prog. Biophys. Mol. Biol.* 1987, *49* (2), 117–237. https://doi.org/10.1016/0079-6107(87)90011-3.

(18) Hartl, F. U.; Bracher, A.; Hayer-Hartl, M. Molecular Chaperones in Protein Folding and Proteostasis. *Nature* 2011, *475* (7356), 324–332. https://doi.org/10.1038/nature10317.

(19) Balchin, D.; Hayer-Hartl, M.; Hartl, F. U. In Vivo Aspects of Protein Folding and Quality Control. *Science* 2016, *353* (6294), 14. https://doi.org/10.1126/science.aac4354.

(20) Netzer, W. J.; Hartl, F. U. Recombination of Protein Domains Facilitated by Co-Translational Folding in Eukaryotes. *Nature* 1997, *388* (6640), 343–349.

(21) Riordan, J. R.; Rommens, J. M.; Kerem, B.-S.; Alon, N.; Rozmahel, R.; Grzelczak, Z.; Zielenski, J.; Lok, S.; Plavsic, N.; Chou, J.-L.; Drumm, M. L.; Iannuzzi, M. C.; Collins, F.; Tsui, L.-C. Identification of the Cystic Fibrosis Gene: Cloning and Characterization of Complementary DNA. *Science* 1989, *245* (4922), 1066-.

(22) Cheng, S. H.; Gregory, R. J.; Marshall, J.; Paul, S.; Souza, D. W.; White, G. A.; O'Riordan, C. R.; Smith, A. E. Defective Intracellular Transport and Processing of CFTR Is the Molecular Basis of Most Cystic Fibrosis. *Cell* 1990, *63* (4), 827–834. https://doi.org/10.1016/0092-8674(90)90148-8.

(23) Hardy, J. A.; Higgins, G. A. Alzheimer's Disease: The Amyloid Cascade Hypothesis. *Science* 1992, *256* (5054), 184-.

(24) Baba, M.; Nakajo, S.; Tu, P.-H.; Tomita, T.; al, et. Aggregation of (Alpha-Synuclein) in Lewy Bodies of Sporadic Parkinson's Disease and Dementia with Lewy Bodies. *Am. J. Pathol. Hagerstown* 1998, *152* (4), 879–884.

(25) Weinreb, P. H.; Zhen, W.; Poon, A. W.; Conway, K. A.; Lansbury, P. T. NACP, A Protein Implicated in Alzheimer's Disease and Learning, Is Natively Unfolded. *Biochemistry* 1996, *35* (43), 13709–13715. https://doi.org/10.1021/bi961799n.

(26) Goldsbury, C.; Goldie, K.; Pellaud, J.; Seelig, J.; Frey, P.; Müller, S. A.; Kistler, J.; Cooper, G. J. S.; Aebi, U. Amyloid Fibril Formation from Full-Length and Fragments of Amylin. *J. Struct. Biol.* 2000, *130* (2), 352–362. https://doi.org/10.1006/jsbi.2000.4268.

(27) Cao, X.; Antonyuk, S. V.; Seetharaman, S. V.; Whitson, L. J.; Taylor, A. B.; Holloway, S. P.; Strange, R. W.; Doucette, P. A.; Valentine, J. S.; Tiwari, A.; Hayward, L. J.; Padua, S.; Cohlberg, J. A.; Hasnain, S. S.; Hart, P. J. Structures of the G85R Variant of SOD1 in Familial Amyotrophic Lateral Sclerosis. *J. Biol. Chem.* 2008, *283* (23), 16169–16177. https://doi.org/10.1074/jbc.M801522200.

(28) Sunde, M.; Richardson, S. J.; Chang, L.; Pettersson, T. M.; Schreiber, G.; Blake, C. C. The Crystal Structure of Transthyretin from Chicken. *Eur. J. Biochem.* 1996, *236* (2), 491–499.

(29) MacDonald, M. E.; Ambrose, C. M.; Duyao, M. P.; Myers, R. H.; Lin, C.; Srinidhi, L.; Barnes, G.; Taylor, S. A.; James, M.; Groot, N.; MacFarlane, H.; Jenkins, B.; Anderson, M. A.; Wexler, N. S.; Gusella, J. F.; Bates, G. P.; Baxendale, S.; Hummerich, H.; Kirby, S.; North, M.; Youngman, S.; Mott, R.; Zehetner, G.; Sedlacek, Z.; Poustka, A.; Frischauf, A.-M.; Lehrach, H.; Buckler, A. J.; Church, D.; Doucette-Stamm, L.; O'Donovan, M. C.; Riba-Ramirez, L.; Shah, M.; Stanton, V. P.; Strobel, S. A.; Draths, K. M.; Wales, J. L.; Dervan, P.; Housman, D. E.; Altherr, M.; Shiang, R.; Thompson, L.; Fielder, T.; Wasmuth, J. J.; Tagle, D.; Valdes, J.; Elmer, L.; Allard, M.; Castilla, L.; Swaroop, M.; Blanchard, K.; Collins, F. S.; Snell, R.; Holloway, T.; Gillespie, K.; Datson, N.; Shaw, D.; Harper, P. S. A Novel Gene Containing a Trinucleotide Repeat That Is Expanded and Unstable on Huntington's Disease Chromosomes. *Cell* 1993, *72* (6), 971–983. https://doi.org/10.1016/0092-8674(93)90585-E.

(30) Chartier-Harlin, M.-C.; Crawford, F.; Houlden, H.; Warren, A.; Hughes, D.; Fidani, L.; Goate, A.; Rossor, M.; Roques, P.; Hardy, J.; Mullan, M. Early-Onset Alzheimer's Disease Caused by

Mutations at Codon 717 of the β-Amyloid Precursor Protein Gene. *Nature* 1991, *353* (6347), 844. https://doi.org/10.1038/353844a0.

(31) Sherrington, R.; Rogaev, E. I.; Liang, Y.; Rogaeva, E. A.; Levesque, G.; Ikeda, M.; Chi, H.; Lin, C.; Li, G.; Holman, K.; Tsuda, T.; Mar, L.; Foncin, J.-F.; Bruni, A. C.; Montesi, M. P.; Sorbi, S.; Rainero, I.; Pinessi, L.; Nee, L.; Chumakov, I.; Pollen, D.; Brookes, A.; Sanseau, P.; Polinsky, R. J.; Wasco, W.; Silva, H. A. R. D.; Haines, J. L.; Pericak-Vance, M. A.; Tanzi, R. E.; Roses, A. D.; Fraser, P. E.; Rommens, J. M.; George-Hyslop, P. H. S. Cloning of a Gene Bearing Missense Mutations in Early-Onset Familial Alzheimer's Disease. *Nature* 1995, *375* (6534), 754. https://doi.org/10.1038/375754a0.

(32) Conway, K. A.; Harper, J. D.; Lansbury, P. T. Accelerated in Vitro Fibril Formation by a Mutant α-Synuclein Linked to Early-Onset Parkinson Disease. *Nat. Med.* 1998, *4* (11), 1318. https://doi.org/10.1038/3311.

(33) Kerner, M. J.; Naylor, D. J.; Ishihama, Y.; Maier, T.; Chang, H.-C.; Stines, A. P.; Georgopoulos, C.; Frishman, D.; Hayer-Hartl, M.; Mann, M.; Hartl, F. U. Proteome-Wide Analysis of Chaperonin-Dependent Protein Folding in Escherichia Coli. *Cell* 2005, *122* (2), 209–220. https://doi.org/10.1016/j.cell.2005.05.028.

(34) Xiao, Y.; Ma, B.; McElheny, D.; Parthasarathy, S.; Long, F.; Hoshi, M.; Nussinov, R.; Ishii, Y. Aβ(1-42) Fibril Structure Illuminates Self-Recognition and Replication of Amyloid in Alzheimer's Disease. *Nat. Struct. Mol. Biol.* 2015, *22* (6), 499–505. https://doi.org/10.1038/nsmb.2991.

(35) Teoh, C. L.; Pham, C. L. L.; Todorova, N.; Hung, A.; Lincoln, C. N.; Lees, E.; Lam, Y. H.; Binger, K. J.; Thomson, N. H.; Radford, S. E.; Smith, T. A.; Müller, S. A.; Engel, A.; Griffin, M. D. W.; Yarovsky, I.; Gooley, P. R.; Howlett, G. J. A Structural Model for Apolipoprotein C-II Amyloid Fibrils: Experimental Characterization and Molecular Dynamics Simulations. *J. Mol. Biol.* 2011, *405* (5), 1246–1266. https://doi.org/10.1016/j.jmb.2010.12.006.

(36) Sipe, J. D.; Cohen, A. S. Review: History of the Amyloid Fibril. *J. Struct. Biol.* 2000, *130* (2–3), 88–98. https://doi.org/10.1006/jsbi.2000.4221.

(37) Brady, J. P.; Garland, D.; Duglas-Tabor, Y.; Robison, W. G.; Groome, A.; Wawrousek, E. F. Targeted Disruption of the Mouse AA-Crystallin Gene Induces Cataract and Cytoplasmic Inclusion

Bodies Containing the Small Heat Shock Protein AB-Crystallin. *Proc. Natl. Acad. Sci.* 1997, *94* (3), 884–889. https://doi.org/10.1073/pnas.94.3.884.

(38) Chiti, F.; Dobson, C. M. Protein Misfolding, Amyloid Formation, and Human Disease: A Summary of Progress Over the Last Decade. *Annu. Rev. Biochem.* 2017, *86* (1), 27–68. https://doi.org/10.1146/annurev-biochem-061516-045115.

(39) Spillantini, M. G.; Schmidt, M. L.; Lee, V. M.-Y.; Trojanowski, J. Q.; Jakes, R.; Goedert, M. α-Synuclein in Lewy Bodies. *Nature* 1997, *388* (6645), 839. https://doi.org/10.1038/42166.

(40) Spillantini, M. G.; Crowther, R. A.; Jakes, R.; Hasegawa, M.; Goedert, M. Alpha-Synuclein in Filamentous Inclusions of Lewy Bodies from Parkinson's Disease and Dementia with Lewy Bodies. *Proc Natl Acad Sci U A* 1998, *95* (11), 6469–6473.

(41) Grazia Spillantini, M.; Anthony Crowther, R.; Jakes, R.; Cairns, N. J.; Lantos, P. L.; Goedert, M. Filamentous α-Synuclein Inclusions Link Multiple System Atrophy with Parkinson's Disease and Dementia with Lewy Bodies. *Neurosci. Lett.* 1998, *251* (3), 205–208. https://doi.org/10.1016/S0304-3940(98)00504-7.

(42) Kitamoto, T.; Tateishi, J.; Tashima, T.; Takeshita, I.; Barry, R. A.; Dearmond, S. J.; Prusiner, S. B. Amyloid plaques in Creutzfeldt-Jakob disease stain with prion protein antibodies. *Ann. Neurol.* 1986, *20* (2), 204–208. https://doi.org/10.1002/ana.410200205.

(43) Medori, R.; Tritschler, H.-J.; LeBlanc, A.; Villare, F.; Manetto, V.; Chen, H. Y.; Xue, R.; Leal, S.; Montagna, P.; Cortelli, P.; Tinuper, P.; Avoni, P.; Mochi, M.; Baruzzi, A.; Hauw, J. J.; Ott, J.; Lugaresi, E.; Autilio-Gambetti, L.; Gambetti, P. Fatal Familial Insomnia, a Prion Disease with a Mutation at Codon 178 of the Prion Protein Gene. *N. Engl. J. Med.* 1992, *326* (7), 444–449. https://doi.org/10.1056/NEJM199202133260704.

(44) Prusiner, S. B. Neurodegenerative Diseases and Prions. *N. Engl. J. Med.* 2001, *344* (20), 1516–1526. https://doi.org/10.1056/NEJM200105173442006.

(45) Grundke-Iqbal, I.; Iqbal, K.; Tung, Y. C.; Quinlan, M.; Wisniewski, H. M.; Binder, L. I. Abnormal Phosphorylation of the Microtubule-Associated Protein Tau (Tau) in Alzheimer Cytoskeletal Pathology. *Proc. Natl. Acad. Sci.* 1986, *83* (13), 4913–4917. https://doi.org/10.1073/pnas.83.13.4913.

(46) Kato, S.; Nakamura, H. Presence of Two Different Fibril Subtypes in the Pick Body: An Immunoelectron Microscopic Study. *Acta Neuropathol. (Berl.)* **1990**, *81* (2), 125–129. https://doi.org/10.1007/bf00334500.

(47) Flament, S.; Delacourte, A.; Verny, M.; Hauw, J.-J.; Javoy-Agid, F. Abnormal Tau Proteins in Progressive Supranuclear Palsy. *Acta Neuropathol. (Berl.)* **1991**, *81* (6), 591–596. https://doi.org/10.1007/BF00296367.

(48) Houlden, H.; Baker, M.; Morris, H. R.; MacDonald, N.; Pickering-Brown, S.; Adamson, J.; Lees, A. J.; Rossor, M. N.; Quinn, N. P.; Kertesz, A.; Khan, M. N.; Hardy, J.; Lantos, P. L.; St. George-Hyslop, P.; Munoz, D. G.; Mann, D.; Lang, A. E.; Bergeron, C.; Bigio, E. H.; Litvan, I.; Bhatia, K. P.; Dickson, D.; Wood, N. W.; Hutton, M. Corticobasal Degeneration and Progressive Supranuclear Palsy Share a Common Tau Haplotype. *Neurology* **2001**, *56* (12), 1702–1706. https://doi.org/10.1212/WNL.56.12.1702.

(49) Spillantini, M. G.; Murrell, J. R.; Goedert, M.; Farlow, M. R.; Klug, A.; Ghetti, B. Mutation in the Tau Gene in Familial Multiple System Tauopathy with Presenile Dementia. *Proc. Natl. Acad. Sci.* **1998**, *95* (13), 7737–7741. https://doi.org/10.1073/pnas.95.13.7737.

(50) DiFiglia, M.; Sapp, E.; Chase, K. O.; Davies, S. W.; Bates, G. P.; Vonsattel, J. P.; Aronin, N. Aggregation of Huntingtin in Neuronal Intranuclear Inclusions and Dystrophic Neurites in Brain. *Science* **1997**, *277* (5334), 1990–1993. https://doi.org/10.1126/science.277.5334.1990.

(51) Randall, R. E.; Williamson, W. C.; Mullinax, F.; Tung, M. Y.; Still, W. J. S. Manifestations of Systemic Light Chain Deposition. *Am. J. Med.* **1976**, *60* (2), 293–299. https://doi.org/10.1016/0002-9343(76)90440-X.

(52) Picken, M. M. Immunoglobulin Light and Heavy Chain Amyloidosis AL/AH: Renal Pathology and Differential Diagnosis. *Kidney Plasma Cell Dyscrasias* **2007**, *153*, 135–155. https://doi.org/10.1159/000096765.

(53) Husby, G.; Marhaug, G.; Dowtor, B.; Sletten, K.; Sipe, J. D. Serum Amyloid A (SAA): Biochemistry, Genetics and the Pathogenesis of AA Amyloidosis. *Amyloid* **1994**, *1* (2), 119–137. https://doi.org/10.3109/13506129409148635.

(54) Westermark, P.; Sletten, K.; Johansson, B.; Cornwell, G. G. Fibril in Senile Systemic Amyloidosis Is Derived from Normal Transthyretin. *Proc. Natl. Acad. Sci. U. S. A.* **1990**, *87* (7), 2843–2845.

(55) Saraiva, M. J.; Birken, S.; Costa, P. P.; Goodman, D. S. Amyloid Fibril Protein in Familial Amyloidotic Polyneuropathy, Portuguese Type. Definition of Molecular Abnormality in Transthyretin (Prealbumin). *J. Clin. Invest.* 1984, *74* (1), 104–119.

(56) Nordlie, M.; Sletten, K.; Husby, G.; Ranløv, P. J. A New Prealbumin Variant in Familial Amyloid Cardiomyopathy of Danish Origin. *Scand. J. Immunol.* 1988, *27* (1), 119–122. https://doi.org/10.1111/j.1365-3083.1988.tb02329.x.

(57) Gorevic, P. D.; Casey, T. T.; Stone, W. J.; DiRaimondo, C. R.; Prelli, F. C.; Frangione, B. Beta-2 Microglobulin Is an Amyloidogenic Protein in Man. *J. Clin. Invest.* 1985, *76* (6), 2425–2429. https://doi.org/10.1172/JCI112257.

(58) Westermark, P.; Mucchiano, G.; Marthin, T.; Johnson, K. H.; Sletten, K. Apolipoprotein A1-Derived Amyloid in Human Aortic Atherosclerotic Plaques. *Am. J. Pathol.* 1995, *147* (5), 1186–1192.

(59) Lohani, S.; Schuiteman, E.; Garg, L.; Yadav, D.; Zarouk, S. Apolipoprotein C-II Deposition Amyloidosis: A Potential Misdiagnosis as Light Chain Amyloidosis. *Case Rep. Nephrol.* 2016, 1–5. https://doi.org/10.1155/2016/8690642.

(60) Nasr, S. H.; Dasari, S.; Hasadsri, L.; Theis, J. D.; Vrana, J. A.; Gertz, M. A.; Muppa, P.; Zimmermann, M. T.; Grogg, K. L.; Dispenzieri, A.; Sethi, S.; Highsmith, W. E.; Merlini, G.; Leung, N.; Kurtin, P. J. Novel Type of Renal Amyloidosis Derived from Apolipoprotein-CII. *J. Am. Soc. Nephrol.* 2017, *28* (2), 439–445. https://doi.org/10.1681/ASN.2015111228.

(61) Pepys, M. B.; Hawkins, P. N.; Booth, D. R.; Vigushin, D. M.; Tennent, G. A.; Soutar, A. K.; Totty, N.; Nguyen, O.; Blake, C. C. F.; Terry, C. J.; Feest, T. G.; Zalin, A. M.; Hsuan, J. J. Human Lysozyme Gene Mutations Cause Hereditary Systemic Amyloidosis. *Nature* 1993, *362* (6420), 553–557. https://doi.org/10.1038/362553a0.

(62) Westermark, P.; Wernstedt, C.; Wilander, E.; Sletten, K. A Novel Peptide in the Calcitonin Gene Related Peptide Family as an Amyloid Fibril Protein in the Endocrine Pancreas. *Biochem. Biophys. Res. Commun.* 1986, *140* (3), 827–831. https://doi.org/10.1016/0006-291X(86)90708-4.

(63) Störkel, S.; Schneider, H. M.; Müntefering, H.; Kashiwagi, S. Iatrogenic, Insulin-Dependent, Local Amyloidosis. *Lab. Investig. J. Tech. Methods Pathol.* 1983, *48* (1), 108–111.

(64) Westermark, P.; Wernstedt, C.; Wilander, E.; Hayden, D. W.; O'Brien, T. D.; Johnson, K. H. Amyloid Fibrils in Human Insulinoma and Islets of Langerhans of the Diabetic Cat Are Derived from a Neuropeptide-like Protein Also Present in Normal Islet Cells. *Proc. Natl. Acad. Sci. U. S. A.* 1987, *84* (11), 3881–3885.

(65) Kang, J.; Lemaire, H. G.; Unterbeck, A.; Salbaum, J. M.; Masters, C. L.; Grzeschik, K. H.; Multhaup, G.; Beyreuther, K.; Müller-Hill, B. The Precursor of Alzheimer's Disease Amyloid A4 Protein Resembles a Cell-Surface Receptor. *Nature* 1987, *325* (6106), 733–736. https://doi.org/10.1038/325733a0.

(66) Prusiner, S. B. Prions. *Proc. Natl. Acad. Sci.* 1998, *95* (23), 13363–13383. https://doi.org/10.1073/pnas.95.23.13363.

(67) Chiti, F.; Dobson, C. M. Protein Misfolding, Functional Amyloid, and Human Disease. *Annu. Rev. Biochem.* 2006, *75* (1), 333–366. https://doi.org/10.1146/annurev.biochem.75.101304.123901.

(68) Lorenzo, A.; Razzaboni, B.; Weir, G. C.; Yankner, B. A. Pancreatic Islet Cell Toxicity of Amylin Associated with Type-2 Diabetes Mellitus. *Nature* 1994, *368* (6473), 756. https://doi.org/10.1038/368756a0.

(69) Falk, R. H.; Comenzo, R. L.; Skinner, M. The Systemic Amyloidoses. *N. Engl. J. Med.* 1997, *337* (13), 898–909. https://doi.org/10.1056/NEJM199709253371306.

(70) EANES, E. D.; GLENNER, G. G. X-RAY DIFFRACTION STUDIES ON AMYLOID FILAMENTS. *J. Histochem. Cytochem.* 1968, *16* (11), 673–677. https://doi.org/10.1177/16.11.673.

(71) Nilsson, M. R. Techniques to Study Amyloid Fibril Formation in Vitro. *Methods* 2004, *34* (1), 151–160. https://doi.org/10.1016/j.ymeth.2004.03.012.

(72) Vassar, P. S.; Culling, C. F. Fluorescent Stains, with Special Reference to Amyloid and Connective Tissues. *Arch. Pathol.* 1959, *68*, 487–498.

(73) Naiki, H.; Higuchi, K.; Hosokawa, M.; Takeda, T. Fluorometric Determination of Amyloid Fibrils in Vitro Using the Fluorescent Dye, Thioflavine T. *Anal. Biochem.* 1989, *177* (2), 244–249. https://doi.org/10.1016/0003-2697(89)90046-8.

(74) Li, B.; Ge, P.; Murray, K. A.; Sheth, P.; Zhang, M.; Nair, G.; Sawaya, M. R.; Shin, W. S.; Boyer, D. R.; Ye, S.; Eisenberg, D. S.; Zhou, Z. H.; Jiang, L. Cryo-EM of Full-Length α-Synuclein Reveals Fibril

Polymorphs with a Common Structural Kernel. *Nat. Commun.* 2018, *9* (1), 3609. https://doi.org/10.1038/s41467-018-05971-2.

(75) Krotee, P.; Griner, S. L.; Sawaya, M. R.; Cascio, D.; Rodriguez, J. A.; Shi, D.; Philipp, S.; Murray, K.; Saelices, L.; Lee, J.; Seidler, P.; Glabe, C. G.; Jiang, L.; Gonen, T.; Eisenberg, D. S. Common Fibrillar Spines of Amyloid-β and Human Islet Amyloid Polypeptide Revealed by Microelectron Diffraction and Structure-Based Inhibitors. *J. Biol. Chem.* 2018, *293* (8), 2888–2902. https://doi.org/10.1074/jbc.M117.806109.

(76) Dobson, C. M. Protein Folding and Misfolding. *Nature* 2003, *426* (6968), 884. https://doi.org/10.1038/nature02261.

(77) Fändrich, M.; Dobson, C. M. The Behaviour of Polyamino Acids Reveals an Inverse Side Chain Effect in Amyloid Structure Formation. *EMBO J.* 2002, *21* (21), 5682–5690.

(78) O'Nuallain, B.; Williams, A. D.; Westermark, P.; Wetzel, R. Seeding Specificity in Amyloid Growth Induced by Heterologous Fibrils. *J. Biol. Chem.* 2004, *279* (17), 17490–17499. https://doi.org/10.1074/jbc.M311300200.

(79) Pauling, L.; Corey, R. B. Configurations of Polypeptide Chains With Favored Orientations Around Single Bonds. *Proc. Natl. Acad. Sci. U. S. A.* 1951, *37* (11), 729–740.

(80) Sunde, M.; Serpell, L. C.; Bartlam, M.; Fraser, P. E.; Pepys, M. B.; Blake, C. C. F. Common Core Structure of Amyloid Fibrils by Synchrotron X-Ray Diffraction11Edited by F. E. Cohen. *J. Mol. Biol.* 1997, *273* (3), 729–739. https://doi.org/10.1006/jmbi.1997.1348.

(81) Litvinovich, S. V.; Brew, S. A.; Aota, S.; Akiyama, S. K.; Haudenschild, C.; Ingham, K. C. Formation of Amyloid-like Fibrils by Self-Association of a Partially Unfolded Fibronectin Type III Module11Edited by R. Huber. *J. Mol. Biol.* 1998, *280* (2), 245–258. https://doi.org/10.1006/jmbi.1998.1863.

(82) Celej, M. S.; Sarroukh, R.; Goormaghtigh, E.; Fidelio, G. D.; Ruysschaert, J.-M.; Raussens, V. Toxic Prefibrillar α-Synuclein Amyloid Oligomers Adopt a Distinctive Antiparallel β-Sheet Structure. *Biochem. J.* 2012, *443* (3), 719–726. https://doi.org/10.1042/BJ20111924.

(83) Kaylor, J.; Bodner, N.; Edridge, S.; Yamin, G.; Hong, D.-P.; Fink, A. L. Characterization of Oligomeric Intermediates in α-Synuclein Fibrillation: FRET Studies of Y125W/Y133F/Y136F α-Synuclein. *J. Mol. Biol.* 2005, *353* (2), 357–372. https://doi.org/10.1016/j.jmb.2005.08.046.

(84) Jarrett, J. T.; Lansbury, P. T. Seeding "One-Dimensional Crystallization" of Amyloid: A Pathogenic Mechanism in Alzheimer's Disease and Scrapie? *Cell* **1993**, *73* (6), 1055–1058. https://doi.org/10.1016/0092-8674(93)90635-4.

(85) Binger, K. J.; Pham, C. L. L.; Wilson, L. M.; Bailey, M. F.; Lawrence, L. J.; Schuck, P.; Howlett, G. J. Apolipoprotein C-II Amyloid Fibrils Assemble via a Reversible Pathway That Includes Fibril Breaking and Rejoining. *J. Mol. Biol.* **2008**, *376* (4), 1116–1129. https://doi.org/10.1016/j.jmb.2007.12.055.

(86) Knowles, T. P. J.; Waudby, C. A.; Devlin, G. L.; Cohen, S. I. A.; Aguzzi, A.; Vendruscolo, M.; Terentjev, E. M.; Welland, M. E.; Dobson, C. M. An Analytical Solution to the Kinetics of Breakable Filament Assembly. *Science* **2009**, *326* (5959), 1533–1537.

(87) Carulla, N.; Caddy, G. L.; Hall, D. R.; Zurdo, J.; Gairí, M.; Feliz, M.; Giralt, E.; Robinson, C. V.; Dobson, C. M. Molecular Recycling within Amyloid Fibrils. *Nature* **2005**, *436* (7050), 554. https://doi.org/10.1038/nature03986.

(88) Cohen, S. I. A.; Linse, S.; Luheshi, L. M.; Hellstrand, E.; White, D. A.; Rajah, L.; Otzen, D. E.; Vendruscolo, M.; Dobson, C. M.; Knowles, T. P. J. Proliferation of Amyloid-B42 Aggregates Occurs through a Secondary Nucleation Mechanism. *Proc. Natl. Acad. Sci.* **2013**, *110* (24), 9758–9763. https://doi.org/10.1073/pnas.1218402110.

(89) Padrick, S. B.; Miranker, A. D. Islet Amyloid: Phase Partitioning and Secondary Nucleation Are Central to the Mechanism of Fibrillogenesis. *Biochemistry* **2002**, *41* (14), 4694–4703. https://doi.org/10.1021/bi0160462.

(90) Sturchler-Pierrat, C.; Abramowski, D.; Duke, M.; Wiederhold, K.-H.; Mistl, C.; Rothacher, S.; Ledermann, B.; Burki, K.; Frey, P.; Paganetti, P. A.; Waridel, C.; Calhoun, M. E.; Jucker, M.; Probst, A.; Staufenbiel, M.; Sommer, B. Two Amyloid Precursor Protein Transgenic Mouse Models with Alzheimer Disease-like Pathology. *Proc. Natl. Acad. Sci.* **1997**, *94* (24), 13287–13292. https://doi.org/10.1073/pnas.94.24.13287.

(91) Kane, M. D.; Lipinski, W. J.; Callahan, M. J.; Bian, F.; Durham, R. A.; Schwarz, R. D.; Roher, A. E.; Walker, L. C. Evidence for Seeding of β-Amyloid by Intracerebral Infusion of Alzheimer Brain Extracts in β-Amyloid Precursor Protein-Transgenic Mice. *J. Neurosci.* **2000**, *20* (10), 3606–3611. https://doi.org/10.1523/JNEUROSCI.20-10-03606.2000.

(92) Clavaguera, F.; Bolmont, T.; Crowther, R. A.; Abramowski, D.; Frank, S.; Probst, A.; Fraser, G.; Stalder, A. K.; Beibel, M.; Staufenbiel, M.; Jucker, M.; Goedert, M.; Tolnay, M. Transmission and Spreading of Tauopathy in Transgenic Mouse Brain. *Nat. Cell Biol.* 2009, *11* (7), 909–913. https://doi.org/10.1038/ncb1901.

(93) Luk, K. C.; Kehm, V. M.; Zhang, B.; O'Brien, P.; Trojanowski, J. Q.; Lee, V. M. Y. Intracerebral Inoculation of Pathological α-Synuclein Initiates a Rapidly Progressive Neurodegenerative α-Synucleinopathy in Mice. *J. Exp. Med.* 2012, *209* (5), 975–986. https://doi.org/10.1084/jem.20112457.

(94) Mougenot, A.-L.; Nicot, S.; Bencsik, A.; Morignat, E.; Verchère, J.; Lakhdar, L.; Legastelois, S.; Baron, T. Prion-like Acceleration of a Synucleinopathy in a Transgenic Mouse Model. *Neurobiol. Aging* 2012, *33* (9), 2225–2228. https://doi.org/10.1016/j.neurobiolaging.2011.06.022.

(95) Gellermann, G. P.; Appel, T. R.; Tannert, A.; Radestock, A.; Hortschansky, P.; Schroeckh, V.; Leisner, C.; Lutkepohl, T.; Shtrasburg, S.; Rocken, C.; Pras, M.; Linke, R. P.; Diekmann, S.; Fandrich, M. Raft Lipids as Common Components of Human Extracellular Amyloid Fibrils. *Proc. Natl. Acad. Sci.* 2005, *102* (18), 6297–6302. https://doi.org/10.1073/pnas.0407035102.

(96) Kim, I. C.; Shirahama, T.; Cohen, A. S. The Lipid Content of Amyloid Fibrils Purified by a Variety of Methods. *Am. J. Pathol.* 1967, *50* (5), 869–886.

(97) Perry, G.; Siedlak, S. L.; Richey, P.; Kawai, M.; Cras, P.; Kalaria, R. N.; Galloway, P. G.; Scardina, J. M.; Cordell, B.; Greenberg, B. D. Association of Heparan Sulfate Proteoglycan with the Neurofibrillary Tangles of Alzheimer's Disease. *J. Neurosci.* 1991, *11* (11), 3679–3683. https://doi.org/10.1523/JNEUROSCI.11-11-03679.1991.

(98) Snow, A. D.; Mar, H.; Nochlin, D.; Kimata, K.; Kato, M.; Suzuki, S.; Hassell, J.; Wight, T. N. The Presence of Heparan Sulfate Proteoglycans in the Neuritic Plaques and Congophilic Angiopathy in Alzheimer's Disease. *Am. J. Pathol.* 1988, *133* (3), 456–463.

(99) Namba, Y.; Tomonaga, M.; Kawasaki, H.; Otomo, E.; Ikeda, K. Apolipoprotein E Immunoreactivity in Cerebral Amyloid Deposits and Neurofibrillary Tangles in Alzheimer's Disease and Kuru Plaque Amyloid in Creutzfeldt-Jakob Disease. *Brain Res.* 1991, *541* (1), 163–166. https://doi.org/10.1016/0006-8993(91)91092-F.

(100) Snow, A. D.; Willmer, J.; Kisilevsky, R. Sulfated Glycosaminoglycans: A Common Constituent of All Amyloids? *Lab. Investig. J. Tech. Methods Pathol.* 1987, *56* (1), 120–123.

(101) Eikelenboom, P.; Stam, F. C. Immunoglobulins and Complement Factors in Senile Plaques: An Immunoperoxidase Study. *Acta Neuropathol. (Berl.)* 1982, *57* (2–3), 239–242. https://doi.org/10.1007/BF00685397.

(102) Calero, M.; Rostagno, A.; Matsubara, E.; Zlokovic, B.; Frangione, B.; Ghiso, J. Apolipoprotein J (Clusterin) and Alzheimer's Disease. *Microsc. Res. Tech.* 2000, *50* (4), 305–315. https://doi.org/10.1002/1097-0029(20000815)50:4<305::AID-JEMT10>3.0.CO;2-L.

(103) Lowe, J.; Landon, M.; Pike, I.; Spendlove, I.; Mcdermott, H.; John Mayer, R. Dementia with β-Amyloid Deposition: Involvement of AB-Crystallin Supports Two Main Diseases. *The Lancet* 1990, *336* (8713), 515–516. https://doi.org/10.1016/0140-6736(90)92075-S.

(104) Outeiro, T. F.; Klucken, J.; Strathearn, K. E.; Liu, F.; Nguyen, P.; Rochet, J.-C.; Hyman, B. T.; McLean, P. J. Small Heat Shock Proteins Protect against α-Synuclein-Induced Toxicity and Aggregation. *Biochem. Biophys. Res. Commun.* 2006, *351* (3), 631–638. https://doi.org/10.1016/j.bbrc.2006.10.085.

(105) Wilhelmus, M. M. M.; Otte-Höller, I.; Wesseling, P.; Waal, R. M. W. D.; Boelens, W. C.; Verbeek, M. M. Specific Association of Small Heat Shock Proteins with the Pathological Hallmarks of Alzheimer's Disease Brains. *Neuropathol. Appl. Neurobiol.* 2006, *32* (2), 119–130. https://doi.org/10.1111/j.1365-2990.2006.00689.x.

(106) Bolognesi, B.; Kumita, J. R.; Barros, T. P.; Esbjorner, E. K.; Luheshi, L. M.; Crowther, D. C.; Wilson, M. R.; Dobson, C. M.; Favrin, G.; Yerbury, J. J. ANS Binding Reveals Common Features of Cytotoxic Amyloid Species. *ACS Chem. Biol.* 2010, *5* (8), 735–740. https://doi.org/10.1021/cb1001203.

(107) Kayed, R.; Head, E.; Thompson, J. L.; McIntire, T. M.; Milton, S. C.; Cotman, C. W.; Glabe, C. G. Common Structure of Soluble Amyloid Oligomers Implies Common Mechanism of Pathogenesis. (Reports). *Science* 2003, *300* (5618), 486-.

(108) Bucciantini, M.; Calloni, G.; Chiti, F.; Formigli, L.; Nosi, D.; Dobson, C. M.; Stefani, M. Prefibrillar Amyloid Protein Aggregates Share Common Features of Cytotoxicity. *J. Biol. Chem.* 2004, *279* (30), 31374–31382. https://doi.org/10.1074/jbc.M400348200.

(109) Panov, A. V.; Gutekunst, C.-A.; Leavitt, B. R.; Hayden, M. R.; Burke, J. R.; Strittmatter, W. J.; Greenamyre, J. T. Early Mitochondrial Calcium Defects in Huntington's Disease Are a Direct Effect of Polyglutamines. *Nat. Neurosci.* 2002, *5* (8), 731. https://doi.org/10.1038/nn884.

(110) Mahul-Mellier, A.-L.; Burtscher, J.; Maharjan, N.; Weerens, L.; Croisier, M.; Kuttler, F.; Leleu, M.; Knott, G. W.; Lashuel, H. A. The Process of Lewy Body Formation, Rather than Simply α-Synuclein Fibrillization, Is One of the Major Drivers of Neurodegeneration. *Proc. Natl. Acad. Sci. U. S. A.* 2020. https://doi.org/10.1073/pnas.1913904117.

(111) Deriziotis, P.; André, R.; Smith, D. M.; Goold, R.; Kinghorn, K. J.; Kristiansen, M.; Nathan, J. A.; Rosenzweig, R.; Krutauz, D.; Glickman, M. H.; Collinge, J.; Goldberg, A. L.; Tabrizi, S. J. Misfolded PrP Impairs the UPS by Interaction with the 20S Proteasome and Inhibition of Substrate Entry. *EMBO J.* 2011, *30* (15), 3065–3077. https://doi.org/10.1038/emboj.2011.224.

(112) Park, S.-H.; Kukushkin, Y.; Gupta, R.; Chen, T.; Konagai, A.; Hipp, M. S.; Hayer-Hartl, M.; Hartl, F. U. PolyQ Proteins Interfere with Nuclear Degradation of Cytosolic Proteins by Sequestering the Sis1p Chaperone. *Cell* 2013, *154* (1), 134–145. https://doi.org/10.1016/j.cell.2013.06.003.

(113) King, M. E.; Kan, H.-M.; Baas, P. W.; Erisir, A.; Glabe, C. G.; Bloom, G. S. Tau-Dependent Microtubule Disassembly Initiated by Prefibrillar β-Amyloid. *J. Cell Biol.* 2006, *175* (4), 541–546. https://doi.org/10.1083/jcb.200605187.

(114) Olzscha, H.; Schermann, S. M.; Woerner, A. C.; Pinkert, S.; Hecht, M. H.; Tartaglia, G. G.; Vendruscolo, M.; Hayer-Hartl, M.; Hartl, F. U.; Vabulas, R. M. Amyloid-like Aggregates Sequester Numerous Metastable Proteins with Essential Cellular Functions. *Cell* 2011, *144* (1), 67–78. https://doi.org/10.1016/j.cell.2010.11.050.

(115) Engel, M. F. M.; Khemtemourian, L.; Kleijer, C. C.; Meeldijk, H. J. D.; Jacobs, J.; Verkleij, A. J.; de Kruijff, B.; Killian, J. A.; Hoppener, J. W. M. Membrane Damage by Human Islet Amyloid Polypeptide through Fibril Growth at the Membrane. *Proc. Natl. Acad. Sci.* 2008, *105* (16), 6033–6038. https://doi.org/10.1073/pnas.0708354105.

(116) Martins, I. C.; Kuperstein, I.; Wilkinson, H.; Maes, E.; Vanbrabant, M.; Jonckheere, W.; Van Gelder, P.; Hartmann, D.; D'Hooge, R.; De Strooper, B.; Schymkowitz, J.; Rousseau, F. Lipids Revert Inert Aβ Amyloid Fibrils to Neurotoxic Protofibrils That Affect Learning in Mice. *EMBO J.* 2008, *27* (1), 224–233. https://doi.org/10.1038/sj.emboj.7601953.

(117) Abeliovich, A.; Schmitz, Y.; Fariñas, I.; Choi-Lundberg, D.; Ho, W.-H.; Castillo, P. E.; Shinsky, N.; Verdugo, J. M. G.; Armanini, M.; Ryan, A.; Hynes, M.; Phillips, H.; Sulzer, D.; Rosenthal, A. Mice Lacking α-Synuclein Display Functional Deficits in the Nigrostriatal Dopamine System. *Neuron* 2000, *25* (1), 239–252. https://doi.org/10.1016/S0896-6273(00)80886-7.

(118) Leng, Y.; Chase, T. N.; Bennett, M. C. Muscarinic Receptor Stimulation Induces Translocation of an α-Synuclein Oligomer from Plasma Membrane to a Light Vesicle Fraction in Cytoplasm. *J. Biol. Chem.* 2001, *276* (30), 28212–28218. https://doi.org/10.1074/jbc.M011121200.

(119) Kahle, P. J.; Neumann, M.; Ozmen, L.; Müller, V.; Jacobsen, H.; Schindzielorz, A.; Okochi, M.; Leimer, U.; Putten, H. van der; Probst, A.; Kremmer, E.; Kretzschmar, H. A.; Haass, C. Subcellular Localization of Wild-Type and Parkinson's Disease-Associated Mutant α-Synuclein in Human and Transgenic Mouse Brain. *J. Neurosci.* 2000, *20* (17), 6365–6373. https://doi.org/10.1523/JNEUROSCI.20-17-06365.2000.

(120) Davidson, W. S.; Jonas, A.; Clayton, D. F.; George, J. M. Stabilization of α-Synuclein Secondary Structure upon Binding to Synthetic Membranes. *J. Biol. Chem.* 1998, *273* (16), 9443–9449. https://doi.org/10.1074/jbc.273.16.9443.

(121) Zarbiv, Y.; Simhi-Haham, D.; Israeli, E.; Elhadi, S. A.; Grigoletto, J.; Sharon, R. Lysine Residues at the First and Second KTKEGV Repeats Mediate α-Synuclein Binding to Membrane Phospholipids. *Neurobiol. Dis.* 2014, *70*, 90–98. https://doi.org/10.1016/j.nbd.2014.05.031.

(122) Bertoncini, C. W.; Jung, Y.-S.; Fernandez, C. O.; Hoyer, W.; Griesinger, C.; Jovin, T. M.; Zweckstetter, M. Release of Long-Range Tertiary Interactions Potentiates Aggregation of Natively Unstructured Alpha-Synuclein. *Proc. Natl. Acad. Sci. U. S. A.* 2005, *102* (5), 1430–1435. https://doi.org/10.1073/pnas.0407146102.

(123) Feany, M. B.; Bender, W. W. A Drosophila Model of Parkinson's Disease. *Nature* 2000, *404* (6776), 394. https://doi.org/10.1038/35006074.

(124) Wakabayashi, K.; Yoshimoto, M.; Tsuji, S.; Takahashi, H. α-Synuclein Immunoreactivity in Glial Cytoplasmic Inclusions in Multiple System Atrophy. *Neurosci. Lett.* 1998, *249* (2), 180–182. https://doi.org/10.1016/S0304-3940(98)00407-8.

(125) Ostrerova-Golts, N.; Petrucelli, L.; Hardy, J.; Lee, J. M.; Farer, M.; Wolozin, B. The A53T α-Synuclein Mutation Increases Iron-Dependent Aggregation and Toxicity. *J. Neurosci.* 2000, *20* (16), 6048–6054. https://doi.org/10.1523/JNEUROSCI.20-16-06048.2000.

(126) Jellinger, K. A. Basic Mechanisms of Neurodegeneration: A Critical Update. *J. Cell. Mol. Med.* 2010, *14* (3), 457–487. https://doi.org/10.1111/j.1582-4934.2010.01010.x.

(127) Troncoso-Escudero, P.; Parra, A.; Nassif, M.; Vidal, R. L. Outside in: Unraveling the Role of Neuroinflammation in the Progression of Parkinson's Disease. *Front. Neurol.* 2018, *9*. https://doi.org/10.3389/fneur.2018.00860.

(128) Fujiwara, H.; Hasegawa, M.; Dohmae, N.; Kawashima, A.; Masliah, E.; Goldberg, M. S.; Shen, J.; Takio, K.; Iwatsubo, T. α-Synuclein Is Phosphorylated in Synucleinopathy Lesions. *Nat. Cell Biol.* 2002, *4* (2), 160–164. https://doi.org/10.1038/ncb748.

(129) Ulmer, T. S.; Bax, A.; Cole, N. B.; Nussbaum, R. L. Structure and Dynamics of Micelle-Bound Human Alpha-Synuclein. *J. Biol. Chem.* 2005, *280* (10), 9595–9603. https://doi.org/10.1074/jbc.M411805200.

(130) Gallegos, S.; Pacheco, C.; Peters, C.; Opazo, C. M.; Aguayo, L. G. Features of Alpha-Synuclein That Could Explain the Progression and Irreversibility of Parkinson's Disease. *Front. Neurosci.* 2015, *9*, 59. https://doi.org/10.3389/fnins.2015.00059.

(131) Fink, A. L. The Aggregation and Fibrillation of α-Synuclein. *Acc. Chem. Res.* 2006, *39* (9), 628–634. https://doi.org/10.1021/ar050073t.

(132) Uversky, V. N.; Li, J.; Fink, A. L. Evidence for a Partially Folded Intermediate in α-Synuclein Fibril Formation. *J. Biol. Chem.* 2001, *276* (14), 10737–10744. https://doi.org/10.1074/jbc.M010907200.

(133) Anderson, J. P.; Walker, D. E.; Goldstein, J. M.; Laat, R. de; Banducci, K.; Caccavello, R. J.; Barbour, R.; Huang, J.; Kling, K.; Lee, M.; Diep, L.; Keim, P. S.; Shen, X.; Chataway, T.; Schlossmacher, M. G.; Seubert, P.; Schenk, D.; Sinha, S.; Gai, W. P.; Chilcote, T. J. Phosphorylation of Ser-129 Is the Dominant Pathological Modification of α-Synuclein in Familial and Sporadic Lewy Body Disease. *J. Biol. Chem.* 2006, *281* (40), 29739–29752. https://doi.org/10.1074/jbc.M600933200.

(134) Smith, W. W.; Margolis, R. L.; Li, X.; Troncoso, J. C.; Lee, M. K.; Dawson, V. L.; Dawson, T. M.; Iwatsubo, T.; Ross, C. A. α-Synuclein Phosphorylation Enhances Eosinophilic Cytoplasmic

Inclusion Formation in SH-SY5Y Cells. *J. Neurosci.* 2005, *25* (23), 5544–5552. https://doi.org/10.1523/JNEUROSCI.0482-05.2005.

(135) Antony, T.; Hoyer, W.; Cherny, D.; Heim, G.; Jovin, T. M.; Subramaniam, V. Cellular Polyamines Promote the Aggregation of α-Synuclein. *J. Biol. Chem.* 2003, *278* (5), 3235–3240. https://doi.org/10.1074/jbc.M208249200.

(136) Buell, A. K.; Galvagnion, C.; Gaspar, R.; Sparr, E.; Vendruscolo, M.; Knowles, T. P. J.; Linse, S.; Dobson, C. M. Solution Conditions Determine the Relative Importance of Nucleation and Growth Processes in α-Synuclein Aggregation. *Proc. Natl. Acad. Sci. U. S. A.* 2014, *111* (21), 7671–7676. https://doi.org/10.1073/pnas.1315346111.

(137) Munishkina, L. A.; Henriques, J.; Uversky, V. N.; Fink, A. L. Role of Protein−Water Interactions and Electrostatics in α-Synuclein Fibril Formation. *Biochemistry* 2004, *43* (11), 3289–3300. https://doi.org/10.1021/bi034938r.

(138) Campioni, S.; Carret, G.; Jordens, S.; Nicoud, L.; Mezzenga, R.; Riek, R. The Presence of an Air-Water Interface Affects Formation and Elongation of α-Synuclein Fibrils. *J. Am. Chem. Soc.* 2014, *136* (7), 2866–2875. https://doi.org/10.1021/ja412105t.

(139) Rivers, R. C.; Kumita, J. R.; Tartaglia, G. G.; Dedmon, M. M.; Pawar, A.; Vendruscolo, M.; Dobson, C. M.; Christodoulou, J. Molecular Determinants of the Aggregation Behavior of α- and β-Synuclein. *Protein Sci. Publ. Protein Soc.* 2008, *17* (5), 887–898. https://doi.org/10.1110/ps.073181508.

(140) Galvagnion, C.; Buell, A. K.; Meisl, G.; Michaels, T. C. T.; Vendruscolo, M.; Knowles, T. P. J.; Dobson, C. M. Lipid Vesicles Trigger α-Synuclein Aggregation by Stimulating Primary Nucleation. *Nat. Chem. Biol.* 2015, *11* (3), 229–234. https://doi.org/10.1038/nchembio.1750.

(141) Giasson, B. I.; Murray, I. V. J.; Trojanowski, J. Q.; Lee, V. M.-Y. A Hydrophobic Stretch of 12 Amino Acid Residues in the Middle of α-Synuclein Is Essential for Filament Assembly. *J. Biol. Chem.* 2001, *276* (4), 2380–2386. https://doi.org/10.1074/jbc.M008919200.

(142) Li, J.; Uversky, V. N.; Fink, A. L. Effect of Familial Parkinson's Disease Point Mutations A30P and A53T on the Structural Properties, Aggregation, and Fibrillation of Human α-Synuclein. *Biochemistry* 2001, *40* (38), 11604–11613. https://doi.org/10.1021/bi010616g.

(143) Greenbaum, E. A.; Graves, C. L.; Mishizen-Eberz, A. J.; Lupoli, M. A.; Lynch, D. R.; Englander, S. W.; Axelsen, P. H.; Giasson, B. I. The E46K Mutation in α-Synuclein Increases Amyloid Fibril Formation. *J. Biol. Chem.* 2005, *280* (9), 7800–7807. https://doi.org/10.1074/jbc.M411638200.

(144) Ghosh, D.; Mondal, M.; Mohite, G. M.; Singh, P. K.; Ranjan, P.; Anoop, A.; Ghosh, S.; Jha, N. N.; Kumar, A.; Maji, S. K. The Parkinson's Disease-Associated H50Q Mutation Accelerates α-Synuclein Aggregation in Vitro. *Biochemistry* 2013, *52* (40), 6925–6927. https://doi.org/10.1021/bi400999d.

(145) Ranjan, P.; Kumar, A. Perturbation in Long-Range Contacts Modulates the Kinetics of Amyloid Formation in α-Synuclein Familial Mutants. *ACS Chem. Neurosci.* 2017, *8* (10), 2235–2246. https://doi.org/10.1021/acschemneuro.7b00149.

(146) Serpell, L. C.; Berriman, J.; Jakes, R.; Goedert, M.; Crowther, R. A. Fiber Diffraction of Synthetic α-Synuclein Filaments Shows Amyloid-like Cross-β Conformation. *Proc. Natl. Acad. Sci.* 2000, *97* (9), 4897–4902. https://doi.org/10.1073/pnas.97.9.4897.

(147) Tuttle, M. D.; Comellas, G.; Nieuwkoop, A. J.; Covell, D. J.; Berthold, D. A.; Kloepper, K. D.; Courtney, J. M.; Kim, J. K.; Barclay, A. M.; Kendall, A.; Wan, W.; Stubbs, G.; Schwieters, C. D.; Lee, V. M. Y.; George, J. M.; Rienstra, C. M. Solid-State NMR Structure of a Pathogenic Fibril of Full-Length Human α-Synuclein. *Nat. Struct. Mol. Biol.* 2016, *23* (5), 409–415. https://doi.org/10.1038/nsmb.3194.

(148) Vilar, M.; Chou, H.-T.; Lührs, T.; Maji, S. K.; Riek-Loher, D.; Verel, R.; Manning, G.; Stahlberg, H.; Riek, R. The Fold of α-Synuclein Fibrils. *Proc. Natl. Acad. Sci.* 2008, *105* (25), 8637–8642. https://doi.org/10.1073/pnas.0712179105.

(149) Rodriguez, J. A.; Ivanova, M. I.; Sawaya, M. R.; Cascio, D.; Reyes, F. E.; Shi, D.; Sangwan, S.; Guenther, E. L.; Johnson, L. M.; Zhang, M.; Jiang, L.; Arbing, M. A.; Nannenga, B. L.; Hattne, J.; Whitelegge, J.; Brewster, A. S.; Messerschmidt, M.; Boutet, B.; Sauter, N. K.; Gonen, T.; Eisenberg, D. S. Structure of the Toxic Core of Alpha-Synuclein from Invisible Crystals. *NATURE* 2015, *525* (7570), 486-+. https://doi.org/10.1038/nature15368.

(150) Griffin, M. D. W.; Mok, M. L. Y.; Wilson, L. M.; Pham, C. L. L.; Waddington, L. J.; Perugini, M. A.; Howlett, G. J. Phospholipid Interaction Induces Molecular-Level Polymorphism in Apolipoprotein

C-II Amyloid Fibrils via Alternative Assembly Pathways. *J. Mol. Biol.* 2008, *375* (1), 240–256. https://doi.org/10.1016/j.jmb.2007.10.038.

(151) Hatters, D. M.; Howlett, G. J. The Structural Basis for Amyloid Formation by Plasma Apolipoproteins: A Review. *Eur. Biophys. J.* 2002, *31* (1), 2–8. https://doi.org/10.1007/s002490100172.

(152) Hatters, D. M.; MacPhee, C. E.; Lawrence, L. J.; Sawyer, W. H.; Howlett, G. J. Human Apolipoprotein C-II Forms Twisted Amyloid Ribbons and Closed Loops. *Biochemistry* 2000, *39* (28), 8276–8283. https://doi.org/10.1021/bi000002w.

(153) O'Brien, K. D.; Olin, K. L.; Alpers, C. E.; Chiu, W.; Ferguson, M.; Hudkins, K.; Wight, T. N.; Chait, A. Comparison of Apolipoprotein and Proteoglycan Deposits in Human Coronary Atherosclerotic Plaques: Colocalization of Biglycan with Apolipoproteins. *Circulation* 1998, *98* (6), 519–527. https://doi.org/10.1161/01.cir.98.6.519.

(154) Wisniewski, T.; Lalowski, M.; Golabek, A.; Frangione, B.; Vogel, T. Is Alzheimer's Disease an Apolipoprotein E Amyloidosis? *The Lancet* 1995, *345* (8955), 956–958. https://doi.org/10.1016/S0140-6736(95)90701-7.

(155) Mak, P. A.; Laffitte, B. A.; Desrumaux, C.; Joseph, S. B.; Curtiss, L. K.; Mangelsdorf, D. J.; Tontonoz, P.; Edwards, P. A. Regulated Expression of the Apolipoprotein E/C-I/C-IV/C-II Gene Cluster in Murine and Human Macrophages: A CRITICAL ROLE FOR NUCLEAR LIVER X RECEPTORS α AND β. *J. Biol. Chem.* 2002, *277* (35), 31900–31908. https://doi.org/10.1074/jbc.M202993200.

(156) Medeiros, L. A.; Khan, T.; Khoury, J. B. E.; Pham, C. L. L.; Hatters, D. M.; Howlett, G. J.; Lopez, R.; O'Brien, K. D.; Moore, K. J. Fibrillar Amyloid Protein Present in Atheroma Activates CD36 Signal Transduction. *J. Biol. Chem.* 2004, *279* (11), 10643–10648. https://doi.org/10.1074/jbc.M311735200.

(157) Havel Richard J.; Shore Virgie G.; Shore Bernard; Bier Dennis M. Role of Specific Glycopeptides of Human Serum Lipoproteins in the Activation of Lipoprotein Lipase. *Circ. Res.* 1970, *27* (4), 595–600. https://doi.org/10.1161/01.RES.27.4.595.

(158) LaRosa, J. C.; Levy, R. I.; Herbert, P.; Lux, S. E.; Fredrickson, D. S. A Specific Apoprotein Activator for Lipoprotein Lipase. *Biochem. Biophys. Res. Commun.* 1970, *41* (1), 57–62. https://doi.org/10.1016/0006-291X(70)90468-7.

(159) MacRaild, C. A.; Howlett, G. J.; Gooley, P. R. The Structure and Interactions of Human Apolipoprotein C-II in Dodecyl Phosphocholine,. *Biochemistry* 2004, *43* (25), 8084–8093. https://doi.org/10.1021/bi049817l.

(160) Binger, K. J.; Griffin, M. D. W.; Howlett, G. J. Methionine Oxidation Inhibits Assembly and Promotes Disassembly of Apolipoprotein C-II Amyloid Fibrils. *Biochemistry* 2008, *47* (38), 10208–10217. https://doi.org/10.1021/bi8009339.

(161) Hatters, D. M.; Lawrence, L. J.; Howlett, G. J. Sub-Micellar Phospholipid Accelerates Amyloid Formation by Apolipoprotein C-II. *FEBS Lett.* 2001, *494* (3), 220–224. https://doi.org/10.1016/S0014-5793(01)02355-9.

(162) Hatters, D. M.; MacRaild, C. A.; Daniels, R.; Gosal, W. S.; Thomson, N. H.; Jones, J. A.; Davis, J. J.; MacPhee, C. E.; Dobson, C. M.; Howlett, G. J. The Circularization of Amyloid Fibrils Formed by Apolipoprotein C-II. *Biophys. J.* 2003, *85* (6), 3979–3990. https://doi.org/10.1016/S0006-3495(03)74812-7.

(163) Hatters, D. M.; Minton, A. P.; Howlett, G. J. Macromolecular Crowding Accelerates Amyloid Formation by Human Apolipoprotein C-II. *J. Biol. Chem.* 2002, *277* (10), 7824–7830. https://doi.org/10.1074/jbc.M110429200.

(164) Ryan, T. M.; Teoh, C. L.; Griffin, M. D. W.; Bailey, M. F.; Schuck, P.; Howlett, G. J. Phospholipids Enhance Nucleation but Not Elongation of Apolipoprotein C-II Amyloid Fibrils. *J. Mol. Biol.* 2010, *399* (5), 731–740. https://doi.org/10.1016/j.jmb.2010.04.042.

(165) Wilson, L. M.; Mok, Y.-F.; Binger, K. J.; Griffin, M. D. W.; Mertens, H. D. T.; Lin, F.; Wade, J. D.; Gooley, P. R.; Howlett, G. J. A Structural Core Within Apolipoprotein C-II Amyloid Fibrils Identified Using Hydrogen Exchange and Proteolysis. *J. Mol. Biol.* 2007, *366* (5), 1639–1651. https://doi.org/10.1016/j.jmb.2006.12.040.

(166) Zlatic, C. O.; Mao, Y.; Todorova, N.; Mok, Y.; Howlett, G. J.; Yarovsky, I.; Gooley, P. R.; Griffin, M. D. W. Polymorphism in Disease-related Apolipoprotein C- II Amyloid Fibrils: A Structural Model for Rod-like Fibrils. *FEBS J.* 2018, *285* (15), 2799–2812. https://doi.org/10.1111/febs.14517.

(167) Balch, W. E.; Morimoto, R. I.; Dillin, A.; Kelly, J. W. Adapting Proteostasis for Disease Intervention. *Science* 2008, *319* (5865), 916–919. https://doi.org/10.1126/science.1141448.

(168) Klaips, C. L.; Jayaraj, G. G.; Hartl, F. U. Pathways of Cellular Proteostasis in Aging and Disease. *J. Cell Biol.* 2018, *217* (1), 51–63. https://doi.org/10.1083/jcb.201709072.

(169) Kakkar, V.; Meister-Broekema, M.; Minoia, M.; Carra, S.; Kampinga, H. H. Barcoding Heat Shock Proteins to Human Diseases: Looking beyond the Heat Shock Response. *Dis. Model. Mech.* 2014, *7* (4), 421–434. https://doi.org/10.1242/dmm.014563.

(170) Hipp, M. S.; Kasturi, P.; Hartl, F. U. The Proteostasis Network and Its Decline in Ageing. *Nat. Rev. Mol. Cell Biol.* 2019, *20* (7), 421–435. https://doi.org/10.1038/s41580-019-0101-y.

(171) Tissiéres, A.; Mitchell, H. K.; Tracy, U. M. Protein Synthesis in Salivary Glands of Drosophila Melanogaster: Relation to Chromosome Puffs. *J. Mol. Biol.* 1974, *84* (3), 389–398. https://doi.org/10.1016/0022-2836(74)90447-1.

(172) Ellis, J. Proteins as Molecular Chaperones. *Nature* 1987, *328* (6129), 378. https://doi.org/10.1038/328378a0.

(173) Kampinga, H. H.; Hageman, J.; Vos, M. J.; Kubota, H.; Tanguay, R. M.; Bruford, E. A.; Cheetham, M. E.; Chen, B.; Hightower, L. E. Guidelines for the Nomenclature of the Human Heat Shock Proteins. *Cell Stress Chaperones* 2009, *14* (1), 105–111.

(174) Lopez, T.; Dalton, K.; Frydman, J. The Mechanism and Function of Group II Chaperonins. *J. Mol. Biol.* 2015, *427* (18), 2919–2930. https://doi.org/10.1016/j.jmb.2015.04.013.

(175) Morimoto, R. I. Proteotoxic Stress and Inducible Chaperone Networks in Neurodegenerative Disease and Aging. *Genes Dev.* 2008, *22* (11), 1427–1438. https://doi.org/10.1101/gad.1657108.

(176) Pelham, H. Activation of Heat-Shock Genes in Eukaryotes. *Trends Genet.* 1985, *1*, 31–35. https://doi.org/10.1016/0168-9525(85)90012-5.

(177) Xiao, H.; Lis, J. T. Germline Transformation Used to Define Key Features of Heat-Shock Response Elements. *Science* 1988, *239* (4844), 1139–1142.

(178) Gomez-Pastor, R.; Burchfiel, E. T.; Thiele, D. J. Regulation of Heat Shock Transcription Factors and Their Roles in Physiology and Disease. *Nat. Rev. Mol. Cell Biol.* 2018, *19* (1), 4–19. https://doi.org/10.1038/nrm.2017.73.

(179) Morimoto, R. I. Regulation of the Heat Shock Transcriptional Response: Cross Talk between a Family of Heat Shock Factors, Molecular Chaperones, and Negative Regulators. *Genes Dev.* 1998, *12* (24), 3788–3796. https://doi.org/10.1101/gad.12.24.3788.

(180) Hipp, M. S.; Park, S.-H.; Hartl, F. U. Proteostasis Impairment in Protein-Misfolding and -Aggregation Diseases. *Trends Cell Biol.* **2014**, *24* (9), 506–514. https://doi.org/10.1016/j.tcb.2014.05.003.

(181) Szabo, A.; Langer, T.; Schroder, H.; Flanagan, J.; Bukau, B.; Hartl, F. U. The ATP Hydrolysis-Dependent Reaction Cycle of the Escherichia Coli Hsp70 System-DnaK, DnaJ, and GrpE. *Proc. Natl. Acad. Sci. U. S. A.* **1994**, *91* (22), 10345–10349.

(182) Greene, M. K.; Maskos, K.; Landry, S. J. Role of the J-Domain in the Cooperation of Hsp40 with Hsp70. *Proc. Natl. Acad. Sci.* **1998**, *95* (11), 6108–6113. https://doi.org/10.1073/pnas.95.11.6108.

(183) Summers, D. W.; Douglas, P. M.; Ramos, C. H. I.; Cyr, D. M. Polypeptide Transfer from Hsp40 to Hsp70 Molecular Chaperones. *Trends Biochem. Sci.* **2009**, *34* (5), 230–233. https://doi.org/10.1016/j.tibs.2008.12.009.

(184) Nillegoda, N. B.; Kirstein, J.; Szlachcic, A.; Berynskyy, M.; Stank, A.; Stengel, F.; Arnsburg, K.; Gao, X.; Scior, A.; Aebersold, R.; Guilbride, D. L.; Wade, R. C.; Morimoto, R. I.; Mayer, M. P.; Bukau, B. Crucial HSP70 Co-Chaperone Complex Unlocks Metazoan Protein Disaggregation. *Nature* **2015**, *524* (7564), 247–251. https://doi.org/10.1038/nature14884.

(185) Rampelt, H.; Kirstein-Miles, J.; Nillegoda, N. B.; Chi, K.; Scholz, S. R.; Morimoto, R. I.; Bukau, B. Metazoan Hsp70 Machines Use Hsp110 to Power Protein Disaggregation. *EMBO J.* **2012**, *31* (21), 4221–4235. https://doi.org/10.1038/emboj.2012.264.

(186) Scior, A.; Buntru, A.; Arnsburg, K.; Ast, A.; Iburg, M.; Juenemann, K.; Pigazzini, M. L.; Mlody, B.; Puchkov, D.; Priller, J.; Wanker, E. E.; Prigione, A.; Kirstein, J. Complete Suppression of Htt Fibrilization and Disaggregation of Htt Fibrils by a Trimeric Chaperone Complex. *EMBO J.* **2018**, *37* (2), 282–299. https://doi.org/10.15252/embj.201797212.

(187) Arrigo, A.-P.; Fakan, S.; Tissières, A. Localization of the Heat Shock-Induced Proteins in Drosophila Melanogaster Tissue Culture Cells. *Dev. Biol.* **1980**, *78* (1), 86–103. https://doi.org/10.1016/0012-1606(80)90320-6.

(188) Velazquez, J. M.; Lindquist, S. Hsp70: Nuclear Concentration during Environmental Stress and Cytoplasmic Storage during Recovery. *Cell* **1984**, *36* (3), 655–662. https://doi.org/10.1016/0092-8674(84)90345-3.

(189) Craven, R. A.; Egerton, M.; Stirling, C. J. A Novel Hsp70 of the Yeast ER Lumen Is Required for the Efficient Translocation of a Number of Protein Precursors. *EMBO J.* 1996, *15* (11), 2640–2650. https://doi.org/10.1002/j.1460-2075.1996.tb00624.x.

(190) Craig, E. A.; Kramer, J.; Shilling, J.; Werner-Washburne, M.; Holmes, S.; Kosic-Smithers, J.; Nicolet, C. M. SSC1, an Essential Member of the Yeast HSP70 Multigene Family, Encodes a Mitochondrial Protein. *Mol. Cell. Biol.* 1989, *9* (7), 3000–3008. https://doi.org/10.1128/MCB.9.7.3000.

(191) Broquet, A. H.; Thomas, G.; Masliah, J.; Trugnan, G.; Bachelet, M. Expression of the Molecular Chaperone Hsp70 in Detergent-Resistant Microdomains Correlates with Its Membrane Delivery and Release. *J. Biol. Chem.* 2003, *278* (24), 21601–21606. https://doi.org/10.1074/jbc.M302326200.

(192) Multhoff, G.; Botzler, C.; Wiesnet, M.; Müller, E.; Meier, T.; Wilmanns, W.; Issels, R. D. A Stress-Inducible 72-KDa Heat-Shock Protein (HSP72) Is Expressed on the Surface of Human Tumor Cells, but Not on Normal Cells. *Int. J. Cancer* 1995, *61* (2), 272–279. https://doi.org/10.1002/ijc.2910610222.

(193) Multhoff, G.; Hightower, L. E. Cell Surface Expression of Heat Shock Proteins and the Immune Response. *Cell Stress Chaperones* 1996, *1* (3), 167–176.

(194) Pockley, A. G.; Henderson, B.; Multhoff, G. Extracellular Cell Stress Proteins as Biomarkers of Human Disease. *Biochem. Soc. Trans.* 2014, *42* (6), 1744–1751. https://doi.org/10.1042/BST20140205.

(195) Mayer, M. P. Hsp70 Chaperone Dynamics and Molecular Mechanism. *Trends Biochem. Sci.* 2013, *38* (10), 507–514. https://doi.org/10.1016/j.tibs.2013.08.001.

(196) Dragovic, Z.; Broadley, S. A.; Shomura, Y.; Bracher, A.; Hartl, F. U. Molecular Chaperones of the Hsp110 Family Act as Nucleotide Exchange Factors of Hsp70s. *EMBO J.* 2006, *25* (11), 2519–2528. https://doi.org/10.1038/sj.emboj.7601138.

(197) Raviol, H.; Sadlish, H.; Rodriguez, F.; Mayer, M. P.; Bukau, B. Chaperone Network in the Yeast Cytosol: Hsp110 Is Revealed as an Hsp70 Nucleotide Exchange Factor. *EMBO J.* 2006, *25* (11), 2510–2518. https://doi.org/10.1038/sj.emboj.7601139.

(198) Ali, M. M. U.; Roe, S. M.; Vaughan, C. K.; Meyer, P.; Panaretou, B.; Piper, P. W.; Prodromou, C.; Pearl, L. H. Crystal Structure of an Hsp90–Nucleotide–P23/Sba1 Closed Chaperone Complex. *Nature* 2006, *440* (7087), 1013. https://doi.org/10.1038/nature04716.

(199) Shiau, A. K.; Harris, S. F.; Southworth, D. R.; Agard, D. A. Structural Analysis of E. Coli Hsp90 Reveals Dramatic Nucleotide-Dependent Conformational Rearrangements. *Cell* 2006, *127* (2), 329–340. https://doi.org/10.1016/j.cell.2006.09.027.

(200) Chen, S.; Smith, D. F. Hop as an Adaptor in the Heat Shock Protein 70 (Hsp70) and Hsp90 Chaperone Machinery. *J. Biol. Chem.* 1998, *273* (52), 35194–35200. https://doi.org/10.1074/jbc.273.52.35194.

(201) Smith, D. F.; Sullivan, W. P.; Marion, T. N.; Zaitsu, K.; Madden, B.; McCormick, D. J.; Toft, D. O. Identification of a 60-Kilodalton Stress-Related Protein, P60, Which Interacts with Hsp90 and Hsp70. *Mol. Cell. Biol.* 1993, *13* (2), 869–876. https://doi.org/10.1128/MCB.13.2.869.

(202) Nathan, D. F.; Lindquist, S. Mutational Analysis of Hsp90 Function: Interactions with a Steroid Receptor and a Protein Kinase. *Mol. Cell. Biol.* 1995, *15* (7), 3917–3925. https://doi.org/10.1128/MCB.15.7.3917.

(203) Xu, Y.; Lindquist, S. Heat-Shock Protein Hsp90 Governs the Activity of Pp60v-Src Kinase. *Proc. Natl. Acad. Sci. U. S. A.* 1993, *90* (15), 7074–7078.

(204) Taipale, M.; Jarosz, D. F.; Lindquist, S. HSP90 at the Hub of Protein Homeostasis: Emerging Mechanistic Insights. *Nat. Rev. Mol. Cell Biol.* 2010, *11* (7), 515–528. https://doi.org/10.1038/nrm2918.

(205) Okamoto, T.; Ishida, R.; Yamamoto, H.; Tanabe-Ishida, M.; Haga, A.; Takahashi, H.; Takahashi, K.; Goto, D.; Grave, E.; Itoh, H. Functional Structure and Physiological Functions of Mammalian Wild-Type HSP60. *Arch. Biochem. Biophys.* 2015, *586*, 10–19. https://doi.org/10.1016/j.abb.2015.09.022.

(206) Cheng, M. Y.; Hartl, F.-U.; Martin, J.; Pollock, R. A.; Kalousek, F.; Neuper, W.; Hallberg, E. M.; Hallberg, R. L.; Horwich, A. L. Mitochondrial Heat-Shock Protein Hsp60 Is Essential for Assembly of Proteins Imported into Yeast Mitochondria. *Nature* 1989, *337* (6208), 620. https://doi.org/10.1038/337620a0.

(207) Ostermann, J.; Horwich, A. L.; Neupert, W.; Hartl, F.-U. Protein Folding in Mitochondria Requires Complex Formation with Hsp60 and ATP Hydrolysis. *Nature* 1989, *341* (6238), 125. https://doi.org/10.1038/341125a0.

(208) Yaffe, M. B.; Farr, G. W.; Miklos, D.; Horwich, A. L.; Sternlicht, M. L.; Sternlicht, H. TCP1 Complex Is a Molecular Chaperone in Tubulin Biogenesis. *Nature* 1992, *358* (6383), 245. https://doi.org/10.1038/358245a0.

(209) Vinh, D. B.-N.; Drubin, D. G. A Yeast TCP-1-Like Protein Is Required for Actin Function In Vivo. *Proc. Natl. Acad. Sci. U. S. A.* 1994, *91* (19), 9116–9120.

(210) Camasses, A.; Bogdanova, A.; Shevchenko, A.; Zachariae, W. The CCT Chaperonin Promotes Activation of the Anaphase-Promoting Complex through the Generation of Functional Cdc20. *Mol. Cell* 2003, *12* (1), 87–100. https://doi.org/10.1016/S1097-2765(03)00244-2.

(211) Yam, A. Y.; Xia, Y.; Lin, H.-T. J.; Burlingame, A.; Gerstein, M.; Frydman, J. Defining the TRiC/CCT Interactome Links Chaperonin Function to Stabilization of Newly Made Proteins with Complex Topologies. *Nat. Struct. Mol. Biol.* 2008, *15* (12), 1255–1262. https://doi.org/10.1038/nsmb.1515.

(212) Jakob, U.; Gaestel, M.; Engel, K.; Buchner, J. Small Heat Shock Proteins Are Molecular Chaperones. *J. Biol. Chem.* 1993, *268* (3), 1517–1520.

(213) Garrido, C.; Paul, C.; Seigneuric, R.; Kampinga, H. H. The Small Heat Shock Proteins Family: The Long Forgotten Chaperones. *Int. J. Biochem. Cell Biol.* 2012, *44* (10), 1588–1592. https://doi.org/10.1016/j.biocel.2012.02.022.

(214) Crippa, V.; Sau, D.; Rusmini, P.; Boncoraglio, A.; Onesto, E.; Bolzoni, E.; Galbiati, M.; Fontana, E.; Marino, M.; Carra, S.; Bendotti, C.; De Biasi, S.; Poletti, A. The Small Heat Shock Protein B8 (HspB8) Promotes Autophagic Removal of Misfolded Proteins Involved in Amyotrophic Lateral Sclerosis (ALS). *Hum. Mol. Genet.* 2010, *19* (17), 3440–3456. https://doi.org/10.1093/hmg/ddq257.

(215) Engelsman, J. den; Keijsers, V.; Jong, W. W. de; Boelens, W. C. The Small Heat-Shock Protein AB-Crystallin Promotes FBX4-Dependent Ubiquitination. *J. Biol. Chem.* 2003, *278* (7), 4699–4704. https://doi.org/10.1074/jbc.M211403200.

(216) Renkawek, K.; Voorter, C. E.; Bosman, G. J.; van Workum, F. P.; de Jong, W. W. Expression of Alpha B-Crystallin in Alzheimer's Disease. *Acta Neuropathol. (Berl.)* 1994, *87* (2), 155–160.

(217) Renkawek, K.; Bosnian, G. J. C. G. M.; Gaestel, M. Increased Expression of Heat-Shock Protein 27 KDa in Alzheimer Disease: A Preliminary Study. *Neuroreport* 1993, *5* (1), 14–16.

(218) Iwaki, T.; Wisniewski, T.; Iwaki, A.; Corbin, E.; Tomokane, N.; Tateishi, J.; Goldman, J. E. Accumulation of Alpha B-Crystallin in Central Nervous System Glia and Neurons in Pathologic Conditions. *Am. J. Pathol.* 1992, *140* (2), 345–356.

(219) Iwaki, T.; Kume-Iwaki, A.; Liem, R. K.; Goldman, J. E. Alpha B-Crystallin Is Expressed in Non-Lenticular Tissues and Accumulates in Alexander's Disease Brain. *Cell* 1989, *57* (1), 71–78. https://doi.org/10.1016/0092-8674(89)90173-6.

(220) Kolb, S. J.; Snyder, P. J.; Poi, E. J.; Renard, E. A.; Bartlett, A.; Gu, S.; Sutton, S.; Arnold, W. D.; Freimer, M. L.; Lawson, V. H.; Kissel, J. T.; Prior, T. W. Mutant Small Heat Shock Protein B3 Causes Motor Neuropathy: Utility of a Candidate Gene Approach. *Neurology* 2010, *74* (6), 502–506. https://doi.org/10.1212/WNL.0b013e3181cef84a.

(221) Vicart, P.; Caron, A.; Guicheney, P.; Li, Z.; Prévost, M. C.; Faure, A.; Chateau, D.; Chapon, F.; Tomé, F.; Dupret, J. M.; Paulin, D.; Fardeau, M. A Missense Mutation in the AlphaB-Crystallin Chaperone Gene Causes a Desmin-Related Myopathy. *Nat. Genet.* 1998, *20* (1), 92–95. https://doi.org/10.1038/1765.

(222) Huang, X.; Luan, B.; Wu, J.; Shi, Y. An Atomic Structure of the Human 26S Proteasome. *Nat. Struct. Mol. Biol.* 2016, *23* (9), 778–785. https://doi.org/10.1038/nsmb.3273.

(223) da Fonseca, P. C. A.; He, J.; Morris, E. P. Molecular Model of the Human 26S Proteasome. *Mol. Cell* 2012, *46* (1), 54–66. https://doi.org/10.1016/j.molcel.2012.03.026.

(224) Meusser, B.; Hirsch, C.; Jarosch, E.; Sommer, T. ERAD: The Long Road to Destruction. *Nat. Cell Biol.* 2005, *7* (8), 766. https://doi.org/10.1038/ncb0805-766.

(225) Nandi, D.; Tahiliani, P.; Kumar, A.; Chandu, D. The Ubiquitin-Proteasome System. *J. Biosci.* 2006, *31* (1), 137–155. https://doi.org/10.1007/BF02705243.

(226) Hershko, A.; Ciechanover, A. The Ubiquitin System. *Annu. Rev. Biochem.* 1998, *67*, 425–479. https://doi.org/10.1146/annurev.biochem.67.1.425.

(227) Hershko, A.; Heller, H.; Elias, S.; Ciechanover, A. Components of Ubiquitin-Protein Ligase System. Resolution, Affinity Purification, and Role in Protein Breakdown. *J. Biol. Chem.* 1983, *258* (13), 8206–8214.

(228) Chau, V.; Tobias, J. W.; Bachmair, A.; Marriott, D.; Ecker, D. J.; Gonda, D. K.; Varshavsky, A. A Multiubiquitin Chain Is Confined to Specific Lysine in a Targeted Short-Lived Protein. *Science* 1989, *243* (4898), 1576–1583. https://doi.org/10.1126/science.2538923.

(229) Esser, C.; Alberti, S.; Höhfeld, J. Cooperation of Molecular Chaperones with the Ubiquitin/Proteasome System. *Biochim. Biophys. Acta BBA - Mol. Cell Res.* 2004, *1695* (1), 171–188. https://doi.org/10.1016/j.bbamcr.2004.09.020.

(230) Feng, Y.; He, D.; Yao, Z.; Klionsky, D. J. The Machinery of Macroautophagy. *Cell Res.* 2014, *24* (1), 24–41. https://doi.org/10.1038/cr.2013.168.

(231) Mizushima, N.; Ohsumi, Y.; Yoshimori, T. Autophagosome Formation in Mammalian Cells. *Cell Struct. Funct.* 2002, *27* (6), 421–429. https://doi.org/10.1247/csf.27.421.

(232) Ravikumar, B.; Duden, R.; Rubinsztein, D. C. Aggregate-Prone Proteins with Polyglutamine and Polyalanine Expansions Are Degraded by Autophagy. *Hum. Mol. Genet.* 2002, *11* (9), 1107–1117. https://doi.org/10.1093/hmg/11.9.1107.

(233) Hamano, T.; Gendron, T. F.; Causevic, E.; Yen, S.-H.; Lin, W.-L.; Isidoro, C.; DeTure, M.; Ko, L. Autophagic-Lysosomal Perturbation Enhances Tau Aggregation in Transfectants with Induced Wild-Type Tau Expression. *Eur. J. Neurosci.* 2008, *27* (5), 1119–1130. https://doi.org/10.1111/j.1460-9568.2008.06084.x.

(234) Cuervo, A. M.; Stefanis, L.; Fredenburg, R.; Lansbury, P. T.; Sulzer, D. Impaired Degradation of Mutant α-Synuclein by Chaperone-Mediated Autophagy. *Science* 2004, *305* (5688), 1292–1295. https://doi.org/10.1126/science.1101738.

(235) Marc, T.; Aziz A., K.; James W., C. Chaperoning Extended Life. *Nature* 1997, No. 6655, 30.

(236) Morley, J. F.; Morimoto, R. I. Regulation of Longevity in Caenorhabditis Elegans by Heat Shock Factor and Molecular Chaperones. *Mol. Biol. Cell* 2003, *15* (2), 657–664. https://doi.org/10.1091/mbc.e03-07-0532.

(237) Walker, G. A.; Lithgow, G. J. Lifespan Extension in C. Elegans by a Molecular Chaperone Dependent upon Insulin-like Signals. *Aging Cell* 2003, *2* (2), 131–139.

(238) Brehme, M.; Voisine, C.; Rolland, T.; Wachi, S.; Soper, J. H.; Zhu, Y.; Orton, K.; Villella, A.; Garza, D.; Vidal, M.; Ge, H.; Morimoto, R. I. A Chaperome Subnetwork Safeguards Proteostasis in Aging and Neurodegenerative Disease. *Cell Rep.* **2014**, *9* (3), 1135–1150. https://doi.org/10.1016/j.celrep.2014.09.042.

(239) Walther, D. M.; Kasturi, P.; Zheng, M.; Pinkert, S.; Vecchi, G.; Ciryam, P.; Morimoto, R. I.; Dobson, C. M.; Vendruscolo, M.; Mann, M.; Hartl, F. U. Widespread Proteome Remodeling and Aggregation in Aging C. Elegans. *Cell* **2015**, *161* (4), 919–932. https://doi.org/10.1016/j.cell.2015.03.032.

(240) Morrow, G.; Tanguay, R. M. Drosophila Melanogaster Hsp22: A Mitochondrial Small Heat Shock Protein Influencing the Aging Process. *Front. Genet.* **2015**, *6*. https://doi.org/10.3389/fgene.2015.00103.

(241) Yamaguchi, T.; Arai, H.; Katayama, N.; Ishikawa, T.; Kikumoto, K.; Atomi, Y. Age-Related Increase of Insoluble, Phosphorylated Small Heat Shock Proteins in Human Skeletal Muscle. *J. Gerontol. Ser. A* **2007**, *62* (5), 481–489. https://doi.org/10.1093/gerona/62.5.481.

(242) Ori, A.; Toyama, B. H.; Harris, M. S.; Bock, T.; Iskar, M.; Bork, P.; Ingolia, N. T.; Hetzer, M. W.; Beck, M. Integrated Transcriptome and Proteome Analyses Reveal Organ-Specific Proteome Deterioration in Old Rats. *Cell Syst.* **2015**, *1* (3), 224–237. https://doi.org/10.1016/j.cels.2015.08.012.

(243) Jiao, W.; Li, P.; Zhang, J.; Zhang, H.; Chang, Z. Small Heat-Shock Proteins Function in the Insoluble Protein Complex. *Biochem. Biophys. Res. Commun.* **2005**, *335* (1), 227–231. https://doi.org/10.1016/j.bbrc.2005.07.065.

(244) Wentink, A.; Nussbaum-Krammer, C.; Bukau, B. Modulation of Amyloid States by Molecular Chaperones. *Cold Spring Harb. Perspect. Biol.* **2019**, *11* (7), a033969. https://doi.org/10.1101/cshperspect.a033969.

(245) Kundel, F.; De, S.; Flagmeier, P.; Horrocks, M. H.; Kjaergaard, M.; Shammas, S. L.; Jackson, S. E.; Dobson, C. M.; Klenerman, D. Hsp70 Inhibits the Nucleation and Elongation of Tau and Sequesters Tau Aggregates with High Affinity. *ACS Chem. Biol.* **2018**, *13* (3), 636–646. https://doi.org/10.1021/acschembio.7b01039.

(246) Månsson, C.; Arosio, P.; Hussein, R.; Kampinga, H. H.; Hashem, R. M.; Boelens, W. C.; Dobson, C. M.; Knowles, T. P. J.; Linse, S.; Emanuelsson, C. Interaction of the Molecular Chaperone DNAJB6 with Growing Amyloid-Beta 42 (Aβ42) Aggregates Leads to Sub-Stoichiometric Inhibition of Amyloid Formation. *J. Biol. Chem.* **2014**, *289* (45), 31066–31076. https://doi.org/10.1074/jbc.M114.595124.

(247) Esposito, G.; Garvey, M.; Alverdi, V.; Pettirossi, F.; Corazza, A.; Fogolari, F.; Polano, M.; Mangione, P. P.; Giorgetti, S.; Stoppini, M.; Rekas, A.; Bellotti, V.; Heck, A. J. R.; Carver, J. A. Monitoring the Interaction between B2-Microglobulin and the Molecular Chaperone AB-Crystallin by NMR and Mass Spectrometry: AB-Crystallin Dissociates B2-Microglobulin Oligomers. *J. Biol. Chem.* **2013**, *288* (24), 17844–17858. https://doi.org/10.1074/jbc.M112.448639.

(248) McLean, P. J.; Kawamata, H.; Shariff, S.; Hewett, J.; Sharma, N.; Ueda, K.; Breakefield, X. O.; Hyman, B. T. TorsinA and Heat Shock Proteins Act as Molecular Chaperones: Suppression of α-Synuclein Aggregation: Chaperone Suppression of α-Synuclein Aggregation. *J. Neurochem.* **2002**, *83* (4), 846–854. https://doi.org/10.1046/j.1471-4159.2002.01190.x.

(249) Mok, S.-A.; Condello, C.; Freilich, R.; Gillies, A.; Arhar, T.; Oroz, J.; Kadavath, H.; Julien, O.; Assimon, V. A.; Rauch, J. N.; Dunyak, B. M.; Lee, J.; Tsai, F. T. F.; Wilson, M. R.; Zweckstetter, M.; Dickey, C. A.; Gestwicki, J. E. Mapping Interactions with the Chaperone Network Reveals Factors That Protect against Tau Aggregation. *Nat. Struct. Mol. Biol.* **2018**, *25* (5), 384–393. https://doi.org/10.1038/s41594-018-0057-1.

(250) Dedmon, M. M.; Christodoulou, J.; Wilson, M. R.; Dobson, C. M. Heat Shock Protein 70 Inhibits α-Synuclein Fibril Formation via Preferential Binding to Prefibrillar Species. *J. Biol. Chem.* **2005**, *280* (15), 14733–14740. https://doi.org/10.1074/jbc.M413024200.

(251) Daturpalli, S.; Waudby, C. A.; Meehan, S.; Jackson, S. E. Hsp90 Inhibits α-Synuclein Aggregation by Interacting with Soluble Oligomers. *J. Mol. Biol.* **2013**, *425* (22), 4614–4628. https://doi.org/10.1016/j.jmb.2013.08.006.

(252) Falsone, S. F.; Kungl, A. J.; Rek, A.; Cappai, R.; Zangger, K. The Molecular Chaperone Hsp90 Modulates Intermediate Steps of Amyloid Assembly of the Parkinson-Related Protein α-Synuclein. *J. Biol. Chem.* **2009**, *284* (45), 31190–31199. https://doi.org/10.1074/jbc.M109.057240.

(253) Xu, L.-Q.; Wu, S.; Buell, A. K.; Cohen, S. I. A.; Chen, L.-J.; Hu, W.-H.; Cusack, S. A.; Itzhaki, L. S.; Zhang, H.; Knowles, T. P. J.; Dobson, C. M.; Welland, M. E.; Jones, G. W.; Perrett, S. Influence of Specific HSP70 Domains on Fibril Formation of the Yeast Prion Protein Ure2. *Philos. Trans. Biol. Sci.* 2013, *368* (1617), 1–13.

(254) Cox, D.; Selig, E.; Griffin, M. D. W.; Carver, J. A.; Ecroyd, H. Small Heat-Shock Proteins Prevent α-Synuclein Aggregation via Transient Interactions and Their Efficacy Is Affected by the Rate of Aggregation. *J. Biol. Chem.* 2016, *291* (43), 22618–22629. https://doi.org/10.1074/jbc.M116.739250.

(255) Pemberton, S.; Madiona, K.; Pieri, L.; Kabani, M.; Bousset, L.; Melki, R. Hsc70 Protein Interaction with Soluble and Fibrillar α-Synuclein. *J. Biol. Chem.* 2011, *286* (40), 34690–34699. https://doi.org/10.1074/jbc.M111.261321.

(256) Schirmer, C.; Lepvrier, E.; Duchesne, L.; Decaux, O.; Thomas, D.; Delamarche, C.; Garnier, C. Hsp90 Directly Interacts, in Vitro, with Amyloid Structures and Modulates Their Assembly and Disassembly. *Biochim. Biophys. Acta BBA - Gen. Subj.* 2016, *1860* (11, Part A), 2598–2609. https://doi.org/10.1016/j.bbagen.2016.07.033.

(257) Cox, D.; Whiten, D. R.; Brown, J. W. P.; Horrocks, M. H.; Gil, R. S.; Dobson, C. M.; Klenerman, D.; Oijen, A. M. van; Ecroyd, H. The Small Heat Shock Protein Hsp27 Binds α-Synuclein Fibrils, Preventing Elongation and Cytotoxicity. *J. Biol. Chem.* 2018, *293* (12), 4486–4497. https://doi.org/10.1074/jbc.M117.813865.

(258) Binger, K. J.; Ecroyd, H.; Yang, S.; Carver, J. A.; Howlett, G. J.; Griffin, M. D. W. Avoiding the Oligomeric State: AB-Crystallin Inhibits Fragmentation and Induces Dissociation of Apolipoprotein C-II Amyloid Fibrils. *FASEB J.* 2013, *27* (3), 1214–1222. https://doi.org/10.1096/fj.12-220657.

(259) Raman, B.; Ban, T.; Sakai, M.; Pasta, S. Y.; Ramakrishna, T.; Naiki, H.; Goto, Y.; Rao, C. M. AB-Crystallin, a Small Heat-Shock Protein, Prevents the Amyloid Fibril Growth of an Amyloid β-Peptide and B2-Microglobulin. *Biochem. J.* 2005, *392* (3), 573–581. https://doi.org/10.1042/BJ20050339.

(260) Behrends, C.; Langer, C. A.; Boteva, R.; Böttcher, U. M.; Stemp, M. J.; Schaffar, G.; Rao, B. V.; Giese, A.; Kretzschmar, H.; Siegers, K.; Hartl, F. U. Chaperonin TRiC Promotes the Assembly of

PolyQ Expansion Proteins into Nontoxic Oligomers. *Mol. Cell* 2006, *23* (6), 887–897. https://doi.org/10.1016/j.molcel.2006.08.017.

(261) Shahmoradian, S. H.; Galaz-Montoya, J. G.; Schmid, M. F.; Yao, C.; Boxue, M.; Christoph, S.; Frydman, J.; Ludtke, S. J.; Wah, C. TRiC's Tricks Inhibit Huntingtin Aggregation. *ELife Camb.* 2013, *2*. http://dx.doi.org.ezp.lib.unimelb.edu.au/10.7554/eLife.00710.

(262) Mannini, B.; Cascella, R.; Zampagni, M.; Waarde-Verhagen, M. van; Meehan, S.; Roodveldt, C.; Campioni, S.; Boninsegna, M.; Penco, A.; Relini, A.; Kampinga, H. H.; Dobson, C. M.; Wilson, M. R.; Cecchi, C.; Chiti, F. Molecular Mechanisms Used by Chaperones to Reduce the Toxicity of Aberrant Protein Oligomers. *Proc. Natl. Acad. Sci.* 2012, *109* (31), 12479–12484. https://doi.org/10.1073/pnas.1117799109.

(263) Rujano, M. A.; Bosveld, F.; Salomons, F. A.; Dijk, F.; van Waarde, M. A. W. H.; van der Want, J. J. L.; de Vos, R. A. I.; Brunt, E. R.; Sibon, O. C. M.; Kampinga, H. H. Polarised Asymmetric Inheritance of Accumulated Protein Damage in Higher Eukaryotes. *Plos Biol.* 2006, *4* (12), e417–e417.

(264) Parsell, D. A.; Kowal, A. S.; Singer, M. A.; Lindquist, S. Protein Disaggregation Mediated by Heat-Shock Protein Hspl04. *Nature* 1994, *372* (6505), 475. https://doi.org/10.1038/372475a0.

(265) Liberek, K.; Lewandowska, A.; Ziętkiewicz, S. Chaperones in Control of Protein Disaggregation. *EMBO J.* 2008, *27* (2), 328–335. https://doi.org/10.1038/sj.emboj.7601970.

(266) Gao, X.; Carroni, M.; Nussbaum-Krammer, C.; Mogk, A.; Nillegoda, N. B.; Szlachcic, A.; Guilbride, D. L.; Saibil, H. R.; Mayer, M. P.; Bukau, B. Human Hsp70 Disaggregase Reverses Parkinson's-Linked α-Synuclein Amyloid Fibrils. *Mol. Cell* 2015, *59* (5), 781–793. https://doi.org/10.1016/j.molcel.2015.07.012.

(267) Laskowska, E.; Wawrzynów, A.; Taylor, A. IbpA and IbpB, the New Heat-Shock Proteins, Bind to Endogenous Escherichia Coli Proteins Aggregated Intracellularly by Heat Shock. *Biochimie* 1996, *78* (2), 117–122. https://doi.org/10.1016/0300-9084(96)82643-5.

(268) Cashikar, A. G.; Duennwald, M.; Lindquist, S. L. A Chaperone Pathway in Protein Disaggregation HSP26 ALTERS THE NATURE OF PROTEIN AGGREGATES TO FACILITATE REACTIVATION BY HSP104. *J. Biol. Chem.* 2005, *280* (25), 23869–23875. https://doi.org/10.1074/jbc.M502854200.

(269) Ehrnsperger, M.; Gräber, S.; Gaestel, M.; Buchner, J. Binding of Non-Native Protein to Hsp25 during Heat Shock Creates a Reservoir of Folding Intermediates for Reactivation. *EMBO J.* 1997, *16* (2), 221–229. https://doi.org/10.1093/emboj/16.2.221.

(270) Duennwald, M. L.; Echeverria, A.; Shorter, J. Small Heat Shock Proteins Potentiate Amyloid Dissolution by Protein Disaggregases from Yeast and Humans. *Plos Biol.* 2012, *10* (6), e1001346–e1001346. https://doi.org/10.1371/journal.pbio.1001346.

(271) Haley, D. A.; Horwitz, J.; Stewart, P. L. The Small Heat-Shock Protein, Ab-Crystallin, Has a Variable Quaternary Structure. *J. Mol. Biol.* 1998, *277* (1), 27–35. https://doi.org/10.1006/jmbi.1997.1611.

(272) Behlke, J.; Lutsch, G.; Gaestel, M.; Bielka, H. Supramolecular Structure of the Recombinant Murine Small Heat Shock Protein Hsp25. *FEBS Lett.* 1991, *288* (1), 119–122. https://doi.org/10.1016/0014-5793(91)81016-2.

(273) Bova, M. P.; Ding, L.-L.; Horwitz, J.; Fung, B. K.-K. Subunit Exchange of AA-Crystallin. *J. Biol. Chem.* 1997, *272* (47), 29511–29517. https://doi.org/10.1074/jbc.272.47.29511.

(274) Kim, K. K.; Kim, R.; Kim, S.-H. Crystal Structure of a Small Heat-Shock Protein. *Nature* 1998, *394* (6693), 595. https://doi.org/10.1038/29106.

(275) van Montfort, R. L.; Basha, E.; Friedrich, K. L.; Slingsby, C.; Vierling, E. Crystal Structure and Assembly of a Eukaryotic Small Heat Shock Protein. *Nat. Struct. Biol.* 2001, *8* (12), 1025–1030.

(276) Jehle, S.; Vollmar, B. S.; Bardiaux, B.; Dove, K. K.; Rajagopal, P.; Gonen, T.; Oschkinat, H.; Klevit, R. E. N-Terminal Domain of AB-Crystallin Provides a Conformational Switch for Multimerization and Structural Heterogeneity. 6.

(277) Bagnéris, C.; Bateman, O. A.; Naylor, C. E.; Cronin, N.; Boelens, W. C.; Keep, N. H.; Slingsby, C. Crystal Structures of α-Crystallin Domain Dimers of AB-Crystallin and Hsp20. *J. Mol. Biol.* 2009, *392* (5), 1242–1252. https://doi.org/10.1016/j.jmb.2009.07.069.

(278) Baranova, E. V.; Beelen, S.; Gusev, N. B.; Strelkov, S. V. The Taming of Small Heat-Shock Proteins: Crystallization of the α-Crystallin Domain from Human Hsp27. *Acta Crystallograph. Sect. F Struct. Biol. Cryst. Commun.* 2009, *65* (12), 1277–1281. https://doi.org/10.1107/S1744309109044571.

(279) Hochberg, G. K. A.; Ecroyd, H.; Liu, C.; Cox, D.; Cascio, D.; Sawaya, M. R.; Collier, M. P.; Stroud, J.; Carver, J. A.; Baldwin, A. J.; Robinson, C. V.; Eisenberg, D. S.; Benesch, J. L. P.; Laganowsky, A. The

Structured Core Domain of B-Crystallin Can Prevent Amyloid Fibrillation and Associated Toxicity. *Proc. Natl. Acad. Sci.* 2014, *111* (16), E1562–E1570. https://doi.org/10.1073/pnas.1322673111.

(280) Laganowsky, A.; Benesch, J. L. P.; Landau, M.; Ding, L.; Sawaya, M. R.; Cascio, D.; Huang, Q.; Robinson, C. V.; Horwitz, J.; Eisenberg, D. Crystal Structures of Truncated AlphaA and AlphaB Crystallins Reveal Structural Mechanisms of Polydispersity Important for Eye Lens Function. *Protein Sci.* 2010, *19* (5), 1031–1043. https://doi.org/10.1002/pro.380.

(281) Liu, Z.; Wang, C.; Li, Y.; Zhao, C.; Li, T.; Li, D.; Zhang, S.; Liu, C. Mechanistic Insights into the Switch of AB-Crystallin Chaperone Activity and Self-Multimerization. *J. Biol. Chem.* 2018, *293* (38), 14880–14890. https://doi.org/10.1074/jbc.RA118.004034.

(282) Aquilina, J. A.; Benesch, J. L. P.; Bateman, O. A.; Slingsby, C.; Robinson, C. V. Polydispersity of a Mammalian Chaperone: Mass Spectrometry Reveals the Population of Oligomers in B-Crystallin. *Proc. Natl. Acad. Sci.* 2003, *100* (19), 10611–10616. https://doi.org/10.1073/pnas.1932958100.

(283) Jovcevski, B.; Kelly, M. A.; Rote, A. P.; Berg, T.; Gastall, H. Y.; Benesch, J. L. P.; Aquilina, J. A.; Ecroyd, H. Phosphomimics Destabilize Hsp27 Oligomeric Assemblies and Enhance Chaperone Activity. *Chem. Biol.* 2015, *22* (2), 186–195. https://doi.org/10.1016/j.chembiol.2015.01.001.

(284) Aquilina, J. A.; Benesch, J. L. P.; Ding, L. L.; Yaron, O.; Horwitz, J.; Robinson, C. V. Phosphorylation of AB-Crystallin Alters Chaperone Function through Loss of Dimeric Substructure. *J. Biol. Chem.* 2004, *279* (27), 28675–28680. https://doi.org/10.1074/jbc.M403348200.

(285) Hochberg, G. K. A.; Benesch, J. L. P. Dynamical Structure of AB-Crystallin. *Prog. Biophys. Mol. Biol.* 2014, *115* (1), 11–20. https://doi.org/10.1016/j.pbiomolbio.2014.03.003.

(286) Baldwin, A. J.; Lioe, H.; Robinson, C. V.; Kay, L. E.; Benesch, J. L. P. AB-Crystallin Polydispersity Is a Consequence of Unbiased Quaternary Dynamics. *J. Mol. Biol.* 2011, *413* (2), 297–309. https://doi.org/10.1016/j.jmb.2011.07.016.

(287) Delbecq, S. P.; Rosenbaum, J. C.; Klevit, R. E. A Mechanism of Subunit Recruitment in Human Small Heat Shock Protein Oligomers. *Biochemistry* 2015, *54* (28), 4276–4284. https://doi.org/10.1021/acs.biochem.5b00490.

(288) Lambert, H.; Charette, S. J.; Bernier, A. F.; Guimond, A.; Landry, J. HSP27 Multimerization Mediated by Phosphorylation-Sensitive Intermolecular Interactions at the Amino Terminus. *J. Biol. Chem.* 1999, *274* (14), 9378–9385. https://doi.org/10.1074/jbc.274.14.9378.

(289) Hayes, D.; Napoli, V.; Mazurkie, A.; Stafford, W. F.; Graceffa, P. Phosphorylation Dependence of Hsp27 Multimeric Size and Molecular Chaperone Function. *J. Biol. Chem.* 2009, *284* (28), 18801–18807. https://doi.org/10.1074/jbc.M109.011353.

(290) Clouser, A. F.; Baughman, H. E.; Basanta, B.; Guttman, M.; Nath, A.; Klevit, R. E. Interplay of Disordered and Ordered Regions of a Human Small Heat Shock Protein Yields an Ensemble of 'Quasi-Ordered' States. *eLife 8*. https://doi.org/10.7554/eLife.50259.

(291) Baughman, H. E. R.; Clouser, A. F.; Klevit, R. E.; Nath, A. HspB1 and Hsc70 Chaperones Engage Distinct Tau Species and Have Different Inhibitory Effects on Amyloid Formation. *J. Biol. Chem.* 2018, *293* (8), 2687–2700. https://doi.org/10.1074/jbc.M117.803411.

(292) Baughman, H. E. R.; Pham, T.-H. T.; Adams, C. S.; Nath, A.; Klevit, R. E. Release of a Disordered Domain Enhances HspB1 Chaperone Activity toward Tau. *Proc. Natl. Acad. Sci.* 2020. https://doi.org/10.1073/pnas.1915099117.

(293) Kulig, M.; Ecroyd, H. The Small Heat-Shock Protein AB-Crystallin Uses Different Mechanisms of Chaperone Action to Prevent the Amorphous versus Fibrillar Aggregation of α-Lactalbumin. *Biochem. J.* 2012, *448* (3), 343–352. https://doi.org/10.1042/BJ20121187.

(294) Lindner, R. A.; Kapur, A.; Mariani, M.; Titmuss, S. J.; Carver, J. A. Structural Alterations of Alpha-Crystallin during Its Chaperone Action. *Eur. J. Biochem.* 1998, *258* (1), 170–183.

(295) Mainz, A.; Peschek, J.; Stavropoulou, M.; Back, K. C.; Bardiaux, B.; Asami, S.; Prade, E.; Peters, C.; Weinkauf, S.; Buchner, J.; Reif, B. The Chaperone [Alpha]B-Crystallin Uses Different Interfaces to Capture an Amorphous and an Amyloid Client. *Nat. Struct. Mol. Biol.* 2015, No. 11, 898. https://doi.org/10.1038/nsmb.3108.

(296) Lee, G. J.; Roseman, A. M.; Saibil, H. R.; Vierling, E. A Small Heat Shock Protein Stably Binds Heat-Denatured Model Substrates and Can Maintain a Substrate in a Folding-Competent State. *EMBO J.* 1997, *16* (3), 659–671. https://doi.org/10.1093/emboj/16.3.659.

(297) Jaya, N.; Garcia, V.; Vierling, E. Substrate Binding Site Flexibility of the Small Heat Shock Protein Molecular Chaperones. *Proc. Natl. Acad. Sci.* 2009, *106* (37), 15604–15609. https://doi.org/10.1073/pnas.0902177106.

(298) Ghosh, J. G.; Shenoy, Ananth K.; Clark, J. I. N- and C-Terminal Motifs in Human AB Crystallin Play an Important Role in the Recognition, Selection, and Solubilization of Substrates. *Biochemistry* 2006, *45* (46), 13847–13854. https://doi.org/10.1021/bi061471m.

(299) Carver, J. A.; Lindner, R. A. NMR Spectroscopy of α-Crystallin. Insights into the Structure, Interactions and Chaperone Action of Small Heat-Shock Proteins. *Int. J. Biol. Macromol.* 1998, *22* (3), 197–209. https://doi.org/10.1016/S0141-8130(98)00017-8.

(300) Freilich, R.; Betegon, M.; Tse, E.; Mok, S.-A.; Julien, O.; Agard, D. A.; Southworth, D. R.; Takeuchi, K.; Gestwicki, J. E. Competing Protein-Protein Interactions Regulate Binding of Hsp27 to Its Client Protein Tau. *Nat. Commun.* 2018, *9*. https://doi.org/10.1038/s41467-018-07012-4.

(301) Aquilina, J. A.; Watt, S. J. The N-Terminal Domain of AB-Crystallin Is Protected from Proteolysis by Bound Substrate. *Biochem. Biophys. Res. Commun.* 2007, *353* (4), 1115–1120. https://doi.org/10.1016/j.bbrc.2006.12.176.

(302) Sharma, K. K.; Kaur, H.; Kester, K. Functional Elements in Molecular Chaperone α-Crystallin: Identification of Binding Sites in AB-Crystallin. *Biochem. Biophys. Res. Commun.* 1997, *239* (1), 217–222. https://doi.org/10.1006/bbrc.1997.7460.

(303) Basha, E.; O'Neill, H.; Vierling, E. Small Heat Shock Proteins and α-Crystallins: Dynamic Proteins with Flexible Functions. *Trends Biochem. Sci.* 2012, *37* (3), 106–117. https://doi.org/10.1016/j.tibs.2011.11.005.

(304) Braun, N.; Zacharias, M.; Peschek, J.; Kastenmüller, A.; Zou, J.; Hanzlik, M.; Haslbeck, M.; Rappsilber, J.; Buchner, J.; Weinkauf, S. Multiple Molecular Architectures of the Eye Lens Chaperone AB-Crystallin Elucidated by a Triple Hybrid Approach. 2011, 6.

(305) McDonald, E. T.; Bortolus, M.; Koteiche, H. A.; Mchaourab, H. S. Sequence, Structure, and Dynamic Determinants of Hsp27 (HspB1) Equilibrium Dissociation Are Encoded by the N-Terminal Domain. *Biochemistry* 2012, *51* (6), 1257–1268. https://doi.org/10.1021/bi2017624.

(306) Treweek, T. M.; Meehan, S.; Ecroyd, H.; Carver, J. A. Small Heat-Shock Proteins: Important Players in Regulating Cellular Proteostasis. *Cell. Mol. Life Sci. CMLS* 2015, *72* (3), 429–451. https://doi.org/10.1007/s00018-014-1754-5.

(307) Hatters, D. M.; Lindner, R. A.; Carver, J. A.; Howlett, G. J. The Molecular Chaperone, α-Crystallin, Inhibits Amyloid Formation by Apolipoprotein C-II. *J. Biol. Chem.* 2001, *276* (36), 33755–33761. https://doi.org/10.1074/jbc.M105285200.

(308) Rekas, A.; Adda, C. G.; Andrew Aquilina, J.; Barnham, K. J.; Sunde, M.; Galatis, D.; Williamson, N. A.; Masters, C. L.; Anders, R. F.; Robinson, C. V.; Cappai, R.; Carver, J. A. Interaction of the Molecular Chaperone AB-Crystallin with α-Synuclein: Effects on Amyloid Fibril Formation and Chaperone Activity. *J. Mol. Biol.* 2004, *340* (5), 1167–1183. https://doi.org/10.1016/j.jmb.2004.05.054.

(309) Shammas, S. L.; Waudby, C. A.; Wang, S.; Buell, A. K.; Knowles, T. P. J.; Ecroyd, H.; Welland, M. E.; Carver, J. A.; Dobson, C. M.; Meehan, S. Binding of the Molecular Chaperone AB-Crystallin to Aβ Amyloid Fibrils Inhibits Fibril Elongation. *Biophys. J.* 2011, *101* (7), 1681–1689. https://doi.org/10.1016/j.bpj.2011.07.056.

(310) Waudby, C. A.; Knowles, T. P. J.; Devlin, G. L.; Skepper, J. N.; Ecroyd, H.; Carver, J. A.; Welland, M. E.; Christodoulou, J.; Dobson, C. M.; Meehan, S. The Interaction of AB-Crystallin with Mature α-Synuclein Amyloid Fibrils Inhibits Their Elongation. *Biophys. J.* 2010, *98* (5), 843–851. https://doi.org/10.1016/j.bpj.2009.10.056.

(311) Ojha, J.; Masilamoni, G.; Dunlap, D.; Udoff, R. A.; Cashikar, A. G. Sequestration of Toxic Oligomers by HspB1 as a Cytoprotective Mechanism. *Mol. Cell. Biol.* 2011, *31* (15), 3146–3157. https://doi.org/10.1128/MCB.01187-10.

(312) Wilhelmus, M. M. M.; Boelens, W. C.; Otte-Höller, I.; Kamps, B.; de Waal, R. M. W.; Verbeek, M. M. Small Heat Shock Proteins Inhibit Amyloid-β Protein Aggregation and Cerebrovascular Amyloid-β Protein Toxicity. *Brain Res.* 2006, *1089* (1), 67–78. https://doi.org/10.1016/j.brainres.2006.03.058.

(313) Bruinsma, I. B.; Bruggink, K. A.; Kinast, K.; Versleijen, A. A. M.; Segers-Nolten, I. M. J.; Subramaniam, V.; Kuiperij, H. B.; Boelens, W.; Waal, R. M. W. de; Verbeek, M. M. Inhibition of α-Synuclein Aggregation by Small Heat Shock Proteins. *Proteins Struct. Funct. Bioinforma.* 2011, *79* (10), 2956–2967. https://doi.org/10.1002/prot.23152.

(314) Alderson, T. R.; Roche, J.; Gastall, H. Y.; Dias, D. M.; Pritišanac, I.; Ying, J.; Bax, A.; Benesch, J. L. P.; Baldwin, A. J. Local Unfolding of the HSP27 Monomer Regulates Chaperone Activity. *Nat. Commun.* 2019, *10*. https://doi.org/10.1038/s41467-019-08557-8.

(315) Augusteyn, R. C. Dissociation Is Not Required for α-Crystallin's Chaperone Function. *Exp. Eye Res.* 2004, *79* (6), 781–784. https://doi.org/10.1016/j.exer.2004.08.010.

(316) Ponni, R.; Tse, E.; Borst, A. J.; Delbecq, S. P.; Shi, L.; Southworth, D. R.; Klevit, R. E. A Conserved Histidine Modulates HSPB5 Structure to Trigger Chaperone Activity in Response to Stress-Related Acidosis. *ELife Camb.* 2015, *4*. http://dx.doi.org.ezp.lib.unimelb.edu.au/10.7554/eLife.07304.

(317) Cabrita, L. D.; Gilis, D.; Robertson, A. L.; Dehouck, Y.; Rooman, M.; Bottomley, S. P. Enhancing the Stability and Solubility of TEV Protease Using in Silico Design. *Protein Sci* 2007, *16* (11), 2360–2367. https://doi.org/10.1110/ps.072822507.

(318) Sambrook, J.; Maniatis, T.; Fritsch, E. F.; Laboratory, C. S. H. *Molecular Cloning : A Laboratory Manual*, 2nd ed.; Cold Spring Harbor, N.Y. : Cold Spring Harbor Laboratory Press, 1987.

(319) Narhi, L.; Wood, S. J.; Steavenson, S.; Jiang, Y.; Wu, G. M.; Anafi, D.; Kaufman, S. A.; Martin, F.; Sitney, K.; Denis, P.; Louis, J.-C.; Wypych, J.; Biere, A. L.; Citron, M. Both Familial Parkinson's Disease Mutations Accelerate α-Synuclein Aggregation. *J. Biol. Chem.* 1999, *274* (14), 9843–9846. https://doi.org/10.1074/jbc.274.14.9843.

(320) Horwitz, J.; Bova, M.; Huang, Q. L.; Ding, L.; Yaron, O.; Lowman, S. Mutation of Alpha B-Crystallin: Effects on Chaperone-like Activity. *Int J Biol Macromol* 1998, *22* (3–4), 263–269.

(321) Clouser, A. F.; Klevit, R. E. PH-Dependent Structural Modulation Is Conserved in the Human Small Heat Shock Protein HSBP1. *Cell Stress Chaperones* 2017, *22* (4), 569–575. https://doi.org/10.1007/s12192-017-0783-z.

(322) Studier, F. W. Protein Production by Auto-Induction in High Density Shaking Cultures. *Protein Expr Purif* 2005, *41* (1), 207–234.

(323) Lindgren, M.; Sörgjerd, K.; Hammarström, P. Detection and Characterization of Aggregates, Prefibrillar Amyloidogenic Oligomers, and Protofibrils Using Fluorescence Spectroscopy. *Biophys. J.* 2005, *88* (6), 4200–4212. https://doi.org/10.1529/biophysj.104.049700.

(324) Ferrari, G. V. D.; Mallender, W. D.; Inestrosa, N. C.; Rosenberry, T. L. Thioflavin T Is a Fluorescent Probe of the Acetylcholinesterase Peripheral Site That Reveals Conformational Interactions between the Peripheral and Acylation Sites. *J. Biol. Chem.* **2001**, *276* (26), 23282–23287. https://doi.org/10.1074/jbc.M009596200.

(325) Ryan, T. M.; Howlett, G. J.; Bailey, M. F. Fluorescence Detection of a Lipid-Induced Tetrameric Intermediate in Amyloid Fibril Formation by Apolipoprotein C-II. *J. Biol. Chem.* **2008**, *283* (50), 35118–35128. https://doi.org/10.1074/jbc.M804004200.

(326) Schuck, P. Size-Distribution Analysis of Macromolecules by Sedimentation Velocity Ultracentrifugation and Lamm Equation Modeling. *Biophys J* **2000**, *78* (3), 1606–1619. https://doi.org/10.1016/S0006-3495(00)76713-0.

(327) MacRaild, C. A.; Hatters, D. M.; Lawrence, L. J.; Howlett, G. J. Sedimentation Velocity Analysis of Flexible Macromolecules: Self-Association and Tangling of Amyloid Fibrils. *Biophys. J.* **2003**, *84* (4), 2562–2569. https://doi.org/10.1016/S0006-3495(03)75061-9.

(328) Schuck, P.; Rossmanith, P. Determination of the Sedimentation Coefficient Distribution by Least-Squares Boundary Modeling. *Biopolymers* **2000**, *54* (5), 328–341. https://doi.org/10.1002/1097-0282(20001015)54:5<328::AID-BIP40>3.0.CO;2-P.

(329) Harding, S. E.; Rowe, A. J.; Horton, J. C. *Analytical Ultracentrifugation in Biochemistry and Polymer Science*; Royal Society of Chemistry: Cambridge England, 1992.

(330) Selkoe, D. J. Folding Proteins in Fatal Ways. *Nature* **2003**, *426* (6968), 900–904. https://doi.org/10.1038/nature02264.

(331) Hans J. Reich. 8-TECH-1 Relaxation in NMR Spectroscopy https://www.chem.wisc.edu/areas/reich/nmr/08-tech-01-relax.htm (accessed Nov 26, 2019).

(332) Williamson, M. P. *How Proteins Work*; Garland Science, 2012.

(333) Delaglio, F.; Grzesiek, S.; Vuister, G. W.; Zhu, G.; Pfeifer, J.; Bax, A. NMRPipe: A Multidimensional Spectral Processing System Based on UNIX Pipes. *J. Biomol. NMR* **1995**, *6* (3), 277–293. https://doi.org/10.1007/BF00197809.

(334) Wishart, D. S.; Bigam, C. G.; Yao, J.; Abildgaard, F.; Dyson, H. J.; Oldfield, E.; Markley, J. L.; Sykes, B. D. 1H, 13C and 15N Chemical Shift Referencing in Biomolecular NMR. *J. Biomol. NMR* **1995**, *6* (2), 135–140. https://doi.org/10.1007/BF00211777.

(335) Ayed, A.; Mulder, F. A.; Yi, G. S.; Lu, Y.; Kay, L. E.; Arrowsmith, C. H. Latent and Active P53 Are Identical in Conformation. *Nat. Struct. Biol.* 2001, *8* (9), 756–760.

(336) Kay, L. E.; Torchia, D. A. Backbone Dynamics of Proteins As Studied by 15NInverse Detected Heteronuclear NMR Spectroscopy: Application to Staphylococcal Nuclease? 8.

(337) Debye, P. Zerstreuung von Röntgenstrahlen. *Ann. Phys.* 1915, *351* (6), 809–823. https://doi.org/10.1002/andp.19153510606.

(338) Panjkovich, A.; Svergun, D. I. CHROMIXS: Automatic and Interactive Analysis of Chromatography-Coupled Small-Angle X-Ray Scattering Data. *Bioinforma. Oxf. Engl.* 2018, *34* (11), 1944–1946. https://doi.org/10.1093/bioinformatics/btx846.

(339) Franke, D.; Petoukhov, M. V.; Konarev, P. V.; Panjkovich, A.; Tuukkanen, A.; Mertens, H. D. T.; Kikhney, A. G.; Hajizadeh, N. R.; Franklin, J. M.; Jeffries, C. M.; Svergun, D. I. ATSAS 2.8: A Comprehensive Data Analysis Suite for Small-Angle Scattering from Macromolecular Solutions. *J. Appl. Crystallogr.* 2017, *50* (Pt 4), 1212–1225. https://doi.org/10.1107/S1600576717007786.

(340) Konarev, P. V.; Volkov, V. V.; Sokolova, A. V.; Koch, M. H. J.; Svergun, D. I. PRIMUS: A Windows PC-Based System for Small-Angle Scattering Data Analysis. *J. Appl. Crystallogr.* 2003, *36* (5), 1277–1282. https://doi.org/10.1107/S0021889803012779.

(341) Svergun, D.; Barberato, C.; Koch, M. H. J. *CRYSOL* – a Program to Evaluate X-Ray Solution Scattering of Biological Macromolecules from Atomic Coordinates. *J. Appl. Crystallogr.* 1995, *28* (6), 768–773. https://doi.org/10.1107/S0021889895007047.

(342) Jehle, S.; Vollmar, B. S.; Bardiaux, B.; Dove, K. K.; Rajagopal, P.; Gonen, T.; Oschkinat, H.; Klevit, R. E. N-Terminal Domain of AlphaB-Crystallin Provides a Conformational Switch for Multimerization and Structural Heterogeneity. *Proc Natl Acad Sci U A* 2011, *108* (16), 6409–6414. https://doi.org/10.1073/pnas.1014656108.

(343) Mymrikov, E. V.; Daake, M.; Richter, B.; Haslbeck, M.; Buchner, J. The Chaperone Activity and Substrate Spectrum of Human Small Heat Shock Proteins. *J. Biol. Chem.* 2017, *292* (2), 672–684. https://doi.org/10.1074/jbc.M116.760413.

(344) Oesterreich, S.; Weng, C.-N.; Qiu, M.; Hilsenbeck, S. G.; Osborne, C. K.; Fuqua, S. A. W. The Small Heat Shock Protein Hsp27 Is Correlated with Growth and Drug Resistance in Human Breast Cancer Cell Lines. *Cancer Res.* 1993, *53* (19), 4443–4448.

(345) Ikeda, R.; Yoshida, K.; Ushiyama, M.; Yamaguchi, T.; Iwashita, K.; Futagawa, T.; Shibayama, Y.; Oiso, S.; Takeda, Y.; Kariyazono, H.; Furukawa, T.; Nakamura, K.; Akiyama, S.; Inoue, I.; Yamada, K. The Small Heat Shock Protein AlphaB-Crystallin Inhibits Differentiation-Induced Caspase 3 Activation and Myogenic Differentiation. *Biol Pharm Bull* 2006, *29* (9), 1815–1819.

(346) Kamradt, M. C.; Chen, F.; Sam, S.; Cryns, V. L. The Small Heat Shock Protein Alpha B-Crystallin Negatively Regulates Apoptosis during Myogenic Differentiation by Inhibiting Caspase-3 Activation. *J Biol Chem* 2002, *277* (41), 38731–38736. https://doi.org/10.1074/jbc.M201770200.

(347) Arai, H.; Atomi, Y. Chaperone Activity of AB-Crystallin Suppresses Tubulin Aggregation through Complex Formation. *Cell Struct. Funct.* 1997, *22* (5), 539–544. https://doi.org/10.1247/csf.22.539.

(348) Hino, M.; Kurogi, K.; Okubo, M. A.; Murata-Hori, M.; Hosoya, H. Small Heat Shock Protein 27 (HSP27) Associates with Tubulin/Microtubules in HeLa Cells. *Biochem Biophys Res Commun* 2000, *271* (1), 164–169. https://doi.org/10.1006/bbrc.2000.2553.

(349) Arrigo, A. P. Hsp27: Novel Regulator of Intracellular Redox State. *IUBMB Life* 2001, *52* (6), 303–307. https://doi.org/10.1080/152165401317291165.

(350) Lee, G. J.; Vierling, E. A Small Heat Shock Protein Cooperates with Heat Shock Protein 70 Systems to Reactivate a Heat-Denatured Protein. *Plant Physiol* 2000, *122* (1), 189–198.

(351) Ahner, A.; Gong, X.; Schmidt, B. Z.; Peters, K. W.; Rabeh, W. M.; Thibodeau, P. H.; Lukacs, G. L.; Frizzell, R. A. Small Heat Shock Proteins Target Mutant Cystic Fibrosis Transmembrane Conductance Regulator for Degradation via a Small Ubiquitin-like Modifier-Dependent Pathway. *Mol Biol Cell* 2013, *24* (2), 74–84. https://doi.org/10.1091/mbc.E12-09-0678.

(352) Evgrafov, O. V.; Mersiyanova, I.; Irobi, J.; Van Den Bosch, L.; Dierick, I.; Leung, C. L.; Schagina, O.; Verpoorten, N.; Van Impe, K.; Fedotov, V.; Dadali, E.; Auer-Grumbach, M.; Windpassinger, C.; Wagner, K.; Mitrovic, Z.; Hilton-Jones, D.; Talbot, K.; Martin, J. J.; Vasserman, N.; Tverskaya, S.; Polyakov, A.; Liem, R. K.; Gettemans, J.; Robberecht, W.; De Jonghe, P.; Timmerman, V. Mutant Small Heat-Shock Protein 27 Causes Axonal Charcot-Marie-Tooth Disease and Distal Hereditary Motor Neuropathy. *Nat Genet* 2004, *36* (6), 602–606. https://doi.org/10.1038/ng1354.

(353) Clark, A. R.; Lubsen, N. H.; Slingsby, C. SHSP in the Eye Lens: Crystallin Mutations, Cataract and Proteostasis. *Int. J. Biochem. Cell Biol.* 2012, *44* (10), 1687–1697. https://doi.org/10.1016/j.biocel.2012.02.015.

(354) Burre, J. The Synaptic Function of Alpha-Synuclein. *J Park. Dis* 2015, *5* (4), 699–713. https://doi.org/10.3233/JPD-150642.

(355) Shinohara, H.; Inaguma, Y.; Goto, S.; Inagaki, T.; Kato, K. Alpha B Crystallin and HSP28 Are Enhanced in the Cerebral Cortex of Patients with Alzheimer's Disease. *J Neurol Sci* 1993, *119* (2), 203–208.

(356) Renkawek, K.; Stege, G. J.; Bosman, G. J. Dementia, Gliosis and Expression of the Small Heat Shock Proteins Hsp27 and Alpha B-Crystallin in Parkinson's Disease. *Neuroreport* 1999, *10* (11), 2273–2276.

(357) Renkawek, K. Expression of Small Heat-Shock Protein Hsp 27 in Reactive Gliosis in Alzheimer Disease and Other Types of Dementia. 9.

(358) Cox, D.; Ecroyd, H. The Small Heat Shock Proteins AlphaB-Crystallin (HSPB5) and Hsp27 (HSPB1) Inhibit the Intracellular Aggregation of Alpha-Synuclein. *Cell Stress Chaperones* 2017, *22* (4), 589–600. https://doi.org/10.1007/s12192-017-0785-x.

(359) Yerbury, J. J.; Gower, D.; Vanags, L.; Roberts, K.; Lee, J. A.; Ecroyd, H. The Small Heat Shock Proteins AlphaB-Crystallin and Hsp27 Suppress SOD1 Aggregation in Vitro. *Cell Stress Chaperones* 2013, *18* (2), 251–257. https://doi.org/10.1007/s12192-012-0371-1.

(360) Der Perng, M.; Su, M.; Wen, S. F.; Li, R.; Gibbon, T.; Prescott, A. R.; Brenner, M.; Quinlan, R. A. The Alexander Disease-Causing Glial Fibrillary Acidic Protein Mutant, R416W, Accumulates into Rosenthal Fibers by a Pathway That Involves Filament Aggregation and the Association of Alpha B-Crystallin and HSP27. *Am J Hum Genet* 2006, *79* (2), 197–213. https://doi.org/10.1086/504411.

(361) Baldwin, A. J.; Hilton, G. R.; Lioe, H.; Bagnéris, C.; Benesch, J. L. P.; Kay, L. E. Quaternary Dynamics of AB-Crystallin as a Direct Consequence of Localised Tertiary Fluctuations in the C-Terminus. *J. Mol. Biol.* 2011, *413* (2), 310–320. https://doi.org/10.1016/j.jmb.2011.07.017.

(362) Pasta, S. Y.; Raman, B.; Ramakrishna, T.; Rao Ch, M. Role of the C-Terminal Extensions of Alpha-Crystallins. Swapping the C-Terminal Extension of Alpha-Crystallin to AlphaB-Crystallin Results in

Enhanced Chaperone Activity. *J Biol Chem* 2002, *277* (48), 45821–45828. https://doi.org/10.1074/jbc.M206499200.

(363) Biancalana, M.; Koide, S. Molecular Mechanism of Thioflavin-T Binding to Amyloid Fibrils. *Biochim Biophys Acta* 2010, *1804* (7), 1405–1412. https://doi.org/10.1016/j.bbapap.2010.04.001.

(364) Gade Malmos, K.; Blancas-Mejia, L. M.; Weber, B.; Buchner, J.; Ramirez-Alvarado, M.; Naiki, H.; Otzen, D. ThT 101: A Primer on the Use of Thioflavin T to Investigate Amyloid Formation. *Amyloid* 2017, *24* (1), 1–16. https://doi.org/10.1080/13506129.2017.1304905.

(365) F, M.; Ym, P.; J, L.; N, B.; T, G.; N, M.; P, B.; Arn, T.; Sc, P.; Rd, F.; R, L. The EMBL-EBI Search and Sequence Analysis Tools APIs in 2019. *Nucleic Acids Res.* 2019, *47* (W1), W636–W641. https://doi.org/10.1093/nar/gkz268.

(366) Chen, K.; Tjandra, N. Direct Measurements of Protein Backbone 15N Spin Relaxation Rates from Peak Line-Width Using a Fully-Relaxed Accordion 3D HNCO Experiment. *J. Magn. Reson. San Diego Calif 1997* 2009, *197* (1), 71–76. https://doi.org/10.1016/j.jmr.2008.12.001.

(367) Lange, O. F.; Lakomek, N.-A.; Farès, C.; Schröder, G. F.; Walter, K. F. A.; Becker, S.; Meiler, J.; Grubmüller, H.; Griesinger, C.; Groot, B. L. de. Recognition Dynamics Up to Microseconds Revealed from an RDC-Derived Ubiquitin Ensemble in Solution. *Science* 2008, *320* (5882), 1471–1475. https://doi.org/10.1126/science.1157092.

(368) Ghosh, J. G.; Estrada, M. R.; Clark, J. I. Interactive Domains for Chaperone Activity in the Small Heat Shock Protein, Human AB Crystallin. *Biochemistry* 2005, *44* (45), 14854–14869. https://doi.org/10.1021/bi0503910.

(369) Alderson, T. R.; Ying, J.; Bax, A.; Benesch, J. L. P.; Baldwin, A. J. Conditional Disorder in Small Heat-Shock Proteins. *J. Mol. Biol.* 2020. https://doi.org/10.1016/j.jmb.2020.02.003.

(370) Watkins, A. M.; Arora, P. S. Anatomy of β-Strands at Protein–Protein Interfaces. *ACS Chem. Biol.* 2014, *9* (8), 1747–1754. https://doi.org/10.1021/cb500241y.

(371) Baranova, E. V.; Weeks, S. D.; Beelen, S.; Bukach, O. V.; Gusev, N. B.; Strelkov, S. V. Three-Dimensional Structure of α-Crystallin Domain Dimers of Human Small Heat Shock Proteins HSPB1 and HSPB6. *J. Mol. Biol.* 2011, *411* (1), 110–122. https://doi.org/10.1016/j.jmb.2011.05.024.

(372) Wilson, M. R.; Easterbrook-Smith, S. B. Clusterin Is a Secreted Mammalian Chaperone. *Trends Biochem. Sci.* 2000, *25* (3), 95–98. https://doi.org/10.1016/s0968-0004(99)01534-0.

(373) Dunker, A. K.; Lawson, J. D.; Brown, C. J.; Williams, R. M.; Romero, P.; Oh, J. S.; Oldfield, C. J.; Campen, A. M.; Ratliff, C. M.; Hipps, K. W.; Ausio, J.; Nissen, M. S.; Reeves, R.; Kang, C.; Kissinger, C. R.; Bailey, R. W.; Griswold, M. D.; Chiu, W.; Garner, E. C.; Obradovic, Z. Intrinsically Disordered Protein. *J. Mol. Graph. Model.* 2001, *19* (1), 26–59. https://doi.org/10.1016/S1093-3263(00)00138-8.

(374) Carver, J. A.; Rekas, A.; Thorn, D. C.; Wilson, M. R. Small Heat-Shock Proteins and Clusterin: Intra- and Extracellular Molecular Chaperones with a Common Mechanism of Action and Function? *IUBMB Life* 2003, *55* (12), 661–668. https://doi.org/10.1080/15216540310001640498.

(375) Humphreys, D. T.; Carver, J. A.; Easterbrook-Smith, S. B.; Wilson, M. R. Clusterin Has Chaperone-like Activity Similar to That of Small Heat Shock Proteins. *J. Biol. Chem.* 1999, *274* (11), 6875–6881. https://doi.org/10.1074/jbc.274.11.6875.

(376) Kida, E.; Choi-Miura, N.-H.; Wisniewski, K. E. Deposition of Apolipoproteins E and J in Senile Plaques Is Topographically Determined in Both Alzheimer's Disease and Down's Syndrome Brain. *Brain Res.* 1995, *685* (1), 211–216. https://doi.org/10.1016/0006-8993(95)00482-6.

(377) Poon, S.; Rybchyn, M. S.; Easterbrook-Smith, S. B.; Carver, J. A.; Pankhurst, G. J.; Wilson, M. R. Mildly Acidic PH Activates the Extracellular Molecular Chaperone Clusterin. *J. Biol. Chem.* 2002, *277* (42), 39532–39540. https://doi.org/10.1074/jbc.M204855200.

(378) Sánchez-Pulido, L.; Devos, D.; Valencia, A. BRICHOS: A Conserved Domain in Proteins Associated with Dementia, Respiratory Distress and Cancer. *Trends Biochem. Sci.* 2002, *27* (7), 329–332. https://doi.org/10.1016/S0968-0004(02)02134-5.

(379) Johansson, H.; Eriksson, M.; Nordling, K.; Presto, J.; Johansson, J. The Brichos Domain of Prosurfactant Protein C Can Hold and Fold a Transmembrane Segment. *Protein Sci. Publ. Protein Soc.* 2009, *18* (6), 1175–1182. https://doi.org/10.1002/pro.123.

(380) Knight, S. D.; Presto, J.; Linse, S.; Johansson, J. The BRICHOS Domain, Amyloid Fibril Formation, and Their Relationship. *Biochemistry* 2013, *52* (43), 7523–7531. https://doi.org/10.1021/bi400908x.

(381) Willander, H.; Askarieh, G.; Landreh, M.; Westermark, P.; Nordling, K.; Keränen, H.; Hermansson, E.; Hamvas, A.; Nogee, L. M.; Bergman, T.; Saenz, A.; Casals, C.; Åqvist, J.; Jörnvall, H.; Berglund, H.; Presto, J.; Knight, S. D.; Johansson, J. High-Resolution Structure of a BRICHOS Domain and Its Implications for Anti-Amyloid Chaperone Activity on Lung Surfactant Protein C. *Proc. Natl. Acad. Sci.* 2012, *109* (7), 2325–2329. https://doi.org/10.1073/pnas.1114740109.

(382) Peng, S.; Fitzen, M.; Jörnvall, H.; Johansson, J. The Extracellular Domain of Bri2 (ITM2B) Binds the ABri Peptide (1-23) and Amyloid Beta-Peptide (Abeta1-40): Implications for Bri2 Effects on Processing of Amyloid Precursor Protein and Abeta Aggregation. *Biochem. Biophys. Res. Commun.* 2010, *393* (3), 356–361. https://doi.org/10.1016/j.bbrc.2009.12.122.

(383) Willander, H.; Presto, J.; Askarieh, G.; Biverstål, H.; Frohm, B.; Knight, S. D.; Johansson, J.; Linse, S. BRICHOS Domains Efficiently Delay Fibrillation of Amyloid β-Peptide. *J. Biol. Chem.* 2012, *287* (37), 31608–31617. https://doi.org/10.1074/jbc.M112.393157.

(384) Nerelius, C.; Gustafsson, M.; Nordling, K.; Larsson, A.; Johansson, J. Anti-Amyloid Activity of the C-Terminal Domain of ProSP-C against Amyloid β-Peptide and Medin †. *Biochemistry* 2009, *48* (17), 3778–3786. https://doi.org/10.1021/bi900135c.

(385) Marino, S. M.; Gladyshev, V. N. Cysteine Function Governs Its Conservation and Degeneration and Restricts Its Utilization on Protein Surface. *J. Mol. Biol.* 2010, *404* (5), 902–916. https://doi.org/10.1016/j.jmb.2010.09.027.

(386) Diaz-Latoud, C.; Buache, E.; Javouhey, E.; Arrigo, A.-P. Substitution of the Unique Cysteine Residue of Murine Hsp25 Interferes with the Protective Activity of This Stress Protein Through Inhibition of Dimer Formation. *Antioxid. Redox Signal.* 2005, *7* (3–4), 436–445. https://doi.org/10.1089/ars.2005.7.436.

(387) Zavialov, A.; Benndorf, R.; Ehrnsperger, M.; Zav'yalov, V.; Dudich, I.; Buchner, J.; Gaestel, M. The Effect of the Intersubunit Disulfide Bond on the Structural and Functional Properties of the Small Heat Shock Protein Hsp25. *Int. J. Biol. Macromol.* 1998, *22* (3), 163–173. https://doi.org/10.1016/S0141-8130(98)00014-2.

(388) Chalova, A. S.; Sudnitsyna, M. V.; Semenyuk, P. I.; Orlov, V. N.; Gusev, N. B. Effect of Disulfide Crosslinking on Thermal Transitions and Chaperone-like Activity of Human Small Heat Shock

Protein HspB1. *Cell Stress Chaperones* 2014, *19* (6), 963–972. https://doi.org/10.1007/s12192-014-0520-9.

(389) Pasupuleti, N.; Gangadhariah, M.; Padmanabha, S.; Santhoshkumar, P.; Nagaraj, R. H. The Role of the Cysteine Residue in the Chaperone and Anti-Apoptotic Functions of Human Hsp27. *J. Cell. Biochem.* 2010, *110* (2), 408–419. https://doi.org/10.1002/jcb.22552.

(390) Arrigo, A.-P.; Virot, S.; Chaufour, S.; Firdaus, W.; Kretz-Remy, C.; Diaz-Latoud, C. Hsp27 Consolidates Intracellular Redox Homeostasis by Upholding Glutathione in Its Reduced Form and by Decreasing Iron Intracellular Levels. 19.

(391) Bruey, J. M.; Ducasse, C.; Bonniaud, P.; Ravagnan, L.; Susin, S. A.; Diaz-Latoud, C.; Gurbuxani, S.; Arrigo, A. P.; Kroemer, G.; Solary, E.; Garrido, C. Hsp27 Negatively Regulates Cell Death by Interacting with Cytochrome c. *Nat. Cell Biol.* 2000, *2* (9), 645–652.

(392) Finkel, T.; Holbrook, N. J. Oxidants, Oxidative Stress and the Biology of Ageing. *Nature* 2000, *408* (6809), 239–247. https://doi.org/10.1038/35041687.

(393) Vanfleteren, J. R. Oxidative Stress and Ageing in Caenorhabditis Elegans. *Biochem. J.* 1993, *292* (2), 605–608. https://doi.org/10.1042/bj2920605.

(394) Jomova, K.; Vondrakova, D.; Lawson, M.; Valko, M. Metals, Oxidative Stress and Neurodegenerative Disorders. *Mol. Cell. Biochem.* 2010, *345* (1), 91–104. https://doi.org/10.1007/s11010-010-0563-x.

(395) Jenner, P.; Olanow, C. W. Understanding Cell Death in Parkinson's Disease. *Ann. Neurol.* 1998, *44* (S1), S72–S84. https://doi.org/10.1002/ana.410440712.